Surface Modification of Metal Oxide Materials with Aryldiazonium Ions

A thesis submitted in partial fulfilment of the requirements for the Degree

of Doctor of Philosophy in Chemistry

in the University of Canterbury

by Kalib Bell

University of Canterbury

2016

Acknowledgements

I would like to thank my supervisors Prof. Alison Downard and Dr. Paula Brooksby for their guidance and support during my project and in making the jump to Chemistry. I am grateful to the past and present members of the Downard research group for their help and companionship. I am also thankful to Assoc. Prof. Martin Allen for his support with the ZnO work. I would like to thank the staff and students in the Nanofabrication lab at the University of Canterbury for access to and assistance with their facilities. Thanks also go to Prof. Peter Steel and Dr. Chris Fitchett for organic chemistry consultations and the technical staff of the Department of Chemistry for their help with experimental apparatus. I would like to thank Dr. Colin Doyle at the University of Auckland for his assistance with XPS data acquisition and interpretation. I am grateful to my family and friends for all of their support throughout my PhD. Finally, I would like to thank the MacDiamid Institute and the University of Canterbury for financial support.

Table of Contents

Abstract

This thesis describes the development of methods to modify metal oxide surfaces with aryldiazonium ions and the characterisation of the effect of modification on the properties of these materials.

SU-8 2005 photoresist surfaces were used as a model system for modifying poorly conducting metal oxides. SU-8 surfaces were modified with nitrophenyl (NP) and methoxyphenyl (MP) groups at pH 7 and pH 10 in aqueous conditions. The thickness of the resulting films was measured by atomic force microscopy (AFM). The grafting reaction at pH 10 was found to have minimal dependence on the aryl substituent whereas at pH 7, MP-films required over 30 min to reach uniform coverage. It is proposed that the formation of the diazohydroxide intermediate at pH 7 is more favoured for the aryldiazonium ions with nitro substitution than methoxy substitution. In non-aqueous conditions, no grafting was observed by AFM after 1 h reaction time in the absence of reducing agent. In the presence of ferrocene as a reducing agent, scattered aggregates were found across the surface, suggesting the grafting reaction was rapid and uncontrolled.

These conditions were then adapted to modify MnO_2 nanoparticles and electrodeposited films and the effect on their electrochemical behaviour as pseudocapacitance materials was investigated. X-ray photoelectron spectroscopy (XPS) showed that attachment of aryl layers to the MnO_2 nanoparticles occurred via covalent bonding though surface O species. The capacitance of MnO_2 films was found by cyclic voltammetry (CV) to generally increase after modification at 50 mV s^{-1} scan rate but decrease at 500 mV s^{-1}. Electrochemical impedance spectroscopy (EIS) measurements indicated that the aryl layer introduced a diffusive resistance in the electrode, limiting charge storage at high scan rates. The origin of the increase in capacitance at low scan rates could not be identified, however, it is proposed that modification of the surface may introduce gap states that provide additional charge storage.

MBE-grown and bulk single crystal ZnO surfaces were modified at pH 8 in aqueous conditions with aryldiazonium ions. MBE-grown surfaces were modified electrochemically and non-electrochemically with a range of aryldiazonium ions, with electrochemical modification giving increased grafting density. These electrochemical modification conditions were then extended to single crystal O-polar, Zn-polar and m-plane ZnO surfaces, however, no signs of aryl layer attachment were observed. XPS analysis of modified MBE-grown and single crystal surfaces showed increased P-content after electrochemical cycling in the presence of aryldiazonium ions, most likely due to adsorption of phosphates from the modification solution. At single crystal surfaces this was found to vary with the

extent of O-termination of the crystal phase. Changes in valence band edge position were observed by XPS for some modified single crystal surfaces, however, this did not directly correlate to P-content at the surface, suggesting further modifications are occurring at the surface.

Abbreviations

AOS - Average oxidation state

AP - 4-aminophenyl

ATR - Attenuated total-reflectance

CE - Calomel electrode

CPE - Constant-phase element

CV - Cyclic voltammogram

EIS - Electrochemical impedance spectroscopy

GC - Glassy carbon

ITO - Indium tin oxide

LED - Light emitting diode

MBD - 4-methoxybenzenediazonium ion

MBE - Molecular beam epitaxy

MP - 4-methoxyphenyl

NBD - 4-nitrobenzenediazonium ion

NP - 4-nitrophenyl

PPF - Pyrolysed photoresist film

PR - Photoresist

PTFE - Polytetrafluoroethylene

RE - Reference electrode

SAM - Self-assembled monolayer

SCE - KCl-saturated calomel electrode

SEM - Scanning electron microscope

TBN	-	Tert-butyl Nitrite
ToF-SIMS	-	Time-of-flight secondary ion mass spectrometry
WE	-	Working electrode
XPS	-	X-ray photoelectron spectroscopy
XRD	-	X-ray powder diffraction

Publication

Bell, K. J.; Brooksby, P. A.; Polson, M. I. J.; Downard, A. J., Evidence for Covalent Bonding of Aryl Groups to MnO_2 Nanorods from Diazonium-Based Grafting. *Chem. Commun.* **2014,** *50* (89), 13687-13690.

1 Introduction

Metal oxides are a class of materials that exhibit a wide range of physical, chemical and electronic properties and can be prepared with diverse morphologies including 0-, 1- and 2-dimensional nanostructures such as nanoparticles, nanorods and thin films. This variety of properties and morphologies allows for a similar breadth of applications including energy generation and storage, catalysis and electronics.[1-3]

In a number of these applications, the properties of the metal oxide surface are vital to the function and stability of the material. For example in catalytic systems, the surfaces of the catalyst and support are involved in the catalytic reaction, as well as being potential sites of degradation of the material due to corrosion or catalytic poisoning.[4] Therefore by controlling the properties of metal oxide surfaces, the performance and stability of these materials can be enhanced. One approach to controlling surface properties is to use chemical modification to attach molecular layers to the surface to influence the behaviour of the underlying material or to add new functionalities.[5]

The work described in this thesis investigates the use of aryldiazonium ion-based grafting to modify MnO_2 and ZnO nanomaterials. The introduction to surface modification by aryldiazonium ion-based grafting is given in this chapter. The application of aryldiazonium ion-based grafting to non-conducting materials will be detailed in Chapter 3. The properties of MnO_2 and ZnO, and prior research on their chemical modification, will be described in Chapters 4 and 6 respectively.

1.1 Aryldiazonium Ion-Based Modification

Aryldiazonium salts have long been studied as reagents for organic synthesis, especially in the production of dyes.[6] The first detailed study of aryldiazonium ion grafting to surfaces was undertaken by Pinson et al., where aryl layers derived from aryldiazonium ions were electrografted to carbon surfaces and the involvement of aryl radicals in the grafting mechanism was proposed.[7] Subsequently aryldiazonium ions have been studied extensively as modification agents due to their ability to form stable covalent bonds to a variety of substrates and to give layers with a range of functionalities.[8-10] Films grafted from aryldiazonium salts have thicknesses ranging from < 1 nm for a monolayer (depending on substituent) to > 1 μm for polymeric films, with typical values being a few nm.[11-13] Aryldiazonium salt-based grafting has been used previously on a range of metal oxides including TiO_2, indium tin oxide (ITO), native oxides on Cu and Al surfaces, ZnO and Fe_3O_4.[14-19]

1.1.1 Synthesis of Aryldiazonium Ions

One of the main advantages of aryldiazonium ions is their straightforward synthesis from readily available aromatic amine derivatives.[8] For use for surface modification, aryldiazonium ions are either prepared as isolated salts or are used '*in situ*' without isolation.

Isolated salts can be prepared by either aqueous or nonaqueous routes. In aqueous conditions, the salt is prepared in ice cold acidic solution from the aromatic amine precursor by reaction with sodium nitrite. The low temperature acidic conditions are necessary as aryldiazonium salts are unstable in aqueous solution above 5 °C and at pH > 2.[9] Non-aqueous preparation of aryldiazonium salts is usually conducted in acetonitrile with tert-butyl nitrite as the diazotising agent. There are safety issues associated with isolated salts as they can be explosive and unstable at room temperature unless they are prepared with bulky counter-ions such as BF_4^-.[9, 10]

In addition to these safety concerns, some aryldiazonium ions of interest, such as 4-aminobenzenediazonium – a useful molecular tether, are very difficult to isolate and thus have to be prepared and used *in situ*. The *in situ* preparation involves reacting the amine with the diazotising agent in either acidic or non-aqueous solution and then immediately grafting from this solution. In this fashion, aryldiazonium ions can be reacted with the substrate without needing to be isolated or stored.[20, 21] Alternatively, the reaction can be conducted entirely in pure isoamyl nitrite which acts as both a solvent and diazotising agent.[10]

1.1.2 Modification Methods

Modification using aryldiazonium ions can be carried out by electrochemical (electrografting) or non-electrochemical reactions (e.g. chemical reduction or spontaneous reaction at room temperature and open-circuit potential). This diversity of methods enables modification of a range of conducting, semiconducting and insulating substrates.

1.1.2.1 Electrografting

The first report of surface modification by electrografting of aryldiazonium ions was the attachment of 4-nitrophenyl (NP) layers to glassy carbon (GC) electrodes by the electrochemical reduction of 4-nitrobenzenediazonium (NBD) BF_4^- salt.[7] Electrochemical grafting proceeds by reduction of the aryldiazonium ion to produce N_2 gas and an aryl radical which then attacks the surface to produce an aryl film grafted to the surface (Scheme 1.1, Steps 1 and 2). Electrografting is typically conducted in aqueous acid or acetonitrile as aryldiazonium ions are stable under these conditions.[9]

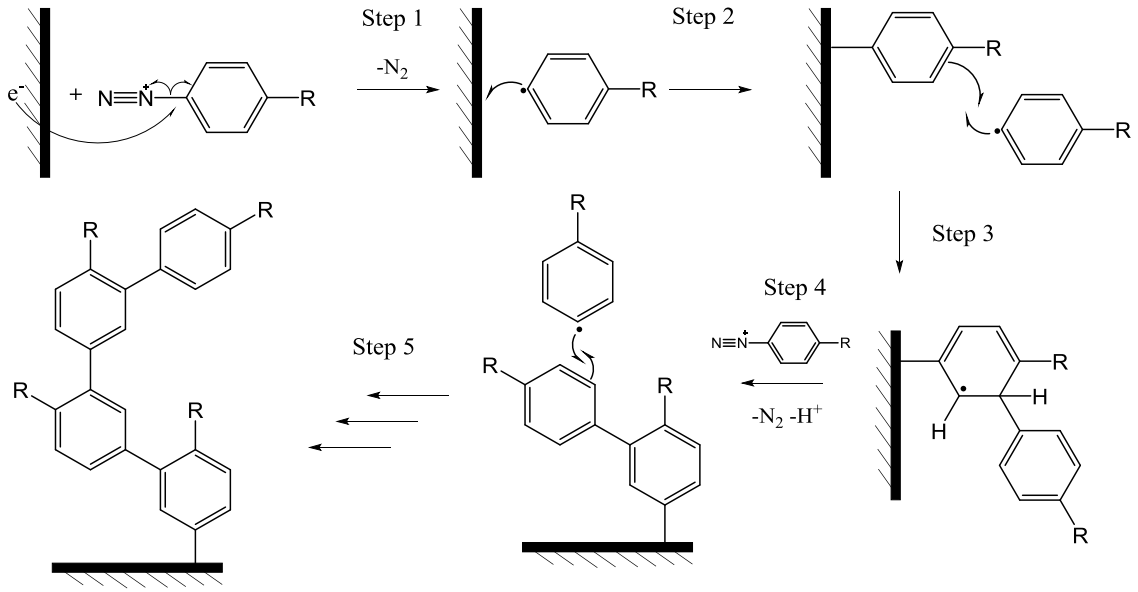

Scheme 1.1: Proposed mechanism for electrografting and multilayer formation by radical reactions of aryldiazonium salts, based on that of Pinson et al.[22]

In addition to grafting to the electrode surface, the reactivity of the radical species results in a number of side reactions. Radicals in solution can terminate by abstracting protons from the solvent or by dimerisation, however, this is less likely during electrografting due to the formation of the radicals close to the substrate. However, radicals produced at the substrate surface can also react with the growing aryl layer to form multilayers (Scheme 1.1, Step 3). Restoration of aromaticity after attack by aryl radicals occurs through an electron transfer to the electrode or reoxidation of the cyclohexadienyl radical by another aryldiazonium ion (Step 4). Multilayer formation by aryl radicals continues by this process until the layer is sufficiently thick to prevent electron transfer out to aryldiazonium ions in solution and thus further grafting (Step 5).[8] However, grafting by non-electrochemical methods (Section 1.1.2.2) has been reported to continue after the formation of a 'blocking' film that prevents electron transfer from the surface.[23]

Several methods have been used to limit aryl layer formation to a monolayer during electrografting. Menanteau et al. explored the use of radical scavengers to limit the multilayer formation by suppressing excess radicals produced during the grafting process at carbon electrodes. It was expected that when radicals are being scavenged from solution, the faster grafting kinetics of attachment to carbon versus the already-grafted film would result in grafting occurring solely at the carbon surface.[24] Surface coverage and film thickness measurements decreased with increasing radical scavenger concentration and were consistent with monolayer formation at a 2 × excess of the radical scavenger (2,2-diphenyl-1-picrylhydrazyl) compared to NBD salt.[12] No measurements of film roughness were provided, however, the monolayer films show signs of variable film density. This

is possibly due to the radical scavenger suppressing radical grafting at the surface in addition to grafting multilayer structures.

An alternative monolayer formation method is to prepare films with the desired modifier protected by bulky cleavable substituents. Subsequent multilayer formation will occur at the protecting groups such that when these groups are cleaved after the grafting reaction, the disordered multilayer film will be removed.[25, 26] Initial work in this area by Nielsen et al. grafted diaryldisulfides to prepare near-monolayers of thiophenolates by reductive cleavage of the disulfide bonds within the film.[25] However, this approach is limited to the preparation of near-monolayers as the diaryldisulfide group is not bulky enough to prevent grafting to the aryl ring below the disulfide bond resulting in multilayer material that is retained after the disulfide bonds are cleaved. An improvement to this strategy by Leroux et al. was the use of triisopropylsilyl as a cleavable protecting group that prevented grafting to the aryl layer by its increased steric bulk, allowing preparation of ethynylphenyl monolayers.[11] This method has been applied recently to prepare amine-terminated monolayers on carbon surfaces by grafting the *tert*-butyloxycarbonyl- and fluorenylmethyloxycarbonyl-protected aryldiazonium salts.[26] After the protecting groups were cleaved, the thickness of the grafted films decreased from ~2 nm to < 1 nm indicating the resulting film was monolayer or near monolayer in thickness. Film coverage measurements were conducted by using amide coupling reactions to immobilise redox probes onto the film surface and calculated coverages were approximately half the expected value for a close-packed monolayer. This low coverage may be due to the variable yield of coupling reactions masking the true quantity of film grafted or the size of the protecting group limiting the initial grafting step to sub-monolayer coverage. These studies suggest that grafting monolayer-thickness films is achievable but further work is needed to improve the uniformity of these surfaces.

Electrografting of aryldiazonium ions has been applied to metal oxides materials to control their surface properties. Tanguy et al. used electrografting aryldiazonium ions to lower the surface reactivity of $Li_{1.1}V_3O_8$ for Li-ion battery applications.[27] The high activity of nanostructured surfaces can lead to unwanted side reactions that reduce the stability of the electrode material. Attaching a thin (< 30 nm) coating to the surface can passivate it against unwanted reactions without restricting charge transfer during the energy storage process. $Li_{1.1}V_3O_8$ nanoparticles were modified with NP films by electrografting 0.2 M NBD salt during the lithium intercalation process in ethylene carbonate-dimethyl carbonate $LiPF_6$ (1 M). After cleaning by sonication, FT-IR of the modified material showed peaks characteristic of NP groups and an absence of diazonium groups indicating the grafting reaction was successful. The binding mode between the aryl layer and the oxide surface

was not studied, however evidence for azo linkages was observed via XPS. Transmission electron microscopy (TEM) images showed formation of a homogeneous ~ 2 nm thick layer around the oxide particles after 60 min modification suggesting formation of a continuous multilayer. The effect of modification on the chemical activity of the electrode was measured by monitoring electrolyte decomposition processes electrochemically. On the modified surface the electrolyte decomposition decreased significantly and the capacity retention of the electrode was improved without altering the electrochemical activity.

1.1.2.2 Non-electrochemical Grafting

Grafting of aryl layers from aryldiazonium ions can also be conducted at open-circuit potential and room temperature by a variety of methods depending on the substrate and reaction conditions. This has the advantage of allowing modification of materials that are insulating or otherwise difficult to form into electrodes.[10]

1.1.2.2.1 Reduction by Chemical Reagents

The most directly analogous method to electrografting is the use of chemical reducing agents to reduce the aryldiazonium ion to an aryl radical in acidic conditions. H_3PO_2 and iron powder are commonly employed for this.[28] As radicals are produced in solution rather than at the surface, the process is much less efficient than electrografting.[8] Abiman et al. compared grafting electroactive aryl layers to carbon powders with the reducing agent H_3PO_2 solution and in pure water.[29] The reducing agent was found to give lower surface coverage than the spontaneous reaction in pure water. Electrochemistry of the grafted layers in the presence of reducing agents only showed a single peak compared to multiple convoluted peaks when films were grafted spontaneously. These differences were proposed to be caused by the spontaneous grafting occurring through several types of linkages which give different redox potentials for the attached groups. Due to the rapid formation of radicals in the presence of a reducing agent, these alternative mechanisms are suppressed and the instability of radicals leads to a short period of film growth. A similar trend in film thickness for films derived by spontaneous reaction versus chemical reduction was observed by Simons et al. on insulating SU-8 substrates.[28] Atomic force microscopy (AFM) film thickness measurements showed that aminophenyl films grafted with H_3PO_2 were approximately half as thick as spontaneously grafted films. This reduced film thickness was due to the reducing agent rapidly converting aryldiazonium ions in solution into radicals that terminate in solution by reaction with each other or the solvent which limits the available radicals to graft to the surface.

1.1.2.2.2 Reduction by Conducting Substrates

Rather than electrons provided by an external circuit or an added reducing agent, sufficiently-reducing substrates can reduce aryldiazonium ions to aryl radicals by reacting with them directly by effectively the same process as shown in Scheme 1.1. This technique is limited by the reducing power of the substrate in relation to the aryldiazonium ion and is thus restricted in terms of what functionalities can be grafted to the surface as the substituents on the aryl ring influence the reduction potential of the aryldiazonium ion.[30] This dependence on the relative reducing power of the substrate has been demonstrated by the spontaneous grafting of aryldiazonium ions with different reduction potentials onto GC surfaces.[30] Of the aryldiazonium salts studied (R = NO_2, NEt_2, NHPh, NPh_2), only NBD was found to readily graft to the GC surface by spontaneous reaction. This was attributed to the ease of reduction of NBD arising from the strong electron-withdrawing character of the NO_2 substituent. The decreased driving-force for modification typically results in spontaneous grafting being less efficient than electrografting, requiring longer reaction times to achieve comparable surface coverage.[31, 32]

Spontaneous aryldiazonium ion reduction has been observed on carbon, metal and semiconductor surfaces.[18, 33, 34] Grafting via spontaneous reduction on carbon surfaces has been exploited industrially by the Cabot corporation to prepare modified carbon powders to use in ink.[35] Hurley and McCreery modified Cu and Cu/Al alloy surfaces via spontaneous reaction in acidic and non-aqueous media and observed attachment via Cu-C and Cu-O-C (to the native oxide) bonding by X-ray photoelectron spectroscopy (XPS).[18] The spontaneous reaction on Cu surfaces was expected to be analogous to the Gattermann and Sandermeyer reactions where copper catalysts reduce aryldiazonium ions to aryl radicals. Spontaneous modification has been used on other reducing metals including: Fe,[36, 37] Pd[34] and Zn.[37] Semiconducting GaAs and Si surfaces were also found by Stewart et al. to spontaneously reduce aryldiazonium ions for grafting of aryl radicals.[34]

1.1.2.2.3 Aryl Cation-Based Grafting

In addition to homolytic dediazoniation to form radicals, aryldiazonium ions have also been shown to spontaneously decompose heterolytically via loss of nitrogen gas to give aryl cations that are able to graft to surfaces in both acidic and non-aqueous solutions.[38] The mechanistic involvement of aryl cations was proposed for the modification of graphite and glassy carbon in the absence of reducing agent.[29] The area of the NP-reduction peak observed after modification with NBD in the absence of reducing agent was found to increase with increasing reaction temperature from 5-70 °C, suggesting thermal decomposition to aryl cations. However, grafting by spontaneous reduction is also possible at these substrates and thus grafting via the aryl cation may not be the dominant mechanism. The

involvement of aryl cations was also proposed by Mesnage et al. to explain the modification of Au surfaces (Scheme 1.2).[39] Despite Au being insufficiently reducing to reduce aryldiazonium ions to form aryl radicals, attachment of the aryl ring directly to the substrate via metal-C bonding was detected by XPS. Successful attachment was observed, independent of the substituent on the aryl ring (R = NO_2, SCH_3, COOH, Br, OCH_3) which exert varying inductive and mesomeric effects. This is in contrast to the reduction-based mechanisms described previously, where the effect of the substituent on the aryldiazonium ion reduction potential, and thus grafting efficiency, is significant. Grafting via the aryl cation mechanism was found to be favoured as pH increased (up to pH 2.68) due to the decreased stability of the aryldiazonium ion and was also favoured by the absence of Cl^- which can quench aryl cations. These experimental observations confirm the involvement of aryl cations as the grafting intermediate, however, the details of the mechanism of attachment to the surface are unclear.

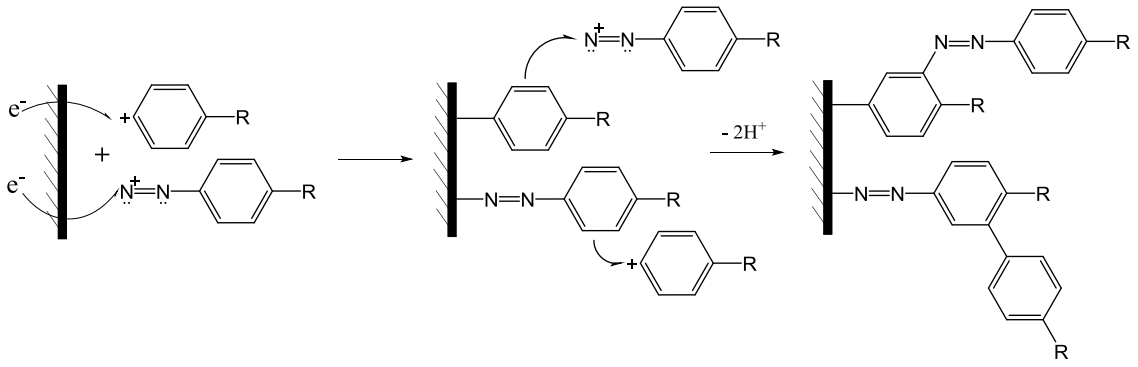

Scheme 1.2: Proposed mechanisms for spontaneous grafting via aryl cations or formation of azo linkages by direct attack of the aryldiazonium ion.[39]

Reaction via aryl cations has also been proposed as one of the dominant mechanisms for multilayer formation (Scheme 1.2) where aryl cations attack the already grafted groups, followed by elimination of H^+.[39] It has been proposed that this mechanism contributes to the continued grafting observed at blocking film surfaces in acetonitrile and aqueous acid where electron transfer into solution is not possible and spontaneous reduction of the aryldiazonium ion is unlikely. Gradual thermal decomposition of the aryldiazonium ion into aryl cations is consistent with the relatively slow reaction rate of multilayer formation compared to the initial film formation by spontaneous reduction at carbon surfaces.[23]

1.1.2.2.4 Direct Aryldiazonium Ion Grafting

The direct attack of the aryldiazonium ion to attach via azo linkages has been proposed as a grafting mechanism in acidic or non-aqueous solutions for inert substrates (Scheme 1.2). Attachment via azo

linkages has been observed via XPS by Mesnage et al. for Au and Ni substrates modified in acid and non-aqueous solution.[39] Azo linkages were observed with all modifiers studied (R = NO_2, SCH_3, COOH, Br, OCH_3), however, Au-N bonding from direct attachment of the aryldiazonium ion to the surface was not observed for COOH or OCH_3 substituted layers despite their electronic similarity to other layers (e.g. R = OCH_3 to SCH_3). This result is unexpected as direct grafting of the aryldiazonium ion is proposed as occurring by electrophilic attack and thus the electronic character of the substituent would affect grafting by influencing the electrophilicity of the aryldiazonium ion.[12] The absence of Au-N bonding in the XPS spectra for these samples may also be caused by low surface concentrations and the surface insensitivity of 1486 eV X-rays resulting in Au-N bonds being undetected. Spontaneous grafting of NBD through azo linkages directly to carbon surfaces has also been observed when the radical grafting mechanisms are quenched by radical scavengers.[12, 40] The proportion of azo linkages on the grafted surface detected by XPS was found to increase with the concentration of radical scavenger and decrease with the thickness of the grafted film. These results suggest that the azo linkages are primarily between the aryl layer and the substrate rather than within the layer. The low concentration of azo linkages within the film was explained as being due to the electron-withdrawing NO_2 group on the already-grafted film deactivating the aryl ring for attack by aryldiazonium ions (via the mechanism in Scheme 1.2). Grafting through azo linkages is favoured at open-circuit potential where there is less driving force for the conversion of aryldiazonium ions to radicals.

1.1.2.2.5 Diazoate-Based Grafting

In contrast to acidic and non-aqueous conditions, at neutral and basic pH, the aryldiazonium ion is highly unstable and instead forms a diazohydroxide which converts to a diazoate. Diazoates and diazohydroxides decompose homolytically to form aryl radicals that can graft to the surface (Scheme 1.3)[41-43] As no reduction by the substrate is required, this method functions on inert substrates like Au.[42] In addition to spontaneous decomposition, radical formation by electrochemical reduction of diazoates has been observed at GC in pH 10 buffer at 0.025 V vs. SCE. This suggests that at sufficiently reducing metals, such as Fe, grafting may also occur via reduction of the diazoate to radicals by the substrate.[42]

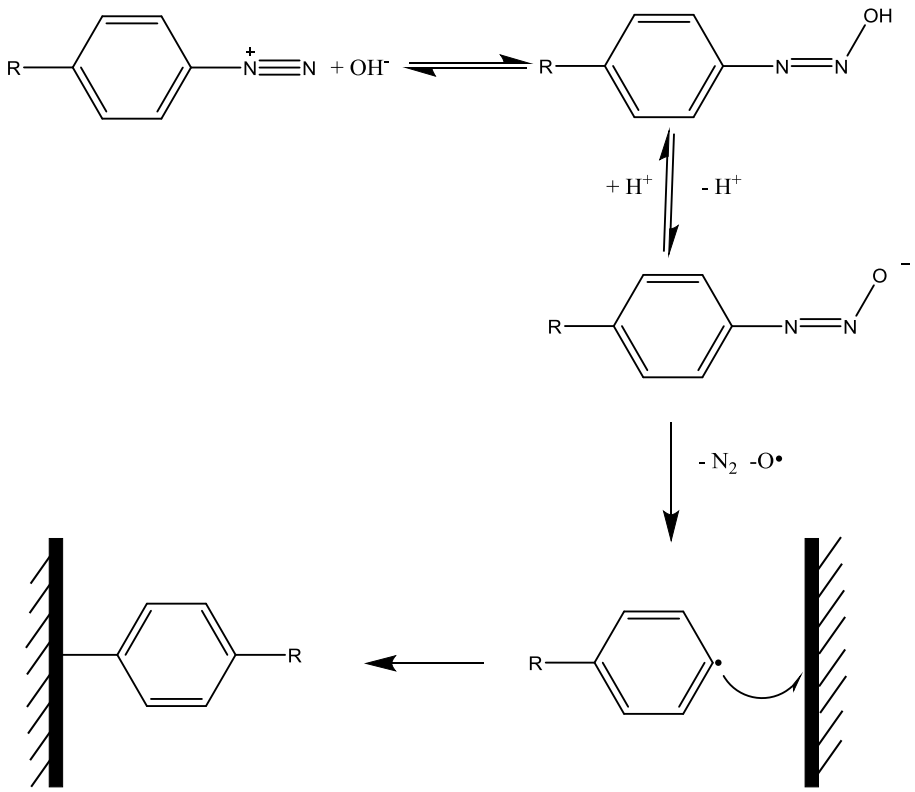

Scheme 1.3: Diazoate formation in high pH solution and surface modification by the resulting aryl radicals.

The diazoate mechanism has been used to modify metals (Fe and Au), insulators (SiO_2) and metal oxides (TiO_2, Fe_3O_4, Gd_2O_3 and Al_2O_3).[42, 44-46] The diazoate mechanism is useful due to the low reducing power of many oxide materials as they are unable to reduce aryldiazonium ions. For example, Griffete et al. modified Fe_3O_4 nanoparticles with aryldiazonium salts at pH 9 to improve their aqueous dispersibility.[46] This modification approach was successful with both pre-formed nanoparticles and using the aryldiazonium grafting process to form a capping layer around the nanoparticles within the particle synthesis solution. The aryl layer was identified on the surface by peaks assigned to C=C bonding in the FT-IR spectra of the modified particles, however, the bonding between the particles and the layer was not characterised. Subsequent work by Brymora et al. used ^{57}Fe Mössbauer spectroscopy to identify grafting through Fe-O-C bonds by on Fe_2O_3 particles modified by the same route.[47]

A related mechanism is grafting via the diazoanhydride which is favoured in neutral conditions. Reaction between a diazoate and another aryldiazonium ion by the Gomberg-Bachmann reaction can lead to the formation of a diazoanhydride which decomposes homolytically to form radicals (Scheme 1.4). This mechanism has been proposed for the modification of carbon nanotubes in pure water and dimethylformamide.[48, 49] Schmidt et al. identified radicals as the key reactive species in

modification of carbon nanotubes in water as grafting reaction was suppressed in the presence of the radical scavenger (2,2,6,6-Tetramethyl-1-piperidinyl)oxidanyl.[48] Analysis by electron spin resonance spectroscopy indicated that the grafting reaction occurs by a radical chain mechanism involving the carbon nanotubes. This reaction is pH dependent and was found to be dominant at neutral pH as the reaction was suppressed in the presence of excess HCl.[48] During grafting in dimethylformamide, the involvement of diazoanhydride-derived radicals was evidenced by the introduction of O species during the grafting process as detected by XPS.[49] Grafting was found to be independent of the substituent used, providing further evidence for radical production by spontaneous decomposition rather than a reduction process. It is difficult to determine from these results any influence on the substituent on the decomposition of the diazoanhydride as a number of the substituents studied introduce O-content into the modified samples in addition to any resulting from grafting by diazoanhydride-derived radicals.

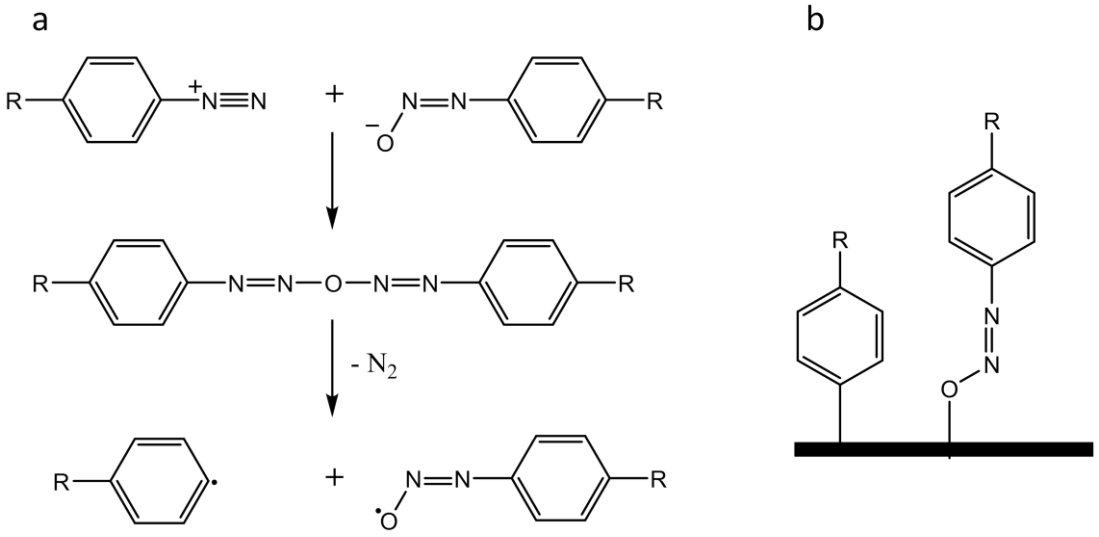

Scheme 1.4: a. Formation of radicals via a diazoanhydride intermediate, b. Bonding between diazoanhydride-derived radicals and a surface.[49]

1.1.2.2.6 Other Methods

In addition to the methods described above, aryldiazonium grafting reactions have been driven by several other methods.

Photochemical grafting is a method that can be used as both a modification and patterning strategy by exploiting photolithography techniques. Aryl layers have been grafted by photochemical methods onto metals and semiconductors.[50, 51] Zhao et al. grafted films from 4-(2-(4-Pyridinyl)ethynyl)benzenediazonium salt to quartz, ITO and Si by immersing the substrate in

non-aqueous aryldiazonium ion solution for 24 hours before irradiating with 200 W UV radiation. UV-vis spectroscopy was used to observe the decomposition of the diazonium group on irradiation of modified quartz substrates. Covalent bonding to the substrate was inferred from the stability of the aryl layers, however, the bonding mode and grafting mechanism were not studied.[50] Photochemical modification has been used to modify Au, Cu and Fe surfaces by visible and UV light. Visible light modification relied on formation of a charge transfer complex between NBD and 1, 4-dimethoxybenzene which had been found previously to decompose to NP and 1,4-dimethoxybenzene cation radicals upon irradiation. Modification of Au surfaces by visible light irradiation was confirmed by IR reflection-absorption spectroscopy and the film thickness was found to be 50 nm (suggesting significant multilayer formation) after 20 min irradiation. Similar results were obtained on the Cu and Fe surfaces. Modification under UV irradiation was achieved on metal surfaces using just the aryldiazonium salt without requiring formation of a charge transfer complex. Film thickness measurements on a modified Cu surface revealed the grafted film was a multilayer (thickness ~36 nm).[51] The mechanism for modification under UV irradiation was not described.

Mechanical decomposition via sonication and ball-milling have also been used to graft aryldiazonium salts to undoped nanodiamonds, GC and ITO surfaces.[52-54] In the ultrasonic modification procedure, solvent sonolysis forms radicals (e.g. $OH^{\bullet}$ and $H^{\bullet}$ in H_2O) that reduce diazonium groups giving aryl radicals which attach to the surface.[52, 54] Mirkhalaf et al. studied the effect of ultrasound frequency on the grafting of NBD to ITO surfaces in acetonitrile.[54] Ultrasound frequencies ranging from 20-1142 kHz were compared using XPS analysis of the resulting films. XPS peak intensity of C and N functionalities arising from grafting were highest at 20 kHz, suggesting an inverse dependence of grafting on the frequency. It was proposed that this trend resulted from increased cavitation collapse rates at higher frequency causing more radicals to form and react in solution rather than at the ITO surface. Additionally, it was observed that the films grafted at high frequency had a higher proportion of reduced-N functionalities (e.g. NH_2), suggesting the high frequency sonication procedure was causing chemical reduction of the NP film. This result has significance for processing of modified materials where sonication steps for cleaning or dispersion (of nanomaterials) may change the chemical nature of the film.

1.1.3 Characterisation of Aryl Layers

Due to the possibility of very low layer thickness when grafting from aryldiazonium ions (< 1 nm for a monolayer film),[12] characterisation of modified surfaces can be difficult. Film characterisation techniques are focused on revealing either the physical properties (e.g. coverage and morphology) or chemical nature (bonding and terminal functionality) of the film.

Film morphology is usually characterised by AFM or TEM which have been used to identify grafted films down to monolayer thickness on surfaces. AFM can be used as a method to measure film thickness on planar substrates by imaging across an edge of the film to the bare substrate. One approach to expose the underlying substrate is to use the AFM tip to scratch the film away and profile across this scratch.[55] Alternatively, patterned substrates can be prepared using photolithography and then film grafted in the exposed areas of the pattern. Subsequent removal of the photoresist reveals bare areas of substrate. Profiling across bare and film-covered areas gives a measure of the film thickness.[28] TEM imaging can also be used to measure film thickness on nanomaterials due to contrast differences between the grafted layer and the substrate.[27] Scanning tunnelling electron microscopy (STM) has been used to characterise film attachment to graphite surfaces. The high resolution of STM enabled bound molecules to be observed at the step-edges of highly-oriented pyrolytic graphite, however, the molecules on the basal planes appeared to be highly mobile rather than attached to the surface and no change of hybridisation due to grafting was detected.[56] Subsequently, work by Greenwood et al. has demonstrated that bonding does occur to the basal plane of highly-oriented pyrolytic graphite but that upon removal of the film, the surface reverts to pristine graphite which masks the changes in hybridisation during grafting.[57]

The quantity of film and strength of attachment has been measured by thermogravimetrc analysis (TGA). Toupin et al. observed a ~5% mass loss due to the NP film on modified carbon powder and the high (> 200 °C) decomposition temperature suggests that the film is stably attached to the surface.[58]

The chemical nature of the film can be investigated by FT-IR, XPS and time-of-flight secondary ion mass spectrometry (ToF-SIMS). In addition to detection of terminal functional groups, FT-IR can be used to monitor grafting reactions by measuring the disappearance of the IR-active diazonium group.[59] XPS has been used to characterise bonding between the aryl layer and the substrate as well as between aryl groups within multilayers. As the binding energy of core electrons is sensitive to the chemical state of the atoms involved, different types of bonding can be identified by peak-fitting the additional features produced by the resulting shifts in binding energy from the main element peak. Peak fitting to the O 1s spectrum can be used to detect metal-O-C bonding to oxide surfaces. The presence of metal-C bonds has been determined from C 1s spectra, and N 1s spectra can give information about azo linkages in the film or to the surface.[15, 18] ToF-SIMS has also been used to characterise the bonding to the surface based on fragments containing substrate-C or substrate-N bonds.[22]

As many of the substrates modified by aryldiazonium ions are electroactive, electrochemical characterisation is extensively used to monitor film functionality and coverage. Successful grafting can be observed by the presence of electroactive groups or the loss of current due to blocking films. Surfaces with pH-responsive modifiers also usually show pH-responsive electrochemical behaviour. Estimates of film coverage and thickness can be made by quantifying the charge transfer to electroactive films - most commonly NP films. Alternatively, redox active groups can be coupled to a non-electroactive layer.[26]

1.2 Aims

The aim of this thesis is to develop methods to modify metal oxide materials with aryldiazonium salts and determine the effect of modification on their material properties and performance with a particular focus on MnO_2 and ZnO.

This thesis is organised as follows:

Chapter 2: *General Experimental Methods*: describes general experimental procedures and equipment used in this thesis.

Chapter 3: *Aryldiazonium ion-based Grafting to Model Non-conducting Surfaces*: describes the modification of SU-8 surfaces in aqueous and non-aqueous conditions as a model non-conducting substrate.

Chapter 4: *Modification of MnO2 Nanoparticles with Aryldiazonium Ions:* describes development of aqueous and non-aqueous conditions for modifying MnO_2 nanoparticles and characterisation of the modified particles.

Chapter 5: *Electrochemical Investigations of Electrodeposited MnO2 Films Modified with Aryldiazonium Ions*: explores the electrochemical behaviour of modified MnO_2 surfaces using electrodeposited MnO_2.

Chapter 6: *Modification of ZnO Surfaces with Aryldiazonium Ions*: describes development of conditions to modify various ZnO materials and characterisation of the modified materials.

Chapter 7: *Conclusion:* summarises the overall thesis work and provides suggestions for future work.

1.3 References

1. Lokhande, C. D.; Dubal, D. P.; Joo, O.-S., Metal Oxide Thin Film Based Supercapacitors. *Curr. Appl. Phys.* **2011,** *11* (3), 255-270.

2. Shen, G.; Chen, P.-C.; Ryu, K.; Zhou, C., Devices and Chemical Sensing Applications of Metal Oxide Nanowires. *J. Mater. Chem.* **2009,** *19* (7), 828-839.
3. Jose, R.; Thavasi, V.; Ramakrishna, S., Metal Oxides for Dye-Sensitized Solar Cells. *J. Am. Ceram. Soc.* **2009,** *92* (2), 289-301.
4. Lee, D. W.; Yoo, B. R., Advanced Metal Oxide (Supported) Catalysts: Synthesis and Applications. *J. of Ind. and Eng. Chem.* **2014,** *20* (6), 3947-3959.
5. Pujari, S. P.; Scheres, L.; Marcelis, A. T. M.; Zuilhof, H., Covalent Surface Modification of Oxide Surfaces. *Angew. Chem. Int. Ed.* **2014,** *53* (25), 6322-6356.
6. Merino, E., Synthesis of Azobenzenes: The Coloured Pieces of Molecular Materials. *Chem. Soc. Rev.* **2011,** *40* (7), 3835-3853.
7. Delamar, M.; Hitmi, R.; Pinson, J.; Saveant, J. M., Covalent Modification of Carbon Surfaces by Grafting of Functionalized Aryl Radicals Produced from Electrochemical Reduction of Diazonium Salts. *J. Am. Chem. Soc.* **1992,** *114* (14), 5883-5884.
8. Belanger, D.; Pinson, J., Electrografting: A Powerful Method for Surface Modification. *Chem. Soc. Rev.* **2011,** *40* (7).
9. Assresahegn, B. D.; Brousse, T.; Bélanger, D., Advances on the Use of Diazonium Chemistry for Functionalization of Materials Used in Energy Storage Systems. *Carbon* **2015,** *92* (0), 362-381.
10. Mohamed, A. A.; Salmi, Z.; Dahoumane, S. A.; Mekki, A.; Carbonnier, B.; Chehimi, M. M., Functionalization of Nanomaterials with Aryldiazonium Salts. *Adv. Colloid Interface Sci.* **2015,** *225*, 16-36.
11. Leroux, Y. R.; Fei, H.; Noël, J.-M.; Roux, C.; Hapiot, P., Efficient Covalent Modification of a Carbon Surface: Use of a Silyl Protecting Group to Form an Active Monolayer. *J. Am. Chem. Soc.* **2010,** *132* (40), 14039-14041.
12. Menanteau, T.; Levillain, E.; Downard, A. J.; Breton, T., Evidence of Monolayer Formation Via Diazonium Grafting with a Radical Scavenger: Electrochemical, AFM and XPS Monitoring. *PCCP* **2015,** *17* (19), 13137-13142.
13. Adenier, A.; Combellas, C.; Kanoufi, F.; Pinson, J.; Podvorica, F. I., Formation of Polyphenylene Films on Metal Electrodes by Electrochemical Reduction of Benzenediazonium Salts. *Chem. Mater.* **2006,** *18* (8), 2021-2029.
14. Griffete, N.; Lamouri, A.; Herbst, F.; Felidj, N.; Ammar, S.; Mangeney, C., Synthesis of Highly Soluble Polymer-Coated Magnetic Nanoparticles Using a Combination of Diazonium Salt Chemistry and the Iniferter Method. *RSC Adv.* **2012,** *2* (3), 826-830.
15. Mesnage, A.; Abdel Magied, M.; Simon, P.; Herlin-Boime, N.; Jégou, P.; Deniau, G.; Palacin, S., Grafting Polymers to Titania Nanoparticles by Radical Polymerization Initiated by Diazonium Salt. *J. of Mater. Sci.* **2011,** *46* (19), 6332-6338.
16. Maldonado, S.; Smith, T. J.; Williams, R. D.; Morin, S.; Barton, E.; Stevenson, K. J., Surface Modification of Indium Tin Oxide Via Electrochemical Reduction of Aryldiazonium Cations. *Langmuir* **2006,** *22* (6), 2884-2891.
17. Merson, A.; Dittrich, T.; Zidon, Y.; Rappich, J.; Shapira, Y., Charge Transfer from TiO_2 into Adsorbed Benzene Diazonium Compounds. *Appl. Phys. Lett.* **2004,** *85* (6), 1075-1076.
18. Hurley, B. L.; McCreery, R. L., Covalent Bonding of Organic Molecules to Cu and Al Alloy 2024 T3 Surfaces Via Diazonium Ion Reduction. *J. Electrochem. Soc.* **2004,** *151* (5), B252-B259.
19. Wang, C.; Huang, N.; Zhuang, H.; Jiang, X., Enhanced Performance of Nanocrystalline ZnO DNA Biosensor Via Introducing Electrochemical Covalent Biolinkers. *ACS Appl. Mater. Interfaces* **2015,** *7* (14), 7605-7612.
20. Baranton, S.; Bélanger, D., Electrochemical Derivatization of Carbon Surface by Reduction of in Situ Generated Diazonium Cations. *J. of Phys. Chem. B* **2005,** *109* (51), 24401-24410.
21. Baranton, S.; Bélanger, D., In Situ Generation of Diazonium Cations in Organic Electrolyte for Electrochemical Modification of Electrode Surface. *Electrochim. Acta* **2008,** *53* (23), 6961-6967.

22. Doppelt, P.; Hallais, G.; Pinson, J.; Podvorica, F.; Verneyre, S., Surface Modification of Conducting Substrates. Existence of Azo Bonds in the Structure of Organic Layers Obtained from Diazonium Salts. *Chem. Mater.* **2007,** *19* (18), 4570-4575.
23. Lehr, J.; Williamson, B. E.; Downard, A. J., Spontaneous Grafting of Nitrophenyl Groups to Planar Glassy Carbon Substrates: Evidence for Two Mechanisms. *J. of Phys. Chem. C* **2011,** *115* (14), 6629-6634.
24. Menanteau, T.; Levillain, E.; Breton, T., Electrografting Via Diazonium Chemistry: From Multilayer to Monolayer Using Radical Scavenger. *Chem. Mater.* **2013,** *25* (14), 2905-2909.
25. Nielsen, L. T.; Vase, K. H.; Dong, M.; Besenbacher, F.; Pedersen, S. U.; Daasbjerg, K., Electrochemical Approach for Constructing a Monolayer of Thiophenolates from Grafted Multilayers of Diaryl Disulfides. *J. Am. Chem. Soc.* **2007,** *129* (7), 1888-1889.
26. Lee, L.; Leroux, Y. R.; Hapiot, P.; Downard, A. J., Amine-Terminated Monolayers on Carbon: Preparation, Characterization, and Coupling Reactions. *Langmuir* **2015,** *31* (18), 5071-5077.
27. Tanguy, F.; Gaubicher, J.; Gaillot, A.-C.; Guyomard, D.; Pinson, J., Lowering Interfacial Chemical Reactivity of Oxide Materials for Lithium Batteries. A Molecular Grafting Approach. *J. Mater. Chem.* **2009,** *19* (27), 4771-4777.
28. Simons, B. M.; Lehr, J.; Garrett, D. J.; Downard, A. J., Formation of Thick Aminophenyl Films from Aminobenzenediazonium Ion in the Absence of a Reduction Source. *Langmuir* **2014,** *30* (17), 4989-4996.
29. Abiman, P.; Wildgoose, G. G.; Compton, R. G., A Mechanistic Investigation into the Covalent Chemical Derivatisation of Graphite and Glassy Carbon Surfaces Using Aryldiazonium Salts. *J. Phys. Org. Chem.* **2008,** *21* (6), 433-439.
30. Le Floch, F.; Simonato, J.-P.; Bidan, G., Electrochemical Signature of the Grafting of Diazonium Salts: A Probing Parameter for Monitoring the Electro-Addressed Functionalization of Devices. *Electrochim. Acta* **2009,** *54* (11), 3078-3085.
31. Combellas, C.; Kanoufi, F.; Pinson, J.; Podvorica, F. I., Time-of-Flight Secondary Ion Mass Spectroscopy Characterization of the Covalent Bonding between a Carbon Surface and Aryl Groups. *Langmuir* **2005,** *21* (1), 280-286.
32. Bahr, J. L.; Tour, J. M., Highly Functionalized Carbon Nanotubes Using in Situ Generated Diazonium Compounds. *Chem. Mater.* **2001,** *13* (11), 3823-3824.
33. Toupin, M.; Bélanger, D., Spontaneous Functionalization of Carbon Black by Reaction with 4-Nitrophenyldiazonium Cations. *Langmuir* **2008,** *24* (5), 1910-1917.
34. Stewart, M. P.; Maya, F.; Kosynkin, D. V.; Dirk, S. M.; Stapleton, J. J.; McGuiness, C. L.; Allara, D. L.; Tour, J. M., Direct Covalent Grafting of Conjugated Molecules onto Si, GaAs, and Pd Surfaces from Aryldiazonium Salts. *J. Am. Chem. Soc.* **2004,** *126* (1), 370-378.
35. Belmont, J. A.; Amici, R. M.; Galloway, C. P. Reaction of Carbon Black with Diazonium Salts, Resultant Carbon Black Products and Their Uses. 1998.
36. Combellas, C.; Delamar, M.; Kanoufi, F.; Pinson, J.; Podvorica, F. I., Spontaneous Grafting of Iron Surfaces by Reduction of Aryldiazonium Salts in Acidic or Neutral Aqueous Solution. Application to the Protection of Iron against Corrosion. *Chem. Mater.* **2005,** *17* (15), 3968-3975.
37. Adenier, A.; Cabet-Deliry, E.; Chaussé, A.; Griveau, S.; Mercier, F.; Pinson, J.; Vautrin-Ul, C., Grafting of Nitrophenyl Groups on Carbon and Metallic Surfaces without Electrochemical Induction. *Chem. Mater.* **2005,** *17* (3), 491-501.
38. S. J. Canning, P.; McCrudden, K.; Maskill, H.; Sexton, B., Rates and Mechanisms of the Thermal Solvolytic Decomposition of Arenediazonium Ions. *J. of the Chem. Soc., Perkin Trans. 2* **1999,** (12), 2735-2740.
39. Mesnage, A.; Lefèvre, X.; Jégou, P.; Deniau, G.; Palacin, S., Spontaneous Grafting of Diazonium Salts: Chemical Mechanism on Metallic Surfaces. *Langmuir* **2012,** *28* (32), 11767-11778.
40. Menanteau, T.; Levillain, E.; Breton, T., Spontaneous Grafting of Nitrophenyl Groups on Carbon: Effect of Radical Scavenger on Organic Layer Formation. *Langmuir* **2014,** *30* (26), 7913-7918.

41. Pazo-Llorente, R.; Bravo-Diaz, C.; Gonzalez-Romero, E., Ph Effects on Ethanolysis of Some Arenediazonium Ions: Evidence for Homolytic Dediazoniation Proceeding through Formation of Transient Diazo Ethers. *Eur. J. Org. Chem.* **2004,** *2004* (15), 3221-3226.
42. Podvorica, F. I.; Kanoufi, F.; Pinson, J.; Combellas, C., Spontaneous Grafting of Diazoates on Metals. *Electrochim. Acta* **2009,** *54* (8), 2164-2170.
43. Sienkiewicz, A.; Szymula, M.; Narkiewicz-Michalek, J.; Bravo-Díaz, C., Formation of Diazohydroxides Arn_2oh in Aqueous Acid Solution: Polarographic Determination of the Equilibrium Constant Kr for the Reaction of 4-Substituted Arenediazonium Ions with H_2o. *J. Phys. Org. Chem.* **2014,** *27* (4), 284-289.
44. Griffete, N.; Ahmad, R.; Benmehdi, H.; Lamouri, A.; Decorse, P.; Mangeney, C., Elaboration of Hybrid Silica Particles Using a Diazonium Salt Chemistry Approach. *Colloids Surf., A* **2013,** *439* (0), 145-150.
45. Dechézelles, J.-F.; Griffete, N.; Dietsch, H.; Scheffold, F., A General Method to Label Metal Oxide Particles with Fluorescent Dyes Using Aryldiazonium Salts. *Part. Part. Syst. Char.* **2013,** *30* (7), 579-583.
46. Griffete, N. b. w.; Herbst, F. d. r.; Pinson, J.; Ammar, S.; Mangeney, C., Preparation of Water-Soluble Magnetic Nanocrystals Using Aryl Diazonium Salt Chemistry. *J. Am. Chem. Soc.* **2011,** *133* (6), 1646-1649.
47. Brymora, K.; Fouineau, J.; Eddarir, A.; Chau, F.; Yaacoub, N.; Grenèche, J.-M.; Pinson, J.; Ammar, S.; Calvayrac, F., Grafting of Diazonium Salts on Oxides Surface: Formation of Aryl-O Bonds on Iron Oxide Nanoparticles. *J. Nanopart. Res.* **2015,** *17* (11), 1-9.
48. Schmidt, G.; Gallon, S.; Esnouf, S.; Bourgoin, J.-P.; Chenevier, P., Mechanism of the Coupling of Diazonium to Single-Walled Carbon Nanotubes and Its Consequences. *Chem. Eur. J.* **2009,** *15* (9), 2101-2110.
49. Lipińska, M. E.; Rebelo, S. L. H.; Pereira, M. F. R.; Gomes, J. A. N. F.; Freire, C.; Figueiredo, J. L., New Insights into the Functionalization of Multi-Walled Carbon Nanotubes with Aniline Derivatives. *Carbon* **2012,** *50* (9), 3280-3294.
50. Zhao, W.; Tong, B.; Pan, Y.; Shen, J.; Zhi, J.; Shi, J.; Dong, Y., Fabrication, Electrochemical, and Optoelectronic Properties of Layer-by-Layer Films Based on (Phthalocyaninato)Ruthenium(Ii) and Triruthenium Dodecacarbonyl Bridged by 4,4'-Bipyridine as Ligand. *Langmuir* **2009,** *25* (19), 11796-11801.
51. Busson, M.; Berisha, A.; Combellas, C.; Kanoufi, F.; Pinson, J., Photochemical Grafting of Diazonium Salts on Metals. *Chem. Commun.* **2011,** *47* (47), 12631-12633.
52. Mangeney, C.; Qin, Z.; Dahoumane, S. A.; Adenier, A.; Herbst, F.; Boudou, J.-P.; Pinson, J.; Chehimi, M. M., Electroless Ultrasonic Functionalization of Diamond Nanoparticles Using Aryl Diazonium Salts. *Diamond Relat. Mater.* **2008,** *17* (11), 1881-1887.
53. Pandurangappa, M.; Ramakrishnappa, T.; Compton, R. G., Functionalization of Glassy Carbon Spheres by Ball Milling of Aryl Diazonium Salts. *Carbon* **2009,** *47* (9), 2186-2193.
54. Mirkhalaf, F.; Mason, T. J.; Morgan, D. J.; Saez, V., Frequency Effects on the Surface Coverage of Nitrophenyl Films Ultrasonically Grafted onto Indium Tin Oxide. *Langmuir* **2011,** *27* (5), 1853-1858.
55. Anariba, F.; DuVall, S. H.; McCreery, R. L., Mono- and Multilayer Formation by Diazonium Reduction on Carbon Surfaces Monitored with Atomic Force Microscopy "Scratching". *Anal. Chem.* **2003,** *75* (15), 3837-3844.
56. Ma, H.; Lee, L.; Brooksby, P. A.; Brown, S. A.; Fraser, S. J.; Gordon, K. C.; Leroux, Y. R.; Hapiot, P.; Downard, A. J., Scanning Tunneling and Atomic Force Microscopy Evidence for Covalent and Noncovalent Interactions between Aryl Films and Highly Ordered Pyrolytic Graphite. *J. Phys. Chem. C* **2014,** *118* (11), 5820-5826.
57. Greenwood, J.; Phan, T. H.; Fujita, Y.; Li, Z.; Ivasenko, O.; Vanderlinden, W.; Van Gorp, H.; Frederickx, W.; Lu, G.; Tahara, K.; Tobe, Y.; Uji-i, H.; Mertens, S. F. L.; De Feyter, S., Covalent

Modification of Graphene and Graphite Using Diazonium Chemistry: Tunable Grafting and Nanomanipulation. *ACS Nano* **2015,** *9* (5), 5520-5535.
58. Toupin, M.; Bélanger, D., Thermal Stability Study of Aryl Modified Carbon Black by in Situ Generated Diazonium Salt. *J. Phys. Chem. C* **2007,** *111* (14), 5394-5401.
59. Hinrichs, K.; Roodenko, K.; Rappich, J.; Chehimi, M. M.; Pinson, J., Analytical Methods for the Characterization of Aryl Layers. In *Aryl Diazonium Salts: New Coupling Agents in Polymer and Surface Science*, 2012; pp 71-101.

2 General Experimental Methods

2.1 General Synthesis and Reagents

2.1.1 Reagents and Solvents

Unless stated otherwise, all solvents and reagents were obtained from commercial sources and used as received. Non-aqueous solutions were prepared in HPLC grade solvents and aqueous solutions were prepared in ultrapure water (resistivity > 18 MΩ cm).

2.1.2 Tetrabutylammonium tetrafluoroborate

Tetrabutylammonium tetrafluoroborate ($TBABF_4$) electrolyte was prepared by mixing tetrabutylammonium hydroxide (TBAOH, 40%) and tetrafluoroboric acid (HBF_4, 48%). HBF_4 (5 mL) was diluted to 25 mL with water and added to diluted TBAOH (20 mL diluted to 100 mL with water) under stirring. The resulting precipitate was washed with water and filtered under vacuum. The $TBABF_4$ electrolyte was dried for 3 days in an oven at 60 °C and then for 2 days under vacuum at 80 °C before storage in a desiccator.

2.1.3 Aryldiazonium Salts

All aryldiazonium salts used in this thesis had been previously reported and were prepared according to a literature method.[1]

Briefly, 4 mL of 25% fluoroboric acid was added slowly with stirring to 5 mmol of aromatic amine derivative in an ice bath. A cold solution of 5 mmol of sodium nitrite dissolved in water was then added dropwise with stirring to the amine solution in the ice bath. The collected product was recrystallised from acetonitrile and diethyl ether, dried and stored in a desiccator.

2.1.4 Buffer Solutions

Buffers were prepared using the Henderson-Hasselbalch equation to estimate the amount of each reagent (Equation 2.1), where pK_a corresponds to the $-\log_{10}$ acid dissociation constant (K_a) for the acid-base pair in each buffer, [HA] is the concentration of the acidic component and $[A^-]$ is the concentration of the conjugate base. For buffer solutions of pH 7-8 , phosphate buffer was prepared using NaH_2PO_4 as the source of acidic $H_2PO_4^-$ (pK_a = 6.86) and NaOH added to produce the conjugate base (HPO_4^{2-}). To prepare pH 10 buffer, $NaHCO_3$ (HCO_3^- pK_a = 10.33) was used with NaOH. In both cases, the buffer pH was measured using a pH meter and adjusted by addition of NaOH or H_2SO_4.

$$pH = pK_a + \log(\frac{[A^-]}{[HA]})$$ Equation 2.1

2.2 Instrumental Methods

2.2.1 X-ray Photoelectron Spectroscopy

XPS data were obtained using a Kratos Axis Ultra DLD spectrometer equipped with a monochromatic Al Kα source operating at 100-150 W. Wide scans were recorded with a step size of 1 eV and pass energy of 160 eV; for narrow scans the corresponding parameters were 0.1 and 20 eV, respectively. Specific sample preparation is described in the corresponding experimental chapters. Peak fitting procedures and data analysis were conducted using CasaXPS software.

2.2.2 pH Meter

pH values were measured using an EDT Instruments GP 353 ATC pH meter.

2.2.3 Scanning Electron Microscopy

SEM images were obtained using a Raith 150 e-beam lithography system operating with a 10 keV acceleration voltage.

2.2.4 X-Ray Powder Diffraction

Samples were ground in a small amount of perfluorinated oil to make a paste and mounted on a glass fibre. Data were collected on a SuperNova, Dual, Cu at zero, Atlas single crystal diffractometer. The samples were kept at 298.0 K during data collection. Data were integrated at 2θ = 0.05° intervals, and corrected for scan speed and baseline corrected.

2.2.5 Fourier Transform-Infrared Spectroscopy

FT-IR spectra were recorded using a Bruker Vertex 70 spectrometer operating OPUS software using a Bruker PLATINUM diamond ATR accessory. Unless otherwise stated, mid-IR spectra were recorded using 64 scans at 4 cm^{-1} resolution from 600 to 4000 cm^{-1} with a liquid N_2 cooled HgCdTe detector.

2.2.6 Atomic Force Microscopy

A Dimension 3100 with Nanoscope IIIa controller (Digital Instruments, Veeco, Plainview, NY) was used for all AFM studies. Images were collected in tapping mode using silicon cantilevers (Tap300Al-G, Budget Sensors, Bulgaria) with resonant frequencies between 200-400 kHz. Scan parameters

including scan rate and feedback control settings were optimised for each image. Image analysis was conducted using Nanoscope Analysis software (Bruker).

2.2.7 Electrochemistry

Unless otherwise stated, electrochemical measurements were performed using an Eco Chemie Autolab PGSTAT302 or PGSTAT302N potentiostat/galvanostat running Autolab General Purpose Electrochemical System (GPES) software version 4.9 or Autolab NOVA versions 1.9-1.11. Unless stated otherwise, all CVs were obtained in deoxygenated solutions with scan rate = 50 mV s^{-1}.

2.3 Electrochemical Methods

2.3.1 Working Electrodes

The GC disk electrodes used in this thesis were fabricated in the Mechanical Workshop of the Department of Chemistry, University of Canterbury and consisted of GC rods sealed in Teflon such that only a flat 3 mm diameter disk of GC was exposed (electrode area = 0.07 cm^2). A brass rod embedded in the Teflon and pressed into the back of the GC rod was used as the electrical contact for the electrode (Figure 2.1A). GC plate electrodes were cut from a 3 mm thick GC slab into ~15 mm x 15 mm pieces (Figure 2.1B).

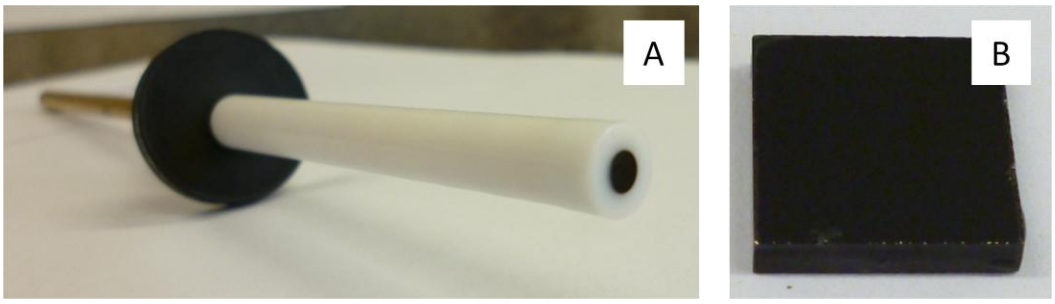

Figure 2.1: GC working electrodes: A. GC disc electrode embedded in a Teflon sheath, B. GC plate electrode.

GC electrodes in both forms were hand polished before use with a slurry of 1 µm alumina powder (Leco Corporation) on a lecloth polishing pad (Leco Corporation) until visible residues, markings and scratches were removed. Electrodes were rinsed with ultrapure water after polishing then sonicated in ultrapure water for 5 min and rinsed again to remove residual alumina from the surface. This procedure was repeated before each set of experiments.

2.3.2 Reference and Counter Electrodes

Unless otherwise stated, a saturated calomel (SCE) reference electrode was used for all aqueous electrochemistry and a calomel electrode (CE) with 1 M LiCl for non-aqueous solutions. All potentials in this thesis are quoted vs. SCE.

Counter electrodes used in this thesis were Pt mesh sealed in glass unless otherwise stated.

2.3.3 Cell Setup

Two types of electrochemical cell were used for electrochemical experiments in this thesis involving GC working electrodes: either a standard glass pear-shaped cell (Figure 2.2A) or a pear-shaped glass cell with a hole in the bottom (Figure 2.2 B and C). For GC disk working electrodes, the standard glass cell was used with ports in the top to introduce the working electrode, counter electrode, reference electrode and bubbler to purge solutions with N_2(g). Electrochemistry on GC plate working electrodes was conducted using the pear-shaped cell with a hole in the base. The cell was sealed to the working electrode surface by a Viton or Kalrez O-ring and held in place onto an insulating strip on a metal base by four springs. The area of the working electrode was defined by the area of the O-ring used (0.79 cm^2 unless stated otherwise). Electrical contact was made to the working electrode by pinning a strip of copper foil underneath the working electrode. Counter and reference electrodes and a gas bubbler were introduced from ports in the top of the cell.

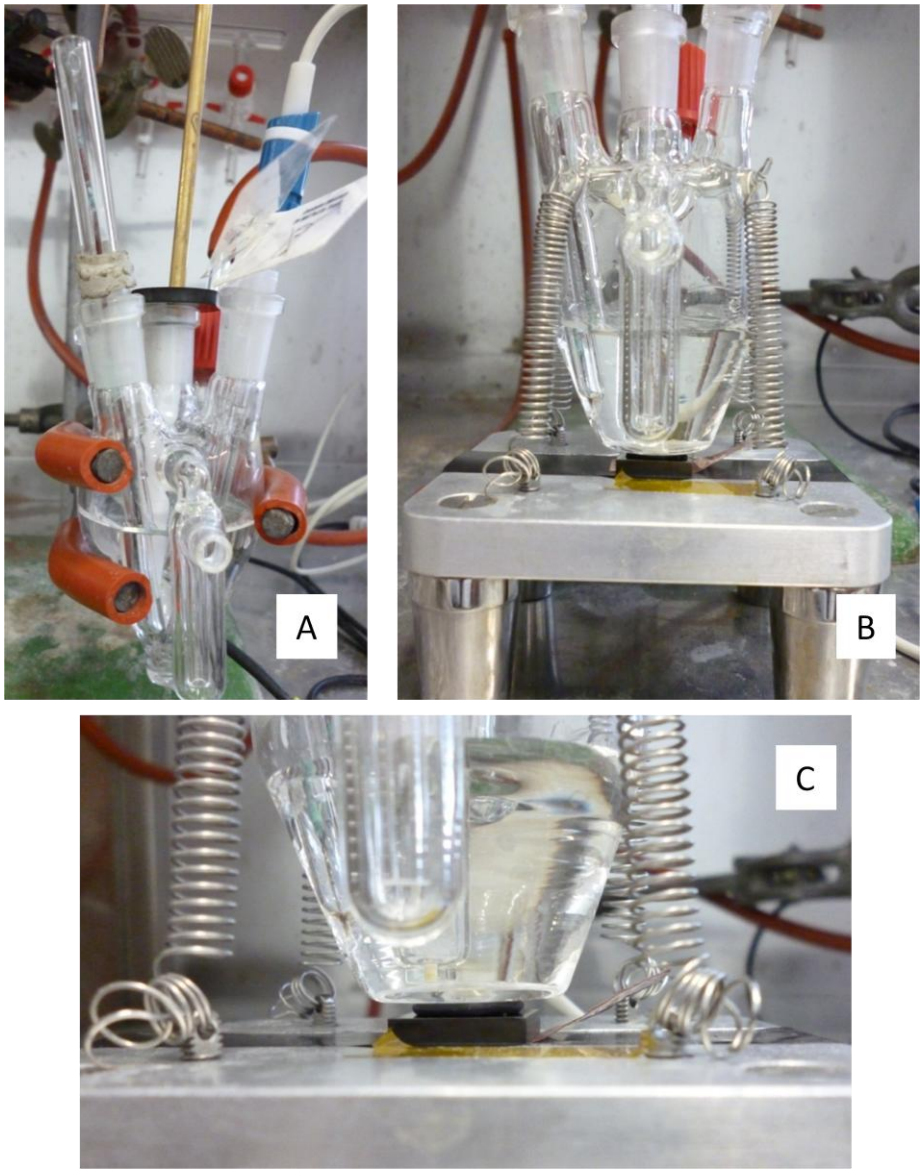

Figure 2.2: Photographs of electrochemical cell setups: A. standard pear-shaped cell for top-loading electrodes e.g. GC disc electrodes, B. cell for bottom-loading electrodes e.g. GC plate electrodes, C. close-up image of bottom-loading cell where it seals to the electrode.

2.3.4 Surface Coverage Calculation by NP-Reduction

Surface coverage of NP-groups (Γ_{NP}) on modified surfaces was calculated using the peak areas of the NP-reduction process determined by CV. Electroreduction of NP groups proceeds by a 4-electron process (Equation 2.2) in aqueous protic media to hydroxylaminophenyl groups which can be further reduced by a 2-electron process (Equation 2.3) to aminophenyl groups. Remaining hydroxylaminophenyl groups in the film undergo a reversible oxidation to form nitrosophenyl groups.[2]

$$surface - Ph - NO_2 + 4H^+ + 4e^- \rightarrow surface - Ph - NHOH + H_2O$$ Equation 2.2

$$surface - Ph - NHOH + 2H^+ + 2e^- \rightarrow surface - Ph - NH_2 + H_2O$$ Equation 2.3

$$surface - Ph - NHOH \rightleftharpoons surface - Ph - NO + 2H^+ + 2e^-$$ Equation 2.4

For the materials used in this thesis, the reversible hydroxylaminophenyl/nitrosophenyl redox couple (Equation 2.4) could not be resolved from the material redox signals and thus the peak area from the overall 6 e^- reduction process (Equation 2.2 and 1.3) was used in Equation 2.5 to determine Γ_{NP}, where v is the scan rate (V s^{-1}), F is the Faraday constant (96485 C mol^{-1}) and A is the geometric area of the working electrode (cm^2). Peak areas were determined by integration using Autolab NOVA versions 1.9-1.11 by fitting a linear baseline to the voltammogram.

$$\Gamma_{NP} = \frac{peak\ area}{6vFA}$$ Equation 2.5

2.4 Experimental Uncertainties

Reported uncertainties are the standard deviation for *n* samples unless stated otherwise. Where *n* = 2, the range is reported instead.

2.5 References

1. Dunker, M. F. W.; Starkey, E. B.; Jenkins, G. L., The Preparation of Some Organic Mercurials from Diazonium Borofluorides. *J. Am. Chem. Soc.* **1936,** *58* (11), 2308-2309.
2. Yu, S. S. C.; Tan, E. S. Q.; Jane, R. T.; Downard, A. J., An Electrochemical and XPS Study of Reduction of Nitrophenyl Films Covalently Grafted to Planar Carbon Surfaces. *Langmuir* **2007,** *23* (22), 11074-11082.

3 Aryldiazonium ion-based Grafting to Model Non-conducting Surfaces

3.1 Introduction

Metal oxides exhibit a range of conductivities, therefore developing techniques to modify non-conducting materials is relevant to the modification of semiconducting and insulating oxides. When modifying these surfaces with aryldiazonium salts, the lack of conductivity limits the available grafting mechanisms as electrografting and spontaneous reduction by the substrate are not possible. Aryldiazonium ions have been used to modify a range of non-conducting substrates including: poly(ethylene terephthalate), polyvinylchloride, polymethylmethacrylate, polyethersulfone membranes, commercial polymer membranes, cyclic olefin copolymer, glass and silica nanoparticles.[1-8]

The most common method for grafting aryldiazonium ions to insulating substrates is by the formation of radicals by addition of a chemical reducing agent such as Fe powder or H_3PO_2. Mévellec et al. prepared mixed AP-polymer films on glass and PTFE surfaces by reaction of amine-teminated aryldiazonium ions with the relevant monomer in the presence of Fe powder in aqueous acid solution.[7] The aryl radicals produced by reduction of the aryldiazonium salt grafted to the surface and acted as polymerisation initiators in solution resulting in a polymeric layer bound to the surface. The presence of the deposited layer was evidenced by contact angle changes after modification. Photochemical grafting methods have also been used to modify non-conducting surfaces in concert with lithographic patterning techniques to produce surfaces with localised modification. These methods also rely on a chemical reducing agent to form aryl radicals by reaction with the aryldiazonium salt, however, the reducing agent in this case is a photosensitiser such as tris(2,2'-bipyridyl)ruthenium(II) which becomes active after irradiation.[2] Reduction of aryldiazonium ions with H_3PO_2 has also been used to graft aminophenyl films to poly(D,L-lactic acid) to prepare phosphonate-terminated bone tissue engineering scaffolds.[9] Modification of the surface was found to increase the formation of calcium containing minerals compared to an untreated scaffold.

Grafting can also be induced by thermal decomposition of the aryldiazonium salt. Chehimi et al. modified polymethylmethacrylate surfaces with a range of aryl layers by immersion of the substrate in aryl amine dissolved in pure isopentylnitrite at 60 °C for 30 min.[3] The isopentylnitrite acts as both a solvent and diazotising agent, converting the aryl amine to the aryldiazonium ion which decomposes at 60 °C to react with the surface. Thermal decomposition reactions of aryldiazonium

salts are typically thought to occur via formation of the aryl cation,[10, 11] however, no grafting was observed in the presence of a radical scavenger which suggests the aryl radical is the intermediate in this case. No reduction source was suggested by the authors as the source of these radicals. [3]

Modification at basic pH has been used to modify insulating SiO_2 and Al_2O_3 nanoparticles.[8, 12] Under these conditions, radicals form from decomposition of the diazoate and graft to the surface (Scheme 1.3). Grafting was used to anchor reactive tethers or polymer initiators to these nanoparticle surfaces. Successful grafting was established by evaluating the effectiveness of subsequent dye attachment to the tethers or polymer formation.

In this thesis, the epoxy-based photoresist (PR) SU-8 (Figure 3.1) was used as a model non-conducting surface to compare grafting under different conditions. SU-8 has been used in a prior aryldiazonium grafting study by Simons et al. as cured SU-8 produces smooth surfaces that are stable in aqueous and nonaqueous reaction conditions.[13] In this prior study, grafting of aminophenyl (AP) films in aqueous acid conditions was compared in the presence and absence of reducing agents (H_3PO_2 and Fe powder). Grafting of the aryldiazonium salt prepared *in situ* was found to occur with and without reducing agent, however, the diamine precursor did not attach to the surface. The effect of reaction time on film thickness measured by AFM with and without H_3PO_2 was also studied. In the presence of reducing agent, the grafting reaction terminated within 30 min, resulting in films of < 10 nm thickness. In the absence of reducing agent, the initial film growth rate was similar to that in the presence of reducing agent but continued gradually over the 2 h reaction time to produce ~14 nm thick films.

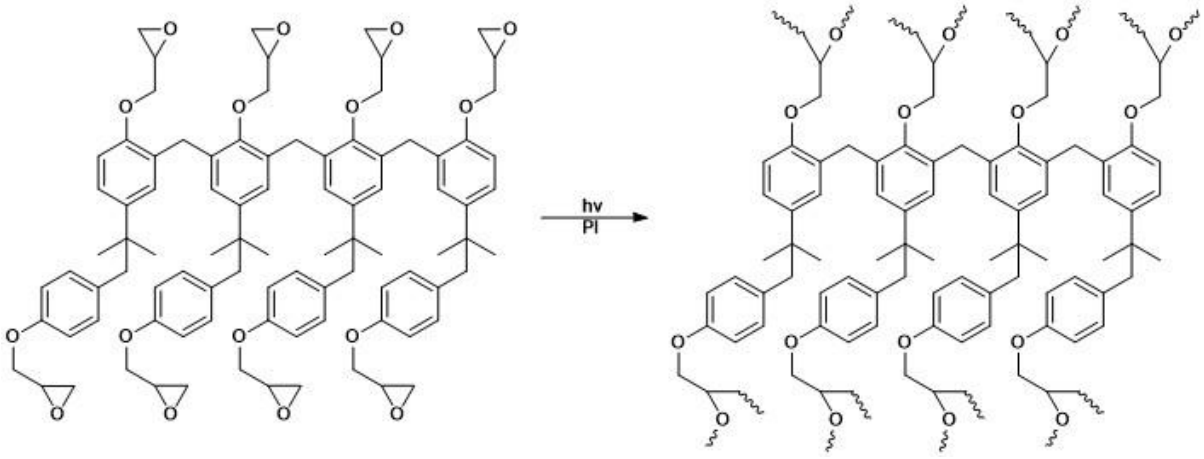

Figure 3.1: SU-8 PR before and after photopolymerisation with a photoinitiator (PI).

The grafting mechanism to SU-8 in the presence of reducing agent is assumed to be primarily due to the formation of aryl radicals by the reduction of the aryldiazonium ion.[11] The rapid termination of

film growth observed was likely due to radicals being consumed by reaction with each other or with the solvent (e.g. proton abstraction), limiting further grafting.

In the absence of a reducing agent, the grafting mechanism to SU-8 is less well understood. Under acidic conditions, the aryldiazonium ion is stable and decomposition to radicals and cations would be slow.[14] Additionally, the positively charged amino substituent makes aryl cation formation disfavoured.[13] Direct attack by the aryldiazonium ion is difficult to determine from the N 1s XPS spectra for amine terminated films as the amine and azo N 1s peaks occur at the same energy.[15] The N:C ratios determined by XPS for films grafted with and without reducing agent were similar, suggesting there were not significant contributions from grafting via direct attack of the aryldiazonium ion. The rapid grafting of thick AP films in the absence of reducing agent may be unique to this modifier as similar experiments with aminomethylbenzenediazonium ion produced only 1.4 nm thick films after 40 min reaction time. It was proposed that the ability of the AP groups to participate in redox reactions promotes catalytic film growth.[13]

The work described in this chapter focuses on studying grafting conditions where the diazoate mechanism is expected to occur (neutral and basic pH), and also on non-aqueous modification at planar SU-8 surfaces. This is of interest as the pH and solvent stability of metal oxides is variable and thus having a range of possible modification conditions is necessary to modify these surfaces. At neutral pH, the grafting mechanism is not well understood due to the formation of the diazoate being less favoured than at higher pH values. The formation of other intermediates such as diazoanhydrides has been proposed in pure water and dimethylformamide.[16, 17] Additionally, as the prior studies on the modification of non-conducting surfaces with diazoates used nanoparticle surfaces which are typically highly active, the viability of this method to modify planar substrates needs to be investigated. The grafting mechanisms to non-conducting substrates in non-aqueous conditions, with and without reducing agents have not been explored previously.

The goal of this work was to explore a range of modification conditions with aryldiazonium salts on a non-conducting substrate. Using SU-8 as a model non-conducting surface, spontaneous reactions via the diazoate route were examined in high pH aqueous solution and the effect of a chemical reducing agent in non-aqueous conditions was investigated.

3.2 Experimental Methods

3.2.1 Preparation of SU-8 Surfaces

SU-8 surfaces were prepared according to the method described in Simons et al.[13] Si wafers were coated with AZ1518 PR (Microchemicals, Germany) to protect the surface from cutting debris and cut into approximately 10 mm x 10 mm pieces. The protecting PR was then removed by sonication in acetone, 2-propanol (IPA) and ethanol for 5 min each and O_2 plasma treatment at 100 W RF power for 2 min. SU-8 2005 PR (Microchemicals, Germany) was spin-coated onto the cleaned Si samples at 2000 rpm for 1 min. The SU-8 films were then treated by 2 min soft-baking at 95 °C on a hotplate and then exposed under UV light using an MA6 mask aligner (Suess Microtec, Germany) in flood exposure mode for 3 cycles with 20 s exposure time. After exposure the samples were soft-baked for 2 min at 95 °C then hard-baked for 30 min at 200 °C on a hot plate.

3.2.2 Patterning and Masking of SU-8 Surfaces

Patterned SU-8 samples were prepared by spin-coating AZ1518 PR onto the cured SU-8 surfaces at 3000 rpm for 30 s and soft-baking for 60 s at 95 °C on a hot plate. A chrome-on-glass photomask was used to expose the PR for 10 s using a mask aligner in vacuum mode. The patterns were developed by soaking the substrates in 2% tetramethylammonium hydroxide for 25 s before being rinsed with H_2O and dried with N_2 gas.

AZ1518 PR was used without lithographic patterning by drop-coating areas of the SU-8 surface and then soft-baking for 5 min at 95 °C on a hotplate.

Polyimide tape (Multicomp) was also used to mask samples for non-aqueous modification by applying two parallel strips of tape to a cleaned hard-baked SU-8 surface leaving an area of exposed surface approximately 5 × 10 mm between them.

3.2.3 Modification of SU-8 Surfaces

3.2.3.1 Modification in Aqueous Solution

Initial tests of modification of patterned SU-8 surfaces were conducted by preparation of aminobenzenediazonium ion *in situ* by dropwise addition of 0.1 M $NaNO_2$ to an equal volume of 0.1 M 1,4-diaminobenzene dissolved in 0.5 M HCl (2 mL typical volume) in the presence of the SU-8 substrate. The reaction solution was agitated for 1 hour on an orbital shaker. Subsequent modification experiments in aqueous conditions were carried out by immersion of the patterned SU-8 surfaces in a 50 mM solution of a previously prepared aryldiazonium salt in 0.1 M HCl, pH 7 or pH

10 buffer for either 15 min, 30 min, 1 h or 8 h. After modification, samples were rinsed with ultrapure water then sonicated in acetone, IPA and ethanol for 5 min each to remove adsorbed material and remaining PR.

3.2.3.2 Modification in Non-Aqueous Solution

PR-patterned substrates were immersed in a solution of 50 mM isolated aryldiazonium salt in acetonitrile with and without 55 mM ferrocene for 1 h on an orbital shaker. After modification, samples were cleaned by 5 min sonication in each of acetonitrile, acetone, IPA and ethanol.

Polyimide-masked samples were modified as above and cleaned sonicated initially in acetone for 1 min to lift the polyimide tape, then acetonitrile, acetone, IPA and ethanol for 5 min after the tape was removed.

3.2.4 Surface Morphology Measurements on SU-8

Film thickness measurements were conducted on patterned substrates by imaging a boundary area between the patterned film and the bare substrates. The boundary height difference was measured using the average height of a 5 µm x 1.5 µm area crossing the boundary. Average film thickness for a sample was determined by averaging the measurements from 3 images at different points on the surface with three height measurements on each image (i.e. the average of 9 total measurements). For samples with discontinuous film coverage, the average of the maximum height difference across 5 linear sections across the film boundary for 3 images was used.

The average RMS surface roughness was calculated from AFM images by measuring the roughness in a 2 µm x 2 µm area at three points in the area of interest (e.g. bare surface or grafted film) at three areas on the sample, giving 9 roughness measurements which were averaged to give the reported value and standard deviation.

3.2.5 XPS on SU-8 Surfaces

XPS data was collected from SU-8 substrates at a 30 ° angle to the detector normal to improve surface sensitivity. A charge neutraliser was used to limit the effect of charge build-up on the surface. Data were charge-corrected to the high resolution C 1s peak at 284.8 eV.

3.2.6 Estimation of Modifier Height (*Avogadro*)

Avogadro 1.1.1 freeware[18] was used to calculate the height of molecules perpendicular to the surface. The structure of each molecule was drawn and optimised to the lowest energy

conformation in the software. The height of the molecule was calculated using trigonometry by measuring the linear distance between the surface and the highest atom in the molecule and the angle between the highest atom and the surface normal.

3.3 Results and Discussion

3.3.1 Sample Preparation

SU-8 surfaces were prepared according to the procedure outlined in Simons et al.[13] The desirable properties of SU-8 substrates reported by Simons et al. are the low surface roughness and stability to sonication. These properties were checked by AFM for the samples prepared in the present work. AFM imaging of the surface (Figure 3.2a) shows that it is smooth and undamaged after sonication in acetone, IPA and ethanol with a surface roughness of 0.35 ± 0.02 nm. Surfaces were then patterned lithographically with AZ1518 PR to provide a height difference for film thickness measurements. Scheme 3.1 shows the patterning method and preparation strategy for aryl-modified and blank SU-8 samples.

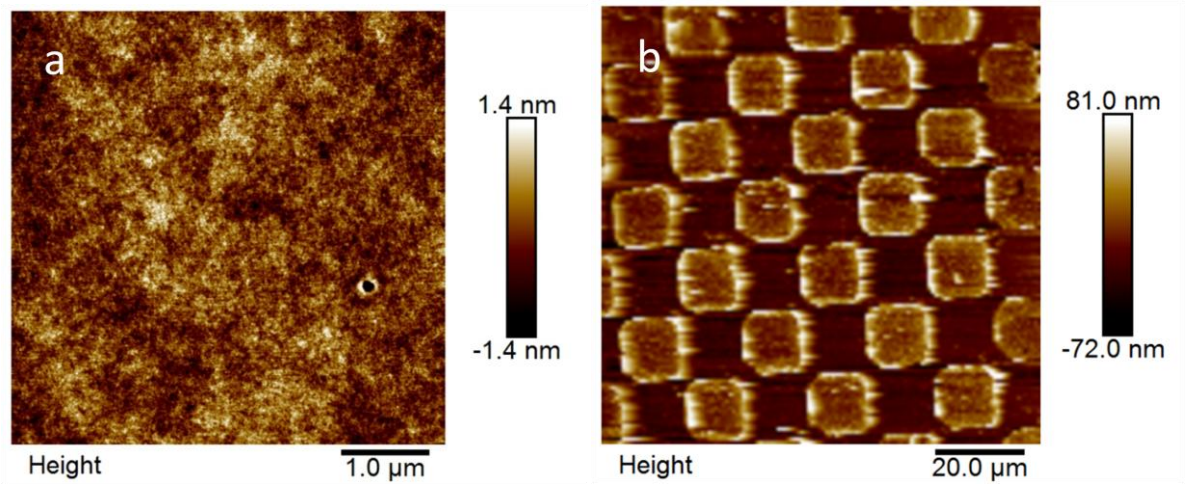

Figure 3.2: AFM height images of a. bare SU-8 surface after sonication in acetone, IPA and ethanol, and b. SU-8 surface with an AP film in a checkerboard pattern.

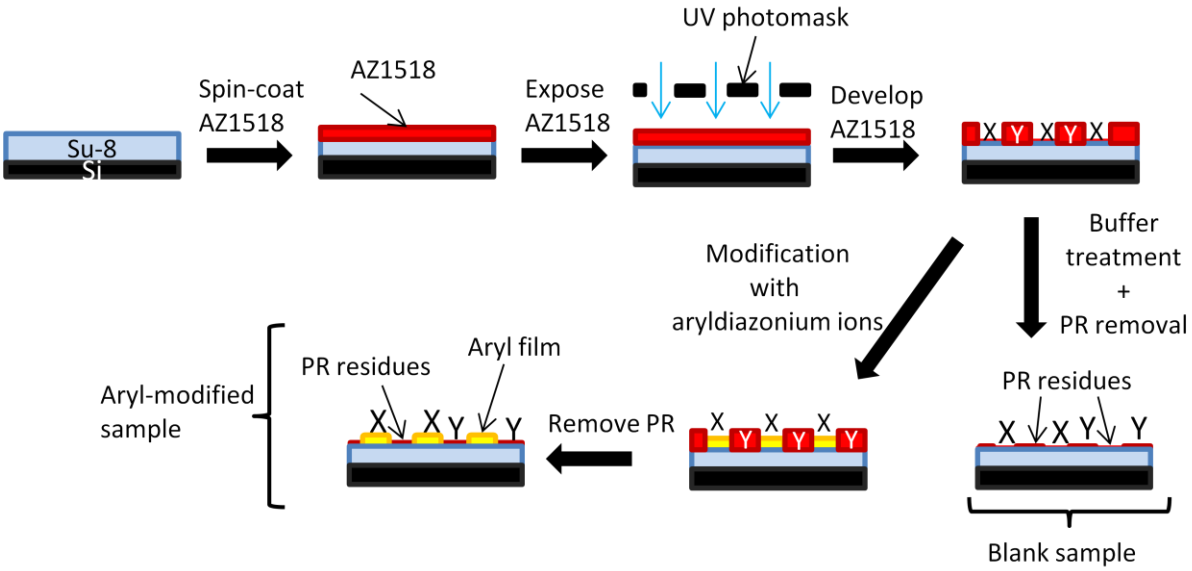

Scheme 3.1: Preparation of patterned SU-8 samples by photolithography of AZ1518 and subsequent buffer treatment or aryldiazonium modification. Region 'X' indicates where exposed PR is removed by developer before buffer treatment or attachment of the aryl layer. Region 'Y' is where unexposed PR is removed by solvent cleaning after buffer treatment or modification.

3.3.2 Modification in Aqueous Conditions

Initially, the modification conditions from Simons et al. were replicated by using acidic conditions to prepare AP films on the exposed areas of the substrate (region X in Scheme 3.1). The surface was imaged by AFM after the remaining PR was removed by solvent cleaning (Figure 3.2b) where it was observed that the AP film replicated the pattern in region X distinct from any PR residues remaining in region Y. Having established that the protocol for grafting patterned films on SU-8 gave the expected results for AP grafting, NP modification was used to compare the effect of pH on film growth in 0.1 M HCl and pH 7 and pH 10 buffer solutions. After modification in 50 mM NBD solution for 1 h and removal of PR, film thickness and roughness were measured by AFM, giving the data shown in Table 3.1.

Table 3.1: Film thickness and RMS roughness measurements for SU-8 after 1 h modification with 50 mM NBD or 1 h treatment without NBD: in 0.1 M HCl, pH 10 buffer or pH 7 buffer.

Modification medium	Sample	Step height (nm)[a]	RMS_X[b]	RMS_Y[c]
HCl	NP-Mod	0.18 ± 0.02	1.03 ± 0.02	0.39 ± 0.01
	Blank	0.15 ± 0.02	0.62 ± 0.03	0.38 ± 0.02
pH 10 Buffer	NP-Mod	1.5 ± 0.3	0.85 ± 0.05	0.55 ± 0.04
	Blank	0.35 ± 0.03	0.68 ± 0.07	0.57 ± 0.05
pH 7 Buffer	NP-Mod	2.4 ± 0.3	1.5 ± 0.4	0.45 ± 0.07
	Blank	0.303 ± 0.008	1.40 ± 0.05	0.42 ± 0.04

[a]Height of region X above region Y (Scheme 3.1). [b]RMS roughness measured in region X. [c]RMS roughness measured in region Y.

AFM imaging at the interface between regions X and Y on the modified sample (Figure 3.3a) shows a clear difference in roughness between each region (1.03 ± 0.02 nm and 0.39 ± 0.01 nm for regions X and Y respectively) and a small height difference (0.18 ± 0.02 nm). The height difference after HCl NBD treatment is less than the thickness of a NP monolayer (0.64 nm on a flat surface) indicating that minimal grafting has occurred. A blank sample was prepared in HCl in the absence of NBD to evaluate the influence of PR residues on the observed height differences. AFM imaging of an HCl-treated blank is shown in Figure 3.3b. The film thickness across the interface between region X and Y after HCl blank treatment was the same within experimental error as for the NP-modified sample (0.15 ± 0.02 nm) but with a lower roughness difference (0.62 ± 0.03 nm and 0.38 ± 0.02 nm for regions X and Y respectively).The low magnitude of the height difference compared to the roughness in the treated area and the similarity in film thickness measured between the NP-modified and blank samples indicates that these film thickness values may be an artifact of the surface roughness difference between regions X and Y rather than a grafted layer. The increased roughness observed in region X on the HCl blank sample may be due to residual exposed PR or swelling of the SU-8 substrate during development of the pattern or acid treatment. However, the low roughness in region Y suggests that the unexposed PR can be removed completely by solvent treatment and may indicate that the roughness in region X is not caused by PR residues. The further increased roughness on treatment with NBD suggests that there is sparse attachment of the aryldiazonium occurring under these conditions but not to a sufficient degree to graft a continuous film. In HCl, the aryldiazonium ion is stable and the only expected film growth mechanism is slow film formation via the aryl cation or direct attack by the aryldiazonium ion.[19, 20] Therefore, treatment with NBD in HCl was used to determine whether interactions between NBD and photoresist result in film growth.

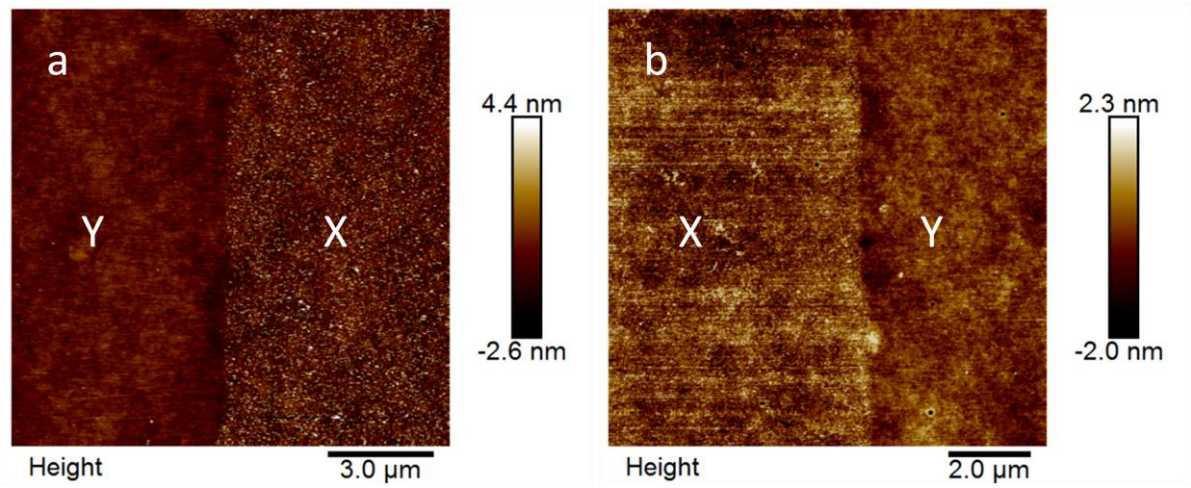

Figure 3.3: AFM height images of SU-8 surface pattern edges. Regions X and Y are labelled according to Scheme 3.1., where X is the region exposed for 1 h in HCl solution in the presence (a) and absence (b) of NBD.

AFM images of SU-8 surfaces after treatment in pH 10 buffer for 1 h in the presence and absence of NBD are shown in Figure 3.4. After modification with NBD at pH 10 there is a continuous film present covering region X (exposed to the NBD solution) that is not present in the pH 10 blank sample. The film thickness was significantly higher in the presence of NBD compared to the pH 10 blank (1.5 ± 0.3 nm compared with 0.35 ± 0.03 nm). The film roughness was also significantly higher than in region Y for the NP-modified sample (0.85 ± 0.05 nm compared with 0.55 ± 0.04 nm) whereas the was no roughness difference between regions X and Y on the pH 10 blank sample. In comparison with the sample treated with NBD in HCl, the measured height difference after modification in pH 10 buffer is much higher (1.5 ± 0.3 nm compared with 0.18 ± 0.02 nm) indicating that grafting is much more extensive at pH 10. Additionally, the NBD solution in HCl showed little change in appearance over the 1 h reaction time whereas the appearance of a brown precipitate was observed within minutes at pH 10, suggesting formation of polymeric aggregates in the pH 10 solution. These results align with the high stability of the aryldiazonium ion in HCl and the expected rapid decomposition to aryl radicals via a diazoate intermediate at high pH.[20, 21] In pH 10 solution, it is expected that the dominant grafting mechanism will be via the diazoate route which is favoured in high pH.

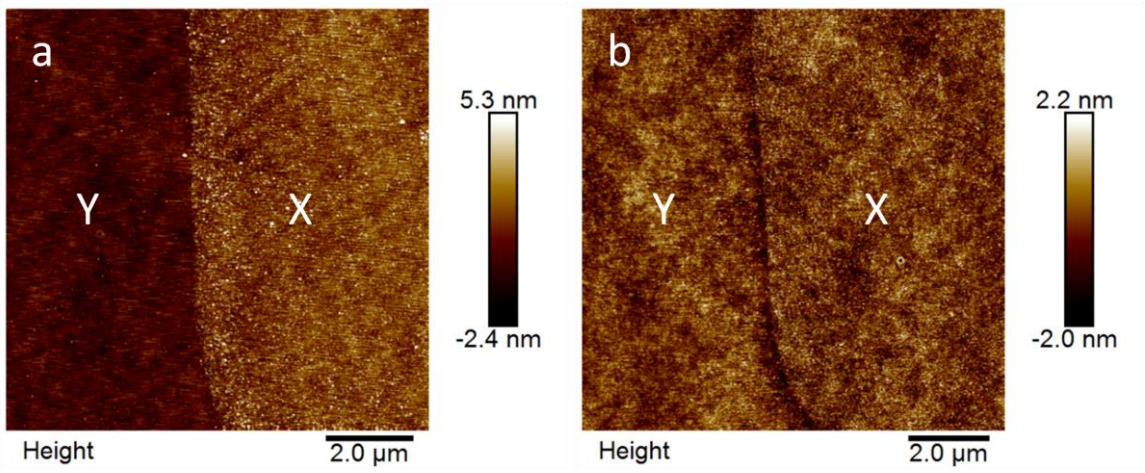

Figure 3.4: AFM height images of SU-8 surface pattern edges. Regions X and Y are labelled according to Scheme 3.1., where X is the region exposed for 1 h in pH 10 buffer solution in the presence (a) and absence (b) of NBD.

Figure 3.5 shows the AFM images of the pattern step-edges of SU-8 surfaces treated in pH 7 buffer solution for 1 h in the presence and absence of NBD. The AFM image of the NBD treated sample (Figure 3.5a) shows a continuous film similar to that obtained for NP-modification at pH 10. Film thickness measurements showed that the NP-modified sample had a larger height difference between regions X and Y than the blank sample (2.4 ± 0.3 nm compared with 0.303 ± 0.008 nm) prepared at pH 7. Additionally, the NP film grafted in pH 7 solution is significantly thicker than the film grafted at pH 10 for the same reaction time and concentration. This increase in film thickness may be due to the increased stability of the aryldiazonium ion at lower pH allowing the grafting reaction to occur over a longer period before the aryldiazonium ion is consumed in side reactions. Formation of a brown precipitate was observed during NP grafting in pH 7 solution, however, the formation process was more gradual than at pH 10.

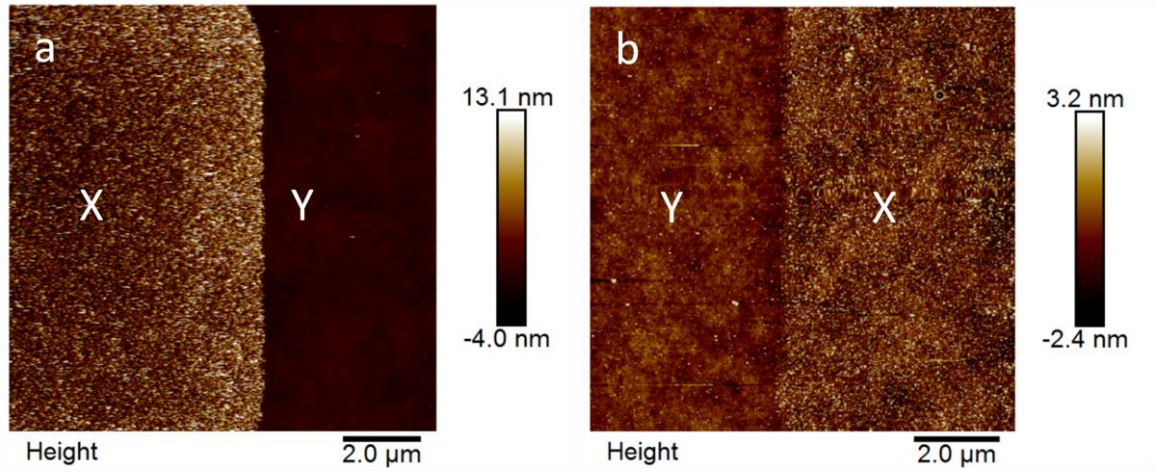

Figure 3.5: AFM height images of SU-8 surface pattern edges. Regions X and Y are labelled according to Scheme 3.1., where X is the region exposed for 1 h in pH 7 buffer solution in the presence (a) and absence (b) of NBD.

The measured roughness in each region was identical for both the pH 7 NP-modified and blank samples. It is expected that region Y would be similar on both samples as this area is masked by photoresist during the treatment process, however, the similar high roughness in region X is unexpected. Additionally, the roughness in region X is significantly higher after pH 7 treatment compared to the other pH values studied. The increased film thickness at pH 7 may explain the increased roughness in region X on the NP-modified sample compared to the pH 10 modified samples as diffusion of the reactive species to the underlying substrate is impeded more by a thick film. This results in a disproportionate amount of grafting to the film compared to the substrate and thus a larger film thickness variation across the surface.[13] The high roughness for the pH 7 blank sample in region X is unexpected and may arise from interaction between the pH 7 buffer components (e.g. phosphates) and the substrate, however, this increased roughness does not negatively affect the reproducibility of the step height measurements. In pH 7 solution, the diazoate mechanism is likely to be less favoured due to the lower pH which may result in a mixture of grafting mechanisms occurring such as via the diazoanhydride intermediate or aryl cation formation as discussed in section 3.1.

3.3.3 Time Dependence of Grafting in Aqueous Conditions

The time dependence of the grafting reaction at pH 7 and pH 10 was examined by grafting from 50 mM NBD solution for 15 min, 30 min, 1 h and 8 h. AFM images of the modified surfaces show

distinct NP film edges at both pH values and all reaction times (Figure 3.6). This suggests that the grafting of NP groups proceeds rapidly at both pH 10 and pH 7 to give continuous films. Measurements of film thickness for NP-modified samples at each reaction time and pH are shown in Figure 3.7. At 15 min reaction time the average film thickness for both pH values is similar (1.1 ± 0.1 nm and 1.3 ± 0.3 nm for pH 10 and 7 respectively), however, at longer reaction times the grafting behaviour at pH 7 and pH 10 begins to deviate. Film growth ceases or becomes very slow in pH 10 solution within the first hour (film thicknesses were 1.3 ± 0.1 nm and 1.5 ± 0.3 nm at 30 min and 1 h respectively) although the thickness at 8 h is highly variable. In pH 7 solution, the grafting reaction continues throughout the 8 h reaction time to give films with higher thickness than in pH 10 solution. The lower film thicknesses measured for some samples at long reaction times at pH 10 is not understood at present, however, it could arise due to variability in the stability of the aryldiazonium salt between experiments, due to uncontrolled factors such as temperature. These results support the hypothesis that the aryldiazonium ion is more stable in pH 7 solution than in pH 10 as in pH 7 solution, grafting continues for 8 h, suggesting that not all the aryldiazonium ions are consumed within a short reaction time.

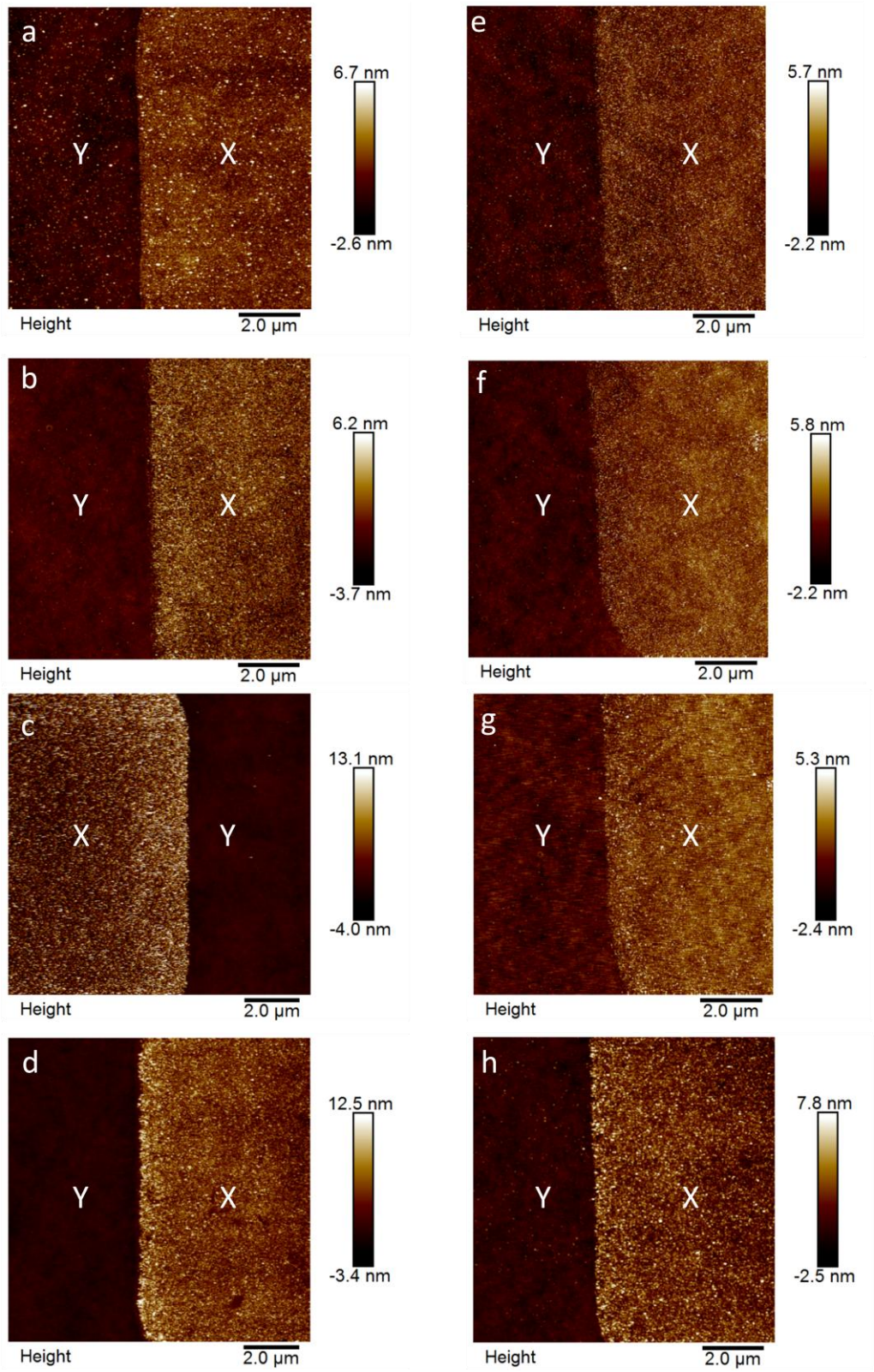

Figure 3.6: AFM images of SU-8 surfaces modified with NP films at pH 7 (a-d) and pH 10 (e-h) at varying reaction time: 15 min (a and e), 30 min (b and f), 1 h (c and g) and 8 h (d and h). Regions X and Y are labelled according to Scheme 3.1

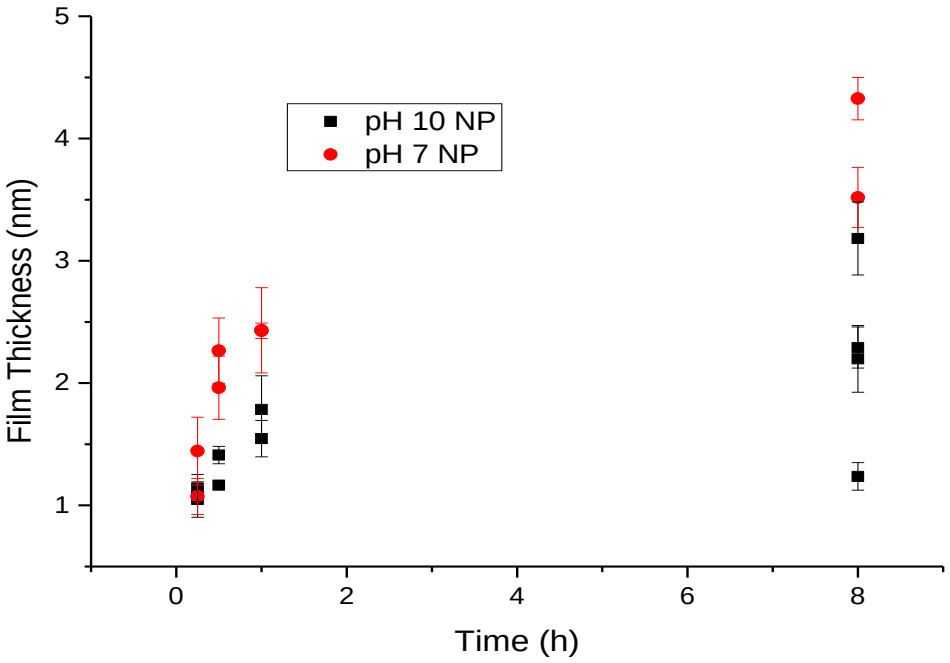

Figure 3.7: AFM film thickness measurements for NP-modified SU-8 surfaces. Each point represents the average film thickness measured for one sample and the error bars show the standard deviation for that sample.

The surface roughness of the NP-modified SU-8 surfaces in region X was also measured from AFM images after each modification time (Figure 3.8). For the pH 7 modified samples, roughness increases with reaction time and is higher than for the pH 10 samples, likely due to the high degree of disorder in thicker multilayer films. Films grafted at pH 10 have very little roughness variation initially but become significantly rougher after 8 h reaction, suggesting gradual multilayer formation despite the variability in film thickness measurements at 8 h.

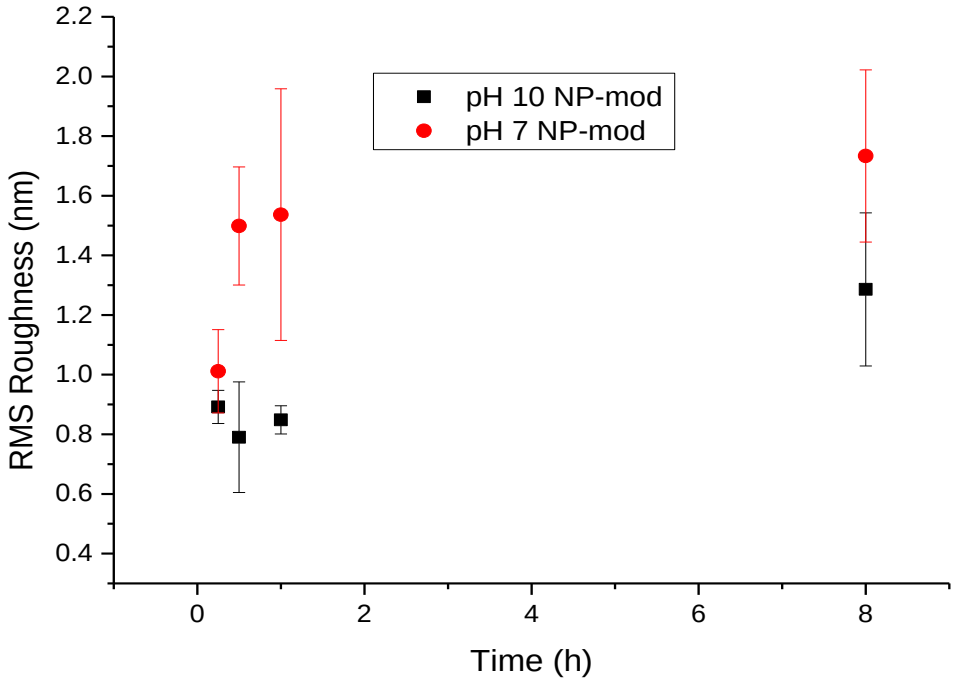

Figure 3.8: Average RMS roughness values across all samples measured in region X from AFM images for SU-8 modified with NP-groups in pH 7 and pH 10 buffers.

3.3.4 Substituent Effects on Grafting from Aqueous Solutions

The effect of the substituent on the grafting reaction was evaluated by grafting 4-methoxybenzenediazonium ion (MBD) under the same conditions as described above for NBD. Methoxy groups have the opposite electronic behaviour to nitro groups (electron donating rather than electron withdrawing) and thus any substituent-dependent grafting mechanisms should result in a different grafting response.

AFM images of SU-8 surfaces modified with methoxyphenyl (MP) groups in pH 7 and pH 10 solutions are shown in Figure 3.9. At 15 min reaction time (Figure 3.9a), pH 7 aryldiazonium ion solution produces minimal modification with only small patches of film visible. After 30 min the pH 7 modified surface has increased coverage but the film is still discontinuous (Figure 3.9b). After 1 h in pH 7 grafting solution the MP film appears uniform (Figure 3.9 c and d). However, MP-modified samples prepared at pH 10 show continuous film coverage at all reaction times (Figure 3.9 e-h). This behaviour is in contrast to modification with NP groups where there was no dependence of film coverage on the pH of the grafting solution (for pH 7 and 10). Precipitate formation was observed during grafting of MP groups at pH 10 but the process was more gradual than during NBD grafting. At pH 7 only minimal precipitate formation was observed after 1 h MBD grafting time.

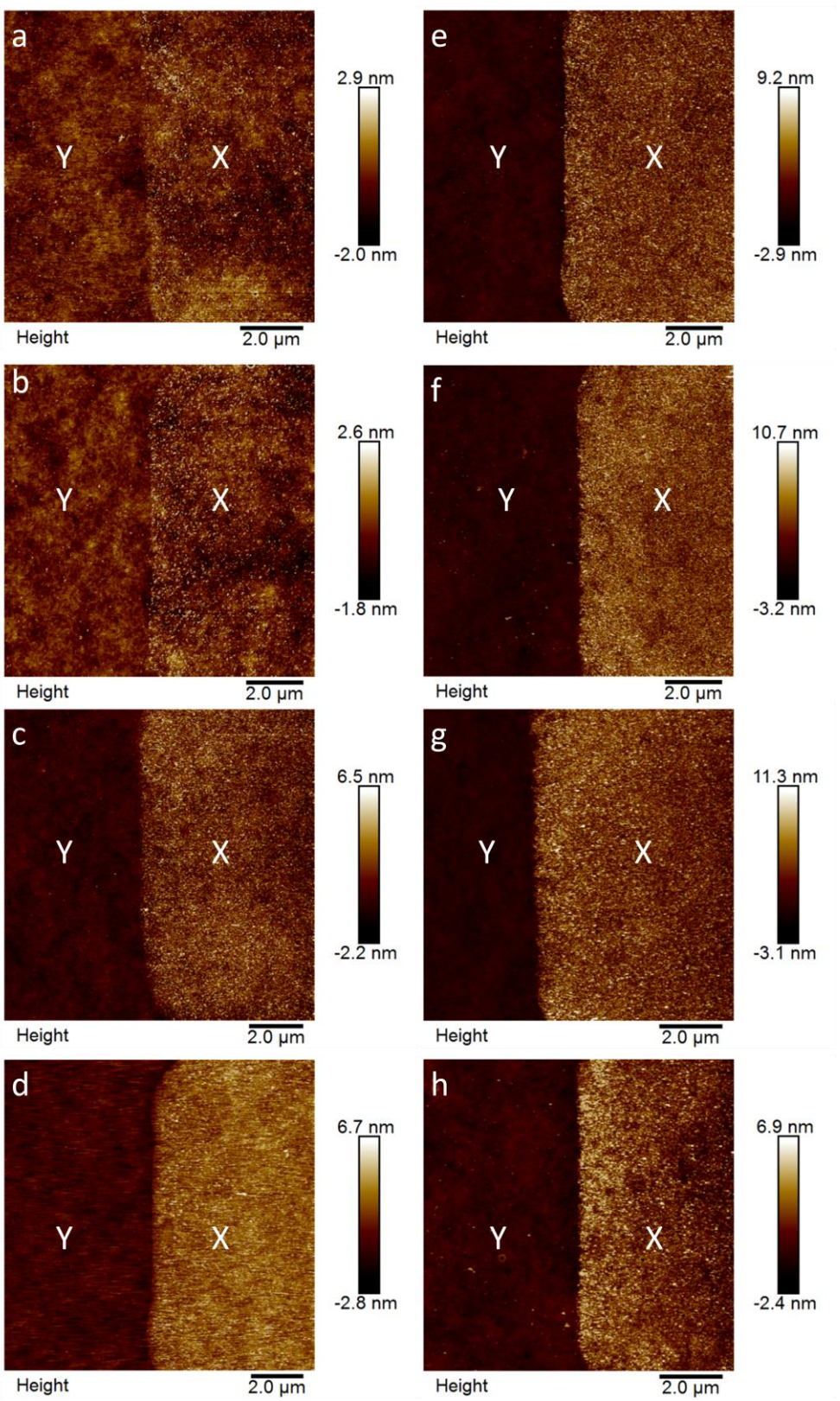

Figure 3.9: AFM images of SU-8 surfaces modified with MP films at pH 7 (a-d) and pH 10 (e-h) at varying reaction time: 15 min (a and e), 30 min (b and f), 1 h (c and g) and 8 h (d and h). Regions X and Y are labelled according to Scheme 3.1.

The pH dependence of MP film growth is also apparent in the film thickness data measured from the AFM images (Figure 3.10). At pH 10, the film growth stops or slows within 30 min whereas in pH 7 solution, film growth continues up to 1 h. It was observed that 8 h reactions sometimes produced thinner films than the shorter time scales. Films grafted in pH 10 solution are consistently thicker than those grafted in pH 7 solution. Under all conditions except 15 min grafting in pH 7 solution, the grafted films are multilayers (the calculated height of a single MP group vertically aligned on a surface is 0.76 nm).

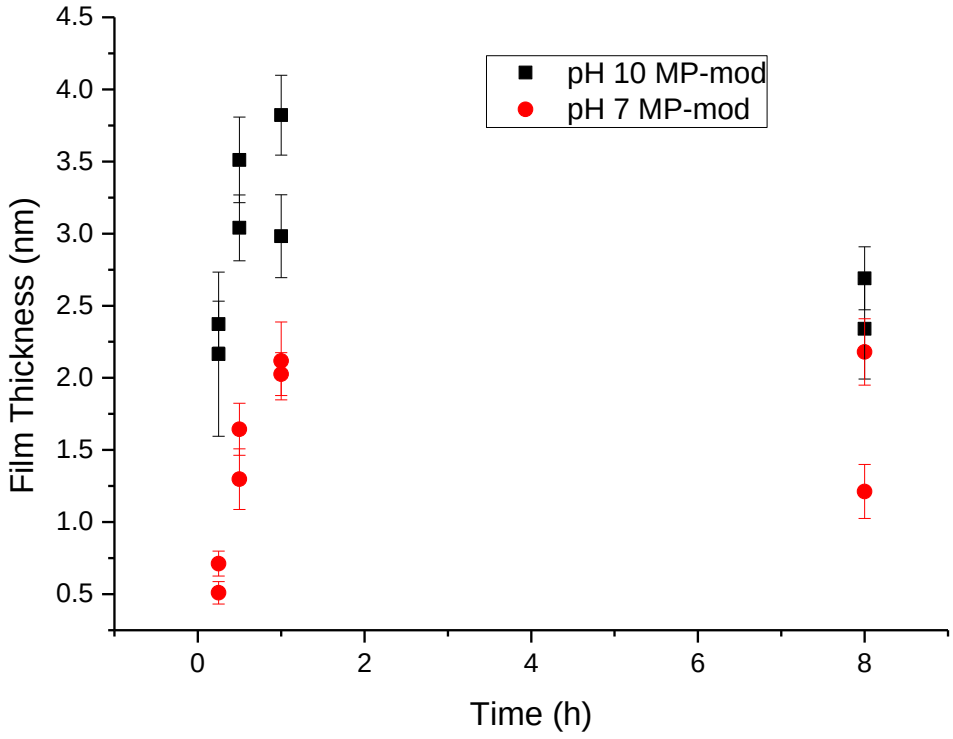

Figure 3.10: AFM film thickness measurements for MP-modified SU-8 surfaces. Each point represents the average film thickness measured for a given sample and the error bars indicate the standard deviation for that sample. Measurements of films grown for 15 and 30 min at pH 7 are based on linear-section averages.

Measurements of film roughness for MP films grafted in pH 7 and pH 10 solutions are shown in Figure 3.11. The sparse films produced at short reaction times at pH 7 result in only a small change in surface roughness compared to the bare substrate. The roughness increases sharply after 1 h modification in pH 7 MBD solution. Reaction in pH 10 solution produces films with a high roughness that does not change with reaction time, consistent with rapid formation of a multilayer.

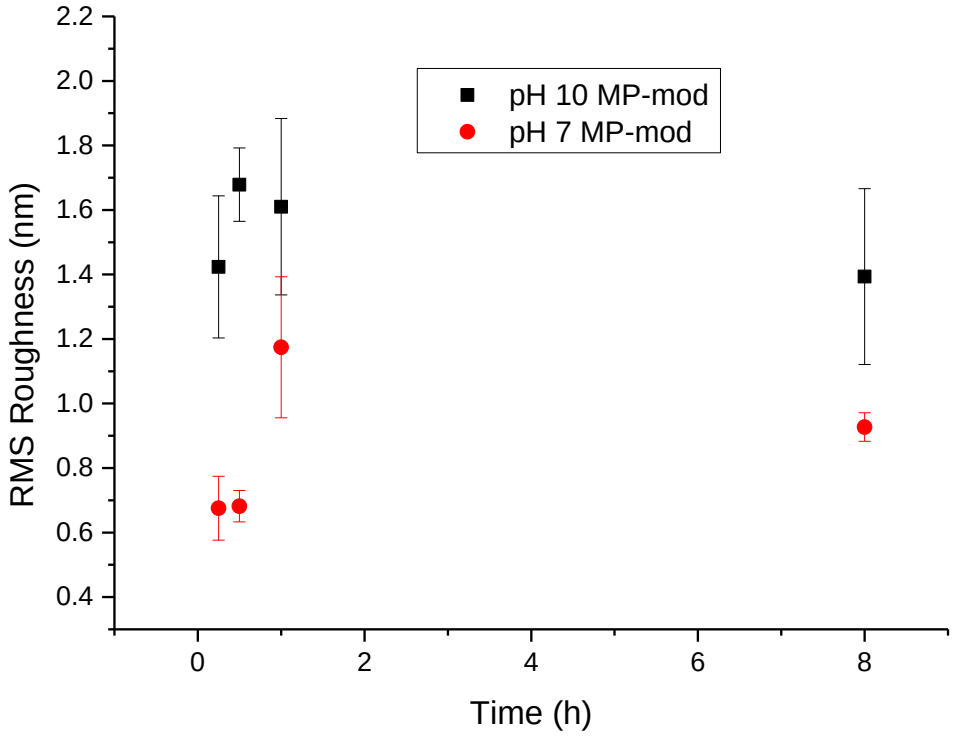

Figure 3.11: Average RMS roughness values across all samples measured in region X from AFM images for SU-8 modified with MP-groups treated in pH 7 and pH 10 buffers.

Comparing the grafting of NP and MP groups reveals that the substituent has a large effect on the grafting reaction at both pH values. In pH 7 solution, the grafting of MP groups is significantly slower than NP groups, requiring 1 h reaction time to produce a continuous film compared with 15 min for NP groups. The resulting MP films are thinner than the NP films. Grafting in pH 10 solution shows the opposite behaviour where modification with NP groups results in thin films with limited growth at longer time scales and grafting of MP films results in rapid growth of multilayer films. The high variability of film thickness for 8 h reaction times makes determination of any differences in the stability of the aryldiazonium ion/diazoate between conditions or modifiers difficult.

In pH 10 solution, the dominant mechanism is expected to be formation of aryl radicals via the diazoate (Scheme 1.3) and the rapid formation of continuous films, regardless of substituent, supports this. In contrast, in pH 7 solutions, the aryl substituent was found to affect the initial grafting step to the substrate: at short grafting times, NBD modification produced continuous films whereas MBD-modification resulted in patchy film coverage. This suggests that the dominant grafting mechanism in pH 7 solution is impeded by the electron-donating substituent and the thick films produced when grafting NP groups indicate that the electron-donating substituents promote the reaction. The mechanistic implications of these observations are discussed in 3.3.4.2.

3.3.4.1 XPS Analysis

Further insight into the grafting mechanism at each pH can be gained by investigating the chemical composition of the grafted film. As discussed in Chapter 1, different intermediates introduce different chemical functionalities within the film which can be identified by XPS. The chemical nature of NP and MP films grafted to SU-8 in pH 7 and pH 10 solutions was investigated by XPS using samples modified by 1 h reactions. PR was used to mask off SU-8 surfaces without lithographic patterning to produce samples with 5 mm × 10 mm exposed strips for modification, and for XPS analysis after PR removal.

Survey spectra of the modified surfaces are shown in Figure 3.12. Atomic concentrations calculated from survey spectra for the modified SU-8 surfaces are presented in Table 3.2. Also included in the table are data reported by Simons et al. for unmodified SU-8.[13] Comparison of the data for modified and unmodified samples indicates that all spectra are dominated by C and O from the SU-8 surface. The measured contributions from N 1s signals in the survey spectra are very low, even for surfaces modified with NP groups. All surfaces contain Si, likely arising from contamination by the Si substrate during SU-8 coating.

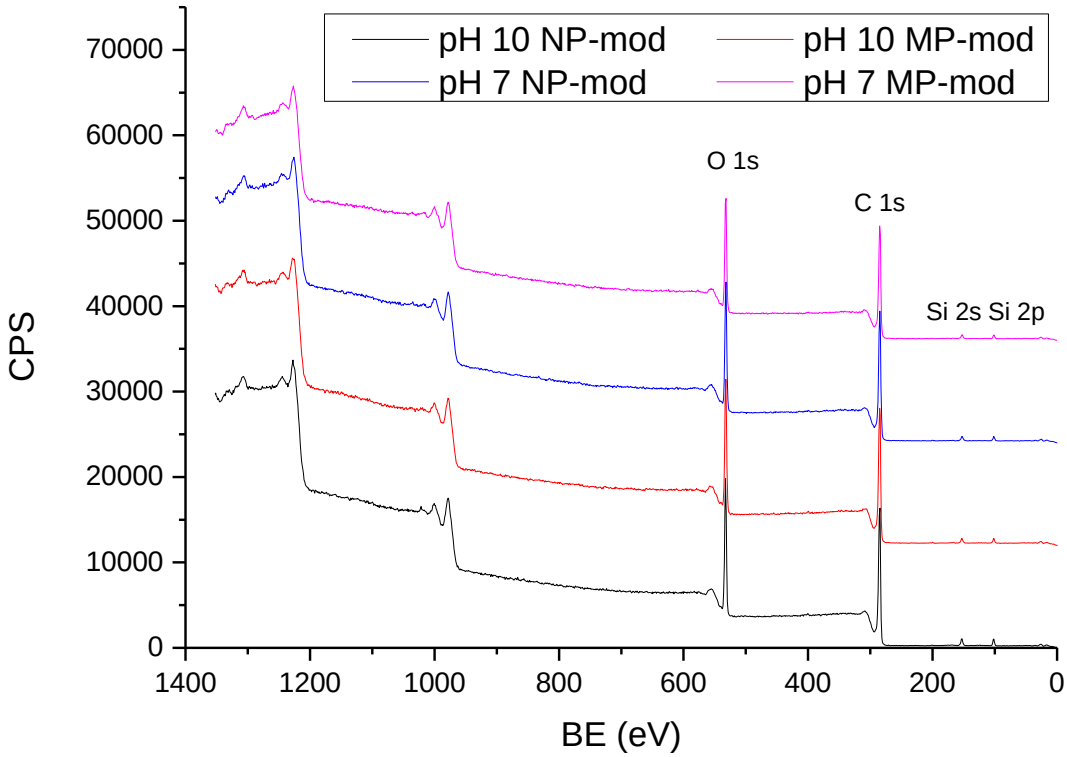

Figure 3.12: XPS survey scans of SU-8 surfaces modified with NP and MP groups in aqueous buffers at pH 7 and pH 10 for 1 h.

Compared to unmodified SU-8 prepared by the same process,[13] the modified surfaces have lower C/O ratios (3.7-3.9) than bare SU-8 (4.9). This increase in O content could arise from the O-containing functionalities (nitro and methoxy) attached during grafting or from introduction of O from diazoanhydride-derived radicals (Scheme 1.4). Further, both the pH 10 and the pH 7 buffer used include O-containing groups (carbonate/bicarbonate and phosphate respectively) that may adsorb to the surface and increase the observed O content.

Table 3.2: Atomic concentrations and ratios for unmodified and 1 h modified SU-8 surfaces.

	C (At %)[a]	O (At %)[a]	Si (At %)[a]	N (At %)[a]	C/O[a]	O1sII/O1sI[b]
Unmodified[c]	82.1	16.6	1.4	0	4.9	-
pH 10 NP[d]	76.0	19.7	3.9	0.4	3.9	0.50
pH 10 MP[d]	77.6	19.5	2.6	0.3	4.0	0.75
pH 7 NP[d]	76.7	20.1	3.0	0.2	3.8	1.05
pH 7 MP[e]	76.3	20.6	3.0	0	3.7	1.36

[a]Calculated from XPS survey spectra, [b]calculated from O 1s spectra: O1sI = peak area at ~533 eV, O1sII = peak at ~534.5 eV, [c]data from [13], [d]PR-masked substrates without patterning, [e]lithographically patterned substrates.

High resolution O 1s spectra for the modified surfaces are shown in Figure 3.13. Bare SU-8 surfaces typically have a single sharp O 1s peak at ~533 eV resulting from C-O-C bonding.[22] In addition to this feature (O1sI), all the surfaces in this work have a second feature at higher binding energy that is independent of substituent (O1sII). Peaks at this energy have previously been assigned to methoxy and carboxy groups and C-O-C bonding at carbon surfaces.[22-24] Walther et al. observed the introduction of an O 1s peak at ~534 eV on SU-8 surfaces after treatment with O_2 plasma that was assigned to the introduction of carbonyl and carboxy groups.[22] For modification at each pH, the O1sII:O1sI ratio is highest in the MP-modified samples suggesting some contribution from methoxy groups (Table 3.2). The O 1s peak for nitro groups occurs at ~533 eV,[25] making it difficult to resolve from the SU-8 C-O-C peak and unlikely to be the origin of peak O1sII for the NP-modified samples. For both modifiers, the O1sII/O1sI ratio is elevated for samples modified in pH 7 solution, possibly arising from a grafting mechanism that is more dominant in pH 7 solution.

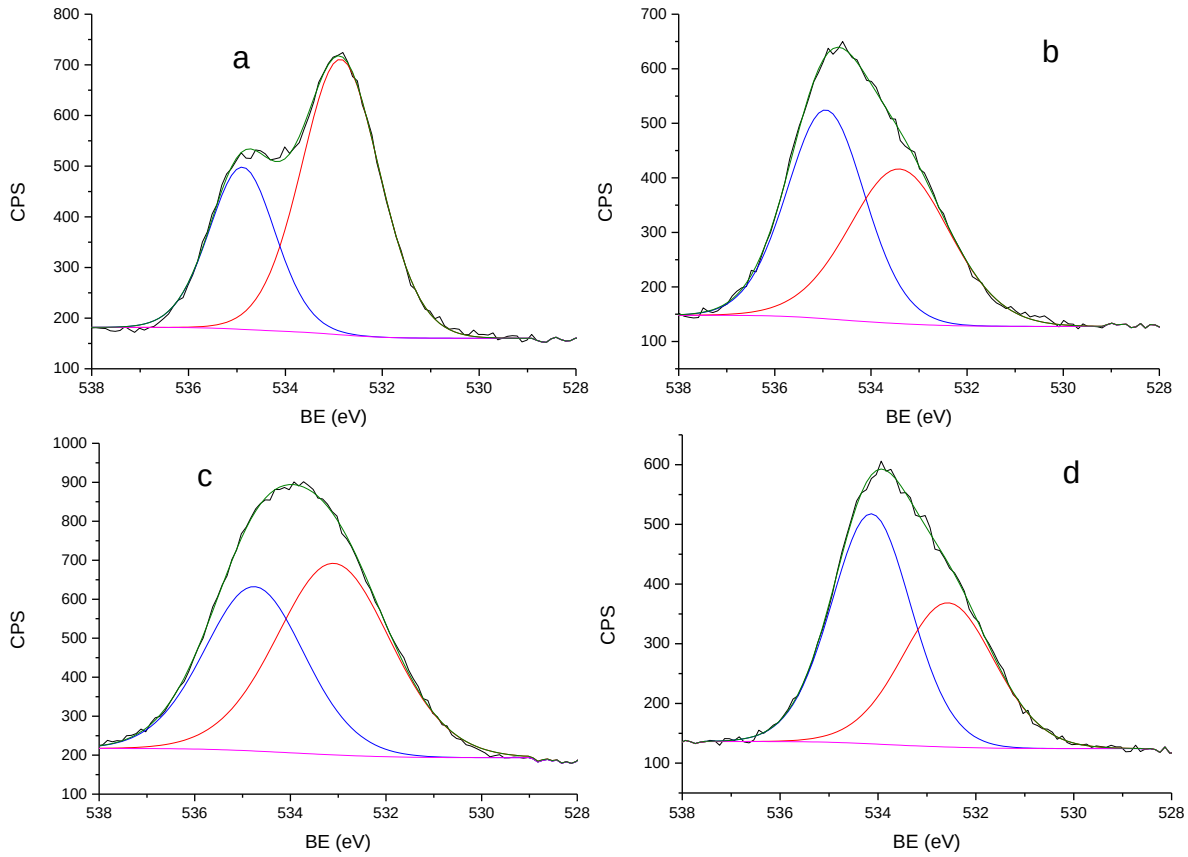

Figure 3.13: O1s XPS spectra of 1 h modified SU-8 surfaces: a. pH 10 NP, b. pH 7 NP, c. pH 10 MP, d. pH 7 MP.

A number of possibilities can be considered to account for the XPS data. Partial oxidation of the SU-8 surface may result in carboxy-type functionalities that would give significant signal at the collection angle used. However, this does not explain the trends in treatment conditions observed. As described in Chapter 1, it has been proposed that O-containing radical species from decomposition of diazoanhydrides formed by the Gomberg-Bachmann reaction of a diazoate with another aryldiazonium ion in DMF and pure water (Scheme 1.4a).[16, 17] Therefore, it is possible that the origin of peak O1sII is the introduction of C-O-N bonding to the surface or the aryl layer (Scheme 1.4b). However, as explained below, the low intensity of N 1s signals for samples modified at pH 7 suggests this mechanism is not occurring. Grafting of aryl radicals to O-containing functionalities naturally present at the surface of the SU-8 may contribute to peak O1sII in all modified samples. Adsorption of buffer components can be eliminated as the origin of O1sII and elevated O signals, as phosphate and carbonate groups are observed at low energy (~530 eV and ~532 eV respectively).[26, 27] Another possible source of O1sII is convolution with peaks from Sb and Sb-oxides from the photoinitiator. [22] Although O1sII is within a few eV of the Sb 3d3/2 peak, there is no evidence for the corresponding Sb 3d5/2 peak at ~528 eV. Additionally, the survey spectra shows none of the other peaks associated

with Sb indicating this is unlikely to be the cause of O1sII. In summary, O1sII likely consists of contributions from species arising from oxidation of the SU-8 surface and C-O functionalities shifted by modification with the aryl layer.

The C 1s XPS spectra for the modified surfaces (Figure 3.14) all can be deconvoluted into two peaks: C-C bonding at 284.8 eV and C-O bonding at ~286.5 eV. Neither the pH of the modification solution or the modifier itself resulted in significant changes in the proportion of these features (1.5:1-2:1). Both of these features are present in unmodified SU-8 in a similar ratio (1.6:1).[22] The lack of new C 1s features after modification is most likely due to the introduced groups being similar to (e.g. methoxy C-O) or overlapping with (e.g. nitro C-N) existing functionalities.[28]

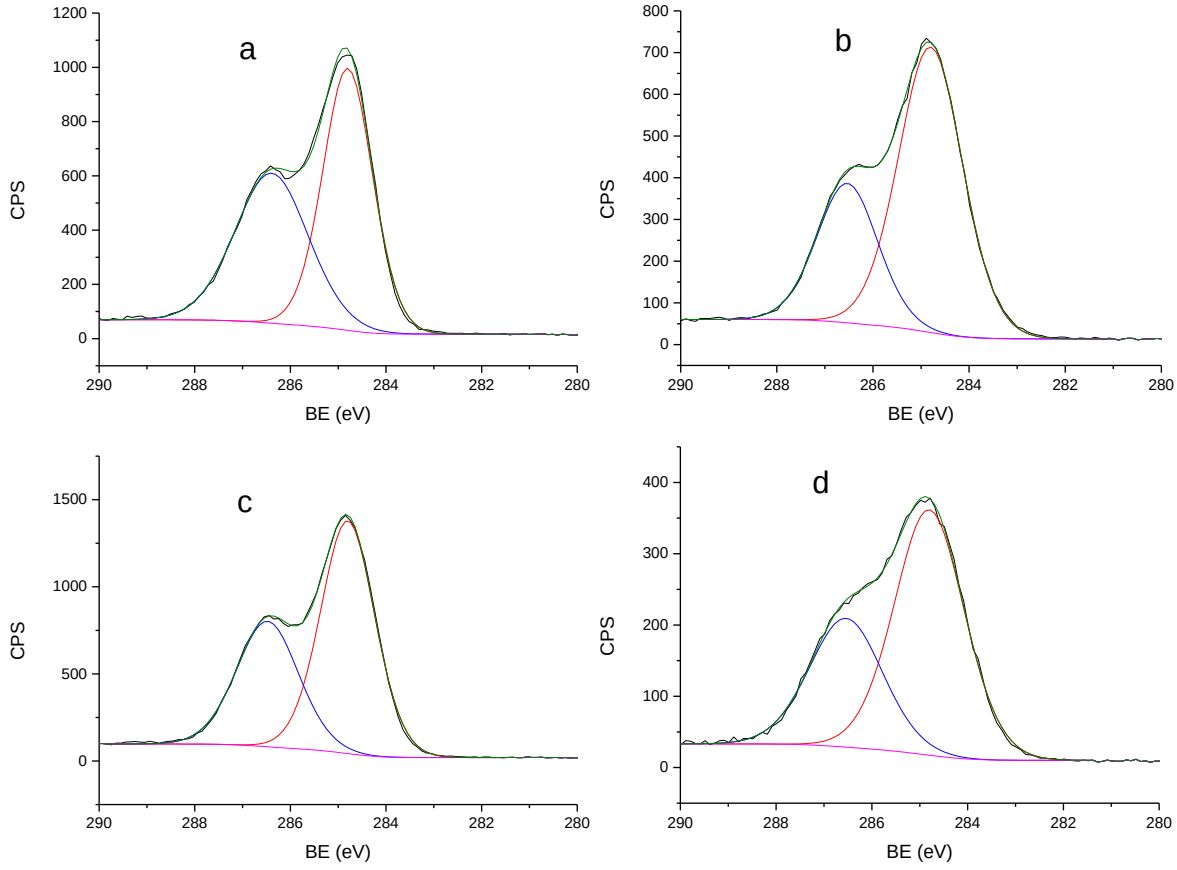

Figure 3.14: C1s XPS spectra of 1h modified SU-8 surfaces: a. pH 10 NP, b. pH 7 NP, c. pH 10 MP, d. pH 7 MP.

Narrow scans in the N 1s region for the modified SU-8 surfaces are shown in Figure 3.15. All samples except MP-modified at pH 7 (pH 7 MP-mod) have low intensity N 1s peaks at ~400 eV. The expected peak at 406 eV associated with nitro groups is not present in either NP-mod sample, suggesting that the nitro groups may have been reduced post-grafting – possibly by the X-ray source or charge neutraliser during XPS analysis.[20] The N 1s peak at 400 eV corresponds to reduced N functionalities

which, for the modifiers used in this study, most likely arise from azo linkages within the film or to the surface, in addition to amine groups for the NP-modified samples. According to the mechanism outlined in Scheme 1.4a, grafting of diazoanhydride-derived radicals is expected to introduce azo linkages in to the film, as well as direct grafting of the aryldiazonium ion to the film or surface (Scheme 1.2). For these samples, a combination of these mechanisms may be occurring. The lack of N-signal in the pH 7 MP-modified sample compared to the relative intensity of O1sII in this sample suggests that grafting via diazoanhydride-derived radicals may not be the origin of O1sII.

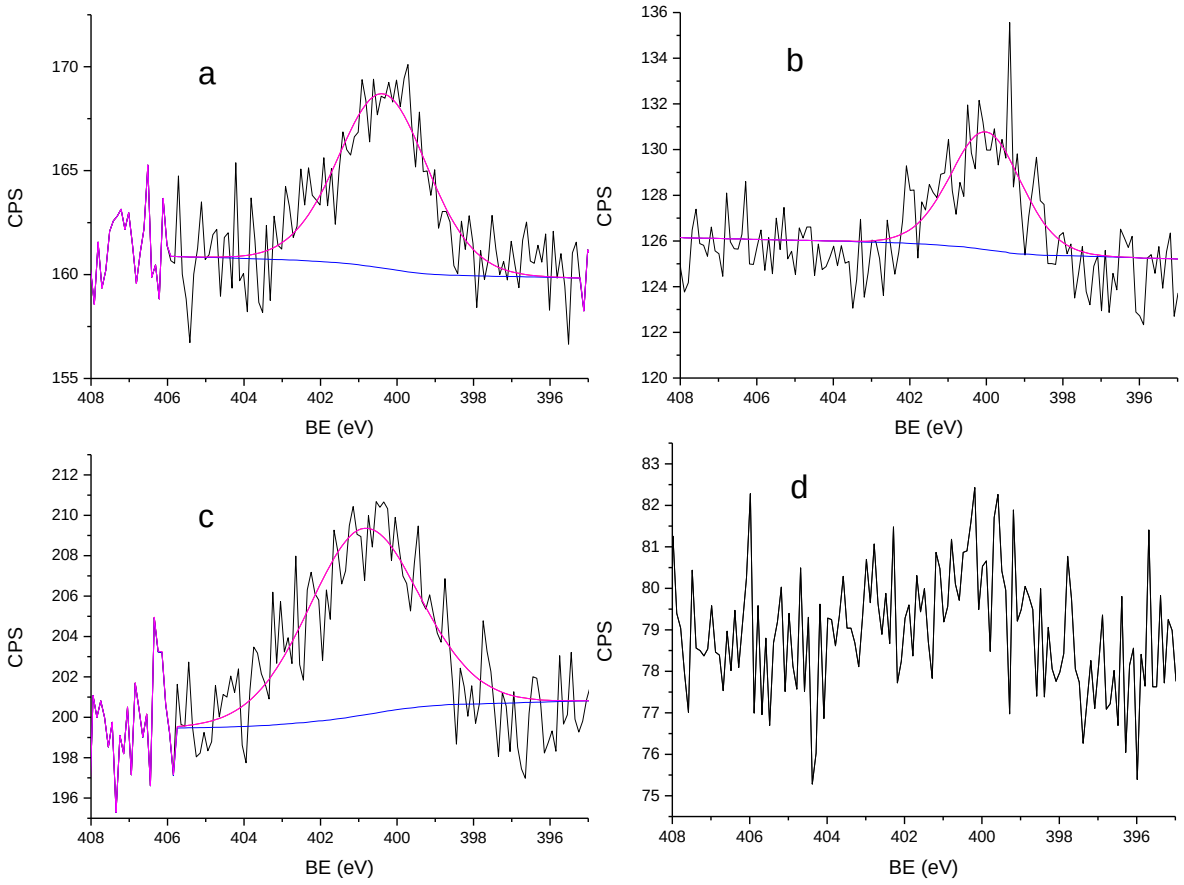

Figure 3.15: N1s XPS spectra of modified SU-8 surfaces: a. pH 10 NP, b. pH 7 NP, c. pH 10 MP, d. pH 7 MP.

3.3.4.2 Proposed Grafting Mechanisms in Aqueous Solution

To summarise the findings from film thickness and XPS measurements, the grafting in aqueous solution at pH 10 and pH 7 appears to occur via a combination of mechanisms. The following grafting mechanisms (presented for convenience in Figure 3.16) are possible under the conditions studied: grafting of aryl radicals formed via a diazoate or diazohydroxide intermediate (Figure 3.16A), grafting of radical decomposition products from a diazoanhydride intermediate (Figure 3.16B), grafting after

heterolytic decomposition of the aryldiazonium ion to aryl cations or by direct attack of the aryldiazonium ion (Figure 3.16C).[16, 20, 21, 29]

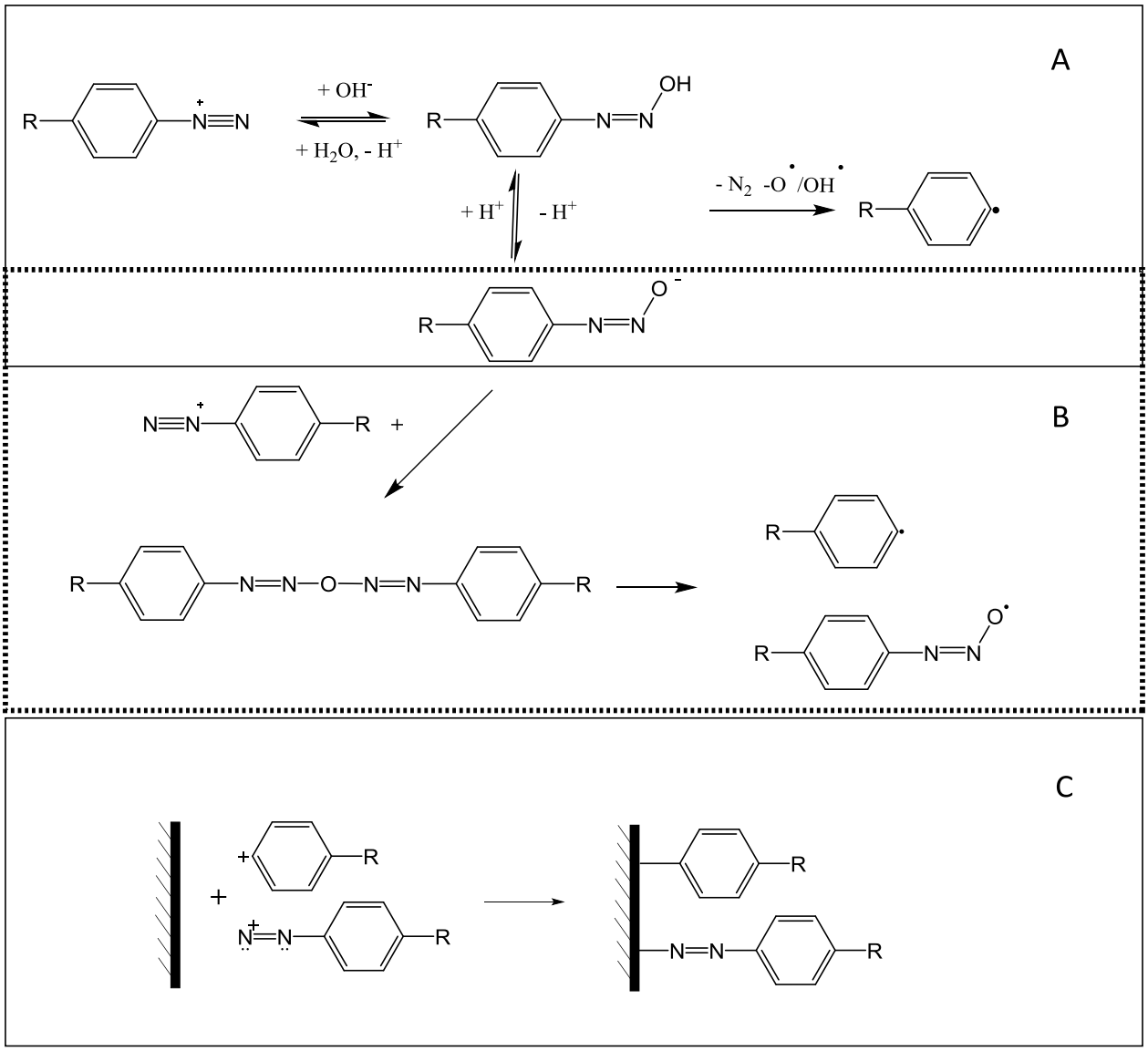

Figure 3.16: Possible aryldiazonium ion grafting mechanisms at non-conducting substrates at pH ≥ 7: A. Formation of the diazohydroxide/diazoate by reaction with OH^- or water and subsequent decomposition to form aryl radicals,[29] B. Formation of a diazohydroxide by reaction of a diazoate with an aryldiazonium ion and decomposition to radicals,[16] C. Grafting via the aryl cation formed by heterolytic decomposition of the aryldiazonium ion and direct attack aryldiazonium ion with a surface.[20]

In pH 10 solution, the aryl film forms within 15 min irrespective of substituent, which is consistent with the reported mechanism of rapid conversion to aryl radicals via the diazoate (Figure 3.16A).[21]

Additionally, the XPS results show reduced N groups present on both NP- and MP-modified surfaces prepared at pH 10, eliminating reduction of NP groups in the X-ray beam as the sole origin of these signals. This suggests either direct attack of the aryldiazonium ion (Figure 3.16C) or the involvement of diazoanhydride-derived radicals (Figure 3.16B). The observation of unidentified O functionalities on both surfaces may support the grafting of diazoanhydride-derived radicals.[17] The involvement of aryl cations cannot be directly excluded, however, it can be inferred from the relative stability of the nitro- and methoxy-substituted aryl cations that this is not a significant route for the grafting process at pH 10.[10] Due to the electron-withdrawing nitro substituent, the nitrophenyl cation is highly unstable. In contrast, the electron-donating methoxy substituent stabilises both the aryldiazonium ion and the aryl cation but this effect is stronger for the aryldiazonium ion and thus this is the more stable species. The observed film thickness differences between MP and NP modification in pH 10 solution suggest the multilayer-formation mechanism is substituent dependent. Although MP films are more activating towards multilayer formation by cationic mechanisms than NP films, this should have minimal effect on reactions involving aryl radicals. However, the expected greater stability of the MBD ion compared to NBD to heterolytic decomposition may improve its lifetime in solution and thus allow the grafting reaction to extend over a longer period to produce thicker films. This is supported by the AFM film thickness results which show minimal change in NP film thickness after 15 min at pH 10 whereas the MP film shows significant film thicknesses up to 30 min. Additionally, the observation of slow precipitate formation during MBD grafting at pH 10 compared to rapid formation in NBD solution provides further evidence of the stability of MBD at high pH.

In pH 7 solution, NP films formed within 15 min and were thicker than those grafted at pH 10 after 30 min reaction time. However, the MP film only reached uniform coverage after 1 hour reaction time. This indicates that grafting at pH 7 is favoured with the electron-withdrawing NO_2 substituent compared to the electron-donating OCH_3 substituent. No significant substituent dependence was observed for grafting in pH 10 solution, suggesting a change in mechanism. XPS results for pH 7 modified samples show some reduced N when grafting NP-groups but none when grafting MP-groups. The lack of N signal for MP-modified surfaces suggests the reduced N signal could arise solely from reduction of NO_2 groups in the X-ray beam rather than by direct attack of the aryldiazonium ion. However, MBD is less electrophilic than NBD and thus less active for formation of azo linkages, which may explain the observed difference between MP and NP films.[10] New O functionalities were observed by XPS for both MP and NP films at a higher proportion than for pH 10 modified samples. Diazoanhydride formation has been as an intermediate at neutral pH and radicals formed from its decomposition may explain the observed increase in O functionalities in these

samples. However, these species should also introduce azo groups into the film (Figure 3.16B) but this was not observed for MP-modified surfaces, where the introduced O functionalities were most significant. Formation of diazohydroxides has also been reported at neutral pH in aqueous solutions via nucleophilic addition of H_2O to the aryldiazonium salt and these species have been shown to homolytically decompose to aryl radicals similarly to diazoates (Figure 3.16A).[29] As H_2O is less nucleophilic than OH^-, it is expected that it would be more sensitive to the electrophilicty of the aryldiazonium ion taking part in the addition reaction and thus it would be expected that the formation of the diazohydroxide would be slower for electron-donating substituents (such as OCH_3) than electron-withdrawing substituents (such as NO_2). This aligns with the observed substituent dependence for grafting in pH 7 solution, suggesting that the primary grafting mechanism at pH 7 is by aryl radicals formed from a diazohydroxide intermediate. The pH dependence of the grafting reaction for MP groups is thus explained as arising from the lower nucleophilicity of H_2O compared to OH^- inhibiting nucleophilic attack at neutral pH.

3.3.5 Modification in Non-Aqueous Conditions

Modification of SU-8 by aryldiazonium ions in acetonitrile is of interest as a model for developing conditions to modify materials with low stability in aqueous solution. The ability to modify the surface by spontaneous reactions in acetonitrile and with ferrocene as an acetonitrile-soluble reducing agent was compared.

Initial experiments to measure the grafting of NP groups to SU-8 surfaces in acetonitrile were conducted using the PR masking method described previously (Scheme 3.1). Reaction in the absence of reducing agent resulted in gradual discoloration of the aryldiazonium ion solution whereas addition of ferrocene resulted in a rapid colour change of the solution from yellow to dark brown and vigorous gas evolution. The amount of modification with and without ferrocene for a 1 h reaction was compared by AFM imaging (Figure 3.17 a and b). The AFM images show that modification in acetonitrile produced surfaces with large quantities of adsorbed debris. After modification in the presence of ferrocene, the edges between modified and unmodified regions are covered in mounds of material 30-50 nm high. Without ferrocene in solution, the surface was covered randomly in 10-20 nm high debris (Figure 3.17b). This is in contrast with modification in aqueous conditions where the pattern was reproduced cleanly by the grafted film (Figure 3.2b). The debris was stable after sonication in acetone, IPA and ethanol indicating it is strongly adsorbed to the surface.

In the absence of aryldiazonium salt, SU-8 surfaces that were immersed in acetonitrile have raised areas ~2 nm high corresponding to the areas exposed to acetonitrile solution (Figure 3.17 c and d), indicating that acetonitrile causes swelling of the SU-8 substrate. However, the lack of debris observed on these surfaces suggests that the debris on the modified surfaces does not arise solely from interactions between acetonitrile and the photoresist. These results imply that the debris observed after immersion in acetonitrile solution containing aryldiazonium ion is due to a reaction between the aryldiazonium ion and AZ1518 PR that has dissolved into the acetonitrile solution. This reaction may lead to polymeric material grafted to, or deposited on, the surface. It is not surprising that if radicals are generated from aryldiazonium ions, they would react with solubilised AZ1518 and it is also possible that aryldiazonium ions themselves may react with solubilised AZ1518 directly. The larger size and increased coverage of debris after grafting in the presence of ferrocene suggests that the reduction of aryldiazonium ions to aryl radicals promotes reaction with the AZ1518. These side reactions with AZ1518 preclude the use of this masking agent.

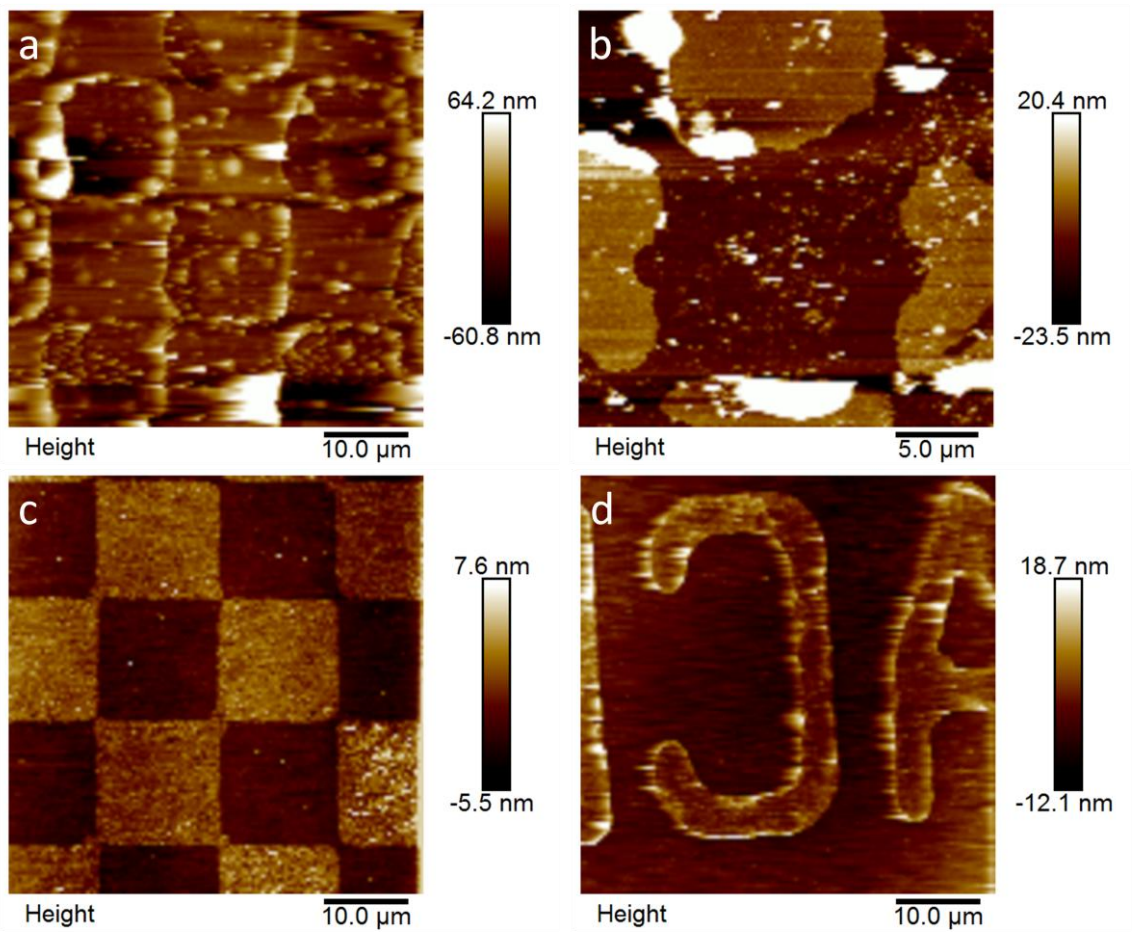

Figure 3.17: AFM images of SU-8 surfaces modified in acetonitrile for 1 h with NP groups with (a) and without (b) ferrocene reducing agent and an acetonitrile blank sample prepared without ferrocene (c and d).

An alternative method for masking substrates for film growth studies is masking using polyimide tape.[30] Polyimide is solvent-resistant and can be prepared with low-residue adhesives; both properties are essential for the present application. The utility of this masking method was tested by modifying a surface with AP groups in aqueous acid conditions as this produces thick, easily identifiable films. A SU-8 surface was masked with polyimide tape to leave a 5 mm x 10 mm strip of exposed substrate for the modification. After 1 h modification, the tape was removed and the surface cleaned by sonication in acetone, IPA and ethanol. As can be seen from the AFM image of this surface in Figure 3.8, there is a clear edge between the grafted film and the unmodified surface – albeit less regular than the PR-masked samples. This may be caused by removal of part of the film when the tape is peeled from the grafted surface or due to spreading of the adhesive on application of the tape. The roughness of the masked areas of the substrate (0.40 ± 0.04 nm) was comparable to the bare areas (0.35 ± 0.02 nm) and thus the masking method is suitable for AFM studies of grafted films.

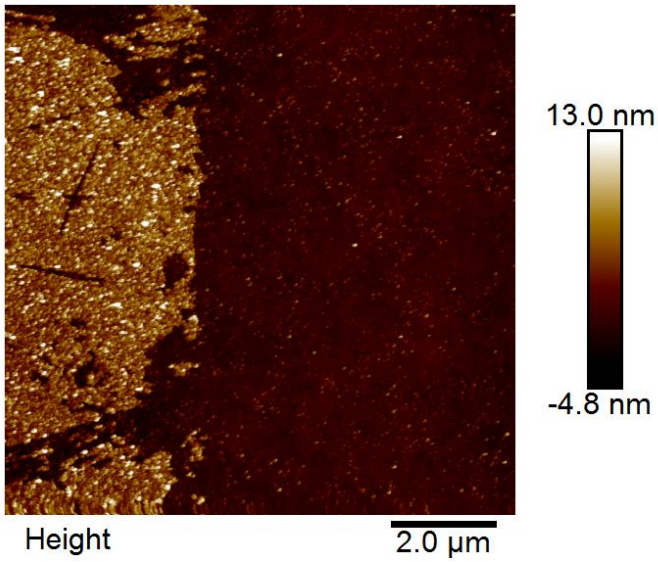

Figure 3.18: AFM image of an SU-8 surface modified with AP groups for 1 h in HCl while masked by polyimide tape.

Polyimide masking was used to prepare SU-8 surfaces modified with NBD and MBD groups in acetonitrile in the presence and absence of ferrocene. After 1 h modification time, the tape was removed and the surfaces were imaged by AFM.

For surfaces modified with NBD in the presence and absence of ferrocene, no clear edge could be observed between the area exposed to the aryldiazonium ion in solution and the area that had been masked with tape. AFM images of areas within the treated and masked areas of NBD-modified samples with and without ferrocene are shown in Figure 3.19. For both modified regions (Figure 3.19 a and b), there was no evidence of a continuous film, however, the sample modified in the presence of ferrocene has a large amount of material scattered on the surface. The scattered nature of the modification prevents the use of film thickness measurements by step height across film edges; instead, feature height was characterised using peak height measurements from linear sections across the image. Average peak height and RMS roughness measurements for modified SU-8 surfaces are presented in Table 3.3 .

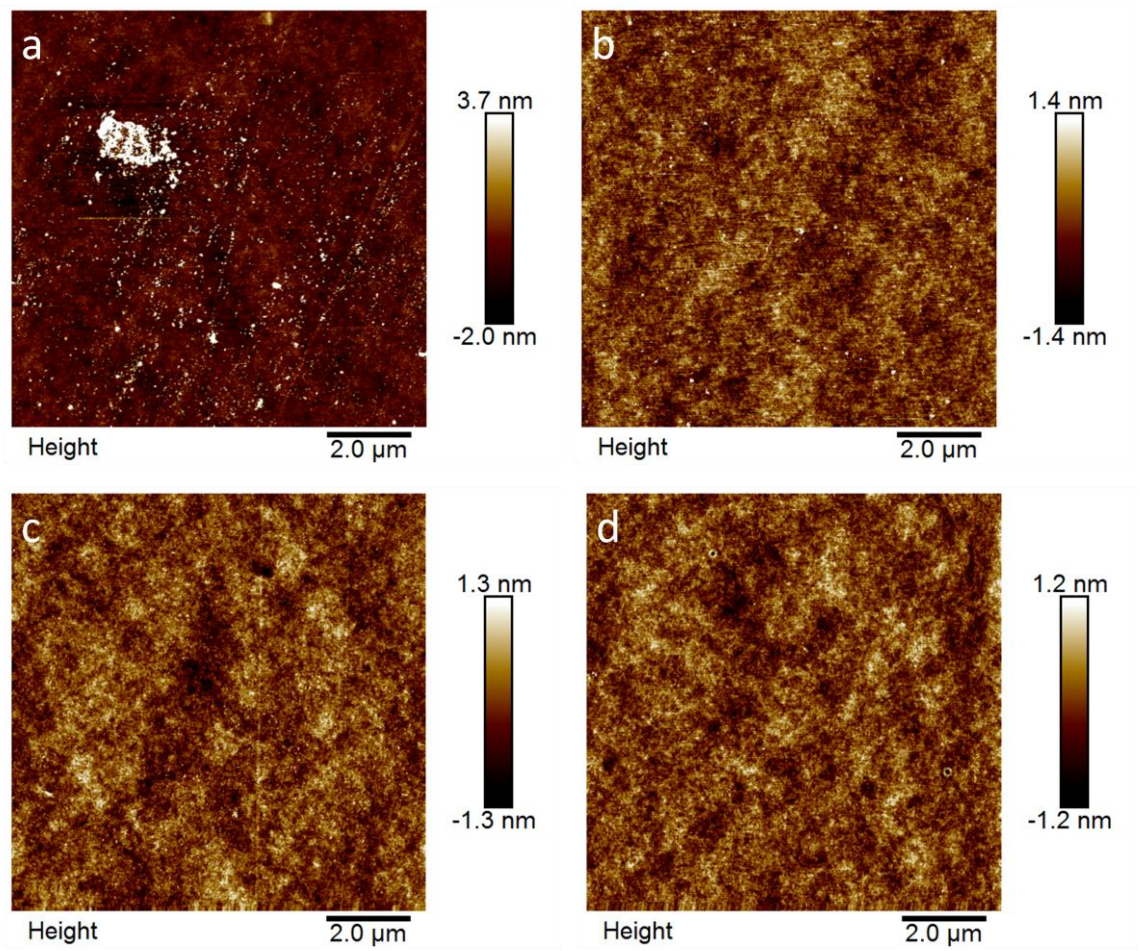

Figure 3.19: AFM images of SU-8 surfaces treated with NBD in acetonitrile for 1 h with (a and b) and without (c and d) ferrocene, NBD-treated areas (a and c) and areas under polyimide tape (b and d).

In the absence of ferrocene, there are a small number of high features, however, similarly sized features were observed on the masked areas and blank samples. The lack of peak height differences suggests that there is no significant modification occurring in the absence of reducing agent, presumably due to the high stability of the aryldiazonium ion in acetonitrile preventing decomposition to reactive species.[31] There were no changes in surface roughness observed in the absence of ferrocene compared to the masked areas or blank samples. In the presence of ferrocene, the surface becomes modified with dispersed material that is polymeric according to the measured feature height and there is an accompanying increase in surface roughness. This patchy modification of the surface likely arises due to rapid reaction with ferrocene forming a large quantity of radicals in solution that are consumed by side reactions (e.g. with ferrocene, solvent or other aryl radicals) and only react sparsely with the surface. Rapid creation and consumption of aryl radicals is consistent with the observed solution colour changes and gas evolution immediately upon addition of ferrocene.

Table 3.3: Peak height and RMS surface roughness measurements for SU-8 surfaces modified in acetonitrile with NP and MP groups or blank samples with or without ferrocene.

		Peak Feature Height (nm)		RMS Roughness (nm)	
		Treated	Bare[a]	Treated	Bare[a]
NP-Mod	With Ferrocene	6 ± 1	1.3 ± 0.1	1.2 ± 0.5	0.43 ± 0.01
	Without Ferrocene	1.31 ± 0.08	0.67 ± 0.09	0.36 ± 0.01	0.35 ± 0.01
MP-Mod	With Ferrocene	5 ± 3	1.32 ± 0.03	0.61 ± 0.01	0.43 ± 0.02
	Without Ferrocene	1.1 ± 0.3	1.0 ± 0.2	0.35 ± 0.01	0.37 ± 0.02
Blank[b]	With Ferrocene	1.0 ± 0.3	0.88 ± 0.08	0.416 ± 0.002	0.46 ± 0.01
	Without Ferrocene	1.0 ± 0.3	0.8 ± 0.3	0.37 ± 0.01	0.37 ± 0.02

[a]Bare data were obtained from areas that were masked during modification. [b]Blank samples were prepared by treatment in acetonitrile with or without ferrocene in the absence of aryldiazonium salt.

Modification with MP groups was conducted under the same conditions and imaged by AFM (Figure 3.20). Addition of ferrocene to methoxybenzenediazonium (MBD) solution resulted in a gradual colour change from red to brown over a few minutes and less gas evolution compared to the reaction with NBD solution. No edge was observed between the area exposed to the aryldiazonium ion solution and the area masked by polyimide tape. AFM imaging of the modified area of the ferrocene treated sample (Figure 3.20a) shows sparse coverage of features a few nm in height (Table 3.3). This coverage is much less than for the NP-modified sample but higher than for either the masked areas or the surfaces prepared without ferrocene. As shown by the data in Table 3.3, the surface roughness is consistent with these observations as it is increased compared to the blank and masked SU-8 surfaces but lower than for the NP-modified sample. In the absence of ferrocene there are no significant features observed by AFM (Figure 3.20b) or changes in roughness after reaction in MBD. These results indicate MBD can be grafted to SU-8 but only in the presence of ferrocene, however, the coverage was much lower than after NBD modification - most likely due to the more negative reduction potential of MBD.[20]

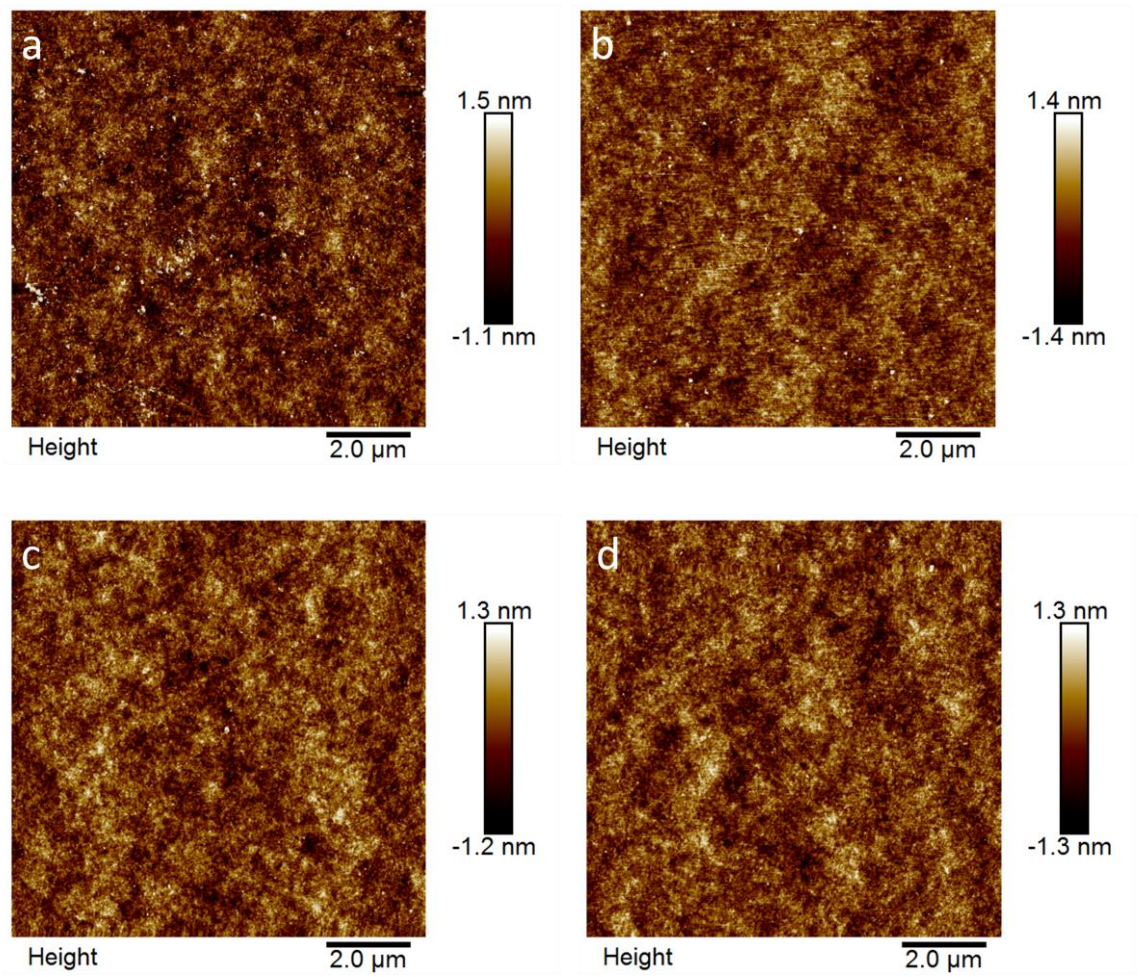

Figure 3.20: AFM images of SU-8 surfaces treated with MBD in acetonitrile for 1 h with (a and b) and without (c and d) ferrocene, areas exposed to MBD solution (a and c) and areas under polyimide tape (b and d).

Based on the results from polyimide masking studies, the facile modification of insulating substrates in acetonitrile requires a reducing agent. The high stability of aryldiazonium ions in acetonitrile makes decomposition to reactive species, and thus the spontaneous grafting reaction, slow.[19] However, it may be possible to achieve significant grafting at long reaction times either by gradual decomposition to reactive species or direct attack of the aryldiazonium ion. In the presence of reducing agent, rapid formation of radicals allows grafting to occur, however, grafting to the surface is uncontrolled and results in sporadic coverage. Tuning the reaction conditions is necessary to achieve practical coverage. For example, gradual introduction of the reducing agent over the reaction time may limit the opportunities for side reactions between radicals in solution, allowing more time for radicals to diffuse to the surface.

3.4 Conclusions

Grafting of aryldiazonium ions to a non-conducting substrate was investigated in aqueous solution at both pH 7 and pH 10. Both films with electron-donating (MP) and electron-withdrawing (NP) substituents were grafted successfully at pH 7 and pH 10. The effects of pH and substituent were investigated at a range of reaction times by AFM film thickness measurements. Grafting at pH 7 was found to be substituent-dependent, with MP films grafting more slowly than NP films whereas grafting at pH 10 showed no dependence on substituent. It is proposed that grafting occurs by aryl radicals produced from decomposition of diazoates and diazohydroxides at pH 10 and pH 7 respectively. As shown by these results, this method allows grafting aryldiazonium ions under mild conditions to non-conducting or semiconducting materials within a wide pH window.

Spontaneous grafting and grafting in the presence of a reducing agent in non-aqueous solution to non-conducting substrates were compared in acetonitrile. Spontaneous grafting of MBD and NBD to SU-8 does not appear to occur or is very slow in non-aqueous conditions. In the presence of ferrocene, grafting of scattered polymeric species to SU-8 was observed after reaction with NBD and, to a lesser extent, MBD. This suggests that the rapid reduction of the aryldiazonium ions in solution results in uncontrolled grafting, primarily between radicals in solution to form polymeric species. These results indicate that grafting to non-conducting substrates in non-aqueous conditions requires a reducing agent and careful control of the reaction conditions to produce uniform surfaces.

The extension of these modification conditions to prepare aryldiazonium-modified metal oxide materials is described in the subsequent chapters. Modification of MnO_2 in aqueous solution at neutral and basic pH and non-aqueous solution in the absence of a reducing agent is described Chapters 4 and 5. Modification of ZnO in non-aqueous solution in the absence of reducing agent and basic aqueous solutions is described in Chapter 6.

3.5 References

1. Garcia, A.; Hanifi, N.; Jousselme, B.; Jégou, P.; Palacin, S.; Viel, P.; Berthelot, T., Polymer Grafting by Inkjet Printing: A Direct Chemical Writing Toolset. *Adv. Funct. Mater.* **2013,** *23* (29), 3668-3674.
2. Bouriga, M.; Chehimi, M. M.; Combellas, C.; Decorse, P.; Kanoufi, F.; Deronzier, A.; Pinson, J., Sensitized Photografting of Diazonium Salts by Visible Light. *Chem. Mater.* **2013,** *25* (1), 90-97.
3. Chehimi, M. M.; Lamouri, A.; Picot, M.; Pinson, J., Surface Modification of Polymers by Reduction of Diazonium Salts: Polymethylmethacrylate as an Example. *J. Mater. Chem. C* **2014,** *2* (2), 356-363.
4. Picot, M.; Rodulfo, R.; Nicolas, I.; Szymczyk, A.; Barrière, F.; Rabiller-Baudry, M., A Versatile Route to Modify Polyethersulfone Membranes by Chemical Reduction of Aryldiazonium Salts. *J. Membrane Sci,* **2012,** *417–418*, 131-136.

5. Le, X. T.; Viel, P.; Jegou, P.; Garcia, A.; Berthelot, T.; Bui, T. H.; Palacin, S., Diazonium-Induced Anchoring Process: An Application to Improve the Monovalent Selectivity of Cation Exchange Membranes. *J. Mater. Chem.* **2010,** *20* (18), 3750-3757.
6. Brisset, F.; Vieillard, J.; Berton, B.; Morin-Grognet, S.; Duclairoir-Poc, C.; Le Derf, F., Surface Functionalization of Cyclic Olefin Copolymer with Aryldiazonium Salts: A Covalent Grafting Method. *Appl. Surf. Sci.* **2015,** *329*, 337-346.
7. Mévellec, V.; Roussel, S.; Tessier, L.; Chancolon, J.; Mayne-L'Hermite, M.; Deniau, G.; Viel, P.; Palacin, S., Grafting Polymers on Surfaces: A New Powerful and Versatile Diazonium Salt-Based One-Step Process in Aqueous Media. *Chem. Mater.* **2007,** *19* (25), 6323-6330.
8. Griffete, N.; Ahmad, R.; Benmehdi, H.; Lamouri, A.; Decorse, P.; Mangeney, C., Elaboration of Hybrid Silica Particles Using a Diazonium Salt Chemistry Approach. *Colloids Surf., A* **2013,** *439* (0), 145-150.
9. Mahjoubi, H.; Kinsella, J. M.; Murshed, M.; Cerruti, M., Surface Modification of Poly(D,L-Lactic Acid) Scaffolds for Orthopedic Applications: A Biocompatible, Nondestructive Route Via Diazonium Chemistry. *ACS Appl. Mater. Interfaces* **2014,** *6* (13), 9975-9987.
10. S. J. Canning, P.; McCrudden, K.; Maskill, H.; Sexton, B., Rates and Mechanisms of the Thermal Solvolytic Decomposition of Arenediazonium Ions. *J. Chem. Soc., Perkin Trans. 2* **1999,** (12), 2735-2740.
11. Abiman, P.; Wildgoose, G. G.; Compton, R. G., A Mechanistic Investigation into the Covalent Chemical Derivatisation of Graphite and Glassy Carbon Surfaces Using Aryldiazonium Salts. *J. Phys. Org. Chem.* **2008,** *21* (6), 433-439.
12. Dechézelles, J.-F.; Griffete, N.; Dietsch, H.; Scheffold, F., A General Method to Label Metal Oxide Particles with Fluorescent Dyes Using Aryldiazonium Salts. *Part. Part. Syst. Char.* **2013,** *30* (7), 579-583.
13. Simons, B. M.; Lehr, J.; Garrett, D. J.; Downard, A. J., Formation of Thick Aminophenyl Films from Aminobenzenediazonium Ion in the Absence of a Reduction Source. *Langmuir* **2014,** *30* (17), 4989-4996.
14. Belanger, D.; Pinson, J., Electrografting: A Powerful Method for Surface Modification. *Chem. Soc. Rev.* **2011,** *40* (7).
15. Lyskawa, J.; Grondein, A.; Bélanger, D., Chemical Modifications of Carbon Powders with Aminophenyl and Cyanophenyl Groups and a Study of Their Reactivity. *Carbon* **2010,** *48* (4), 1271-1278.
16. Schmidt, G.; Gallon, S.; Esnouf, S.; Bourgoin, J.-P.; Chenevier, P., Mechanism of the Coupling of Diazonium to Single-Walled Carbon Nanotubes and Its Consequences. *Chem. Eur. J.* **2009,** *15* (9), 2101-2110.
17. Lipińska, M. E.; Rebelo, S. L. H.; Pereira, M. F. R.; Gomes, J. A. N. F.; Freire, C.; Figueiredo, J. L., New Insights into the Functionalization of Multi-Walled Carbon Nanotubes with Aniline Derivatives. *Carbon* **2012,** *50* (9), 3280-3294.
18. Hanwell, M. D.; Curtis, D. E.; Lonie, D. C.; Vandermeersch, T.; Zurek, E.; Hutchison, G. R., Avogadro: An Advanced Semantic Chemical Editor, Visualization, and Analysis Platform. *J. Cheminf.* **2012,** *4* (1), 1-17.
19. Lehr, J.; Williamson, B. E.; Downard, A. J., Spontaneous Grafting of Nitrophenyl Groups to Planar Glassy Carbon Substrates: Evidence for Two Mechanisms. *J. Phys. Chem. C* **2011,** *115* (14), 6629-6634.
20. Mesnage, A.; Lefèvre, X.; Jégou, P.; Deniau, G.; Palacin, S., Spontaneous Grafting of Diazonium Salts: Chemical Mechanism on Metallic Surfaces. *Langmuir* **2012,** *28* (32), 11767-11778.
21. Podvorica, F. I.; Kanoufi, F.; Pinson, J.; Combellas, C., Spontaneous Grafting of Diazoates on Metals. *Electrochim. Acta* **2009,** *54* (8), 2164-2170.
22. Walther, F.; Drobek, T.; Gigler, A. M.; Hennemeyer, M.; Kaiser, M.; Herberg, H.; Shimitsu, T.; Morfill, G. E.; Stark, R. W., Surface Hydrophilization of Su-8 by Plasma and Wet Chemical Processes. *Surf. Interface Anal.* **2010,** *42* (12-13), 1735-1744.

23. Wildgoose, G. G.; Lawrence, N. S.; Leventis, H. C.; Jiang, L.; Jones, T. G. J.; Compton, R. G., X-Ray Photoelectron Spectroscopy Studies of Graphite Powder and Multiwalled Carbon Nanotubes Covalently Modified with Fast Black K: Evidence for a Chemical Release Mechanism Via Electrochemical Reduction. *J. Mater. Chem.* **2005,** *15* (9), 953-959.
24. Zhong, R.-S.; Qin, Y.-H.; Niu, D.-F.; Tian, J.-W.; Zhang, X.-S.; Zhou, X.-G.; Sun, S.-G.; Yuan, W.-K., Effect of Carbon Nanofiber Surface Functional Groups on Oxygen Reduction in Alkaline Solution. *J. Power Sources* **2013,** *225*, 192-199.
25. Toupin, M.; Belanger, D., Spontaneous Functionalization of Carbon Black by Reaction with 4-Nitrophenyldiazonium Cations. *Langmuir* **2008,** *24* (5), 1910-1917.
26. Puziy, A. M.; Poddubnaya, O. I.; Socha, R. P.; Gurgul, J.; Wisniewski, M., XPS and NMR Studies of Phosphoric Acid Activated Carbons. *Carbon* **2008,** *46* (15), 2113-2123.
27. Liu, B.; Liu, L.-M.; Lang, X.-F.; Wang, H.-Y.; Lou, X. W.; Aydil, E. S., Doping High-Surface-Area Mesoporous TiO_2 Microspheres with Carbonate for Visible Light Hydrogen Production. *Energy Environ. Sci.* **2014,** *7* (8), 2592-2597.
28. Biniak, S.; Szymański, G.; Siedlewski, J.; Świątkowski, A., The Characterization of Activated Carbons with Oxygen and Nitrogen Surface Groups. *Carbon* **1997,** *35* (12), 1799-1810.
29. Sienkiewicz, A.; Szymula, M.; Narkiewicz-Michalek, J.; Bravo-Díaz, C., Formation of Diazohydroxides ArN_2OH in Aqueous Acid Solution: Polarographic Determination of the Equilibrium Constant Kr for the Reaction of 4-Substituted Arenediazonium Ions with H_2O. *J. Phys. Org. Chem.* **2014,** *27* (4), 284-289.
30. Shul, G.; Weissmann, M.; Bélanger, D., Electrochemical Formation of an Ultrathin Electroactive Film from 1,10-Phenanthroline on a Glassy Carbon Electrode in Acidic Electrolyte. *Langmuir* **2014,** *30* (22), 6612-6621.
31. Assresahegn, B. D.; Brousse, T.; Bélanger, D., Advances on the Use of Diazonium Chemistry for Functionalization of Materials Used in Energy Storage Systems. *Carbon* **2015,** *92* (0), 362-381.

4 Modification of MnO_2 Nanoparticles with Aryldiazonium Ions

4.1 Introduction

MnO_2, especially in nanostructured forms, is a material with promising applications in energy storage, sensing and catalysis. This promise arises from MnO_2 being an inexpensive, easily-synthesised and environmentally friendly alternative to existing materials such as RuO_2.[1-3]

4.1.1 Structure of MnO_2

MnO_2 is more specifically a class of Mn oxides that are typically nonstoichiometric, have mixed valency, incorporated cations and structural vacancies.[4] MnO_2 also exists in a number of structural polymorphs constructed by different combinations of edge and face sharing between MnO_6 octahedra. These polymorphs typically have tunnel (one- and two-dimensional) or cavity (3-dimensional) structures that can be occupied by foreign cations (Figure 4.1). These incorporated cations can act to balance the charge at Mn (III) sites present in mixed valence oxides or produced during electrochemical reactions (see section 4.1.3.1). This structural diversity enables the MnO_2 polymorph to be selected such that it matches the desired application for example by maximising ionic conductivity in electrochemical energy storage materials. MnO_2 is a semiconductor with the band gap of the material depending on the crystal structure and morphology of the material.[5, 6]

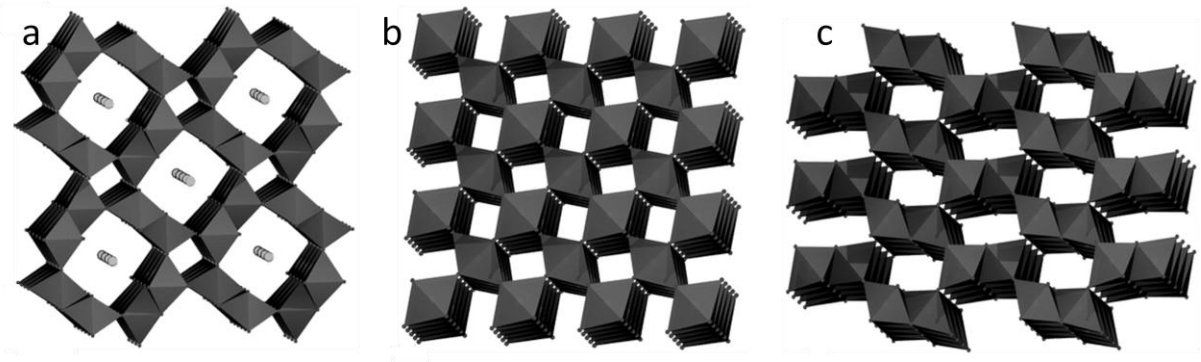

Figure 4.1: MnO_2 crystal structures: a. cryptomelane-type α-MnO_2 with incorporated cations, b. pyrolusite-type β-MnO_2 and c. pyrolusite-type γ-MnO_2 Adapted from reference 7.

4.1.2 Synthesis of MnO_2

MnO_2 nanoparticles are typically prepared by a coprecipitation method using the comproportionation reaction between Mn^{2+} and MnO_4^- in aqueous solution (Equation 4.1).[4] The

properties of the resulting material such as crystal structure and morphology can be tuned by controlling the reaction conditions. A wide range of MnO_2 materials have been prepared by varying the pH, reactant ratios and temperature of the precipitation reaction.[8,9]

$$2MnO_4^- + 3Mn^{2+} + 2H_2O \rightarrow 5MnO_2 + 4H^+$$ Equation 4.1

Alternatively, a single source of Mn can be reacted with an oxidant or reductant (for Mn^{2+} and MnO_4^- respectively) to produce MnO_2 by a range of reactions at ambient temperature[9] or hydrothermally.[10,11,12]

When preparing composite electrodes of MnO_2 with carbon materials, it is possible to prepare the MnO_2 *in situ* on the substrate surface by redox deposition between carbon and MnO_4^- ions (Equation 4.2).[13] This process results in a self-terminating thin layer of MnO_2 coating the carbon substrate. The growth process typically initiates at defect sites on the carbon substrates and requires harsher reaction conditions (lower solution pH, microwave irradiation or reflux) at carbon substrates with a low defect density.[14] This approach is desirable for electrochemical applications due to the increased contact between the MnO_2 and the substrate favouring stability and electrical conductivity.[15]

$$4MnO_4^- + 3C + 2H_2O \rightleftarrows 4MnO_2 + 3CO_2 + 4OH^-$$ Equation 4.2

In addition to preparation by solution phase redox reactions, MnO_2 is also commonly produced by electrochemical deposition from Mn solutions under anodic or cathodic conditions. Anodically prepared MnO_2 is also known as electrolytic manganese dioxide and has been used extensively in battery electrodes. Anodic deposition is typically conducted in acidic or neutral conditions and occurs with the overall reaction outlined in Equation 4.3 but the actual reaction pathway followed depends on the pH of the solution.[16]

$$Mn^{2+} + 2H_2O \rightarrow MnO_2 + 4H^+ + 2e^-$$ Equation 4.3

Cathodic deposition is less commonly employed, however, it has the possible advantages of allowing co-deposition of metals and preventing damaging oxidation to metallic substrates during the deposition process.[17] Cathodic electrodeposition is carried out in neutral aqueous conditions according to Equation 4.4.[18]

$$MnO_4^- + 2H_2O + 3e^- \rightarrow MnO_2 + 4OH^-$$ Equation 4.4

The properties of the resulting electrodeposited MnO_2 can be varied by changing the deposition parameters such as pH, Mn concentration, deposition potential, current density and temperature.

Careful manipulation of the deposition and growth kinetics through these parameters has been used to prepare electrodeposited MnO_2 films with controlled morphology and crystallinity.[18, 19]

4.1.3 Applications of MnO_2

The work on MnO_2 described in this thesis focuses on its application as an electrode material in energy storage devices, especially pseudocapacitors, so this will be described in detail along with some other common applications of MnO_2.

4.1.3.1 Electrochemical Energy Storage

4.1.3.1.1 Battery Electrodes

The most important historical application of MnO_2 is as a cathode material in batteries such as the Leclanché cell and zinc-carbon dry cells.[4] In addition to these primary batteries, MnO_2 has been studied extensively as a material for rechargeable Li-ion batteries in aqueous and non-aqueous media.[1] Compared to Fe-, Co- and Ni- based electrodes, MnO_2 is of interest due to its lower toxicity, cost and improved operating voltage and capacity.[20] Charge storage in MnO_2 electrodes in Li-ion batteries occurs according to the 'conversion' mechanism (Equation 4.5) where Li is incorporated into the electrode through reversible redox reactions.[1]

$$MnO_2 + 4Li^+ + 4e^- \rightleftarrows Mn + 2Li_2O \qquad \text{Equation 4.5}$$

However, in many systems, capacity loss occurs on cycling due to the large structural rearrangements of the electrode that occur on Li intercalation and the efficiency of the charge and discharge process is reduced by the poor conductivity of MnO_2.[20] Performance and stability improvements for MnO_2 battery electrodes have been achieved by using porous nanostructures to facilitate the Li-ion diffusion process and composite electrodes with conducting nanomaterials such as graphene or carbon nanotubes to improve conductivity and provide mechanical support in the electrode.[21-23]

4.1.3.1.2 Pseudocapacitor Electrodes

In addition to energy storage via battery electrodes, an emerging application is the use of MnO_2 in pseudocapacitor electrodes. Pseudocapacitors store charge through Faradaic processes where the active electrode material undergoes rapid reversible redox reactions that store and release electrons. This Faradaic component distinguishes pseudocapacitance from conventional and double-layer capacitance where there is no charge transfer across the electrode interface and thus pseudocapacitance is not a true capacitive behaviour (hence 'pseudo'). The capacitor-like response

of the electrode arises due to these processes displaying similar linear dependence of charge storage on the width of the potential window.[24] This behaviour is distinct from the Faradaic reactions at battery electrodes which display non-linear charge storage dependence and are typically irreversible due to phase changes and high overpotentials.[25] Li-ion intercalation electrodes display an intermediate behaviour between batteries and pseudocapacitors due to their highly linear discharge curves.[26] This is referred to as 'extrinsic' pseudocapacitance as the capacitor-like behaviour arises from the short diffusion pathways associated with nanostructured electrodes rather than the material itself.[24, 27] Combinations of redox processes can lead to a capacitive response (linear charge storage dependence) overlaid with peaks at fixed potentials from other Faradaic processes.[28, 29]

Early research on Faradaic pseudocapacitance was centred on electrosorption of monolayers of protons and metals on noble metal electrodes and metal oxide monolayers.[26, 30, 31] Subsequently, transition metal oxides, conducting polymers and chemically modified carbon materials have all been investigated as pseudocapacitor electrodes.[32] An ideal pseudocapacitance material is RuO_2 due to its combination of high theoretical capacitance (~2000 Fg^{-1}), wide potential window, chemical stability and high conductivity.[33] The charge storage mechanism of RuO_2 in acidic solution relies on reversible electrochemical protonation (Equation 4.6 where x = 1 or 2)[34] which can proceed rapidly due to the high diffusion rate of protons.[35] However, despite its favourable electrochemical properties, the high cost and toxicity of RuO_2 limits its application to small-scale devices and has resulted in a search for alternative materials that are more readily available.[32]

$$RuO_2 + xH^+ + xe^- \rightleftarrows RuO_{2-x}(OH)_x \qquad \text{Equation 4.6}$$

Initially reported by Lee et al.,[35, 36] MnO_2 is a promising pseudocapacitance material due to its comparable performance to RuO_2 (theoretical capacitance of MnO_2 >1000 F g^{-1})[37] but lower cost and toxicity. Pseudocapacitance behaviour in MnO_2 involves reversible conversion between the Mn (IV) and Mn (III) oxidation states (Equation 4.7). This change in charge of the electrode material is balanced by electrolyte ions (A^+) which either adsorb onto the electrode surface or diffuse into the electrode material depending on whether the conversion reaction takes place at the surface or in the material bulk.[38] These diffusion processes are typically rate limiting in pseudocapacitors and are responsible for the lower charge/discharge rate compared to double layer capacitors.[32] MnO_2-based pseudocapacitors are currently held back by two main issues: poor electrical conductivity and limited cycling stability.

$$Mn(IV)O_2 + xA^+ + xe^- \rightleftarrows Mn(IV)_{1-x}Mn(III)_xO_2A_x \quad \text{Equation 4.7}$$

MnO_2 has an intrinsically low conductivity (~10^{-6} S cm^{-1}), especially when compared to higher performing, but more expensive, alternatives such as RuO_2 (~10^3 S cm^{-1}).[39] This low conductivity makes the production of high capacitance MnO_2 electrodes difficult as increasing the active mass of the electrode results in the electrode becoming more resistive. The low conductivity of MnO_2 can be offset by the addition of conducting additive materials, however, these increase the bulk of the electrode with a lower energy-density material, requiring larger devices to achieve the same energy storage.[40] Additionally, the junctions between additives and the electrode material in a composite electrode raise the contact resistance of the electrode, reducing energy storage performance.[41] Other methods to improve the conductivity of the MnO_2 include: doping with conducting elements,[42, 43] or through the use of novel electrode architectures.[44, 45]

The poor stability of MnO_2 electrodes arises from a combination of physical and chemical breakdown processes that occur as the electrode is cycled.[43] As shown in Equation 4.7, the Faradaic process responsible for charge storage in MnO_2 results in incorporation of charge balancing cations into the electrode structure. As these ions move into the electrode, the electrode swells to accommodate them and correspondingly contracts as the ions flow out on discharge. Due to the brittle nature of MnO_2, this motion results in gradual cracking and flaking off of the electrode material, resulting in a decline in capacitance.[46] Strategies to improve the physical stability of MnO_2 electrodes include incorporation of conducting polymers to improve electrode flexibility[47-49] or other metal oxides such as cobalt and nickel that have more favourable structural parameters.[50, 51]

Chemical breakdown of the electrode material occurs due to the irreversible conversion of Mn oxides to soluble Mn^{2+}, causing the MnO_2 electrode to dissolve. This process is particularly dominant in acidic media where the Mn^{2+} oxidation state is favoured. This effectively limits the useful voltage window and pH in aqueous electrolytes. Non-aqueous electrolytes can increase the voltage window of a capacitor system by removing the limitation resulting from water oxidation allowing higher positive potentials to compensate for the voltage window being limited to above 0 V (vs. SCE).[52] Organic electrolytes[53-55] and ionic liquids[56-58] have been explored as alternatives to aqueous electrolytes and were successfully used to extend the voltage window of MnO_2 capacitors. However, large ion sizes, poor ionic conductivity and high viscosity limit the capacitance and rate capability of these devices.[53, 58] The limited voltage window of MnO_2 can also be circumvented by using an asymmetric device with a MnO_2 cathode and an anode that is more stable at negative potential such as activated carbon.[59, 60]

4.1.3.2 Other Applications

MnO_2 has been widely studied as a material for catalysis due to its low environmental impact, structural versatility and range of stable oxidation states.[61] Although cheaper than the noble metal catalysts currently employed, the activity of MnO_2 is generally lower.[62] Approaches to improve the activity of MnO_2 usually involve controlling the structure and morphology of the MnO_2 materials. Fine synthetic control over MnO_2 materials has been used to produce nanostructured and mixed valence catalysts with activity towards amine oxidation for the synthesis of imines[63] and oxidative decomposition of ozone[61] and a range organic contaminants.[64-67] The viability of MnO_2 materials for electrocatalysis is limited by high overpotentials arising due to its poor conductivity. Synthesis of controlled nanostructures, mixed valence materials and doping with conducting elements has been found to lower the overpotential of MnO_2 for water oxidation[3, 68, 69] and oxygen reduction.[70, 71] Preparing MnO_2 defect structures with oxygen vacancies is another approach for improving the surface activity of MnO_2 catalysts,[72] this was found to enhance the activity of MnO_2 towards oxygen reduction.[62, 73]

The electrochemical properties of MnO_2 that are utilised for electrocatalysis and energy storage can also be exploited to prepare electrochemical sensors. These sensors typically operate using potentiometric or amperometric signals generated by electrocatalytic conversion of the analyte by the MnO_2 electrode. Sensors based on MnO_2 have been used for detection of hydrazine,[74, 75] formaldehyde,[76] phenolic compounds,[77, 78] ascorbic acid,[79] nitrate, [80] biomolecules[2, 81] and H_2O_2.[79, 80, 82] H_2O_2 can also be used as a signal amplifier in enzymatic biosensors,[83] further extending the sensing applications of MnO_2. MnO_2 sensor electrodes are typically prepared as composites with conducting carbon nanomaterials to improve the electrode surface area and counteract the poor conductivity of MnO_2.[80, 81]

4.1.4 Surface Modification of MnO_2

As both the energy storage and electrode breakdown processes occur at the electrode surface, surface modification of MnO_2 may result in electrodes with enhanced performance and stability. Electrode architectures that reduce the conduction path between the MnO_2 and the current collector should limit the influence of the low MnO_2 conductivity on the electrode performance.

At the time of this work, there have been few reports of surface modification of MnO_2. Wang et al. used the dye pyrocatechol violet to improve the dispersibility of MnO_2 nanoparticles for composite electrodes.[84] It was suggested that the dye bound through the catechol group as these have been demonstrated to bind to metal oxides.[85-87] Another method used to modify MnO_2 was the deposition

of conducting polymers onto MnO_2 surfaces either electrochemically or spontaneously.[88-90] Rather than tuning the properties of the MnO_2 material, the conducting polymers were used to prepare composites with improved conductivity and stability. The mechanism of attachment of the conducting polymer to the MnO_2 surface was not explored.

One possible electrode architecture is a nanoparticle array immobilised on a conducting support through molecular tethers (Figure 4.2). This enables a 3D electrode structure for higher active mass while shortening the conduction path between the MnO_2 and the conducting additive. Tethered assemblies should also allow superior electrolyte access to the MnO_2 surface due to their open structure. As nanostructured materials have an increased surface-area-to-volume ratio, nanomaterial-based electrodes have the additional benefit of improved volumetric performance.

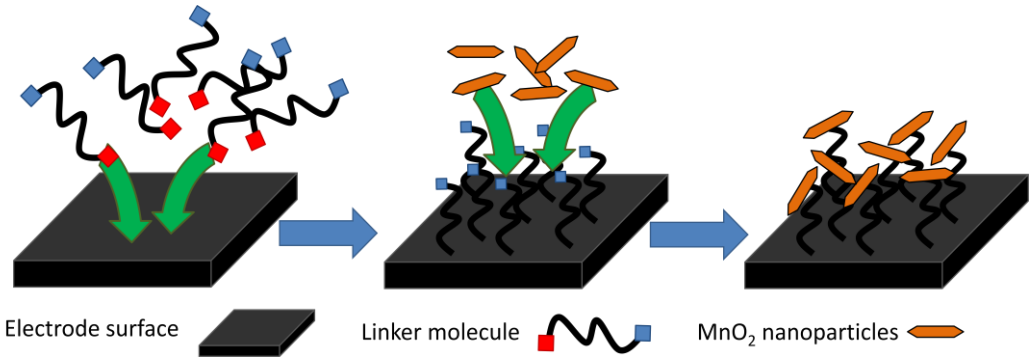

Figure 4.2: Proposed method for preparation of tethered covalent assemblies of MnO_2 nanoparticles.

At the time this work was completed, modification of MnO_2 with aryldiazonium salts had not been reported, requiring modification conditions to be developed. As discussed in Chapter 1, the most commonly employed grafting conditions for aryldiazonium salts are aqueous acid conditions which are unsuitable for MnO_2 modification due to its solubility in acid. Therefore grafting at elevated pH via the diazoate will be used in aqueous media. Modification by this approach has been reported previously on other metal oxides including: indium tin oxide[91], LiV_3O_8[92], SiO_2[93], SnO_2[94], Fe_3O_4[95],TiO_2[96], Al_2O_3 (alumina)[97], Gd_2O_3[97] and the native oxides on copper[98] and chromium [99] surfaces. In addition to aqueous modification, aryldiazonium ion grafting has also been demonstrated in acetonitrile which should be compatible with MnO_2 modification. Subsequent work in this area has been conducted by Belanger et al.[100] and this will be discussed below in context of this thesis work.

This chapter describes the preparation and characterisation of MnO_2 nanoparticles, the subsequent modification of these particles with aryldiazonium salts and investigations of the properties of the

modified materials. Also, attempts to produce tethered MnO_2 nanoparticle assemblies with carbon materials through aryldiazonium ion-based grafting will be discussed.

Portions of this work have been published in reference [101].

4.2 Experimental Methods

4.2.1 MnO_2 Nanoparticle Preparation

MnO_2 nanoparticles were prepared by a method adapted from Portehault et al.[8] 20 mmol of $KMnO_4$ and 30 mmol of $MnSO_4$ were dissolved in 1 M H_2SO_4 (75 mL and 150 mL respectively) and purged with N_2. The $KMnO_4$ solution was then added to the $MnSO_4$ solution with vigorous stirring under N_2. The volume of the resulting solution was adjusted to 250 mL and aged in a 60 °C oven for a week. The nanoparticles were then washed by 5 cycles of sonication and centrifugation in ultrapure water. The washed nanoparticle suspension was then dried to a powder under vacuum and stored under atmosphere.

4.2.2 Nanoparticle Electrochemistry

Nanoparticle samples were prepared for electrochemistry by suspending in water and drop coating onto the end of a GC rod. Suspensions of up to 2 mg mL^{-1} were prepared by sonication in ultrapure water. Drop coating was conducted by transferring 5 µL by micropipette onto the surface of a polished GC electrode mounted in an upright position. The coated electrode was dried in an oven at ~60 °C for 15 minutes before cooling at ambient temperature. The nanoparticle-coated electrode was then used as the working electrode in a 3-electrode cell

Alternatively, nanoparticle electrodes were prepared by mixing in varying ratios with conductive carbon powders and a binder to produce paste electrodes. TIMREX KS6 Primary Synthetic Graphite (TIMCAL) with ~2 µm particle size was used as the conducting additive and bound using PTFE powder (1 µm). These components were mixed and dispersed in absolute ethanol which was allowed to dry. The mixtures were then packed into an insulating sheath with back-contact made by a brass rod to give an electrode area of 0.05 cm^2. The packed electrode was then smoothed on clean paper.

4.2.3 SEM, XPS & FT-IR Characterisation

Nanoparticle samples were mounted for SEM imaging by drop casting using similar suspensions as for electrochemical measurement. These suspensions were drop-cast onto GC plates.

XPS data were collected as described in chapter 2 with MnO_2 powder samples mounted by pressing them into indium.

FT-IR spectra for MnO_2 nanoparticle samples were collected by pressing the nanoparticle powder directly onto the diamond ATR prism

4.2.4 Nanoparticle Modification

Modification by aryldiazonium salt grafting was conducted using spontaneous grafting conditions in aqueous base or acetonitrile.

4.2.4.1 Basic Conditions

MnO_2 nanoparticles and a solid sample of the aryldiazonium tetrafluoroborate salt were mixed in ultrapure water before adding 1 M NaOH solution, resulting in a reaction solution containing: 2 mg mL^{-1} suspended nanoparticles, 50 mM aryldiazonium salt and 0.1 M NaOH in a typical volume of 200 mL. This solution was reacted for 1 hour under stirring or sonication. Alternatively, pH 10 $NaOH/NaHCO_3$ buffer was used in place of 0.1 M NaOH. After modification, the particles were washed by 5 cycles of sonication/centrifugation in ultrapure water and ethanol sequentially. The resulting suspension was then dried under vacuum and stored under atmosphere.

4.2.4.2 Non-aqueous Conditions

50 mM of the required aniline derivative was added to sufficient MnO_2 nanoparticles to produce a 2 mg mL^{-1} suspension in acetonitrile in a typical volume of 200 mL. After dissolution of the aniline derivative and suspension of the nanoparticles, the aryldiazonium salt was formed in-situ via the addition of 50 mM of tert-butylnitrite (TBN). The reaction was left to proceed under stirring for 1 hour. Once modification was complete, the particles were filtered over a Millipore PVDF filter (0.22 µm pore size) with acetonitrile. The retentate was then collected and washed and dried using the same procedure as for aqueous-modified samples.

4.2.5 Average Oxidation State (AOS) Determination

AOS of MnO_2 nanoparticles before and after modification was determined through a combination of potentiometric titrations and XPS.

4.2.5.1 Potentiometric Titration

Following the method described by Dose and Donne;[102] 0.1 g MnO_2 sample was dissolved in 25 mL of 0.25 M $(NH_4)_2Fe(SO_4)_2$/0.1 M H_2SO_4 solution (Equation 4.8) .

$$MnO_x + (2x-2)Fe^{2+} \rightarrow Mn^{2+} + (2x-2)Fe^{3+} \quad \text{Equation 4.8}$$

$$MnO_4^- + 5Fe^{2+} \rightarrow Mn^{2+} + 5Fe^{3+} \quad \text{Equation 4.9}$$

$$4Mn^{2+} + MnO_4^- + 8H^+ + 15H_2P_2O_7^{2-} \rightarrow 5Mn(H_2P_2O_7)_3^{3-} + 4H_2O \quad \text{Equation 4.10}$$

This solution was then titrated against standardised (oxalate method)[103] 0.2 M $KMnO_4$ solution (Equation 4.9) with the volume of permanganate for this titration denoted V_1. An excess of sodium pyrophosphate (~15 g) was then added to stabilise the complex formed in the subsequent titration (Equation 4.10) and after dissolution the pH was adjusted by the addition of sulphuric acid to 6-7. A second titration with permanganate was then conducted to give volume V_2. A blank titration of the iron ammonium sulphate solution without any dissolved MnO_2 was also conducted to quantify the effect of air oxidation of the iron ammonium sulphate solution (V_0). These volumes were then used to calculate the average oxidation state by:

$$x = 1 + \frac{5(V_0 - V_1)}{2(V_2 - V_1)} \quad \text{Equation 4.11}$$

4.2.5.2 XPS Method

The AOS of the manganese ions in MnO_2 were calculated using the splitting of the peaks in the Mn 3s XPS spectrum. The splitting values of MnO_2 samples with known oxidation states from titrations (this work) and literature values[104] were used to derive a calibration curve. The equation for this curve was then used to calculate unknown average oxidation states from measured Mn 3s splitting values.

4.2.6 Nanoparticle Tethering

4.2.6.1 Tethering to Planar Carbon

4.2.6.1.1 Grafting modified MnO_2 to bare carbon

NP-modified MnO_2 (NP-MnO_2) was drop-coated on a GC disk electrode. NP groups were electrochemically reduced in 0.1 M KCl in 1:9 ethanol:water mixture to give a mixed aryl layer containing AP groups. Alternatively AP-modified MnO_2 (AP-MnO_2) was prepared directly by the non-aqueous modification method described above and drop-coated onto a GC disk electrode. The dried AP-MnO_2 electrode was then converted into a diazonium-terminated film by immersion in 5 mL 50 mM TBN in acetonitrile for one hour with stirring. These diazonium-terminated nanoparticles were

then electrografted to the underlying GC disk electrode in 0.1 M KCl 1:9 ethanol:ultrapure water by cycling potential between 0.8 and -1.5 V at a scan rate of 50 mV s^{-1}.

4.2.6.1.2 Grafting bare MnO_2 to modified carbon

AP films were electrografted to GC plate electrodes from aminobenzenediazonium ions prepared in situ in 0.5 M HCl from 5 mM p-phenylene diamine. These AP-modified GC surfaces were then converted to diazonium-terminated surfaces through reaction with 50 mM TBN in 5 mL acetonitrile in 2 mg/ml MnO_2 nanoparticle suspension for 1 hour with stirring in order to graft the nanoparticles spontaneously.

4.2.6.2 Tethering to Carbon Powder

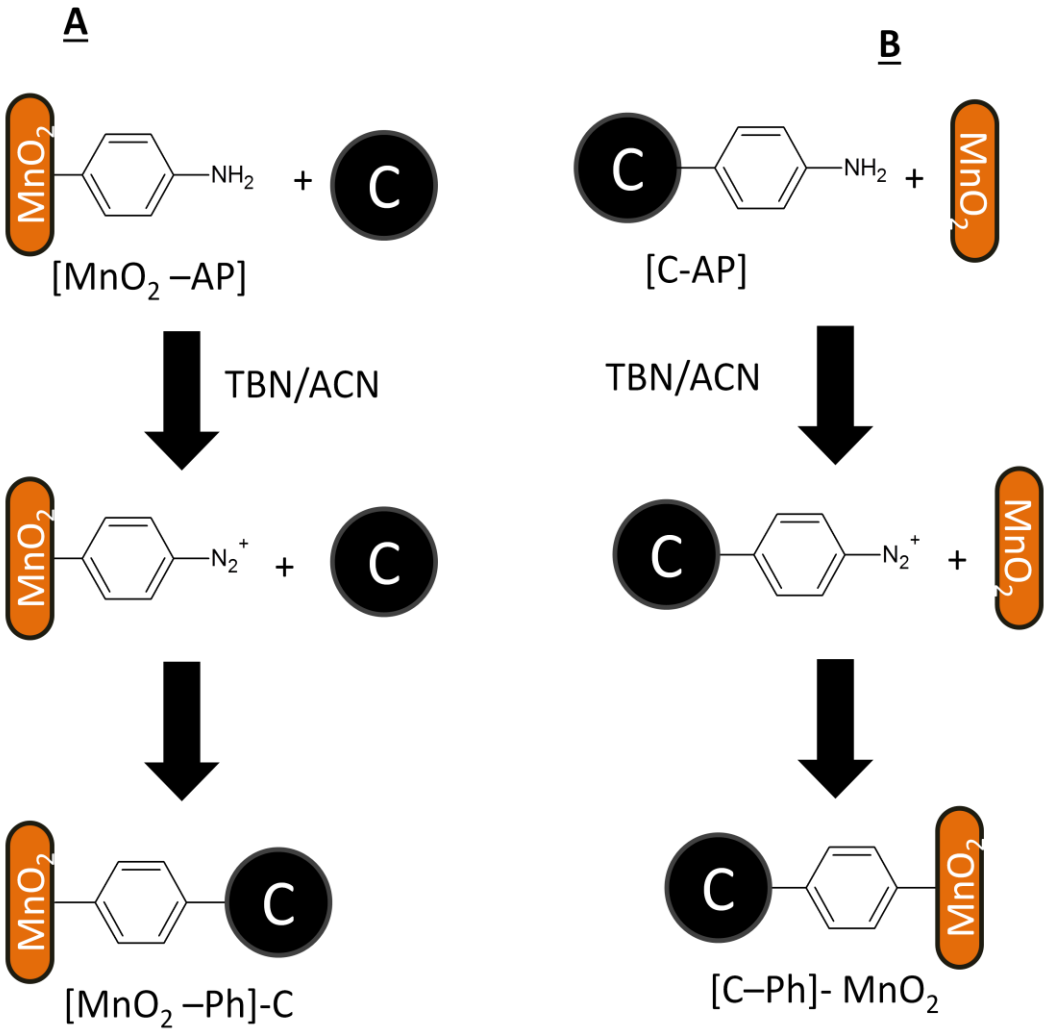

Scheme 4.1: Preparation of tethered assemblies of MnO_2 and carbon materials: A. tethering bare carbon to modified MnO_2 and B. tethering bare MnO_2 to modified carbon.

Carbon-tethered MnO_2 nanoparticle materials were prepared by either reacting AP-modified MnO_2 nanoparticles with unmodified carbon powder (Scheme 4.1A), or unmodified MnO_2 with AP-modified carbon powder (Scheme 4.1B). Tethered assemblies were prepared using either the ~2 µm TIMREX KS6 carbon powder described above or ~40 nm carbon black, acetylene 99.9+%, 50% compressed (Alfa Aesar) in MnO_2:C ratios of 9:1 and 1:1, respectively. Tethering reactions were undertaken by converting the AP-terminated films on the modified material to diazonium-terminated films using 50 mM TBN in the presence of the unmodified material suspended in acetonitrile. Reactions were typically carried out in 200 mL volume with continuous stirring for one hour with 2 mg/mL MnO_2 suspension and the amount of carbon powder selected to give the appropriate MnO_2:C ratio. The resulting solid material was then separated by filtration over a Millipore PVDF filter (0.22 µm pore size) and washed by 5 centrifugation and re-suspension cycles sequentially in ethanol and ultrapure water. Blank samples were prepared using identical reaction conditions to the modification experiments but in the absence of TBN so that tethering could not occur. These materials were characterised by cyclic voltammetry and SEM.

4.3 Results and Discussion

4.3.1 Characterisation of As-prepared Nanoparticles

4.3.1.1 Morphology & Structure

The morphology and electrochemical properties of the nanoparticles were measured to ensure that they were suitable for use in modification experiments.

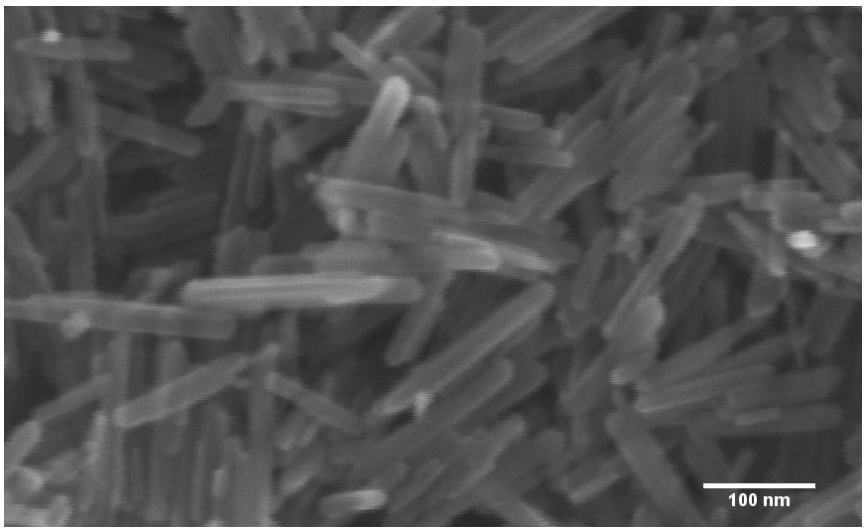

Figure 4.3: SEM image of drop-cast as-prepared MnO_2 nanoparticles.

SEM imaging of particle suspensions drop-coated onto conductive surfaces confirmed the particles were nanoscale rods with length of ~150 nm and diameter of ~25 nm (Figure 4.3). The crystal structure of the MnO_2 nanoparticles was determined by powder XRD. Comparison with literature patterns shows that the nanoparticles have the cryptomelane (α-MnO_2) structure (Figure 4.4) that was expected from the preparation procedure used.[8] This structure consists of 2 by 2 tunnels made from MnO_6 octahedra, frequently with cations trapped within the tunnels (Figure 4.1a).

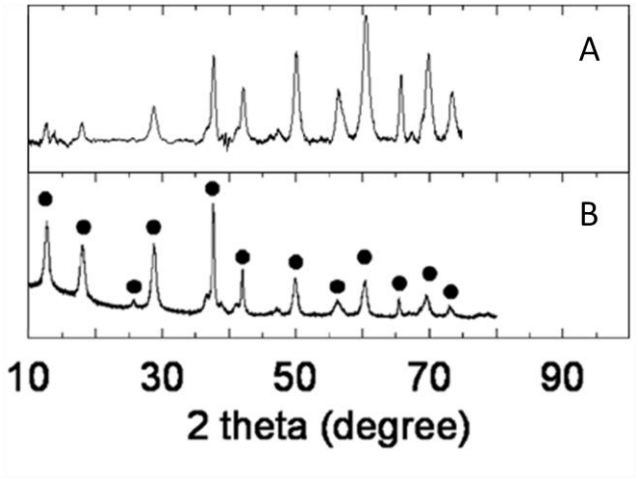

Figure 4.4: XRD patterns of MnO_2. A. This work, B. cryptomelane sample, figure adapted from reference 8.

4.3.1.2 Electrochemical Behaviour of MnO_2

The electrochemical properties of MnO_2 were measured by cyclic voltammetry (scan rate = 50 mV s^{-1}) on surfaces prepared on glassy carbon rods by drop coating. Over a limited potential range (0 V to 0.8 V), the MnO_2 particles showed a quasi-rectangular voltammetric response typical of a pseudocapacitor (Figure 4.5 a and b).[24] In 0.5 M KCl, a broad reversible peak at 0.6 V is present. In 0.5 M Na_2SO_4, there are peaks at a similar potential that decrease rapidly on repeat scans. Shifts in peak potentials during cycling of MnO_2 electrodes are usually assigned to structural changes affecting the intercalation/de-intercalation mechanism.[105] These changes may be observable in Na_2SO_4 due to the acidity of the electrolyte (pH ~6) promoting dissolution/redeposition reactions via conversion to Mn^{2+}.[106] The sloping baseline, particularly obvious when scanning in Na_2SO_4 is also typical of pseudocapacitors due to the dependence of the pseudocapacitor reaction on the extent of charge of the material.[107] At potentials below 0 V, large reduction peaks occur in both electrolytes, leading to the appearance of new features at higher potentials. In KCl solution there is a sharp feature around -0.3 V with a shoulder at more negative potential, leading to the appearance of a sharp peak at 0.3 V. In Na_2SO_4 solution, both the reduction and associated oxidation features are

broader and there is also an accompanying increase in the background capacitance of the material. Although the details of these processes were not investigated further, other researchers do not usually apply potentials more negative than 0 V vs. SCE, due to irreversible reduction processes.[108, 109]

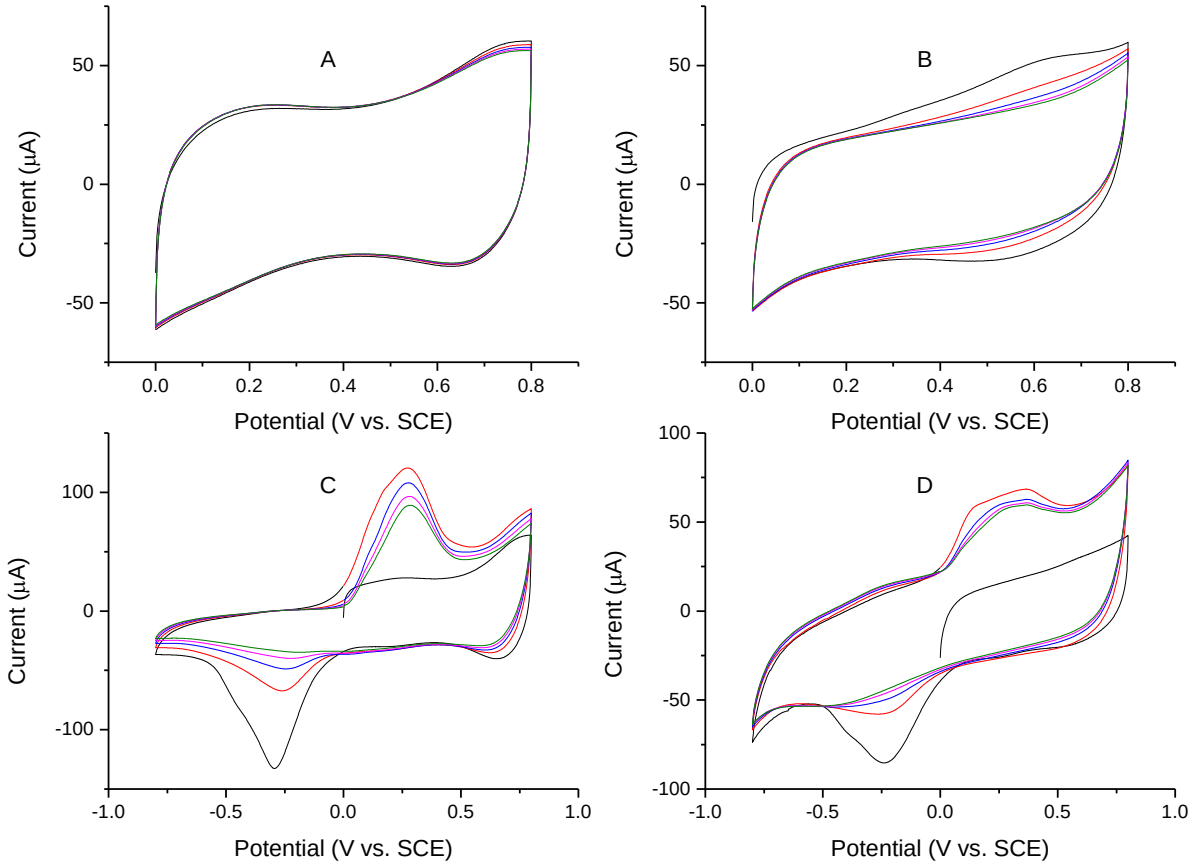

Figure 4.5: CV curves (scans 1-5) of drop-coated as-prepared MnO_2 on GC at 50 mV s^{-1} in 0.5 M KCl (A and C) and 0.5 M Na_2SO_4 (B and D).

The irreversible reduction in both electrolytes could be due to elimination of hydroxyls and protons incorporated during synthesis from the surface which allows for further intercalation of metal cations. This process was described by Kanoh et al.[29] in birnessite MnO_2 where hydroxyl groups were electrochemically incorporated into the MnO_2 structure and metal cations and protons incorporated through non-electrochemical ion exchange processes (Figure 4.6). However, the reverse process they describe where hydroxyls are re-incorporated is impossible under the conditions used here, as the potential limits are too low for water oxidation. The differences in behaviour in the two electrolytes are likely due to the differing abilities of the cations to adsorb onto surface sites and

intercalate into the electrode structure. The smaller hydrated ion size of K^+ is assumed to give easier access to the surface.

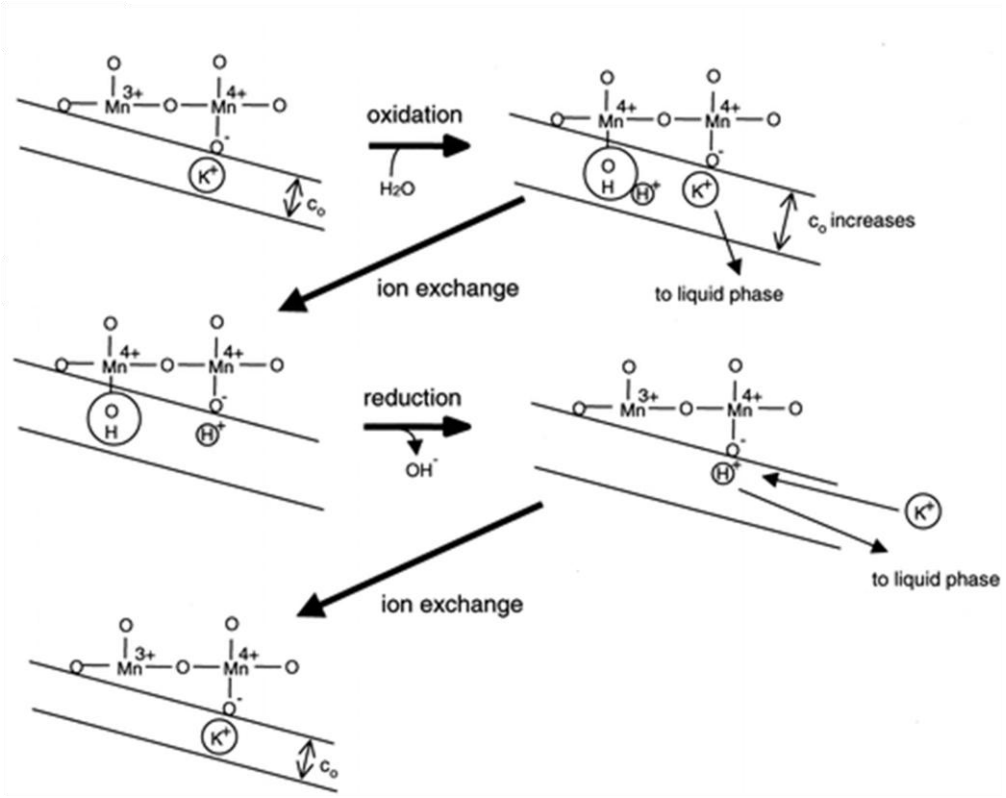

Figure 4.6: Schematic diagram of the electrochemical intercalation/de-intercalation reactions of K^+ in birnessite MnO_2. Adapted from reference 29.

The capacitance of the nanoparticle films was calculated by integrating the voltammograms over the scan window to calculate the charge transferred. Capacitance is calculated from CV curves by:

$$C = \frac{\int_{E_1}^{E_2} i(E)dE}{2(E_2 - E_1)v}$$ Equation 4.12

Where *C* (in F) is the capacitance of the material, *i* is the measured current (in A), *E* is the applied potential (in V), E_1 and E_2 are the lower and upper potential limits respectively (in V) and *v* is the scan rate (Vs^{-1}). Typically, the capacitance value for a 5 µL drop of 2 mg/mL MnO_2 suspension is approximately 0.4 mF under the conditions examined, however, there is a large amount of between-sample variation.

The effects of electrolyte and scan rate on the electrochemical behaviour of the MnO_2 nanoparticles were examined in 0.5 M KCl and 0.5M Na_2SO_4 from 0 V to 0.8 at scan rates of 5, 50 and 500 mVs^{-1} (Figure 4.7). Scans conducted in KCl show an additional feature at 0.25 V at 5 mVs^{-1} scan rate (Figure

4.7A) which increases in intensity with cycling. At increasing scan rate this feature is suppressed, suggesting it is diffusion dependent.

It would be expected that the switching between charge and discharge processes would show scan rate dependence due to the process relying on the movement of counter-ions at or into the electrode surface. This switching-rate dependence typically appears as deviation at the switching potentials from the rectangular CV of an ideal capacitor (i.e. there is curvature at the switching potentials). This curvature should increase at higher scan rate as the diffusion processes are unable to keep up with the switching rate. Some curvature is present in all the voltammograms in Figure 4.7 and is more marked at higher scan rates as can be seen when comparing data collected at 50 and 500 mV s^{-1} (Figure 4.7 C-F). However, in KCl, scans at 5 mVs^{-1} show the highest degree of curvature (Figure 4.7A). This suggests that there are slow processes that are contributing significantly to the capacitance of the electrode and masking the faster processes that dominate at higher scan rates.

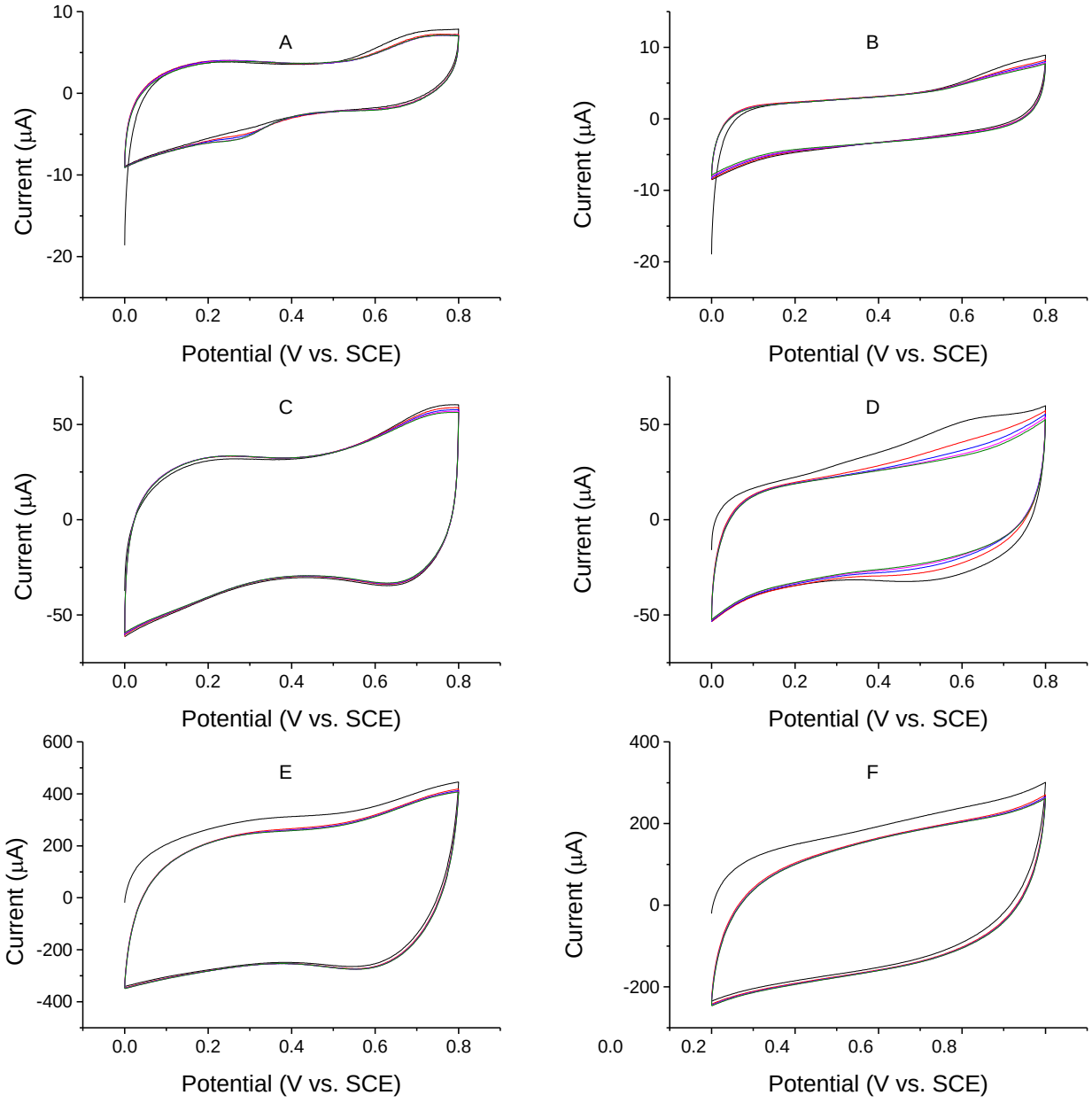

Figure 4.7: CV curves (scans 1-5) of drop-coated as-prepared MnO_2 on GC in 0.5 M KCl (A, C and E) and 0.5 M Na_2SO_4 (B, D and F) at 5 mV s^{-1} (A and B), 50 mV s^{-1} (C and D, reproduced from Figure 4.5) and 500 mV s^{-1} (E and F).

Capacitance measurements from the integrated voltammograms (Table 4.1) show decreasing capacitance as scan rate increases and increased capacitance in KCl compared to Na_2SO_4. The scan rate dependence is likely due to either porosity of the MnO_2 nanoparticles themselves or their packing on the GC electrode causing porosity resulting in difficult to access areas of the electrode that are not active at fast scan rates. This difference is likely due to the smaller hydrated-ion size and higher ionic conductivity of K^+ compared to Na^+ making the diffusional components of the

pseudocapacitance process easier.[59] Compared to reported values (180-220 F g^{-1} for MnO_2-C composites at 5 mV s^{-1}), the capacitance values of the material in this work are significantly lower – most likely due to the limited accessible surface area of the drop-cast MnO_2 nanoparticles on the GC surface.[100, 110, 111]

Table 4.1: Capacitance data from CV scan 5 at various scan rates of MnO_2 nanoparticles drop cast on GC (0.01 mg nanoparticle loading) in 0.5 M KCl or 0.5 M Na_2SO_4.

	KCl[a]	Na_2SO_4[a]
Scan Rate (mV s^{-1})	C (F g^{-1})	C (F g^{-1})
5	60 ± 20	63 ± 3
50	60 ± 10	40 ± 20
500	46 ± 6	29 ± 2

[a]n = 3

4.3.2 Modification of MnO_2 Nanoparticles

4.3.2.1 Aqueous Base Modification

As explained in Chapter 1, when a aryldiazonium ion is added to aqueous base, it is converted into a diazoate that spontaneously decays to form the radical and forms a bond with the surface.[112] This is a promising approach for the modification of MnO_2 materials due to their stability in basic conditions. It was observed in experiments described in Chapter 3 that grafting aryldiazonium ions at high pH was successful on non-conducting SU-8 surfaces and thus this method is likely to be successful at conducting substrates like MnO_2. As a proof-of-concept system, MnO_2 nanoparticles were modified with NP groups as these can be detected electrochemically. This modified material is termed 'NP-Mod' MnO_2. The modification was carried out by dissolving nitrobenzenediazonium tetrafluoroborate in an aqueous suspension of MnO_2 nanoparticles, followed by the addition of sodium hydroxide. Alternatively, aqueous pH 10 buffer was used in place of sodium hydroxide solution. Reaction conditions were selected to promote the reaction between the aryl radicals and the MnO_2 rather than solely with other radicals by ensuring the nanoparticles were well suspended during the reaction and that the aryldiazonium ion had sufficient time to soak into any pores on the nanoparticle surface before base was added as the aryldiazonium ion is more stable in ultrapure water (pH ≈ 6). To determine the effect of base treatment on MnO_2, blank samples were produced by treatment of MnO_2 nanoparticles under identical basic conditions in the absence of aryldiazonium salt. These samples are referred to as 'NaOH blank' nanoparticles.

4.3.2.2 Non-aqueous Modification

Non-aqueous modification of MnO_2 was conducted by reacting suspensions of MnO_2 nanoparticles with 50 mM p-phenylenediamine in acetonitrile with the addition of equimolar tert-butyl nitrite as a diazotisation agent. The resulting material is referred to as 'AP-Mod' MnO_2. These reactions were conducted in the absence of a reducing agent. Although it was observed in experiments described in Chapter 3 that NP and MP groups would not graft to non-conducting SU-8 surfaces in acetonitrile in the absence of a reducing agent, spontaneous reduction of the aryldiazonium ion by the MnO_2 nanoparticles may be possible. Additionally, the modification of SU-8 in acid conditions with AP groups in the absence of reducing agent has been demonstrated by Simons et al., possibly via a mechanism unique to this modifier.[113] Blank samples were prepared by treatment of nanoparticles with tert-butyl nitrite in acetonitrile in the absence of aryl amine (referred to as 'ACN blank' nanoparticles).

4.3.2.3 Characterisation of Aryl Layers

To establish successful modification of the MnO_2 nanoparticles, a number of methods were used to detect the modifying layer and characterise its attachment to the MnO_2 surface.

4.3.2.3.1 Electrochemistry

Successful NP-modification was initially confirmed by electrochemical reduction of the NP groups. This was conducted in 1:9 ethanol:water with 0.1 M KCl rather than acid in order to prevent the MnO_2 from dissolving. In this electrolyte, NaOH blank nanoparticles (Figure 4.8a) show identical electrochemical behaviour to the as-prepared nanoparticles observed previously (Figure 4.5c). Upon modification with NP-groups (Figure 4.8b), another irreversible reduction appears at -0.9 V assigned to the reduction of NP groups. This corresponds to the reduction peak at a NP-modified GC rod (Figure 4.8c) and is absent from the NaOH blank. Based on the processes outlined in Chapter 2, the area of the NP reduction peaks and resulting reversible oxidation peaks can be used to determine the coverage of NP groups on the MnO_2 material.

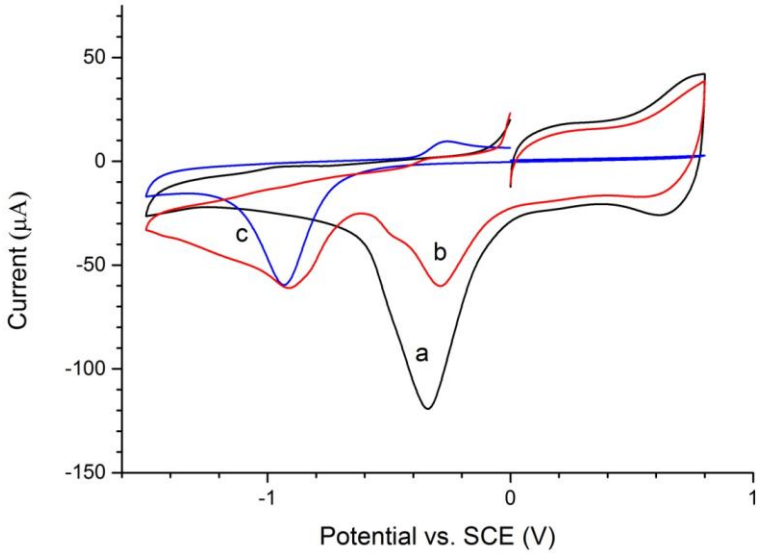

Figure 4.8: CV curves (scan 1) of: a. NaOH Blank MnO_2, b. NP-mod MnO_2 and c. NP-mod GC in 0.1 M KCl, 1:9 ethanol:water, 50 mV s^{-1}.

This approach gives NP coverage of 6.7 ± 0.8 × 10^{-9} mol cm^{-2} (n = 5) based on the geometric area of the underlying GC rod substrate. Alternatively, using the measured specific surface area for nanoparticles prepared under similar conditions[8] (90 m^2 g^{-1}) gives a coverage of 5.3 ± 0.6 × 10^{-11} mol cm^{-2} (n = 5). Monolayer coverage by aryldiazonium ion-derived aryl layers are typically on the order of ~2 × 10^{-10} mol cm^{-2} which is intermediate between these values.[114] These values are consistent with either sub-monolayer coverage across the entire surface or multilayer coverage on the electrochemically accessible areas of the nanoparticle surface. As there are no steps taken during this modification process to limit multilayer formation, it is likely that the surface is partially covered by a multilayer film.

4.3.2.3.2 TGA

TGA was conducted on NP- and AP- modified MnO_2 nanoparticles and the corresponding blanks at a rate of 2 °C min^{-1} up to 800 °C under N_2 atmosphere (Figure 4.9). All samples show a series of gradual mass losses typical of MnO_2: loss of surface and structural water up to ~550 °C and a sharp mass loss after this associated with the conversion of MnO_2 to Mn_2O_3.[67, 102] The modified samples show these mass losses and additional losses starting from ~200 °C. In the case of NP-MnO_2 (Figure 4.9A), the mass-loss between 200 and 330 °C is assigned to the loss of NP groups. Studies on NP-modified carbon black by Toupin and Bélanger using mass spectrometry coupled with TGA showed mass losses associated with the NP-groups from 150-600 °C.[115] Catalytic decomposition of the NP-groups

by the MnO_2 surface is a possible explanation for the NP-groups being completely lost at a lower temperature on MnO_2 than on carbon. Catalytic decomposition of aromatic hydrocarbons has been observed at MnO_2 surfaces by Suib et al. in an Ar atmosphere between 200-400 °C, supporting this suggestion.[66] The additional mass loss in AP-MnO_2 (Figure 4.9B) occurs gradually between ~200-500 °C; Bélanger et al. reported the same behaviour on AP-modified carbon powder.[116] The larger mass loss in the AP-MnO_2 sample compared to NP-MnO_2 may suggest the presence of a disordered multilayer or polymeric species attached to the nanoparticle surfaces as similar TGA curves were observed by Ni et al. for MnO_2-polyaniline composites.[117]

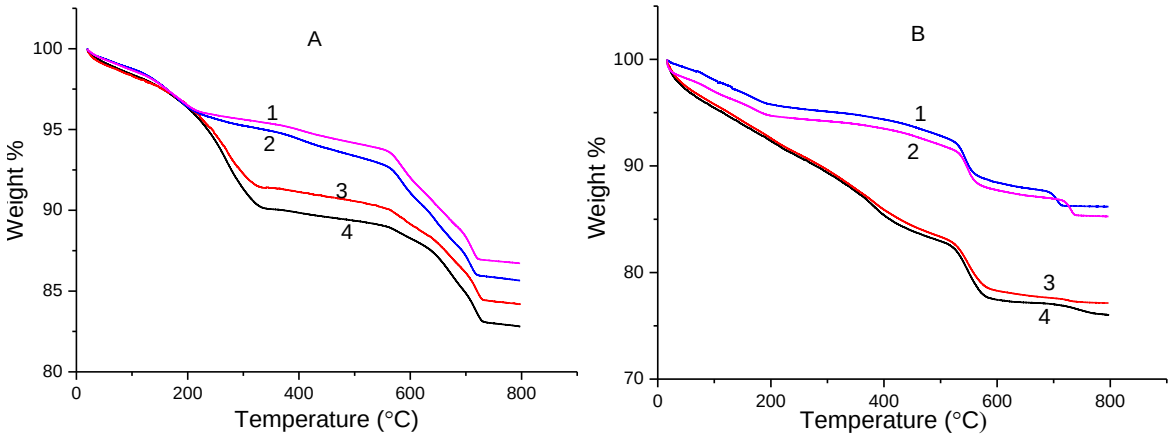

Figure 4.9: TGA curves of A: NaOH Blank (1 and 2) and NP-Mod (3 and 4) MnO_2 nanoparticles; B: ACN Blank (1and 2) and AP-mod (3 and 4) MnO_2 nanoparticles. Duplicate samples were prepared by separate modification processes using the same batch of MnO_2 nanoparticles.

4.3.2.3.3 FT-IR Spectroscopy

Fourier-transform infrared spectroscopy (FT-IR) was used to characterise the modified nanoparticles. Spectra were collected in ATR mode as powders pressed against the prism using air as a background. Baseline-corrected mid-IR spectra for as-prepared, modified and blank nanoparticle samples are shown in Figure 4.10. The spectra for all MnO_2 samples show broad features around 3500-3000 cm^{-1} and 1700-800 cm^{-1} assigned to O-H stretching and bending modes respectively due to hydroxylation of the surface and adsorbed water. The shape and intensity of these features varies between samples but it appears not to be related to the treatment conditions and most likely arises from variation in adsorbed water content. The features present around 2400 cm^{-1} and between 2300-1900 cm^{-1} arise from the experimental setup and are caused by CO_2 and the vibrations of the diamond ATR prism rather than the MnO_2 materials. This variety of features native to the material makes it difficult to identify contributions from the aryl layers. This is especially true for AP-MnO_2 due to the generally weak absorptions associated with amine groups. In the case of NP-MnO_2, there

are two strong absorbances characteristic of NO_2 groups that can be clearly seen at 1518 cm^{-1} and 1345 cm^{-1} assigned to the asymmetric and symmetric N=O stretches respectively, providing further evidence for NP-modification. Neither modified sample has clear evidence of the N≡N stretching mode (band at 2280 cm^{-1}) associated with the aryldiazonium ion, suggesting that there is no unreacted aryldiazonium salt trapped within the MnO_2.[95] Both the NP- and AP-modified samples show features between 3000-2750 cm^{-1} which could be due to C-H stretching. These are at relatively low wavenumbers compared to where aromatic C-H stretches are expected (~3000 for aryl C-H stretches), possibly due to the effect of the substituents on the aryl ring. The intensity of these vibrations appears increased in the AP-modified sample compared to NP-modified MnO_2 which is consistent with the TGA results indicating the aryl layer is thicker or has higher coverage on the AP-modified samples. There appears to be very weak bands in a similar wavenumber range for the NaOH blank sample, possibly due to C-H stretching from organic contaminants within the sample. The ACN-treated blank sample shows no evidence of C-H or C≡N stretching from trapped solvent.

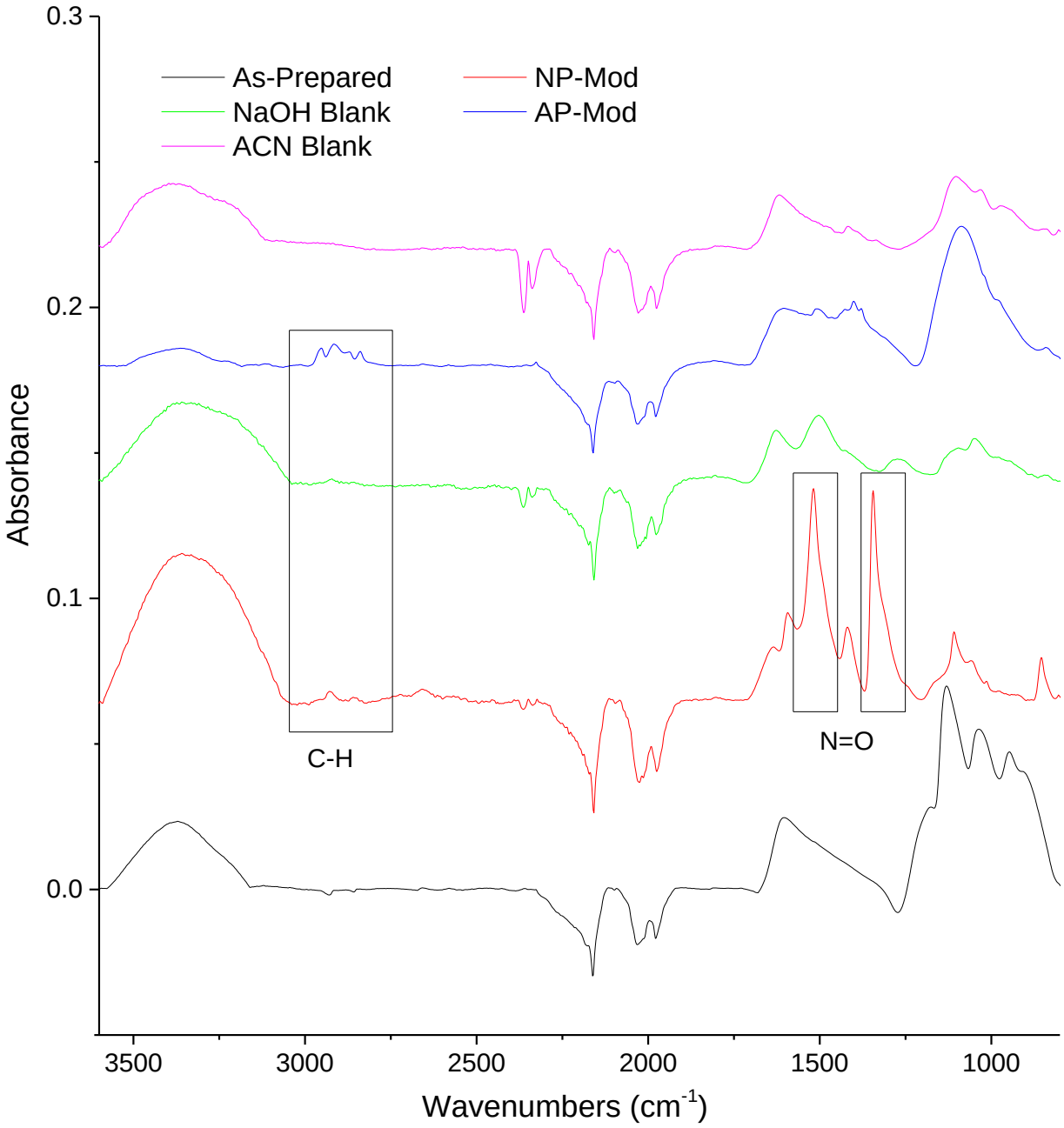

Figure 4.10: FT-IR ATR spectra of MnO_2 nanoparticles as-prepared, treated in aqueous 0.1 M NaOH with (NP-Mod) and without (NaOH Blank) NBD, and treated in acetonitrile with (AP-Mod) and without (ACN Blank) *in situ*-prepared ABD. Spectra were normalised to the O-H bending band at 1600 cm^{-1}.

4.3.2.3.4 Survey XPS

The effect of modification with aryl groups on the elemental composition of MnO_2 materials was investigated by XPS. The values given in Table 4.2 were calculated from XPS survey scans of the as prepared MnO_2, modified samples and their corresponding blanks (Figure 4.11). The composition of the as prepared MnO_2 nanoparticles appears anomalous as it exhibits a much higher O to Mn ratio

than would be expected (3:1 compared with 2:1 based on the chemical formula) and an unusually high N content. As these composition differences are not present in the blank MnO_2 samples, it is likely the result of contaminants that are removed on subsequent solvent-based processing.

Table 4.2: XPS survey scan atomic percent data for MnO_2 nanoparticles

	At%					
MnO_2 Sample	Mn	O	C	N	K	Na
As Prepared	18.2	62.3	13.9	3.5	2.2	-
NaOH Blank	21.3	53.2	17.2	-	3.2	5.1
NP-MnO_2	17.3	47.9	23.7	3.1	2.6	5.3
ACN Blank	24.4	55.6	16.8	-	3.2	-
AP-MnO_2	21.6	56.1	18.1	1.5	2.8	-

Both modified samples show significant N signals that are absent from the blanks and an increase in C content. This provides further evidence for there being aryl groups on the surface contributing to both the elevated C and N content. The C present in the blank nanoparticles is assumed to be adventitious C deposited during the XPS measurements.

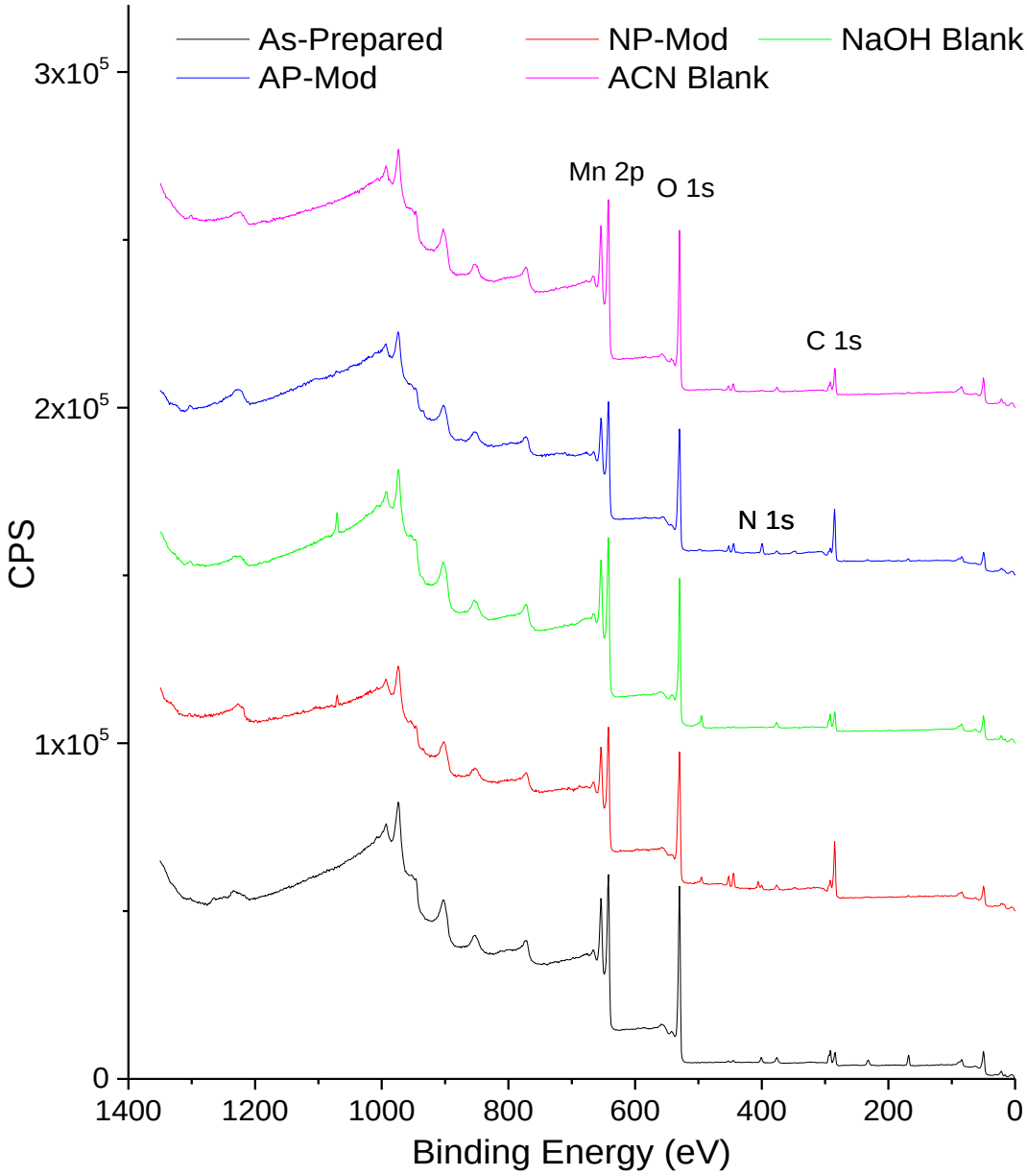

Figure 4.11: XPS survey spectra of MnO_2 nanoparticles as-prepared, treated in aqueous 0.1 M NaOH with (NP-Mod) and without (NaOH Blank) NBD, and treated in acetonitrile with (AP-Mod) and without (ACN Blank) *in situ*-prepared ABD.

4.3.3 Investigation of Bonding Mode

The idealised reaction for aryldiazonium ion grafting involves attachment of the aryl layer via covalent bonding to the surface. This is the desirable outcome from a stability standpoint. However, physisorption of the aryl layer to the surface is also common and despite the number of reports of aryldiazonium ion modification of oxide materials, covalent bonding had only been demonstrated prior to the commencement of this work on the native oxides on Cu and Al.[98, 118] Later reports have demonstrated covalent bonding to MnO_2 and Fe_2O_3.[100, 118] The electrochemistry, TGA and IR

characterisations of the modified materials described in the previous sections only demonstrate that aryl groups are associated with the material. They do not indicate that the groups are attached to the surface. In order to investigate the nature of the interaction between the aryl layer and the MnO_2 surface, XPS was used to characterise the modified material.

4.3.3.1 X-Ray Photoelectron Spectroscopy

In addition to confirming the presence of aryl layers via the increased C and N content from the survey spectra discussed previously, high resolution XPS spectra can be used to detect chemical shift changes for the modified MnO_2 materials caused by the new bonding to the aryl layer. XPS spectra were collected for the Mn 2p, O 1s, C 1s and N 1s core levels.

4.3.3.1.1 Mn 2p Core Spectra

Detection of the formation of Mn-C bonds after the aryldiazonium grafting reaction should be possible by fitting the Mn 2p XPS spectra. A shift in Mn binding energy is expected if Mn is bound to the aryl layer. This analysis is complicated by the high degree of multiplet splitting exhibited by Mn (III) and Mn (IV) compounds arising from coupling between the unpaired electron generated upon ejection of the photoelectron and an unpaired electron in the outer shell.[119] This electrostatic coupling causes a number of final states resulting in a number of multiplet peaks instead of a single core electron peak. Figure 4.12 shows the Mn 2p XPS spectra for as prepared, modified and blank nanoparticles fitted using parameters calculated by Nesbitt and Banerjee[119] using Hartree-Fock calculations from Gupta and Sen.[120, 121] It can be seen from these spectra that the number of peaks necessary to account for the splitting makes it difficult to isolate any differences between the spectra that are significant above the variation between samples and in the fitting results. Therefore no additional information about the nature of the bonding between the modifying layer and the MnO_2 surfaces can be gained from these spectra.

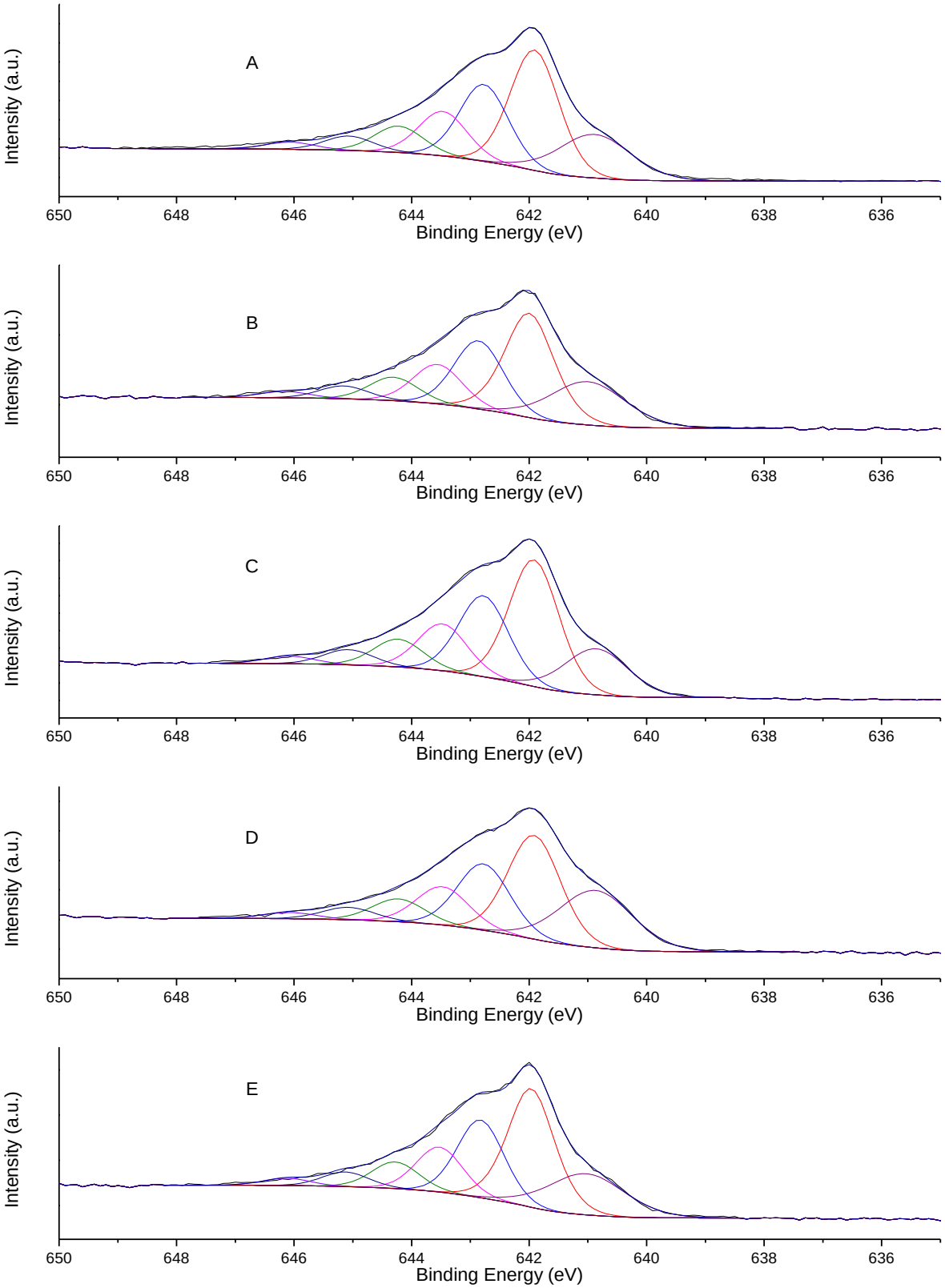

Figure 4.12: Mn 2p XPS spectra of MnO_2 nanoparticles as-prepared, treated in aqueous 0.1 M NaOH with (NP-Mod) and without (NaOH Blank) NBD, and treated in acetonitrile with (AP-Mod) and without (ACN Blank) *in situ*-prepared ABD.

4.3.3.1.2 O 1s Core Spectra

The other likely candidate for bonding between the aryl layers and the MnO_2 surface (other than Mn-C bonding) is Mn-O-C bonding through surface O functionalities. The presence of this bonding mode would be expected to cause chemical shifts resulting in new components in the O 1s and C 1s spectra. The O 1s spectrum of the unmodified material (Figure 4.13) contains three components: oxide (O^{2-}) O (529.5 eV), hydroxyl (OH^-) O (531 eV) and adsorbed water (532.5 eV).[119] Subsequent modification with NP and AP groups results in an additional peak at high binding energy (533 eV) that is absent from blank samples treated with the modification conditions without aryldiazonium salt. This new peak is assigned to Mn-O-C bonding through to the aryl layer. There is a possibility that this peak could be due to N-O bonding in the NP group (typically observed at 532.7 eV)[122] in NP-MnO_2, however, as this peak occurs at the same binding energy in AP-MnO_2 which doesn't contain this functionality, Mn-O-C bonding is the most likely assignment. Additionally, literature reports on the modification of other oxide materials with aryldiazonium ions report metal-O-C bonding at similar binding energies.[98] These results provide strong evidence that these layers are attached covalently to the surface rather than physisorbed. The existence of metal-O-C bonding to metal oxides has also been observed by ^{57}Fe Mössbauer spectroscopy on aryldiazonium ion-modified Fe_2O_3 nanoparticles.[118]

It would be expected that formation of Mn-O-C linkages would be accompanied by a decrease in the surface hydroxyl concentration as H is replaced by the aryl layer. Comparison of the peak areas of the hydroxyl peaks in blank and modified samples shows that a decrease is observed in the AP-modified sample. No decrease is seen for the NP-modified sample, however, the corresponding blank sample (NaOH blank) has a particularly small amount of hydroxyl O. The reason for this difference is unknown. In comparison with the as-prepared MnO_2 sample, all modified samples and blanks show decreased hydroxyl content. This suggests that treatment under a range of conditions can cause changes in hydroxyl content which may be masking the effect of modification.

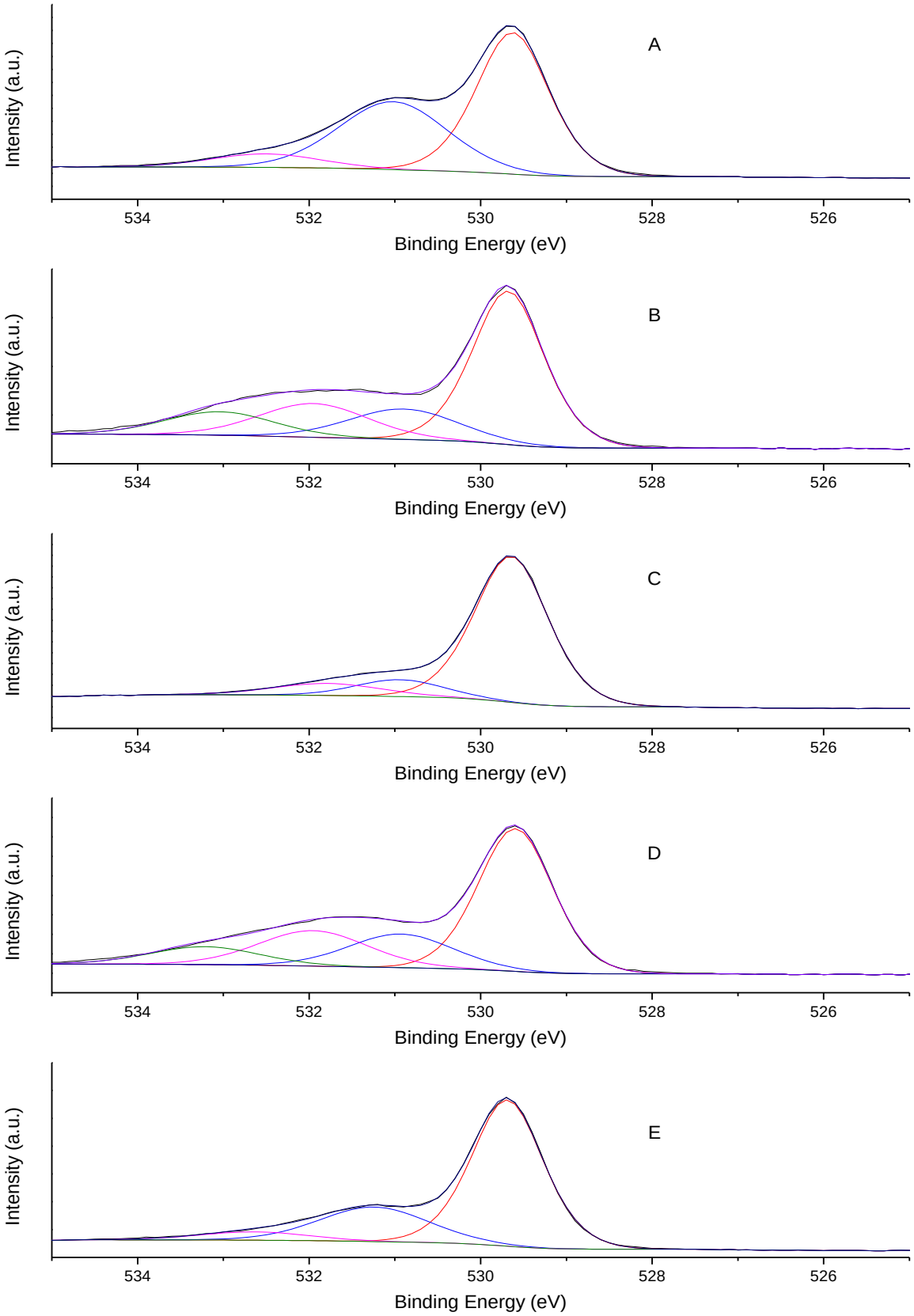

Figure 4.13: O 1s XPS spectra of MnO_2 nanoparticles as-prepared, treated in aqueous 0.1 M NaOH with (NP-Mod) and without (NaOH Blank) NBD, and treated in acetonitrile with (AP-Mod) and without (ACN Blank) *in situ*-prepared ABD.

4.3.3.1.3 C 1s Core Spectra

Examination of the chemical states of C in the aryl-modified MnO_2 materials might appear to be an ideal method to investigate how these organic layers are attached to the surface as C signals should only arise from the modifier. However, without stringent control over air exposure or extreme cleaning (e.g. Ar sputtering), samples will accumulate a layer of 'adventitious' C consisting of hydrocarbon species containing a range of O functionalities.[123] This can be seen in the C 1s spectra for as-prepared MnO_2 (Figure 4.14A) where several peaks are present. The main peak at 284.8 eV is assigned to C-H and C-C bonding and the fitted peak at 286.5 eV is likely to contain contributions from aromatic C-C, C-OH, C-O and C=O bonding, with the assignment of these different regions frequently overlapping between different studies.[122, 124, 125] All blank and modified samples also show an additional peak at 289 eV that is associated with –COOH functionalities in adventitious carbon.

After modification with AP and NP groups, features associated with C-N and C-O-Mn bonding would be expected to be introduced into the C 1s spectrum. Previous studies on NBD grafting have assigned peaks in the 286.3-285.9 eV range to C-N bonding in grafted NP groups.[124] As mentioned above, C-O bonding also gives a C 1s signal in this range and changes in this region could be due to any combination of these features.[125, 126] Comparison between the modified and blank samples reveals only a very slight shift in the binding energy in the second component from 286.3 eV to 285.9 eV which could be associated with an increase in C-O or C-N bonding but the significance of this is difficult to determine.

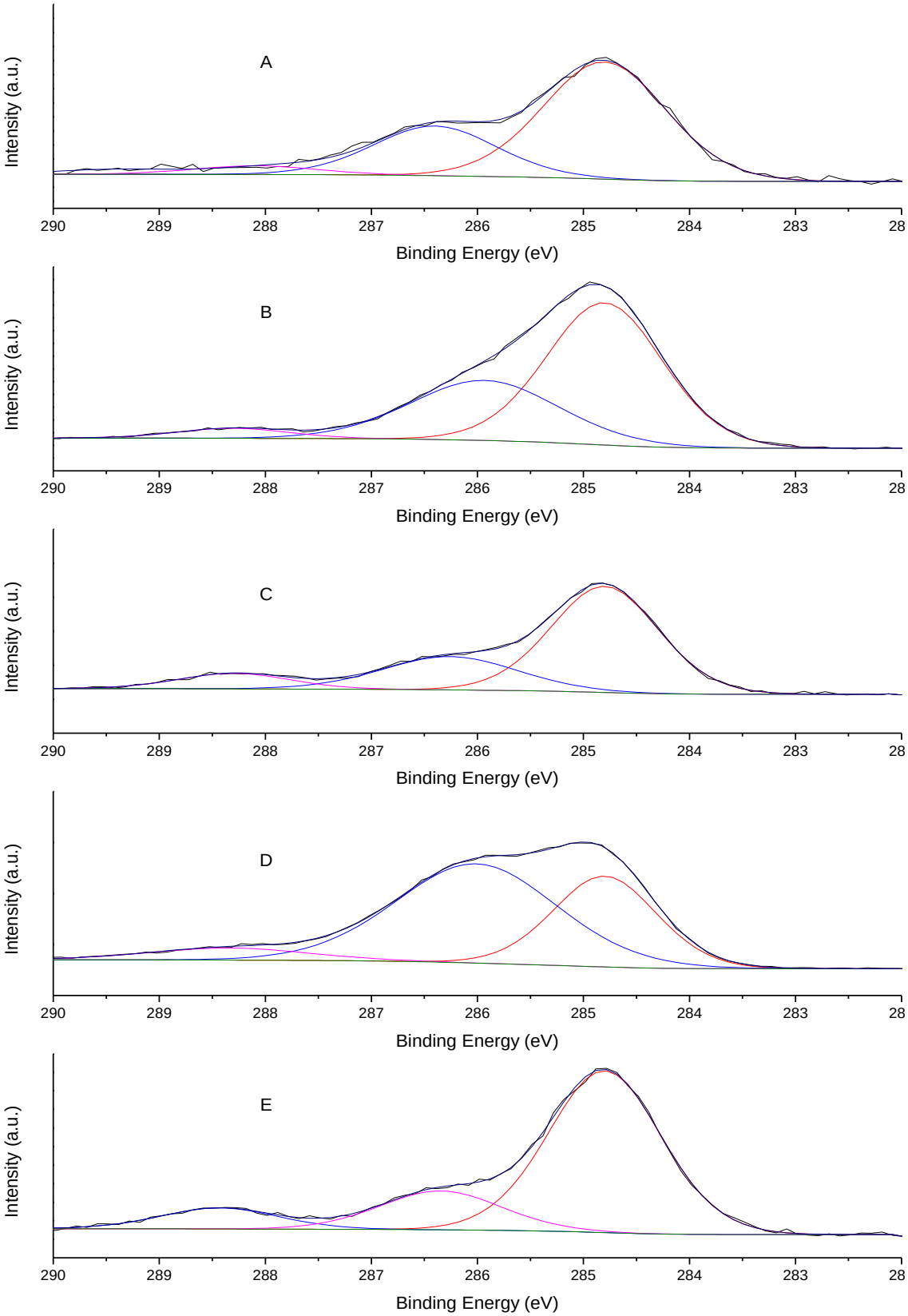

Figure 4.14: C 1s XPS spectra of MnO_2 nanoparticles as-prepared, treated in aqueous 0.1 M NaOH with (NP-Mod) and without (NaOH Blank) NBD, and treated in acetonitrile with (AP-Mod) and without (ACN Blank) *in situ*-prepared ABD.

4.3.3.1.4 N 1s Core Spectra

As both aryldiazonium ions used in this study produce nitrogen-containing aryl layers, the number and location of peaks in the N 1s spectra provide information about the chemical nature of the grafted film. The N 1s spectra of the as-prepared MnO_2 and blank samples show a single peak at 400 eV, typically associated with reduced N functionalities. As the preparation of these samples should not result in N functionalities on the surface, the origin of these N 1s signals is unknown. Nitrogen-containing groups in adventitious C contamination are a possible source, or trapped acetonitrile in the case of the ACN blank sample. The NP-modified sample N 1s spectrum contains two peaks: an intense peak at 406 eV and a weaker peak at 400 eV. The high energy peak is due to N-O present in the nitro group, indicating that these groups are mostly stable on the surface.[127] The peak at 400 eV is again due to reduced N, however, in this sample it could arise from reduction of NP groups in the X-ray beam, azo-linkages in the film from direct attack of the aryldiazonium ion (as discussed in Chapter 1) or contamination.[127] The AP-modified sample spectrum only has a peak at 400 eV associated with N in the AP groups and probable contributions by azo-linkages and contamination. As neither characteristic N 1s peak for aryldiazonium ions (403.8 and 405.1 eV) was observed, no unreacted aryldiazonium ion is present at the surface.[128] From these results, it cannot be conclusively determined if the aryl layer is attached to the MnO_2 surface by azo linkages as there are other plausible origins of reduced N species and azo linkages to the surface cannot be distinguished from azo linkages present within the aryl film.

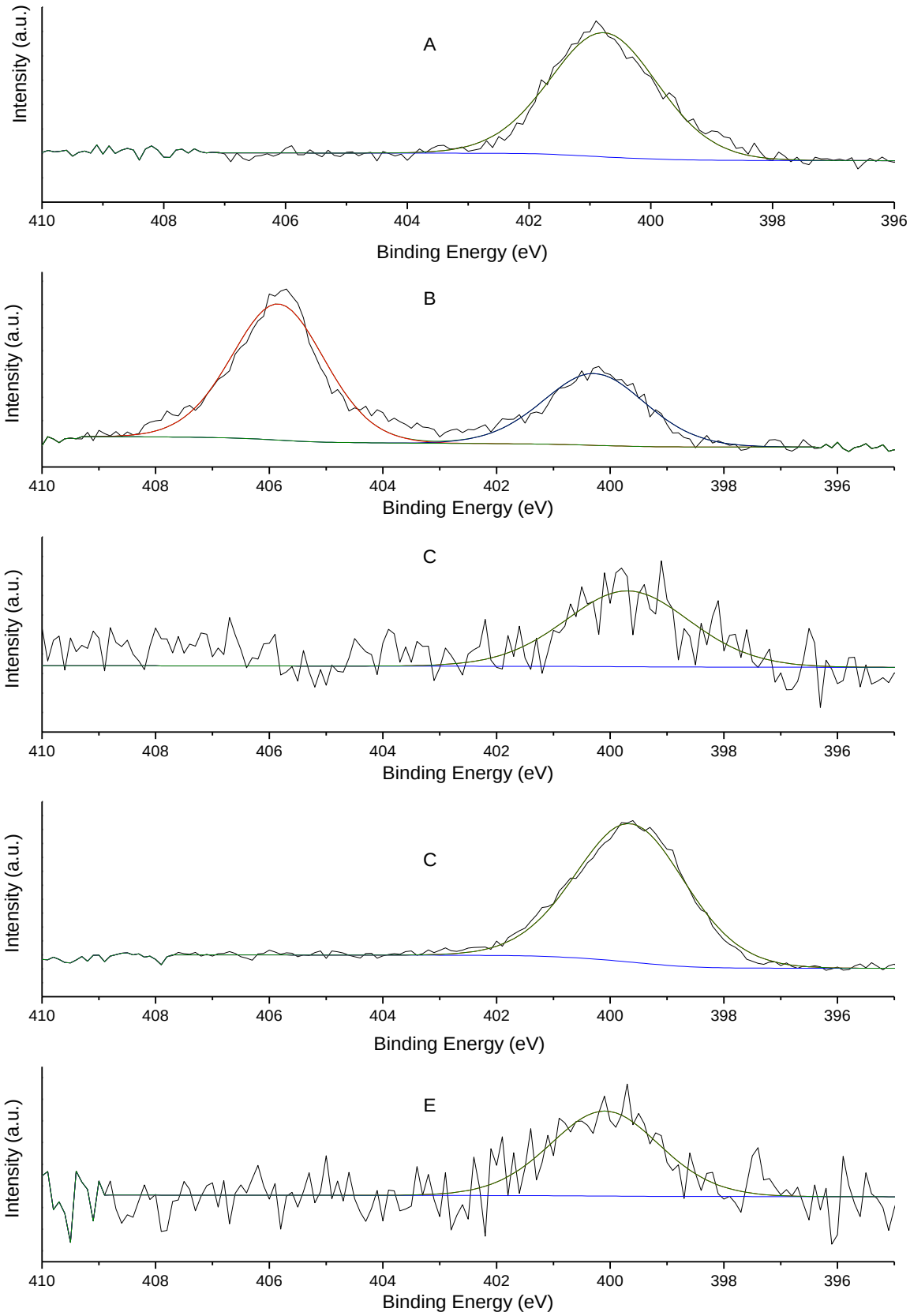

Figure 4.15: N 1s XPS spectra of MnO_2 nanoparticles as-prepared, treated in aqueous 0.1 M NaOH with (NP-Mod) and without (NaOH Blank) NBD, and treated in acetonitrile with (AP-Mod) and without (ACN Blank) *in situ*-prepared ABD.

4.3.4 Properties of Modified MnO_2 Nanoparticles

4.3.4.1 Elemental Composition

As MnO_2 is a conducting material, it is possible that the MnO_2 material itself can spontaneously reduce the aryldiazonium ion (Scheme 1.1). This reaction would result in changes in the Mn oxidation state and the concentration of charge-balancing counter-ions present in the material.

The concentration of charge-balancing cations (Na^+ and K^+) in the MnO_2 materials was calculated from the XPS survey scans shown in Figure 4.11. This is represented in Table 4.3 by the C^+:Mn ratio, where C^+ is the combined Na^+ and K^+ content. For the AP-Mod and ACN blank samples, the C^+:Mn ratio of 0.13 is close to the expected value for cryptomelane (chemical composition $C^+Mn_8O_{16}$). However, after treatment in basic conditions, both NP-Mod and NaOH blank samples have increased C^+:Mn ratios due to an increase in Na^+ content. This could be due to either a decrease in the average oxidation state of the MnO_2 after exposure to basic conditions or simply a replacement of charge-balancing H^+ incorporated into the structure during synthesis with Na^+ during base treatment.

Table 4.3: Cation content and average oxidation state of MnO_2 nanoparticles as-prepared, treated in aqueous 0.1 M NaOH with (NP-Mod) and without (NaOH Blank) NBD, and treated in acetonitrile with (AP-Mod) and without (ACN Blank) *in situ*-prepared ABD.

MnO_2 Sample	C^+/Mn[a]	AOS	AOS Error
As-Prepared	0.12	3.91[b]	0.02[d]
NaOH Blank	0.39	3.992[b]	0.005[d]
NP-Mod	0.46	3.97[c]	0.07[e]
ACN Blank	0.13	3.86[b]	0.04[d]
AP-Mod	0.13	3.65[c]	0.07[e]

[a]C^+ is concentration of charge-balancing cations (Na^+ and K^+) measured from survey XPS spectra; [b]AOS measurement from potentiometric titration; [c]AOS measurement from XPS splitting data; [d]standard error of mean (3 samples); [e]standard error of the regression.

The possibility of oxidation state changes on base treatment was investigated by determining the average oxidation state (AOS) of the blank and modified samples. AOS was initially measured by potentiometric titration where the MnO_2 sample was reacted with $(NH_4)_2Fe(SO_4)_2$ and titrated with $KMnO_4$ as described in Section 4.2.5.1. This method was investigated to determine the AOS of as prepared, NP-Mod, AP-Mod, NaOH blank and ACN blank MnO_2 nanoparticles. For as-prepared and blank MnO_2 samples, AOS values determined by this method are shown in Table 4.3. However, this

method was found to be unsuitable for modified materials as they did not dissolve in the acidified $(NH_4)_2Fe(SO_4)_2$ solution. These samples were also found to be insoluble in KI and conc. HCl after both soaking overnight and sonication. This increased resistance to dissolution may have applications for improving the stability of MnO_2 materials in sensors and pseudocapacitor electrodes.

To determine the AOS of NP- and AP-modified MnO_2 nanoparticles, the Mn 3s XPS signal was analysed. The splitting of this signal (Figure 4.16A) varies linearly based on the Mn oxidation state, allowing the AOS of the sample to be determined from a linear correlation with splitting data from known samples.[108, 104] The correlation curve for these values using data from samples in this work and data reported in the literature is shown in Figure 4.16B.

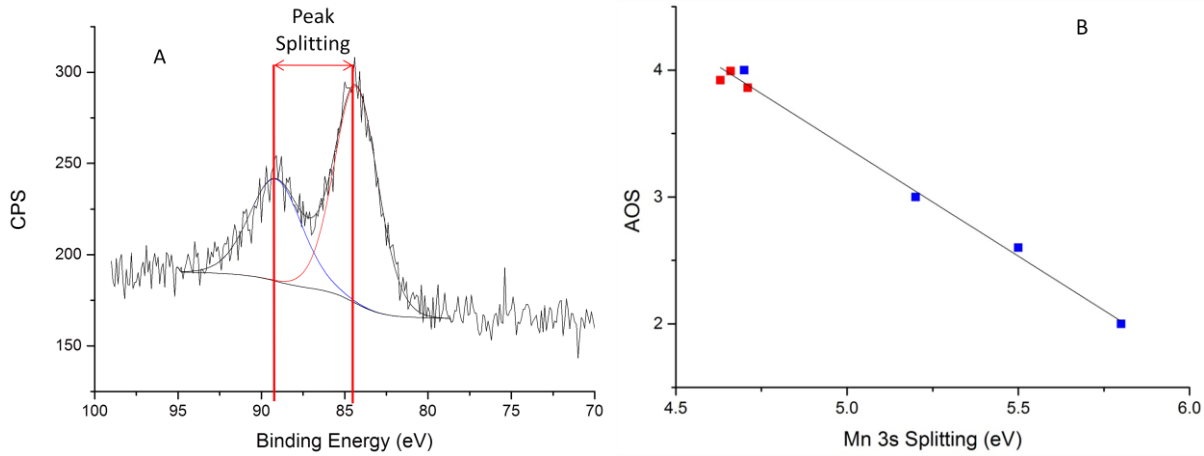

Figure 4.16: A. Example Mn 3s XPS spectrum showing the calculation of the peak splitting value. B. Correlation curve between Mn 3s splitting and AOS, Red – this work, Blue – literature data from [104].

The equation for this linear regression is shown in Equation 4.13 where E_{sp} is the peak splitting value in eV determined from the Mn 3s XPS spectrum.

$$AOS = -1.68 \times E_{sp} + 11.8 \qquad \text{Equation 4.13}$$

The AOS values determined by this method for NP- and AP-modified MnO_2 are shown in Table 4.3. The data in Table 4.3 shows that the as-prepared, NP-modified and NaOH blank MnO_2 samples have AOS values very close to the value of pure MnO_2 (AOS = 4.0). From this it is apparent that treatment and modification in NaOH solution does not significantly change the AOS of MnO_2 and that the increase in cation ratio observed by XPS is most likely due to replacement of H^+ with Na^+ rather than an oxidation state change. Both acetonitrile-treated samples show a decrease in AOS, however, this change was only significant for the AP-modified sample compared to other MnO_2 samples. A possible explanation for the decrease MnO_2 AOS is reduction by AP groups. Oxidation of AP groups

has been observed electrochemically, however, the oxidation product is unknown, but is commonly assumed to be a phenol derivative.[129] Oxidation of AP groups may also explain the lower observed N content in the AP-modified sample.

As was described in Chapter 3, grafting at pH 10 occurred without a reduction source (either from the substrate or added in solution), whereas grafting in acetonitrile required addition of a reducing agent. As the AOS of the MnO_2 materials was found to remain the same or decrease after modification in NaOH and acetonitrile, spontaneous reduction of the aryldiazonium salt by the MnO_2 nanoparticles seems unlikely, as this would require a concomitant oxidation of the MnO_2 surface and thus an increase in AOS. Therefore the grafting of AP groups to MnO_2 must occur by a spontaneous mechanism specific to ABD as was observed by Simons et al. on SU-8 surfaces.[113]

4.3.4.2 Morphology and Crystallinity

SEM imaging was used to evaluate the effect of modification on MnO_2 nanoparticle morphology. Figure 4.17 shows that the basic morphology is unchanged after modification with the particles being distinctly rod-shaped. However, it is possible that the dimensions of the nanoparticles could have changed due to a dissolution process during the modification reaction.

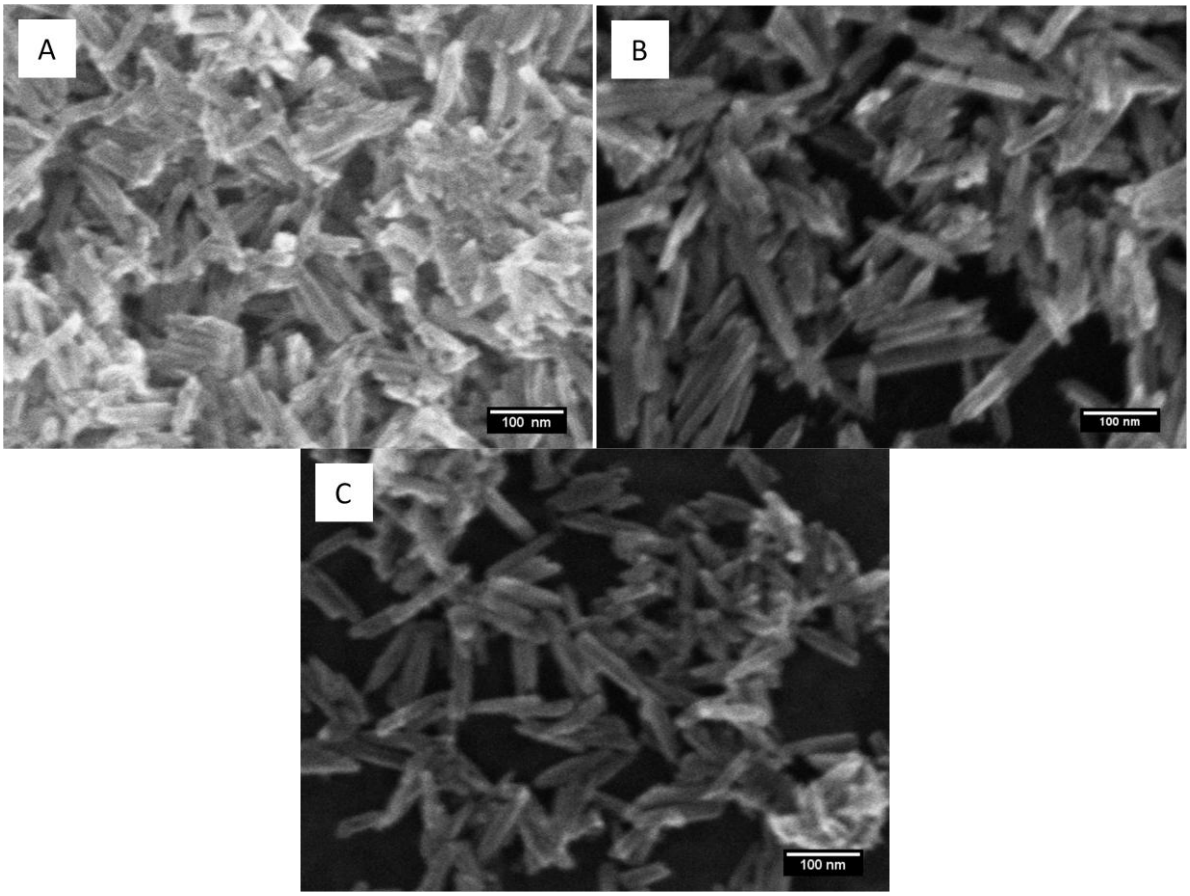

Figure 4.17: SEM images of MnO_2 nanoparticles: A. As-prepared, B. NP-modified and C. AP-modified.

The dimensions of as-prepared and treated MnO_2 nanoparticles were measured from SEM images. Nanoparticle diameter was consistently ~23 nm with no significant differences observed between the samples, however very small changes would not be detectable given the resolution limit for the SEM instrument. Histograms of length measurements of as prepared, modified and blank nanoparticles are shown in Figure 4.18, average nanoparticle length and standard deviation for each sample are presented in Table 4.4. As-prepared MnO_2 nanoparticles had average lengths of 140 ± 20 nm and this was unchanged after base treatment in the absence of aryldiazonium ion (130 ± 20 nm for the NaOH blank sample). However, modification in NaOH with NP groups resulted

in an increase in average length to 160 nm ± 20 nm. Both ACN-treated samples appear to be shorter on average (120 nm ± 20 nm for AP-mod and ACN blank).

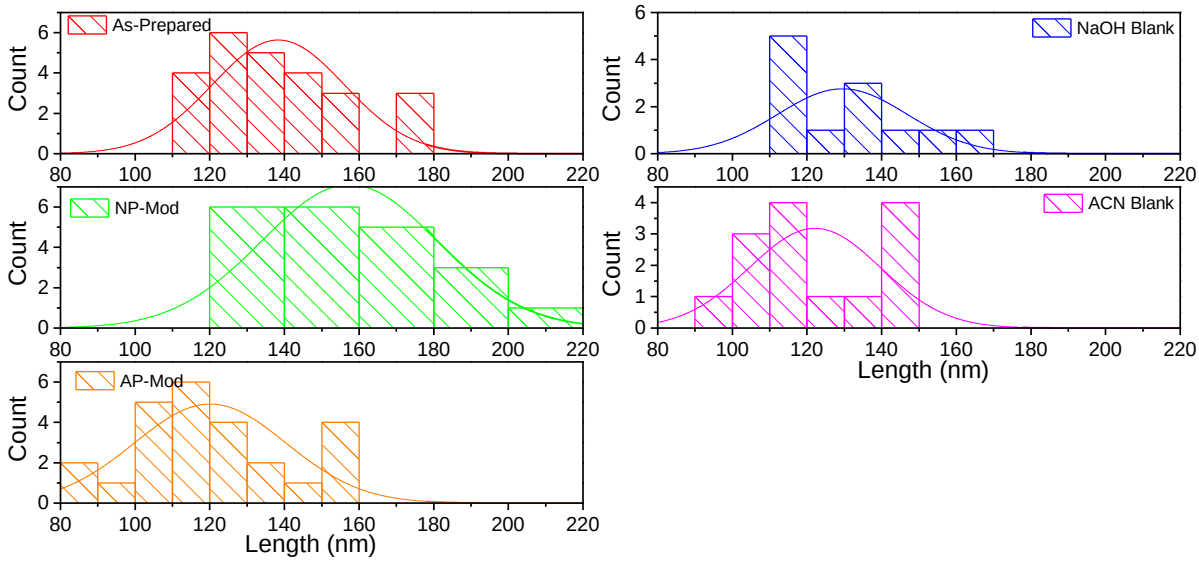

Figure 4.18: Histograms of length measurements for MnO_2 nanoparticles as-prepared, treated in aqueous 0.1 M NaOH with (NP-Mod) and without (NaOH Blank) NBD, and treated in acetonitrile with (AP-Mod) and without (ACN Blank) *in situ*-prepared ABD.

The significance of these changes in length was investigated by an independent-samples t-test to compare nanoparticle length for modified and blank samples with the as-prepared material. The parameters and test statistics for this analysis are presented in Table 4.4. From these results it is apparent that the changes in average length for the NP-modified, AP-modified and ACN blank samples are significant (*p*-values of 0.004, 0.001 and 0.01 respectively). The apparent increase in length for NP-modified samples could arise from a dissolution-redeposition process occurring preferentially at the ends of the nanoparticles, however, there is no sign of pitting on the nanoparticles from dissolution. An alternative explanation for the apparent length change is that the modification with NP-groups improves the dispersibility of the nanoparticles such that larger nanoparticles are able to stay in suspension. This would increase the population of longer nanoparticles in the drop-cast sample and thus the average nanoparticle length. It was observed that the NP-modified samples were able to disperse more readily and produced more stable suspensions, supporting this hypothesis. The decrease in length observed in the acetonitrile-treated samples was also significant and suggests that a dissolution process is occurring. However, the mechanism of this process is unknown.

Table 4.4: Length data measured from SEM and independent-samples t-test parameters for MnO_2 nanoparticles as-prepared, treated in aqueous 0.1 M NaOH with (NP-Mod) and without (NaOH Blank) NBD, and treated in acetonitrile with (AP-Mod) and without (ACN Blank) *in situ*-prepared ABD.

	Average Length (nm)	s^a	t^b	p^b	df^b
As-Prepared	140	20	-	-	-
NP-Mod	160	20	3.1	0.004	37
NaOH Blank	130	20	1.4	0.2	22
AP-Mod	120	20	3.4	0.001	47
ACN Blank	120	20	2.8	0.01	27

[a]Sample standard deviation, [b]Parameters from independent-samples t-test: test statistic (*t*), *p*-value (*p*) and degrees of freedom (*df*).

The effect of modification and treatment on the crystal structure of the MnO_2 nanoparticles was investigated by XRD. From the XRD patterns for these samples (Figure 4.19) it is apparent that no changes in the crystal structure or crystallinity of the samples occur after modification or treatment in either aqueous NaOH solution or acetonitrile. This provides further evidence that dissolution-redeposition mechanisms do not occur to a significant degree during modification.

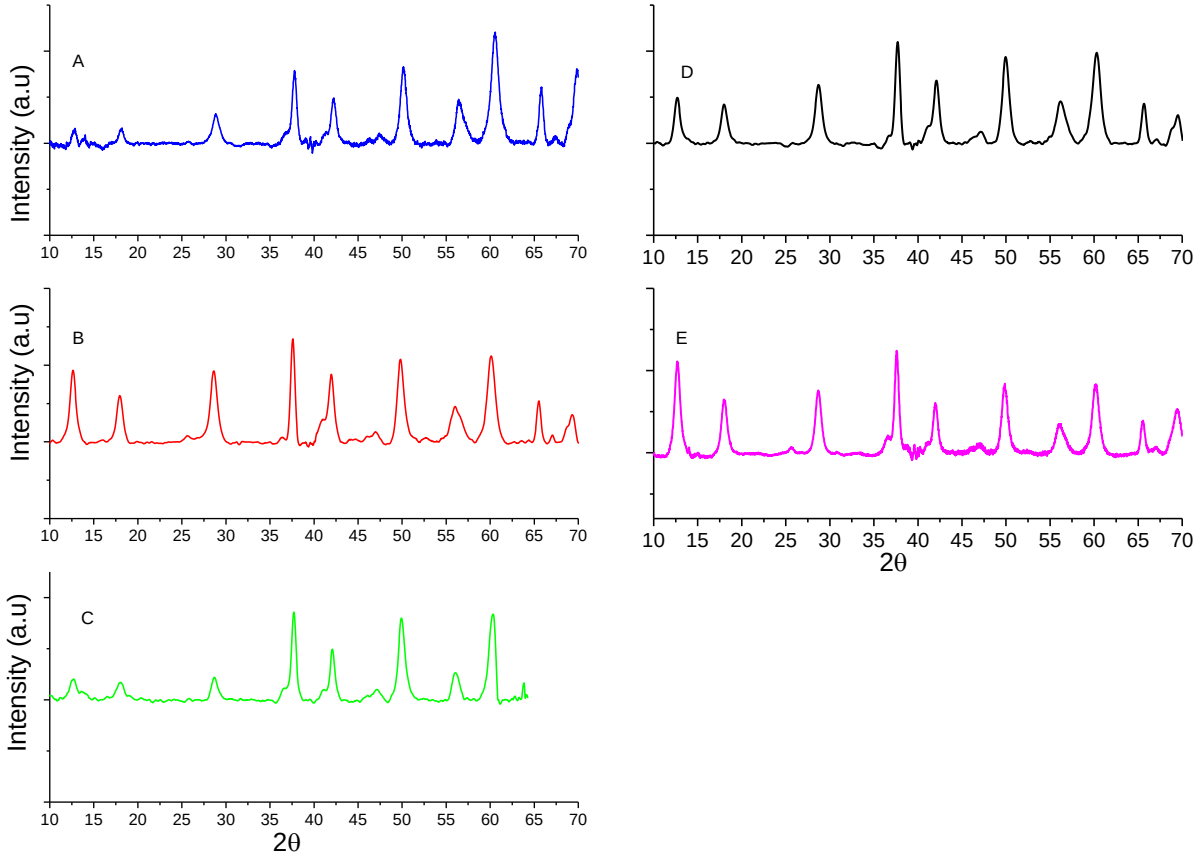

Figure 4.19: XRD data MnO_2 nanoparticles for A. As-prepared, B. NP-MnO_2, C. NaOH Blank, D. AP-mod and E. ACN Blank MnO_2 nanoparticles.

4.3.5 Electrochemical Properties of Modified MnO_2 nanoparticles

4.3.5.1 Drop-cast MnO_2 Nanoparticle Electrodes

The electrochemical behaviour of modified and blank nanoparticles was investigated by drop-coating treated nanoparticles onto GC disc electrodes. The CV response over a wide potential range was examined in both 0.5 M KCl and 0.5 M Na_2SO_4 (Figure 4.20). The CV curves for all the treated samples have similar features in both media: two reduction peaks at -0.25 and -0.5 V (sometimes appearing as one broad peak) and multiple oxidation peaks. The peak height and width of these oxidation peaks varies between samples and media in the curves shown, however, these differences do not appear to vary systematically with either aqueous NaOH or acetonitrile treatment. Comparison with CV curves of as-prepared nanoparticles (Figure 4.5 C and D) reveals no systemic trends in the CV curves which could be attributed to the effects of modification or the modification conditions and it appears that modification with aryl layers does not add additional electrochemical processes.

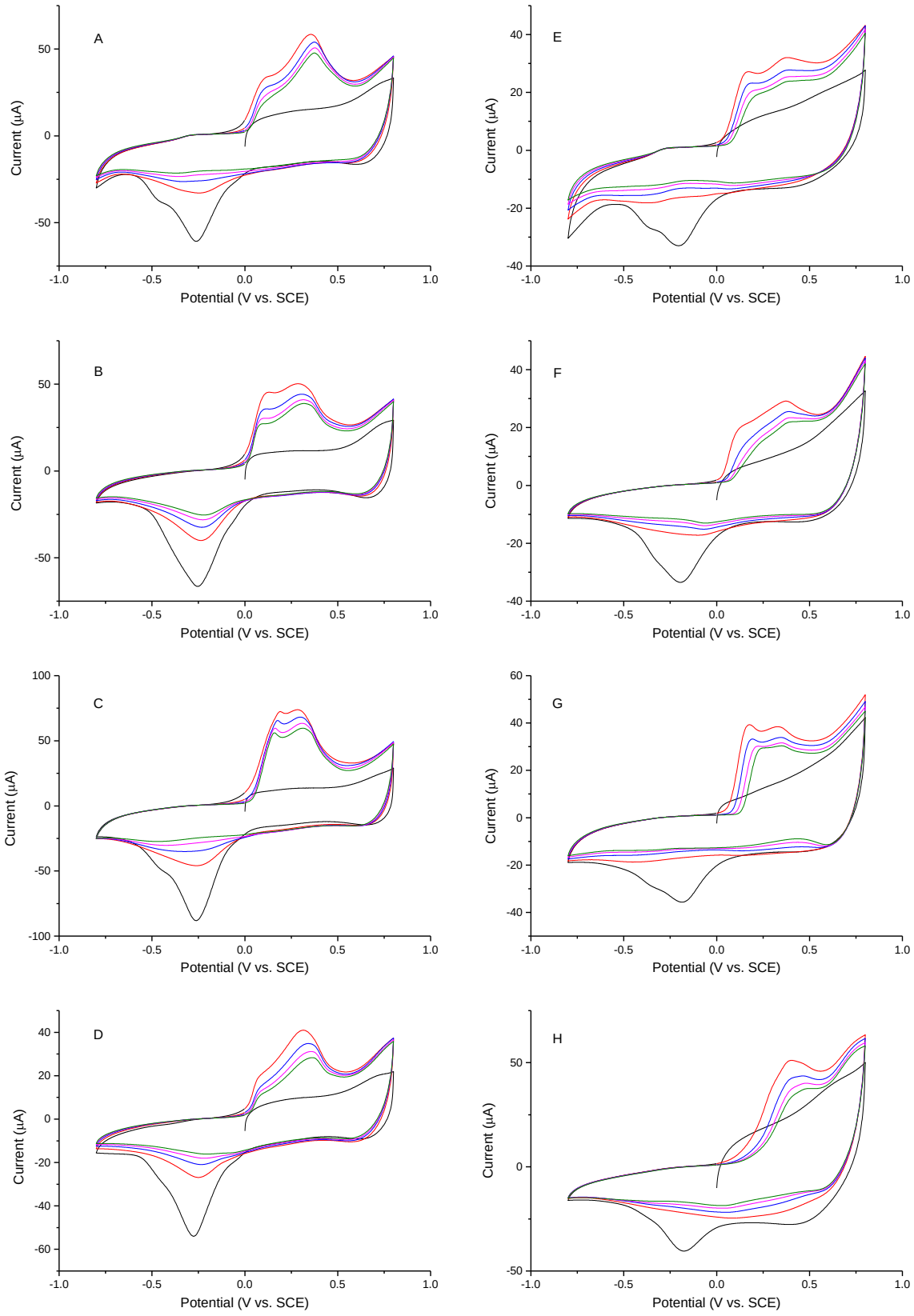

Figure 4.20: CV curves (scans 1-5) of MnO_2 nanoparticles in 0.5 M KCl (A-D) or 0.5 M Na_2SO_4 (E-H) at 50 mV s^{-1}: NP-modified (A and E), NaOH blank (B and F), AP-modified (C and G) and ACN blank (D and H).

The effect of modification on the capacitance of the nanoparticles was measured by CV (Figure 4.21-Figure 4.24) over the stable potential window (0-0.8 V vs. SCE) in 0.5 M KCl and 0.5 M Na_2SO4. Capacitance values were measured at 5 mV s^{-1}, 50 mV s^{-1} and 500 mV s^{-1} scan rates for NP-MnO_2, AP-MnO_2 and their corresponding blanks. Comparison of the voltammograms over this region with those for as-prepared MnO_2 in Figure 4.7 shows that all samples have similar quasi-rectangular responses. Capacitance values calculated by integrating the voltammograms are listed in Table 4.5. For convenience, data for as-prepared samples, calculated from Figure 4.7, are also included. The capacitance values are comparable between treatments and, in general, show the trends observed in the as-prepared data of decreasing capacitance with increasing scan rate and between KCl and Na_2SO_4. All of the capacitance values for the treated samples appear to be lower than the as-prepared samples, however, these differences may not be significant. CV of 5 NP-MnO_2 samples in Na_2SO_4 gives average capacitance values of 50 ± 20 F g^{-1}, 30 ± 10 F g^{-1} and 22 ± 8 F g^{-1} at 5, 50 and 500 mVs^{-1} respectively, which has the expected trend of decreasing average capacitance with scan rate but the magnitude of this difference is less than the between-sample variation. Similarly, comparison of the capacitance of NP-MnO_2 at 50 mV s^{-1} in Na_2SO_4 (30 ± 10 F g^{-1}) with the average as-prepared MnO_2 capacitance (40 ± 20 F g^{-1}) indicates that any capacitance variation due to modification is masked by the between-sample variation in both sample types.

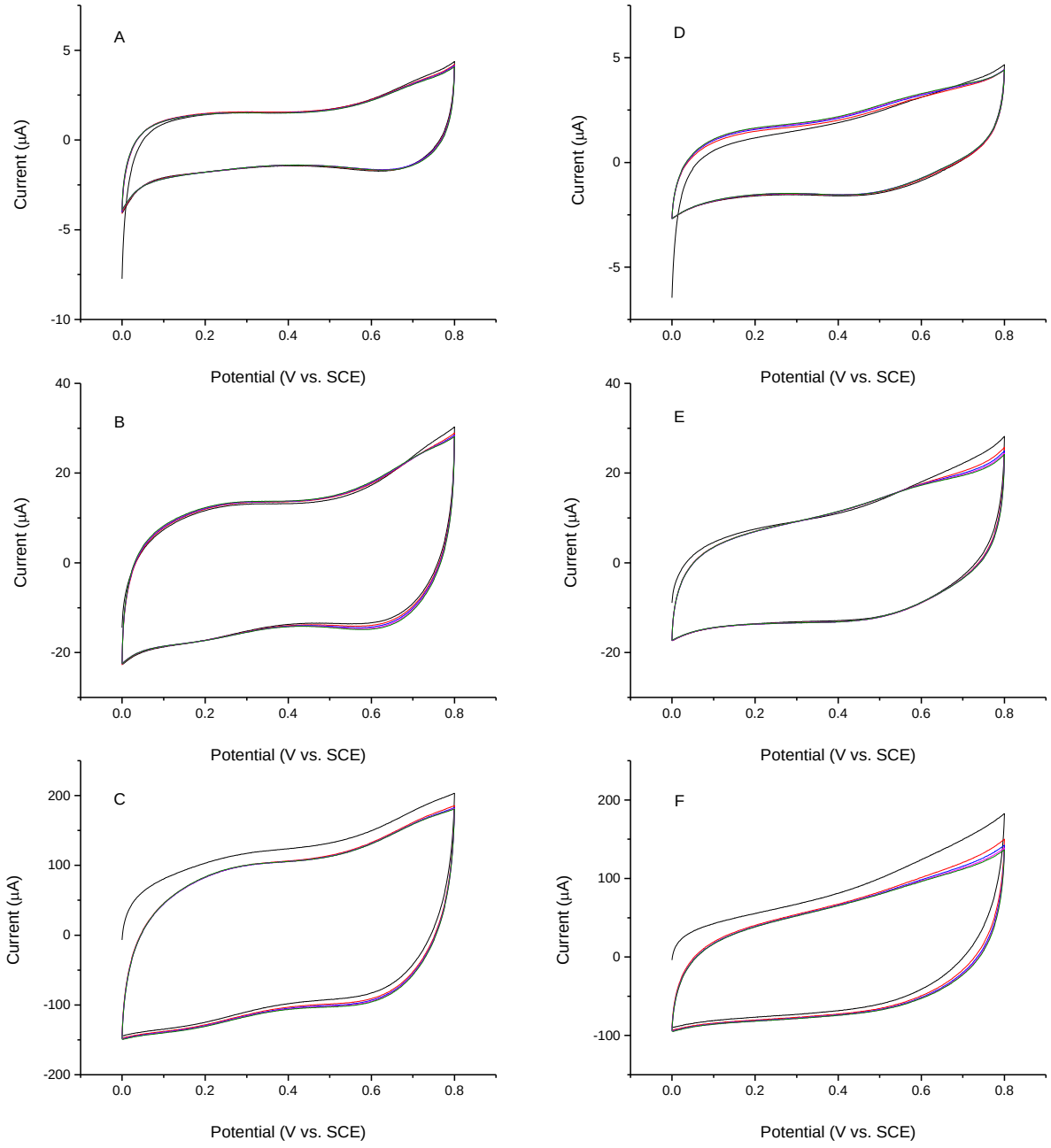

Figure 4.21: CV curves (scans 1-5) of NP-modified MnO_2 nanoparticles in 0.5 M KCl (A-C) or 0.5 M Na_2SO_4 (D-F). Scans were carried out at 5 mV s^{-1} (A and B), 50 mV s^{-1} (C and D) and 500 mV s^{-1} (E and F).

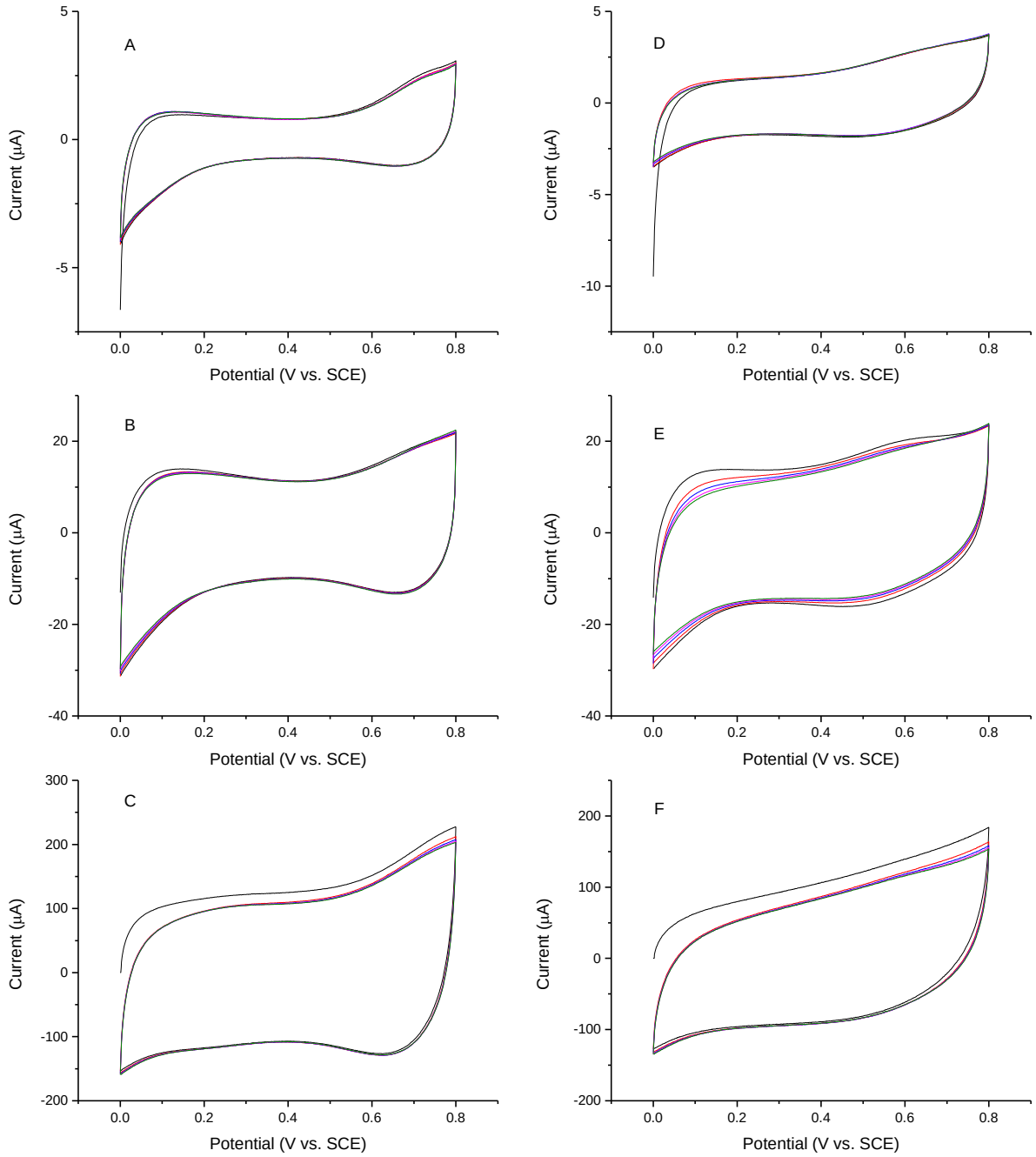

Figure 4.22: CV curves (scans 1-5) of NaOH blank MnO_2 nanoparticles in 0.5 M KCl (A-C) or 0.5 M Na_2SO_4 (D-F). Scans were carried out at 5 mV s^{-1} (A and B), 50 mV s^{-1} (C and D) and 500 mV s^{-1} (E and F).

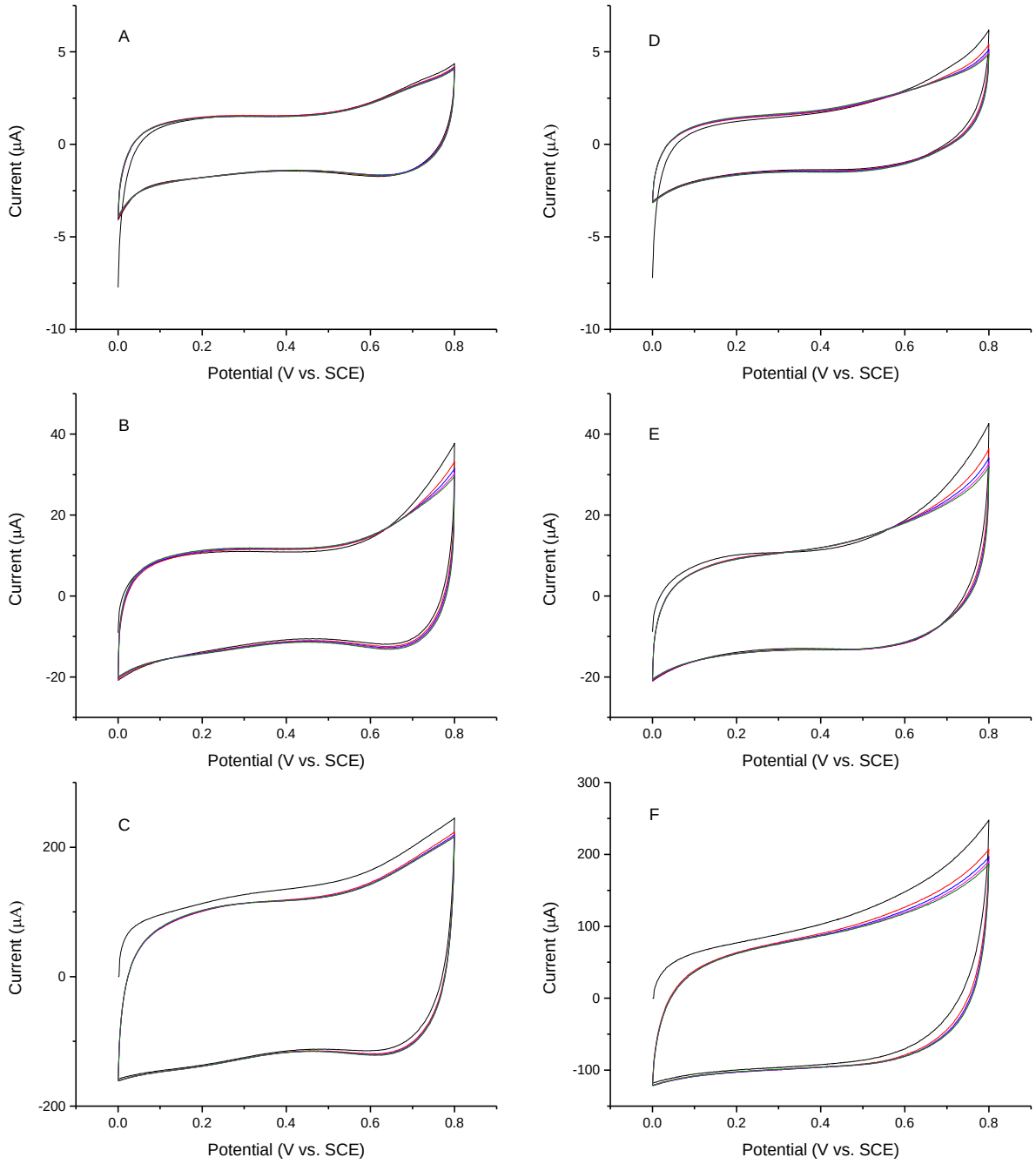

Figure 4.23: CV curves (scans 1-5) of AP-modified MnO_2 nanoparticles in 0.5 M KCl (A-C) or 0.5 M Na_2SO_4 (D-F). Scans were carried out at 5 mV s^{-1} (A and B), 50 mV s^{-1} (C and D) and 500 mV s^{-1} (E and F).

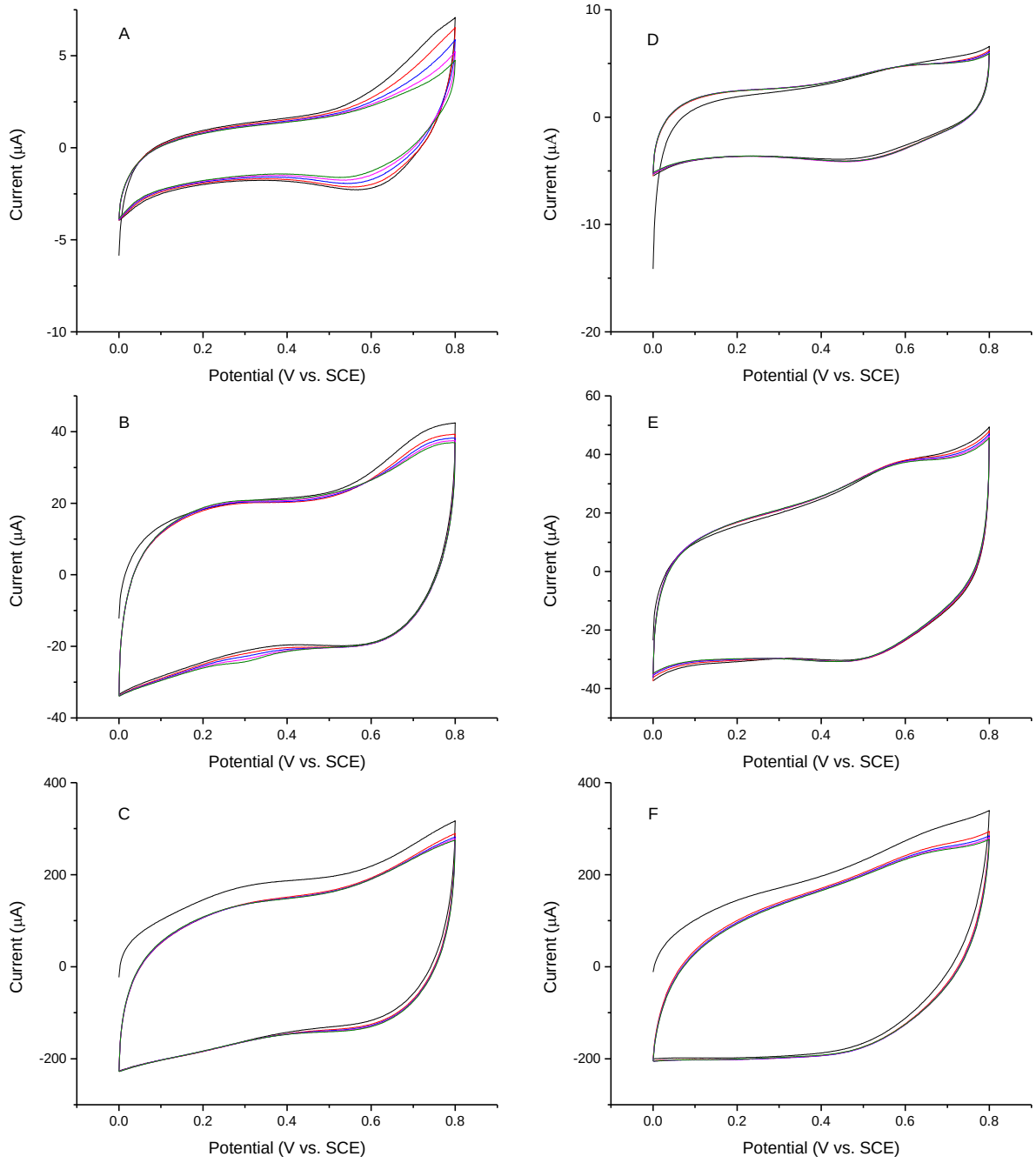

Figure 4.24: CV curves (scans 1-5) of NaOH blank MnO_2 nanoparticles in 0.5 M KCl (A-C) or 0.5 M Na_2SO_4 (D-F). Scans were carried out at 5 mV s^{-1} (A and B), 50 mV s^{-1} (C and D) and 500 mV s^{-1} (E and F).

Table 4.5: Capacitance data from CV scan 5 at various scan rates of as-prepared, NP-modified, NaOH blank, AP-modified and ACN blank MnO_2 nanoparticles drop cast on GC in 0.5 M KCl and 0.5 M Na_2SO_4.

Sample	Scan Rate (mV s^{-1})	KCl C (F g^{-1})	Na_2SO_4 C (F g^{-1})
As-Prepared[a]	5	60	63
	50	60	40
	500	46	29
NP-Mod[b]	5	33	33
	50	29	22
	500	20	12
NaOH Blank[b]	5	23	33
	50	26	26
	500	22	15
AP-Mod[b]	5	22	33
	50	26	25
	500	23	17
ACN Blank[b]	5	27	24
	50	21	17
	500	18	14

[a]Average capacitance data (n = 3) reproduced from Table 4.1, [b]Data from single samples

This high degree of capacitance variation between samples even persists within the same batch of MnO_2 material and is likely due to the random nature of the drop-coated nanoparticle films. The electrochemically-accessible surface area of the nanoparticle film is determined by the packing of the nanoparticles on the GC electrode surface. This will result in variable exposed areas between samples and thus varying capacitance. In an attempt to prepare reproducible surfaces, carbon paste electrodes incorporating MnO_2 nanorods were investigated (see below). For these electrodes, small variations in nanoparticle packing are likely to average out over the bulk of the material. In an alternative strategy, nanostructured MnO_2 films prepared by electrodeposition were used; this work is described in Chapter 5.

4.3.5.2 MnO_2/Carbon Powder Composite Electrodes

An alternative electrode setup for testing MnO_2 materials is to form a paste with the MnO_2 material, a conducting additive (usually carbon powder) and a binder (such as PTFE). This paste is then compressed onto an electrical contact to form an electrode. The mechanical and electrochemical properties of these electrodes can be adjusted by varying the composition of the paste. When preparing MnO_2 paste electrodes, the low conductivity of MnO_2 limits the amount of MnO_2 that can

be added without increasing electrode resistance. With a small proportion of MnO_2 it is difficult to evaluate the properties of the MnO_2 compared to the conducting additive. This can be somewhat mitigated by using an electrode with a large contact area between the electrical contact and electrode material to offset the high resistance by shortening the conduction path.

Initially, test electrodes containing only carbon powder (KS6 synthetic graphite) and PTFE binder were prepared by this method. The electrochemical suitability of these test electrodes was examined by cycling in hydroxymethylferrocene solution which showed a typical reversible response (Figure 4.25).

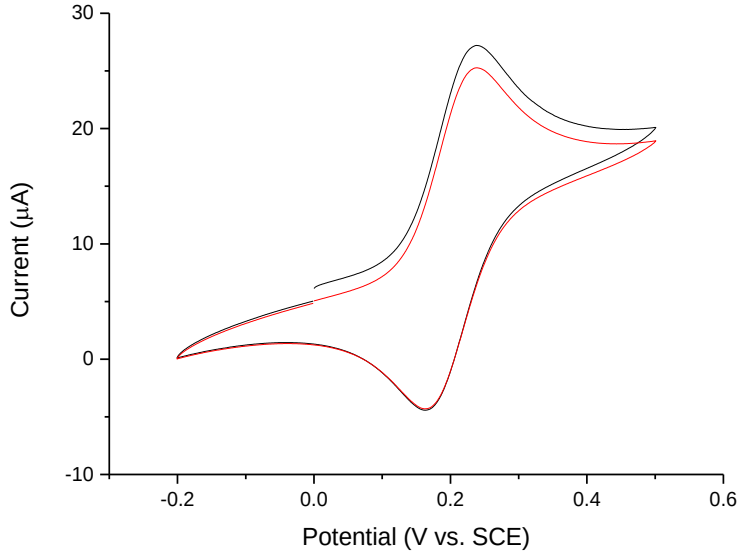

Figure 4.25: CV curves (scan 1 and 2) for KS6 carbon powder paste electrode at 50 mV s^{-1} in 1 mM hydroxymethylferrocene, 0.1 M KCl solution.

PTFE bound MnO_2 electrodes were prepared by mixing MnO_2 and carbon powder in 1:1, 4:1 and 8:1 ratios with 10 wt% (based on total electrode mass) PTFE binder.[37] Increasing the proportion of MnO_2 nanoparticles in the electrode paste resulted in brittle electrodes that would not polish effectively, however, lowering the MnO_2 content made it difficult to determine the effect of modification on the MnO_2 electrochemistry. The 4:1 MnO_2:C ratio produced electrodes that could be polished while retaining a higher proportion of MnO_2. The electrochemical behaviour of these electrodes was measured by cyclic voltammetry at a range of scan rates in 0.5 M KCl and Na_2SO_4 solutions (Figure 4.26). At low scan rates, the electrodes show a typical quasi-rectangular response with greater capacitance in Na_2SO_4. As the scan rate increases, the response becomes less rectangular and more resistive, particularly in KCl, with a corresponding decrease in capacitance. This scan rate dependence suggests that large proportions of the electrode area are difficult to access and at

higher scan rates, the charge balancing cations are unable to diffuse into the electrode surface which limits the available capacitance. The sharper decrease in capacitance with increase in scan rate in the presence of K^+ is in contrast with the drop-cast nanoparticle films examined on GC (Figure 4.5 A and B). It was expected that the smaller hydrated size of K^+ than Na^+ would result in a relatively lower diffusion barrier for K^+ at faster scan rates however the opposite is observed. It has been reported that on activated carbon electrodes double-layer capacitance increased with increasing hydrated ion size and decreasing ion mobility.[130] It was suggested that the more mobile ions diffuse further out into the electrolyte bulk during charging and discharging of the double layer, causing them to take longer to readsorb to the electrode and thus lowering the capacitance at higher scan rates. This indicates that these composite paste electrodes have a significant contribution from double-layer capacitance compared to the drop-cast nanoparticles. Over extended cycling, the electrolyte seeps into the electrode paste, causing the electrode material to break apart into the solution. This makes these electrodes unsuitable for studies of the effects of surface modification of MnO_2 nanorods. This work was not pursued further.

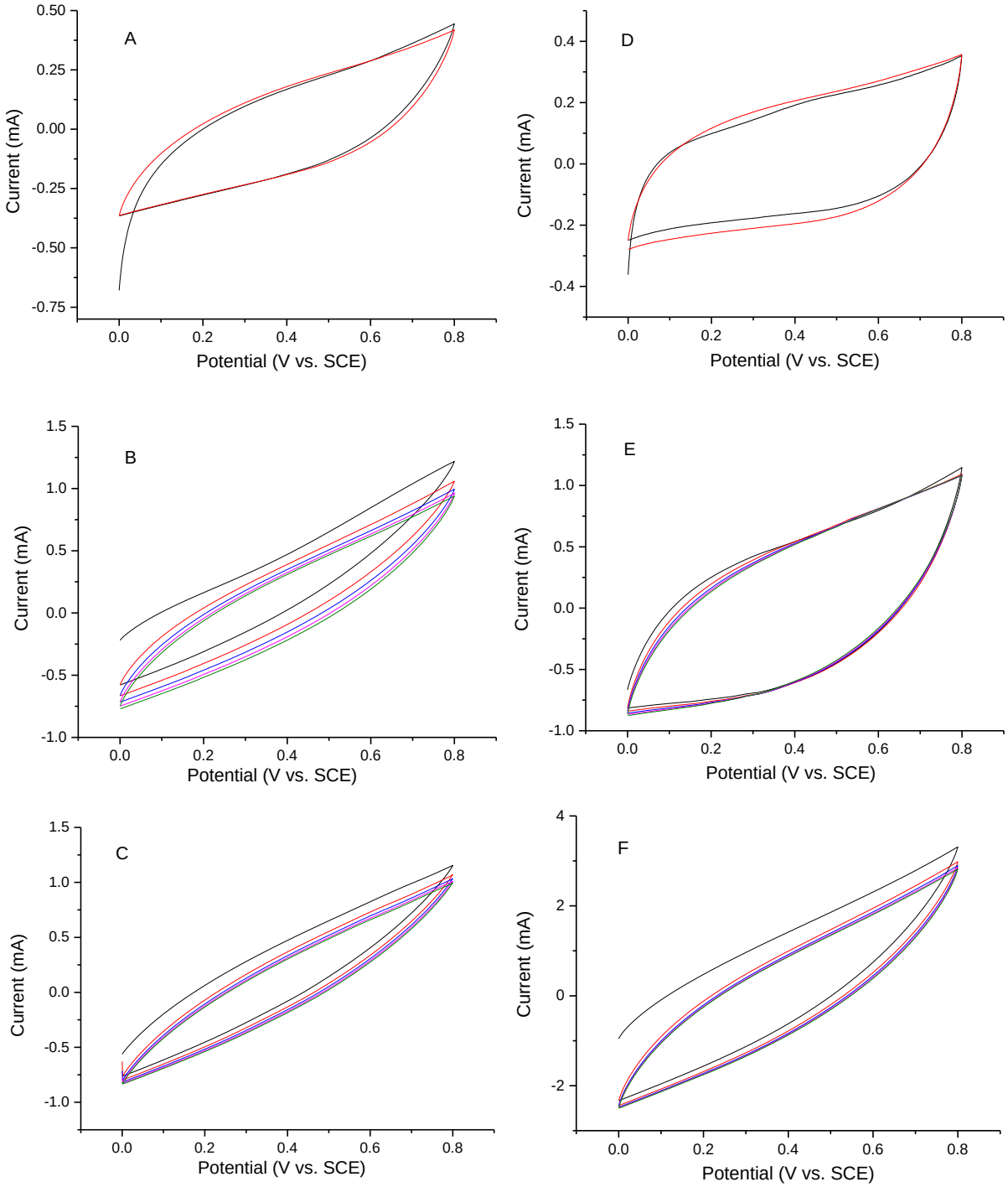

Figure 4.26: CV curves of 4:1 MnO_2:Carbon KS6 carbon powder paste electrodes in 0.5 M KCl (A-C) or 0.5 M Na_2SO_4 (D-F). Scans were carried out at 5 mV s^{-1} (A and B, Scans 1 and 2), 50 mV s^{-1} (C and D, Scans 1-5) and 500 mV s^{-1} (E and F, Scans 1-5).

4.3.6 Preparation of Tethered Nanoparticle Assemblies

Tethering of MnO_2 nanoparticles to carbon materials may offer a method to produce MnO_2 electrodes with an open, flexible structure. Such a structure should overcome stability and conductivity problems by allowing the electrode material to expand and contract while improving electrolyte access. Preparation of tethered nanoparticle assemblies was attempted by using the MnO_2 modification conditions previously discussed to achieve tethering through aryldiazonium salt grafting chemistry. Both planar carbon and carbon powders were used as tethering substrates and several tethering routes were investigated, as shown in Scheme 4.1 (reproduced here for convenience). After completion of this work, Ramirez-Castro et al. reported preparation of grafted assemblies of MnO_2 on carbon powder using aryldiazonium ion-based grafting.[100] Their findings will be discussed in the context of this work below.

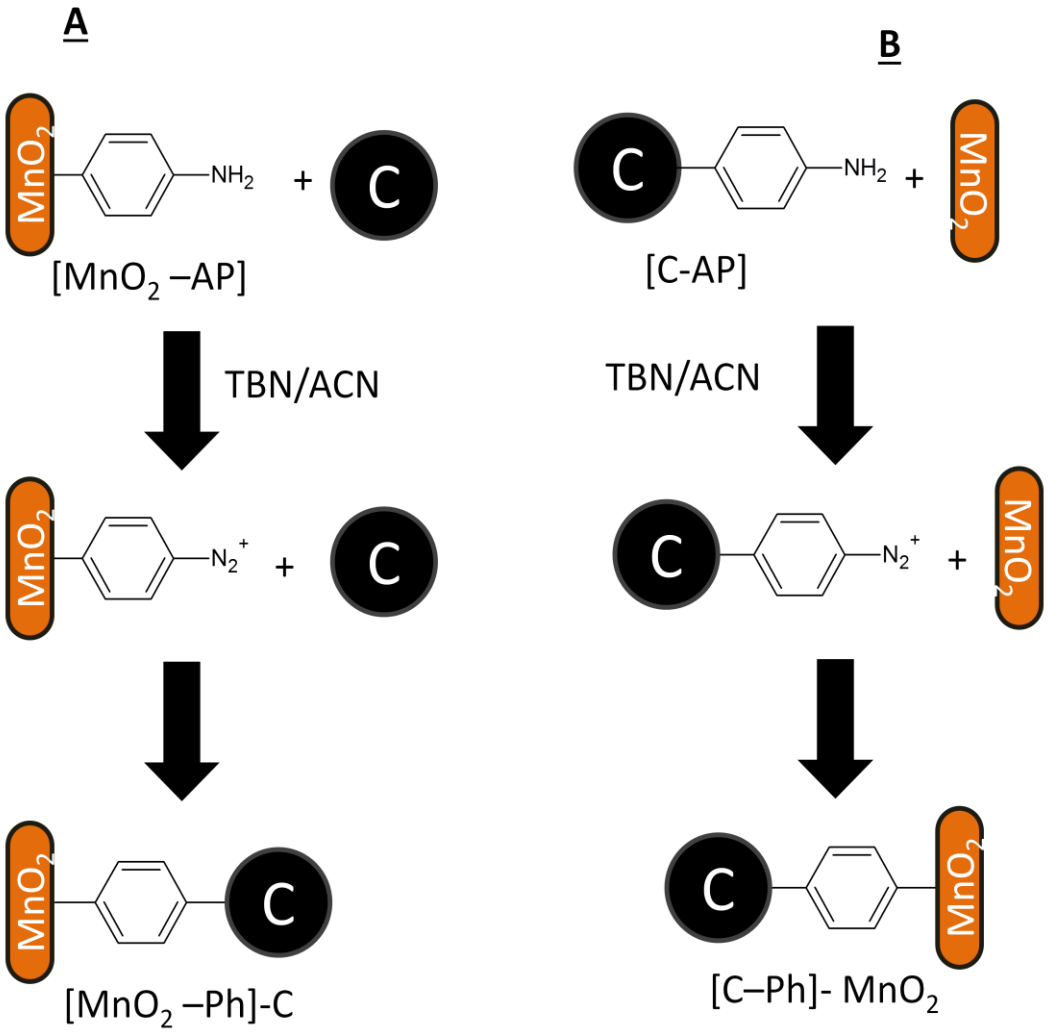

Scheme 4.1: Preparation of tethered assemblies of MnO_2 and carbon materials: A. tethering bare carbon to modified MnO_2 and B. tethering unmodified MnO_2 to modified carbon. TBN – tert-butyl nitrite, ACN – acetonitrile.

4.3.6.1 Preparation of Tethered Assemblies of MnO_2 Nanoparticles and Planar Carbon

4.3.6.1.1 Grafting reduced NP-MnO_2 to GC (Route A, Scheme 4.1)

Building on previous success with grafting NP groups to MnO_2 nanoparticles, this modified material was used as a starting point for producing tethered assemblies. By electrochemically reducing the NP groups on the surface of the nanoparticles, a mixed layer of amine and hydroxylamine groups is formed enabling the preparation of a diazonium-terminated surface for further grafting. Figure 4.27A shows the reduction of NP-MnO_2 on a glassy carbon surface; this reduced-NP film was then converted into a diazonium-terminated film by immersion in tert-butyl nitrite in acetonitrile.

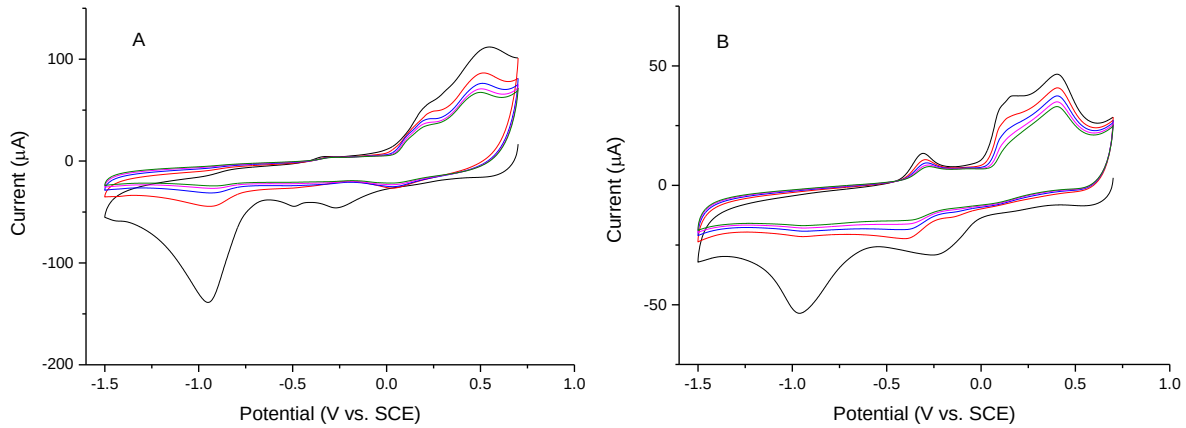

Figure 4.27: CV curves (scans 1-5) of MnO_2 nanoparticles at GC in 0.1 M KCl, 1:9 ethanol:H_2O solution: A. NP-MnO_2 reduction, B. Reduction of N_2^+-MnO_2 produced from reduced NP-MnO_2 to the GC electrode.

Initially the diazonium-terminated nanoparticles (N_2^+-MnO_2) were electrografted to the GC electrode in aqueous conditions however no grafting peak could be detected in the presence of the MnO_2 response (Figure 4.27B). Sonication (5 min in ultrapure water) of the surface was attempted to see if grafting had improved the adhesion of the nanoparticles to the surface. CV curves of the sonicated surface showed only a very small response (Figure 4.28A). A surface drop-coated with NP-modified nanoparticles (without subsequent grafting procedures) and treated with the same sonication procedure showed very similar CV response (Figure 4.28B), suggesting no enhancement in adhesion from the grafting process.

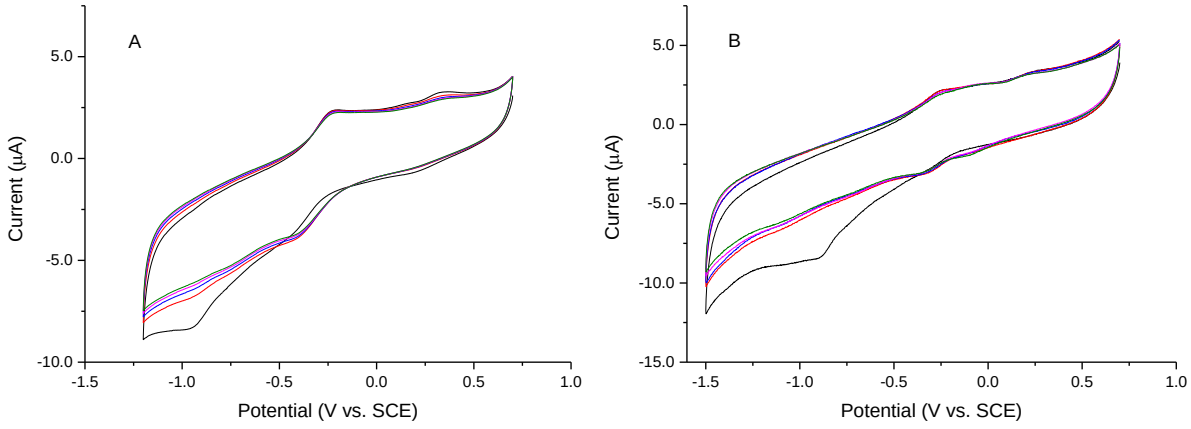

Figure 4.28: CV curves (scans 1-5) in 0.5 M Na_2SO_4 at 50 mV s^{-1} of A. reduced N_2^+-MnO_2 and B. NP-modified MnO_2 on GC after 5 min sonication in ultrapure water.

4.3.6.1.2 Grafting AP-MnO_2 to GC (Route A, Scheme 4.1)

To avoid the ill-defined nature of the reduced NP films, AP-modified MnO_2 was used instead to tether to carbon. AP-MnO_2 (prepared by the method described in Section 4.2.4.2) was drop-coated onto glassy carbon and then converted *in situ* to N_2^+-MnO_2 and grafted spontaneously to the GC surface. Control surfaces with AP-MnO_2 deposited without any grafting reaction were also prepared for comparison. The grafted surfaces were then sonicated and imaged by SEM to determine if the grafting reaction increased the stability of the MnO_2 nanoparticles on the surface. However, SEM imaging of these samples showed that neither the grafted sample nor the blank shows a significant density of nanoparticles, suggesting that grafting was unsuccessful or that sonication was too intense and ruptured the bonds to the surface.

4.3.6.1.3 Grafting Unmodified MnO_2 to AP-GC (Scheme 4.1, Route B)

In an alternative strategy to attach nanoparticles to carbon surfaces, an AP film is grafted to the carbon surface and then converted *in situ* to a diazonium-terminated film in the presence of unmodified MnO_2 nanoparticles. Again, these samples were sonicated and then examined by SEM. As shown in Figure 4.29, the grafted sample showed MnO_2 across the entire surface but with a higher density within the modified area (Figure 4.29B). However, the significance of this difference is difficult to determine. The tendency of MnO_2 to non-specifically adsorb onto the surface of the carbon substrate makes it difficult to determine if the tethering reactions are successful as treatments such as sonication are expected to be able to remove even grafted nanoparticles from the carbon surface.

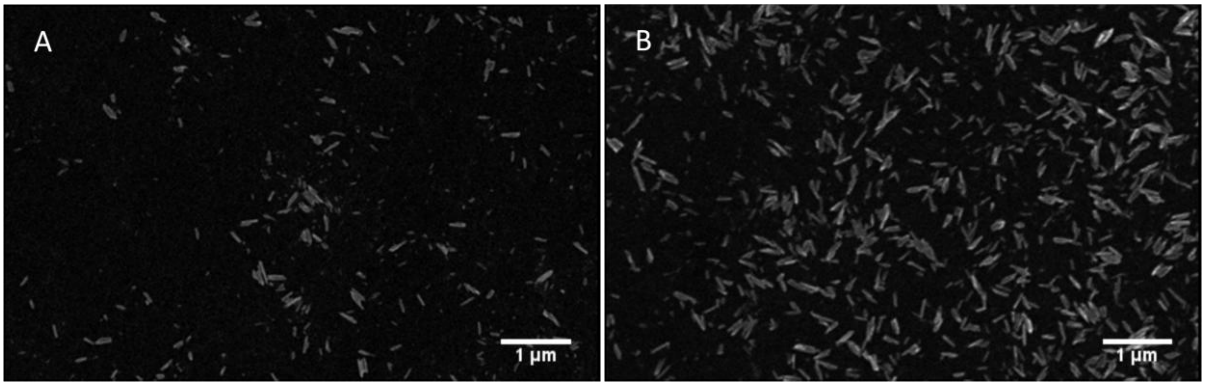

Figure 4.29: SEM images of MnO_2 nanorods after spontaneous reaction on unmodified (A) and diazonium-terminated (B) regions of a GC electrode.

Considering the problems outlined above, carbon powders were examined as the tethering substrate in subsequent experiments.

4.3.6.2 Preparation of Tethered Assemblies of MnO_2 Nanoparticles and Carbon Powder

4.3.6.2.1 Tethering Process

Attachment of MnO_2 to carbon powder can be undertaken by either of two routes: tethering AP-modified MnO_2 nanoparticles to unmodified carbon powder or vice versa (Routes A and B in Scheme 4.1 respectively). Due to the uncontrolled nature of the aryldiazonium grafting reaction that will produce multi-layer films and connect indiscriminately between reactants, it is likely these two routes would produce materials with different arrangements of MnO_2 and carbon.

AP-modified MnO_2 nanoparticles and carbon powders were prepared as described in Section 4.2.4.2. These materials were mixed with unmodified carbon powder or MnO_2 nanorods respectively, in acetonitrile in the presence of tert-butyl nitrite to convert the AP-film to a diazonium-terminated film. Two different MnO_2:C ratios (1:1 and 9:1) were used with two sizes of carbon powder (40 nm acetylene black and 2 μm KS6). The larger carbon powder was used with the higher MnO_2:C ratio to provide sufficient coverage of the large carbon particles. As the acetylene black was similarly-sized to the nanoparticles, a 1:1 ratio was used. Physical mixtures of AP-MnO_2 and AP-carbon with bare carbon/MnO_2 without the tethering reaction were prepared as blanks to test the effect of tethering the components.

The morphology and electrochemical behaviour of these assemblies were compared with physical mixtures by SEM and cyclic voltammetry respectively.

4.3.6.2.2 Morphology of Tethered Assemblies

One of the expected advantages of the tethered assembly electrode architecture is that it allows for better contact between the electrode materials than discrete mixtures as the two materials are held together by covalent bonding. Representative SEM images showing the distribution of the MnO_2 and carbon components in tethered assemblies and physical mixtures are presented in Figure 4.30. From these images, the differences in relative size between the two carbon particle types used and the MnO_2 nanoparticles is apparent where the larger KS6 carbon results in composites with individual carbon particles coated in nanoparticles whereas the acetylene black particles are sized such that they mix more evenly with the MnO_2. The distribution of the components in the assemblies and mixtures was investigated by drop-casting suspensions onto carbon substrates and imaging at different points across the dried materials. In the acetylene black materials, both the assembly (Figure 4.30A) and mixture (Figure 4.30B) had similar structures where the two materials were mostly well-incorporated but had regions where the nanoparticles and carbon powder had formed

separate aggregates. In the KS6 carbon-containing materials (Figure 4.30 C and D), the large size of the carbon powder precluded the formation of aggregates and the surfaces of the carbon particles were coated in nanoparticles in both cases. However, there were still a number of nanoparticle aggregates within the sample. The similarity between the tethered assemblies and physical mixtures appears to stem from the tendency of these materials to physisorb strongly to surfaces. This causes the mixtures to display similar behaviour to the assemblies by forming physisorbed clusters as well as resulting in aggregates of un-bonded material in the assemblies.

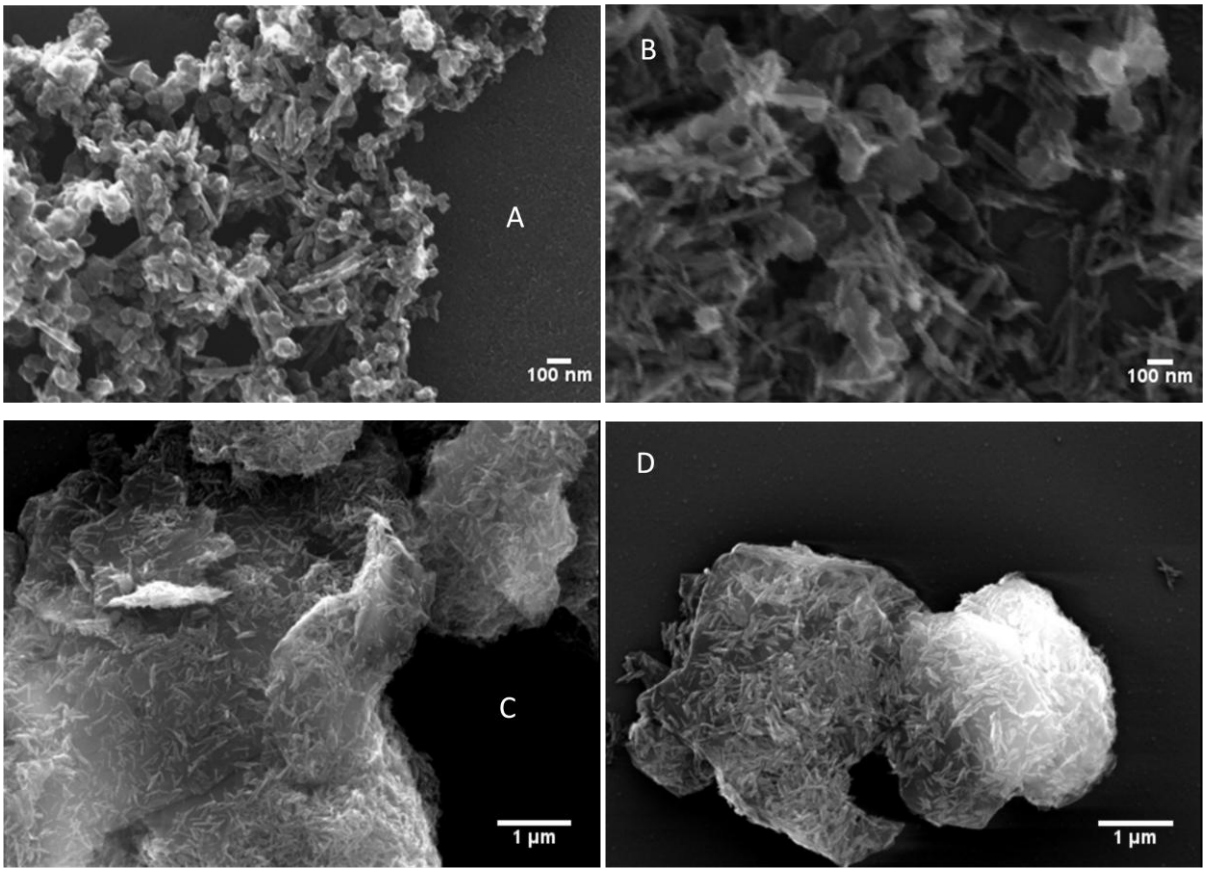

Figure 4.30: SEM images of MnO_2-carbon powder composites drop-cast onto GC: A. 1:1 tethered assembly of MnO_2 nanoparticles and acetylene black, B. 1:1 physical mixture of AP-modified MnO2 and acetylene black, C. 9:1 tethered assembly of MnO_2 and KS6 synthetic graphite and D. 9:1 physical mixture of MnO_2 and AP-modified KS6.

4.3.6.2.3 Electrochemical Behaviour of Tethered Assemblies

CV was used to compare the electrochemical behaviour of the nanoparticle assemblies with physical mixtures by drop-coating the materials onto GC electrodes. Comparison between the MnO_2 containing materials and the isolated carbon powders (Figure 4.31) show that the carbon powders have much lower capacitance without the MnO_2 materials and have relatively featureless

electrochemistry (apart from an adsorption peak on the KS6 material). Both the tethered-assemblies (Figure 4.31 B and E) and physical mixtures (Figure 4.31 C and F) have similar electrochemical response which is dominated by the MnO_2 electrochemistry. There are differences in peak intensity, shape and position between the different samples, however, this is likely due to between-sample variation rather than changes due to structural differences.

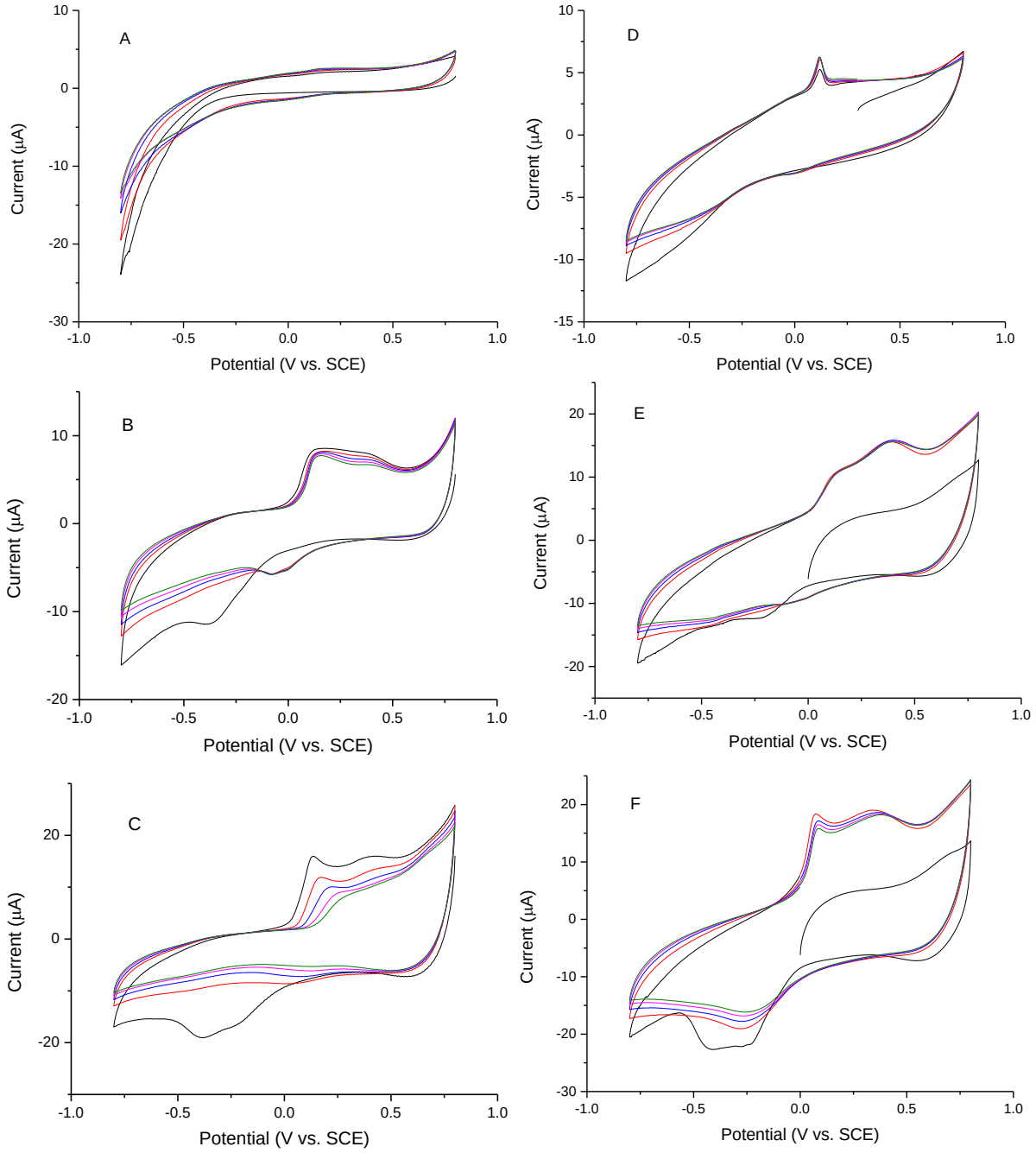

Figure 4.31: CV curves (scans 1-5) at 50 mV s^{-1} in 0.5 M KCl of GC electrodes drop-coated with acetylene black (A-C) and KS6 (D-F) carbon powder unmodified (A and D), and in tethered-assemblies (B and E) or physical mixtures (C and F) with MnO_2 nanoparticles.

In order to improve separation of the unreacted material from assemblies, further separation steps were used. These experiments were carried out using the [KS6-Ph]-MnO_2 assemblies as the larger size carbon powder compared to the MnO_2 material should allow for more effective separation. Centrifugation was used to separate the assemblies from the unreacted material using a slow rotor speed to favour the settling of the larger assemblies over the smaller unreacted nanoparticles. The precipitates from tethered assemblies and physical mixtures prepared via this method were then analysed by CV (Figure 4.32) and SEM (Figure 4.33).

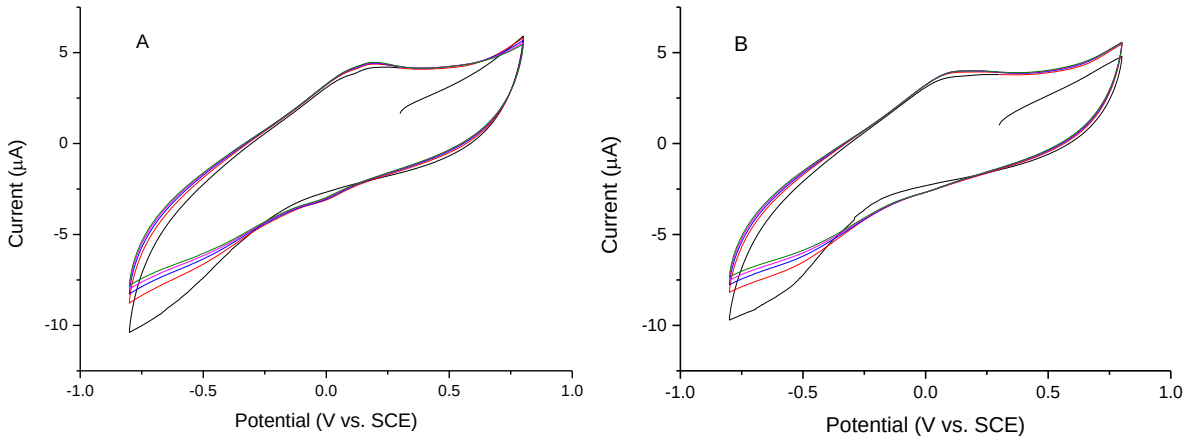

Figure 4.32: CV curves (scans 1-5) at 50 mV s^{-1} in 0.5 M KCl of the precipitate produced from centrifugation of 9:1 MnO_2:KS6 composites drop cast onto GC: A. Tethered assembly of MnO_2 nanoparticles and KS6 and B. physical mixture of MnO_2 nanoparticles and AP-modified KS6.

Comparison of the electrochemical response for the precipitates shows nearly identical response for the assembly and the physical mixtures. The features associated with the MnO_2 nanoparticles have decreased significantly compared to the initially-prepared assemblies, indicating that the separation process is at least partially effective at removing unreacted nanoparticles from the sample. SEM imaging also shows that the assemblies have similar structure to the physical mixtures and that despite the additional separation there is still a significant amount of loose MnO_2 and MnO_2 aggregates in both samples. These results indicate that in addition to requiring further separation, different solution or solvent conditions are needed to properly suspend these aggregates.

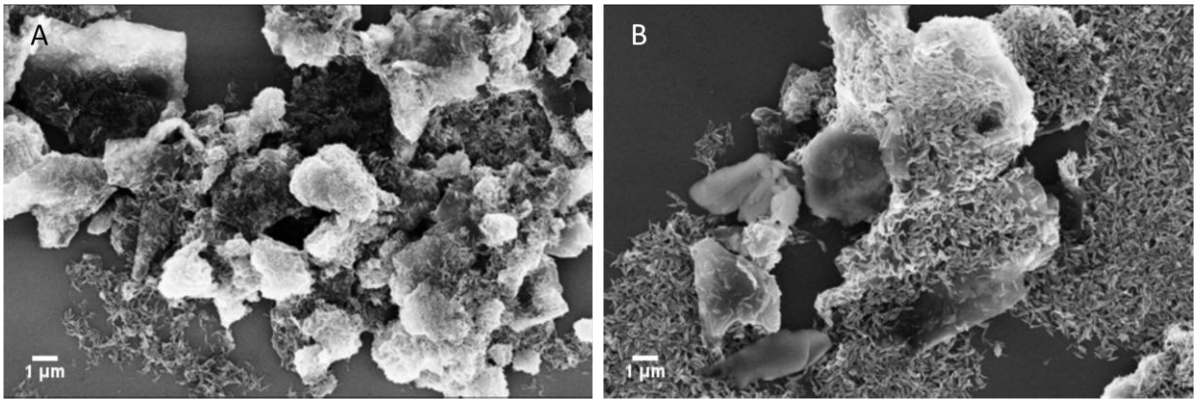

Figure 4.33: SEM images of the precipitate produced from centrifugation of 9:1 MnO_2:KS6 composites drop-cast onto GC: A. 9:1 tethered assembly of MnO_2 and KS6 synthetic graphite and B. 9:1 physical mixture of MnO_2 and AP-modified KS6.

Recently, Ramirez-Castro et al. reported preparation and electrochemical characterisation of carbon/MnO_2 composites bridged by a similar aryldiazonium ion-grafting strategy.[100] In their work, carbon black was modified with AP groups by overnight spontaneous reaction in aqueous acid and was bridged to amorphous MnO_2 particles by *in situ* diazotisation and spontaneous grafting in acetonitrile/tert-butyl nitrite solution for 4 hours (Scheme 4.2). This tethered assembly was contrasted with a physical mixture of amorphous MnO_2 and carbon powder by TEM, SEM, XPS and CV.

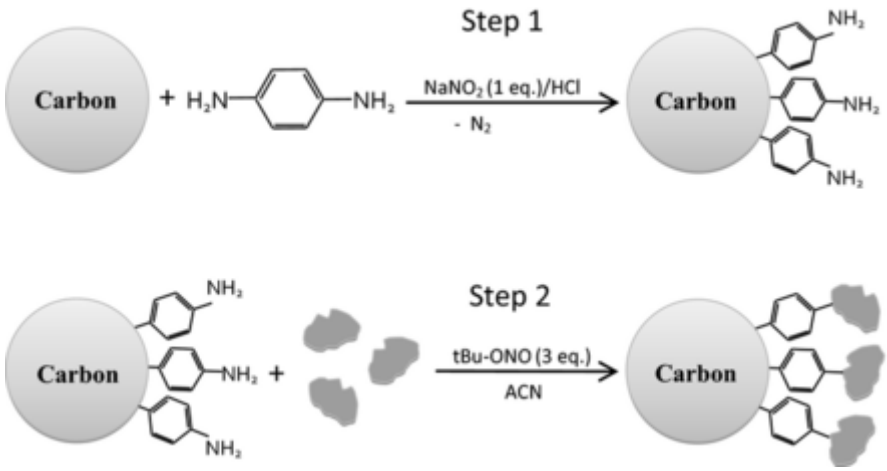

Scheme 4.2: Preparation of MnO_2-C tethered assemblies. Step 1 corresponds to the formation of AP-modified carbon powder and step 2 to the diazotisation and *in situ* grafting of the modified carbon powder to the MnO_2 particles. Reproduced from reference 100.

TEM and SEM images showed that the tethered assembly had more uniform distribution of the MnO_2 particles across the carbon powder which tended to form aggregates in the physical mixture.

XPS analysis showed an O 1s bonding feature present only in the tethered assembly at similar energy to those described in this thesis work for Mn-O-C bonding in the modified MnO_2 samples in this work. CV of these materials showed the tethered assembly had enhanced capacitance and maintained capacitance better at high scan rates compared to the physical mixture. The improvements in electrochemical behaviour of the tethered assemblies were attributed to the tight coupling between the carbon and MnO_2 particles improving electron transfer and the improved dispersion of the particles increasing the amount of MnO_2 that is electrochemically active.

The observation of improved dispersion of tethered assemblies by Ramirez-Castro et al. is in contrast to the samples described in this chapter where both MnO_2 aggregates and a high coverage of MnO_2 adsorbed non-specifically to the carbon surfaces was observed regardless of covalent attachment. The differences in material distribution between studies could arise due to the additional sonication steps used in the cleaning process in this thesis work improving the dispersion of the materials compared to just rinsing. Additionally, the differences between the physical mixtures in this work and the work by Ramirez-Castro et al. could arise due to the physical mixtures in their work being of unmodified material rather than the appropriate AP-modified starting material. It was observed above that the dispersibility of MnO_2 was improved after aryldiazonium ion modification and thus physical mixtures involving modified materials may disperse more easily. The reported XPS analysis suggests that coupling between the MnO_2 and carbon powder is successful due to the introduction of a feature at ~534 eV assigned to Mn-O-C bonding which could only arise from the phenyl linker molecule. However, carboxyl features have also been observed by XPS at the same energy on carbon powder surfaces and were found to be enhanced after the modification process.[131]

The improvements in the properties of the tethered assemblies over physical mixtures observed by Ramirez-Castro et al that were not found in this work could be explained by their use of a longer reaction time (4 h compared to 1 h in this work). The increased bonding between the MnO_2 and carbon materials would improve the contact between the particles and thus their electrochemical performance. Although it was found in this thesis work that modification of MnO_2 with AP-groups occurred within 1 h reaction time, the conversion of the grafted AP film to an aryldiazonium-terminated film and subsequent grafting reaction between the MnO_2 and carbon particles may be slower than the initial grafting step. Alternatively, the differences Ramirez-Castro et al. observed between their tethered assembly and physical mixture may be due to the poor dispersion of the physical mixture compared to the mixture used in this thesis work. In both covalently bound and physically mixed systems in this work, the MnO_2 and carbon powders were well mixed as evidenced by SEM imaging, suggesting uniform distribution of material is possible without covalent bonding.

Regardless of the origin of this effect, the work by Ramirez-Castro et al. provides evidence that well-dispersed composite materials have enhanced properties and thus the tethered assembly approach is viable for producing effective pseudocapacitor electrodes.

4.4 Conclusions

Conditions were developed to modify MnO_2 nanoparticles with aryl layers using aryldiazonium salts in aqueous and non-aqueous conditions. The layers were found to be covalently bound through O to the MnO_2 surface. Characterisation of the effect of modification on the electrochemical and physical properties was complicated by the difficulty in preparing reproducible MnO_2 nanoparticle electrodes. Any change in capacitance or stability after modification must be small compared to the sample-to-sample variation. To attempt to address this difficulty, electrodeposited MnO_2 films were prepared; this work is discussed in Chapter 5.

Aryldiazonium salt-based grafting was used to attach tether molecules to MnO_2 and carbon particles to prepare tethered MnO_2-Ph-C assemblies. However, any effects of this on electrode properties could not be established due to the large amount of non-specific adsorption and unreacted aggregated material within the modified samples. Further development of separation and characterisation methods are needed to fully explore the possibilities of surface modification to control the properties of MnO_2 and produce new electrode architectures.

4.5 References

1. Zhang, K.; Han, X.; Hu, Z.; Zhang, X.; Tao, Z.; Chen, J., Nanostructured Mn-Based Oxides for Electrochemical Energy Storage and Conversion. *Chem. Soc. Rev.* **2015,** *44* (3), 699-728.
2. Yuan, Y.; Wu, S.; Shu, F.; Liu, Z., An Mno_2 Nanosheet as a Label-Free Nanoplatform for Homogeneous Biosensing. *Chem. Commun.* **2014,** *50* (9), 1095-1097.
3. Kuo, C.-H.; Mosa, I. M.; Poyraz, A. S.; Biswas, S.; El-Sawy, A. M.; Song, W.; Luo, Z.; Chen, S.-Y.; Rusling, J. F.; He, J.; Suib, S. L., Robust Mesoporous Manganese Oxide Catalysts for Water Oxidation. *ACS Catal.* **2015,** *5* (3), 1693-1699.
4. Xu, C.; Kang, F.; Li, B.; Du, H., Recent Progress on Manganese Dioxide Based Supercapacitors. *J. Mater. Res.* **2010,** *25* (08), 1421-1432.
5. Young, M. J.; Holder, A. M.; George, S. M.; Musgrave, C. B., Charge Storage in Cation Incorporated A-MnO_2. *Chem. Mater.* **2015,** *27* (4), 1172-1180.
6. Gao, T.; Glerup, M.; Krumeich, F.; Nesper, R.; Fjellvåg, H.; Norby, P., Microstructures and Spectroscopic Properties of Cryptomelane-Type Manganese Dioxide Nanofibers. *J. Phys. Chem. C* **2008,** *112* (34), 13134-13140.
7. Dong, Y.; Li, K.; Jiang, P.; Wang, G.; Miao, H.; Zhang, J.; Zhang, C., Simple Hydrothermal Preparation of α-, β-, and γ-MnO_2 and Phase Sensitivity in Catalytic Ozonation. *RSC Adv.* **2014,** *4* (74), 39167-39173.
8. Portehault, D.; Cassaignon, S.; Baudrin, E.; Jolivet, J.-P., Structural and Morphological Control of Manganese Oxide Nanoparticles Upon Soft Aqueous Precipitation through MnO_4^-/Mn^{2+} Reaction. *J. Mater. Chem.* **2009,** *19* (16), 2407-2416.

9. Luo, J.; Zhang, Q.; Suib, S. L., Mechanistic and Kinetic Studies of Crystallization of Birnessite. *Inorg. Chem.* **2000,** *39* (4), 741-747.
10. Wang, X.; Li, Y., Synthesis and Formation Mechanism of Manganese Dioxide Nanowires/Nanorods. *Chem. Eur. J.* **2003,** *9* (1), 300-306.
11. Zhang, L.-C.; Liu, Z.-H.; Lv, H.; Tang, X.; Ooi, K., Shape-Controllable Synthesis and Electrochemical Properties of Nanostructured Manganese Oxides. *J. Phys. Chem. C* **2007,** *111* (24), 8418-8423.
12. Kumar, N.; Dineshkumar, P.; Rameshbabu, R.; Sen, A., Morphological Analysis of Ultra Fine A-MnO_2 Nanowires under Different Reaction Conditions. *Mater. Lett.* **2015,** *158*, 309-312.
13. Wang, J.-G.; Kang, F.; Wei, B., Engineering of MnO_2-Based Nanocomposites for High-Performance Supercapacitors. *Prog. Mater Sci.* **2015,** *74*, 51-124.
14. Wang, J.-G.; Yang, Y.; Huang, Z.-H.; Kang, F., Coaxial Carbon Nanofibers/MnO_2 Nanocomposites as Freestanding Electrodes for High-Performance Electrochemical Capacitors. *Electrochim. Acta* **2011,** *56* (25), 9240-9247.
15. Ma, S.-B.; Ahn, K.-Y.; Lee, E.-S.; Oh, K.-H.; Kim, K.-B., Synthesis and Characterization of Manganese Dioxide Spontaneously Coated on Carbon Nanotubes. *Carbon* **2007,** *45* (2), 375-382.
16. Biswal, A.; Chandra Tripathy, B.; Sanjay, K.; Subbaiah, T.; Minakshi, M., Electrolytic Manganese Dioxide (EMD): A Perspective on Worldwide Production, Reserves and Its Role in Electrochemistry. *RSC Advances* **2015,** *5* (72), 58255-58283.
17. Ali, G. A. M.; Yusoff, M. M.; Ng, Y. H.; Lim, H. N.; Chong, K. F., Potentiostatic and Galvanostatic Electrodeposition of Manganese Oxide for Supercapacitor Application: A Comparison Study. *Curr. Appl. Phys.* **2015,** *15* (10), 1143-1147.
18. Cao, J.; Li, X.; Wang, Y.; Walsh, F. C.; Ouyang, J.-H.; Jia, D.; Zhou, Y., Materials and Fabrication of Electrode Scaffolds for Deposition of MnO_2 and Their True Performance in Supercapacitors. *J. Power Sources* **2015,** *293*, 657-674.
19. Wei, W.; Cui, X.; Mao, X.; Chen, W.; Ivey, D. G., Morphology Evolution in Anodically Electrodeposited Manganese Oxide Nanostructures for Electrochemical Supercapacitor Applications—Effect of Supersaturation Ratio. *Electrochim. Acta* **2011,** *56* (3), 1619-1628.
20. Deng, Y.; Wan, L.; Xie, Y.; Qin, X.; Chen, G., Recent Advances in Mn-Based Oxides as Anode Materials for Lithium Ion Batteries. *RSC Adv.* **2014,** *4* (45), 23914-23935.
21. Li, L.; Nan, C.; Lu, J.; Peng, Q.; Li, Y., α-Mno_2 Nanotubes: High Surface Area and Enhanced Lithium Battery Properties. *Chem. Commun.* **2012,** *48* (55), 6945-6947.
22. Li, Y.; Zhang, Q.; Zhu, J.; Wei, X.-L.; Shen, P. K., An Extremely Stable MnO_2 Anode Incorporated with 3d Porous Graphene-Like Networks for Lithium-Ion Batteries. *J. Mater. Chem. A* **2014,** *2* (9), 3163-3168.
23. Li, X.; Li, D.; Qiao, L.; Wang, X.; Sun, X.; Wang, P.; He, D., Interconnected Porous MnO Nanoflakes for High-Performance Lithium Ion Battery Anodes. *J. Mater. Chem.* **2012,** *22* (18), 9189-9194.
24. Brousse, T.; Bélanger, D.; Long, J. W., To Be or Not to Be Pseudocapacitive? *J. Electrochem. Soc.* **2015,** *162* (5), A5185-A5189.
25. Conway, B. E.; Pell, W. G., Double-Layer and Pseudocapacitance Types of Electrochemical Capacitors and Their Applications to the Development of Hybrid Devices. *J. Solid State Electrochem.* **2003,** *7* (9), 637-644.
26. Conway, B. E.; Birss, V.; Wojtowicz, J., The Role and Utilization of Pseudocapacitance for Energy Storage by Supercapacitors. *J. Power Sources* **1997,** *66* (1–2), 1-14.
27. Simon, P.; Gogotsi, Y.; Dunn, B., Where Do Batteries End and Supercapacitors Begin? *Science* **2014,** *343* (6176), 1210-1211.
28. Ghodbane, O.; Ataherian, F.; Wu, N.-L.; Favier, F., In Situ Crystallographic Investigations of Charge Storage Mechanisms in MnO_2-Based Electrochemical Capacitors. *J. Power Sources* **2012,** *206* (0), 454-462.

29. Kanoh, H.; Tang, W.; Makita, Y.; Ooi, K., Electrochemical Intercalation of Alkali-Metal Ions into Birnessite-Type Manganese Oxide in Aqueous Solution. *Langmuir* **1997,** *13* (25), 6845-6849.
30. Hadzi-Jordanov, S.; Angerstein-Kozlowska, H.; Vukovič, M.; Conway, B. E., Reversibility and Growth Behavior of Surface Oxide Films at Ruthenium Electrodes. *J. Electrochem. Soc.* **1978,** *125* (9), 1471-1480.
31. Mozota, J.; Conway, B. E., Surface and Bulk Processes at Oxidized Iridium Electrodes—I. Monolayer Stage and Transition to Reversible Multilayer Oxide Film Behaviour. *Electrochim. Acta* **1983,** *28* (1), 1-8.
32. Wang, G.; Zhang, L.; Zhang, J., A Review of Electrode Materials for Electrochemical Supercapacitors. *Chem. Soc. Rev.* **2012,** *41* (2).
33. Zhao, X.; Sanchez, B. M.; Dobson, P. J.; Grant, P. S., The Role of Nanomaterials in Redox-Based Supercapacitors for Next Generation Energy Storage Devices. *Nanoscale* **2011,** *3* (3).
34. Zheng, J. P.; Jow, T. R., A New Charge Storage Mechanism for Electrochemical Capacitors. *J. Electrochem. Soc.* **1995,** *142* (1), L6-L8.
35. Lee, H. Y.; Manivannan, V.; Goodenough, J. B., Electrochemical Capacitors with KCl Electrolyte. *C. R. Acad. Sci., Ser. IIC: Chim.* **1999,** *2* (11–13), 565-577.
36. Lee, H. Y.; Goodenough, J. B., Supercapacitor Behavior with KCl Electrolyte. *J. Solid State Chem.* **1999,** *144* (1), 220-223.
37. Brousse, T.; Toupin, M.; Dugas, R.; Athouël, L.; Crosnier, O.; Bélanger, D., Crystalline MnO_2 as Possible Alternatives to Amorphous Compounds in Electrochemical Supercapacitors. *J. Electrochem. Soc.* **2006,** *153* (12), A2171-A2180.
38. Kuo, S.-L.; Wu, N.-L., Investigation of Pseudocapacitive Charge-Storage Reaction of $MnO_2 \cdot nH_2O$ Supercapacitors in Aqueous Electrolytes. *J. Electrochem. Soc.* **2006,** *153* (7), A1317-A1324.
39. Lang, X.; Hirata, A.; Fujita, T.; Chen, M., Nanoporous Metal/Oxide Hybrid Electrodes for Electrochemical Supercapacitors. *Nat Nano* **2011,** *6* (4), 232-236.
40. Lu, Q.; Chen, J. G.; Xiao, J. Q., Nanostructured Electrodes for High-Performance Pseudocapacitors. *Angew. Chem. Int. Ed.* **2013,** *52* (7), 1882-1889.
41. Zhu, G.; He, Z.; Chen, J.; Zhao, J.; Feng, X.; Ma, Y.; Fan, Q.; Wang, L.; Huang, W., Highly Conductive Three-Dimensional MnO_2-Carbon Nanotube-Graphene-Ni Hybrid Foam as a Binder-Free Supercapacitor Electrode. *Nanoscale* **2014,** *6* (2), 1079-1085.
42. Kang, J.; Hirata, A.; Kang, L.; Zhang, X.; Hou, Y.; Chen, L.; Li, C.; Fujita, T.; Akagi, K.; Chen, M., Enhanced Supercapacitor Performance of MnO_2 by Atomic Doping. *Angew. Chem. Int. Ed.* **2013**, 1664-1667.
43. Li, X.; Zhang, L.; Dong, H.; Xia, T.; Huang, Z., Bismuth Oxide Coated Amorphous Manganese Dioxide for Electrochemical Capacitors. *Solid State Sci.* **2015,** *43* (0), 46-52.
44. Lu, Q.; Chen, J. G.; Xiao, J. Q., Nanostructured Electrodes for High-Performance Pseudocapacitors. *Angew. Chem. Int. Ed.* **2013**, 1882-1889.
45. Zhao, X.; Zhang, L.; Murali, S.; Stoller, M. D.; Zhang, Q.; Zhu, Y.; Ruoff, R. S., Incorporation of Manganese Dioxide within Ultraporous Activated Graphene for High-Performance Electrochemical Capacitors. *ACS Nano* **2012,** *6* (6), 5404-5412.
46. Hsieh, Y.-C.; Lee, K.-T.; Lin, Y.-P.; Wu, N.-L.; Donne, S. W., Investigation on Capacity Fading of Aqueous $MnO_2 \cdot nH_2O$ Electrochemical Capacitor. *J. Power Sources* **2008,** *177* (2), 660-664.
47. Sivakkumar, S. R.; Ko, J. M.; Kim, D. Y.; Kim, B. C.; Wallace, G. G., Performance Evaluation of CNT/Polypyrrole/MnO_2 Composite Electrodes for Electrochemical Capacitors. *Electrochim. Acta* **2007,** *52* (25), 7377-7385.
48. Liu, R.; Lee, S. B., MnO_2/Poly(3,4-Ethylenedioxythiophene) Coaxial Nanowires by One-Step Coelectrodeposition for Electrochemical Energy Storage. *J. Am. Chem. Soc.* **2008,** *130* (10), 2942-2943.
49. Yan, D.; Li, Y.; Liu, Y.; Zhuo, R.; Geng, B.; Wu, Z.; Wang, J.; Ren, P.; Yan, P., Design and Influence of Mass Ratio on Supercapacitive Properties of Ternary Electrode Material Reduced

Graphene Oxide@MnO_2@ Poly(3,4-Ethylenedioxythiophene)-Poly(Styrene Sulfonate). *Electrochim. Acta* **2015,** *169*, 317-325.
50. Chang, J.-K.; Lee, M.-T.; Huang, C.-H.; Tsai, W.-T., Physicochemical Properties and Electrochemical Behavior of Binary Manganese–Cobalt Oxide Electrodes for Supercapacitor Applications. *Mater. Chem. Phys.* **2008,** *108* (1), 124-131.
51. Prasad, K. R.; Miura, N., Potentiodynamically Deposited Nanostructured Manganese Dioxide as Electrode Material for Electrochemical Redox Supercapacitors. *J. Power Sources* **2004,** *135* (1–2), 354-360.
52. Zhong, C.; Deng, Y.; Hu, W.; Qiao, J.; Zhang, L.; Zhang, J., A Review of Electrolyte Materials and Compositions for Electrochemical Supercapacitors. *Chem. Soc. Rev.* **2015,** *44* (21), 7484-7539.
53. Chen, L. Y.; Kang, J. L.; Hou, Y.; Liu, P.; Fujita, T.; Hirata, A.; Chen, M. W., High-Energy-Density Nonaqueous MnO_2@Nanoporous Gold Based Supercapacitors. *J. Mater. Chem. A* **2013,** *1* (32), 9202-9207.
54. Li, Z.-S.; Wang, H.-Q.; Huang, Y.-G.; Li, Q.-Y.; Wang, X.-Y., Manganese Dioxide-Coated Activated Mesocarbon Microbeads for Supercapacitors in Organic Electrolyte. *Colloids Surf., A* **2010,** *366* (1–3), 104-109.
55. Perera, S. D.; Rudolph, M.; Mariano, R. G.; Nijem, N.; Ferraris, J. P.; Chabal, Y. J.; Balkus Jr, K. J., Manganese Oxide Nanorod–Graphene/Vanadium Oxide Nanowire–Graphene Binder-Free Paper Electrodes for Metal Oxide Hybrid Supercapacitors. *Nano Energy* **2013,** *2* (5), 966-975.
56. Lee, M.-T.; Tsai, W.-T.; Deng, M.-J.; Cheng, H.-F.; Sun, I. W.; Chang, J.-K., Pseudocapacitance of MnO_2 Originates from Reversible Insertion/Desertion of Thiocyanate Anions Studied Using in Situ X-Ray Absorption Spectroscopy in Ionic Liquid Electrolyte. *J. Power Sources* **2010,** *195* (3), 919-922.
57. Chang, J.-K.; Lee, M.-T.; Tsai, W.-T.; Deng, M.-J.; Sun, I. W., X-Ray Photoelectron Spectroscopy and in Situ X-Ray Absorption Spectroscopy Studies on Reversible Insertion/Desertion of Dicyanamide Anions into/from Manganese Oxide in Ionic Liquid. *Chem. Mater.* **2009,** *21* (13), 2688-2695.
58. Castro Ruiz, C. A.; Bélanger, D.; Rochefort, D., Electrochemical and Spectroelectrochemical Evidence of Redox Transitions Involving Protons in Thin MnO_2 Electrodes in Protic Ionic Liquids. *J. Phys. Chem. C* **2013,** *117* (40), 20397-20405.
59. Qu, Q.; Zhang, P.; Wang, B.; Chen, Y.; Tian, S.; Wu, Y.; Holze, R., Electrochemical Performance of MnO_2 Nanorods in Neutral Aqueous Electrolytes as a Cathode for Asymmetric Supercapacitors. *J. Phys. Chem. C* **2009,** *113* (31), 14020-14027.
60. Long, J. W.; Belanger, D.; Brousse, T.; Sugimoto, W.; Sassin, M. B.; Crosnier, O., Asymmetric Electrochemical Capacitors-Stretching the Limits of Aqueous Electrolytes. *MRS Bull.* **2011,** *36* (7), 513-522.
61. Wang, C.; Ma, J.; Liu, F.; He, H.; Zhang, R., The Effects of Mn^{2+} Precursors on the Structure and Ozone Decomposition Activity of Cryptomelane-Type Manganese Oxide (OMS-2) Catalysts. *J. of Phys. Chem. C* **2015,** *119* (40), 23119-23126.
62. Cheng, F.; Zhang, T.; Zhang, Y.; Du, J.; Han, X.; Chen, J., Enhancing Electrocatalytic Oxygen Reduction on MnO_2 with Vacancies. *Angew. Chem. Int. Ed.* **2013,** *52* (9), 2474-2477.
63. Biswas, S.; Dutta, B.; Mullick, K.; Kuo, C.-H.; Poyraz, A. S.; Suib, S. L., Aerobic Oxidation of Amines to Imines by Cesium-Promoted Mesoporous Manganese Oxide. *ACS Catal.* **2015,** *5* (7), 4394-4403.
64. Yang, Y.; Zhang, S.; Wang, S.; Zhang, K.; Wang, H.; Huang, J.; Deng, S.; Wang, B.; Wang, Y.; Yu, G., Ball Milling Synthesized MnO_x as Highly Active Catalyst for Gaseous Pops Removal: Significance of Mechanochemically Induced Oxygen Vacancies. *Environ. Sci. Technol.* **2015,** *49* (7), 4473-4480.
65. Hou, J.; Li, Y.; Mao, M.; Ren, L.; Zhao, X., Tremendous Effect of the Morphology of Birnessite-Type Manganese Oxide Nanostructures on Catalytic Activity. *ACS Appl. Mater. Interfaces* **2014,** *6* (17), 14981-14987.

66. Genuino, H. C.; Dharmarathna, S.; Njagi, E. C.; Mei, M. C.; Suib, S. L., Gas-Phase Total Oxidation of Benzene, Toluene, Ethylbenzene, and Xylenes Using Shape-Selective Manganese Oxide and Copper Manganese Oxide Catalysts. *J. Phys. Chem. C* **2012,** *116* (22), 12066-12078.
67. Qiu, G.; Huang, H.; Dharmarathna, S.; Benbow, E.; Stafford, L.; Suib, S. L., Hydrothermal Synthesis of Manganese Oxide Nanomaterials and Their Catalytic and Electrochemical Properties. *Chem. Mater.* **2011,** *23* (17), 3892-3901.
68. Li, X.; Liu, J.; Zhao, Y.; Zhang, H.; Du, F.; Lin, C.; Zhao, T.; Sun, Y., Significance of Surface Trivalent Manganese in the Electrocatalytic Activity of Water Oxidation in Undoped and Doped MnO_2 Nanowires. *ChemCatChem* **2015,** *7* (12), 1848-1856.
69. Delgado, D.; Minakshi, M.; McGinnity, J.; Kim, D.-J., Co/Mo Bimetallic Addition to Electrolytic Manganese Dioxide for Oxygen Generation in Acid Medium. *Sci. Rep.* **2015,** *5*, 15208.
70. Huang, Z.; Zhang, M.; Cheng, J.; Gong, Y.; Li, X.; Chi, B.; Pu, J.; Jian, L., Silver Decorated Beta-Manganese Oxide Nanorods as an Effective Cathode Electrocatalyst for Rechargeable Lithium–Oxygen Battery. *J. Alloys Compd.* **2015,** *626*, 173-179.
71. Li, P.-C.; Hu, C.-C.; Noda, H.; Habazaki, H., Synthesis and Characterization of Carbon Black/Manganese Oxide Air Cathodes for Zinc–Air Batteries: Effects of the Crystalline Structure of Manganese Oxides. *J. Power Sources* **2015,** *298*, 102-113.
72. Tompsett, D. A.; Parker, S. C.; Islam, M. S., Rutile (B-)MnO_2 Surfaces and Vacancy Formation for High Electrochemical and Catalytic Performance. *J. Am. Chem. Soc.* **2014,** *136* (4), 1418-1426.
73. Ma, Y.; Wang, R.; Wang, H.; Key, J.; Ji, S., Control of MnO_2 Nanocrystal Shape from Tremella to Nanobelt for Ehancement of the Oxygen Reduction Reaction Activity. *J. Power Sources* **2015,** *280*, 526-532.
74. He, Y.; Huang, W.; Liang, Y.; Yu, H., A Low-Cost and Label-Free Assay for Hydrazine Using MnO_2 Nanosheets as Colorimetric Probes. *Sens. Actuators, B* **2015,** *220*, 927-931.
75. Wang, M.; Wang, C.; Wang, G.; Zhang, W.; Bin, F., Synthesis of MnO_2/MWNTs Nanocomposites Using a Sonochemical Method and Application for Hydrazine Detection. *Electroanalysis* **2010,** *22* (10), 1123-1129.
76. Yamaguchi, R.; Sato, A.; Iwai, S.; Tomono, K.; Nakayama, M., A Novel Formaldehyde Sensor Based on the Pseudocapacitive Catalysis of Birnessite. *Electrochem. Commun.* **2013,** *29* (0), 55-58.
77. Tang, J.; Jin, B., A Voltammetric Sensor Based on Multi-Walled Carbon Nanotube-MnO_2 Nanowire Composite Film for Simultaneous Determination of Hydroquinone and Catechol. *Anal. Methods* **2015,** *7* (21), 9218-9225.
78. Lou, J.; Wang, W.; Yan, L.; Ruan, C.; Sun, X.; Sun, W.; Li, P., Sensitive Electrochemical Detection of Bisphenol a with Chitosan and Urchinlike MnO_2 Microsphere Modified Carbon Ionic Liquid Electrode. *Int. J. Environ. Anal. Chem.* **2015,** *95* (10), 911-921.
79. Beyene, N. W.; Kotzian, P.; Schachl, K.; Alemu, H.; Turkušić, E.; Čopra, A.; Moderegger, H.; Švancara, I.; Vytřas, K.; Kalcher, K., (Bio)Sensors Based on Manganese Dioxide-Modified Carbon Substrates: Retrospections, Further Improvements and Applications. *Talanta* **2004,** *64* (5), 1151-1159.
80. Šljukić, B.; Compton, R. G., Manganese Dioxide Graphite Composite Electrodes Formed Via a Low Temperature Method: Detection of Hydrogen Peroxide, Ascorbic Acid and Nitrite. *Electroanalysis* **2007,** *19* (12), 1275-1280.
81. Zhang, Y.; Su, M.; Ge, L.; Ge, S.; Yu, J.; Song, X., Synthesis and Characterization of Graphene Nanosheets Attached to Spiky MnO_2 Nanospheres and Its Application in Ultrasensitive Immunoassay. *Carbon* **2013,** *57*, 22-33.
82. Wang, A.-J.; Zhang, P.-P.; Li, Y.-F.; Feng, J.-J.; Dong, W.-J.; Liu, X.-Y., Hydrogen Peroxide Sensor Based on Glassy Carbon Electrode Modified with B-Manganese Dioxide Nanorods. *Microchim Acta* **2011,** *175* (1-2), 31-37.
83. Hocevar, S. B.; Ogorevc, B.; Schachl, K.; Kalcher, K., Glucose Microbiosensor Based on MnO_2 and Glucose Oxidase Modified Carbon Fiber Microelectrode. *Electroanalysis* **2004,** *16* (20), 1711-1716.

84. Wang, Y.; Liu, Y.; Zhitomirsky, I., Surface Modification of MnO_2 and Carbon Nanotubes Using Organic Dyes for Nanotechnology of Electrochemical Supercapacitors. *J. Mater. Chem. A* **2013,** *1* (40), 12519-12526.
85. Ye, Q.; Zhou, F.; Liu, W., Bioinspired Catecholic Chemistry for Surface Modification. *Chem. Soc. Rev.* **2011,** *40* (7), 4244-4258.
86. Li, S.-C.; Wang, J.-g.; Jacobson, P.; Gong, X. Q.; Selloni, A.; Diebold, U., Correlation between Bonding Geometry and Band Gap States at Organic−Inorganic Interfaces: Catechol on Rutile TiO_2(110). *J. Am. Chem. Soc.* **2009,** *131* (3), 980-984.
87. Ata, M. S.; Liu, Y.; Zhitomirsky, I., A Review of New Methods of Surface Chemical Modification, Dispersion and Electrophoretic Deposition of Metal Oxide Particles. *RSC Adv.* **2014,** *4* (43), 22716-22732.
88. Chong, W.; Yang, Z.; Lingxia, W.; Yuanyuan, L.; Jinping, L., High-Voltage and High-Rate Symmetric Supercapacitor Based on MnO_2-Polypyrrole Hybrid Nanofilm. *Nanotechnology* **2014,** *25* (30), 305401.
89. Bahloul, A.; Nessark, B.; Briot, E.; Groult, H.; Mauger, A.; Zaghib, K.; Julien, C. M., Polypyrrole-Covered MnO_2 as Electrode Material for Supercapacitor. *J. Power Sources* **2013,** *240*, 267-272.
90. Jaidev; Jafri, R. I.; Mishra, A. K.; Ramaprabhu, S., Polyaniline/MnO_2 Nanotube Hybrid Nanocomposite as Supercapacitor Electrode Material in Acidic Electrolyte. *J. Mater. Chem.* **2011,** *21* (44), 17601-17605.
91. Maldonado, S.; Smith, T. J.; Williams, R. D.; Morin, S.; Barton, E.; Stevenson, K. J., Surface Modification of Indium Tin Oxide Via Electrochemical Reduction of Aryldiazonium Cations. *Langmuir* **2006,** *22* (6), 2884-2891.
92. Tanguy, F.; Gaubicher, J.; Gaillot, A.-C.; Guyomard, D.; Pinson, J., Lowering Interfacial Chemical Reactivity of Oxide Materials for Lithium Batteries. A Molecular Grafting Approach. *J. Mater. Chem.* **2009,** *19* (27), 4771-4777.
93. Griffete, N.; Ahmad, R.; Benmehdi, H.; Lamouri, A.; Decorse, P.; Mangeney, C., Elaboration of Hybrid Silica Particles Using a Diazonium Salt Chemistry Approach. *Colloid Surf., A* **2013,** *439* (0), 145-150.
94. Drevet, R.; Legros, C.; Berardan, D.; Ribot, P.; Chaussé, A.; Andrieux, M., Nanocrystallized SnO_2 Thin Films Deposited on Si and $LaAlO_3$ Substrates by Pulsed-MOCVD Technique for Electrochemical Applications. *Surf. Coat. Technol.* **2013,** *230* (0), 180-185.
95. Griffete, N. b. w.; Herbst, F. d. r.; Pinson, J.; Ammar, S.; Mangeney, C., Preparation of Water-Soluble Magnetic Nanocrystals Using Aryl Diazonium Salt Chemistry. *J. Am. Chem. Soc.* **2011,** *133* (6), 1646-1649.
96. Mesnage, A.; Abdel Magied, M.; Simon, P.; Herlin-Boime, N.; Jégou, P.; Deniau, G.; Palacin, S., Grafting Polymers to Titania Nanoparticles by Radical Polymerization Initiated by Diazonium Salt. *J. Mater. Sci.* **2011,** *46* (19), 6332-6338.
97. Dechézelles, J.-F.; Griffete, N.; Dietsch, H.; Scheffold, F., A General Method to Label Metal Oxide Particles with Fluorescent Dyes Using Aryldiazonium Salts. *Part. Part. Syst. Char.* **2013,** *30* (7), 579-583.
98. Hurley, B. L.; McCreery, R. L., Covalent Bonding of Organic Molecules to Cu and Al Alloy 2024 T3 Surfaces Via Diazonium Ion Reduction. *J. Electrochem. Soc.* **2004,** *151* (5), B252-B259.
99. Hinge, M.; Ceccato, M.; Kingshott, P.; Besenbacher, F.; Pedersen, S. U.; Daasbjerg, K., Electrochemical Modification of Chromium Surfaces Using 4-Nitro- and 4-Fluorobenzenediazonium Salts. *New J. Chem.* **2009,** *33* (12), 2405-2408.
100. Ramirez-Castro, C.; Crosnier, O.; Athouël, L.; Retoux, R.; Bélanger, D.; Brousse, T., Electrochemical Performance of Carbon/MnO_2 Nanocomposites Prepared Via Molecular Bridging as Supercapacitor Electrode Materials. *J. Electrochem. Soc.* **2015,** *162* (5), A5179-A5184.
101. Bell, K. J.; Brooksby, P. A.; Polson, M. I. J.; Downard, A. J., Evidence for Covalent Bonding of Aryl Groups to MnO_2 Nanorods from Diazonium-Based Grafting. *Chem. Commun.* **2014,** *50* (89), 13687-13690.

102. Dose, W. M.; Donne, S. W., Manganese Dioxide Structural Effects on Its Thermal Decomposition. *Mater. Sci. Eng., B* **2011,** *176* (15), 1169-1177.
103. Vogel, A. I., Vogel's Textbook of Quantitative Chemical Analysis. 5th ed. / ed.; Jeffery, G. H.; Vogel, A. I., Eds. Longman Scientific & Technical ; Harlow, Essex, England :, 1989.
104. Oku, M.; Hirokawa, K.; Ikeda, S., X-Ray Photoelectron Spectroscopy of Manganese—Oxygen Systems. *J. Electron. Spectrosc. Relat. Phenom.* **1975,** *7* (5), 465-473.
105. Athouel, L.; Moser, F.; Dugas, R.; Crosnier, O.; Belanger, D.; Brousse, T., Variation of the MnO_2 Birnessite Structure Upon Charge/Discharge in an Electrochemical Supercapacitor Electrode in Aqueous Na_2so_4 Electrolyte. *J. Phys. Chem. C* **2008,** *112* (18), 7270-7277.
106. Wei, W.; Cui, X.; Chen, W.; Ivey, D. G., Improved Electrochemical Impedance Response Induced by Morphological and Structural Evolution in Nanocrystalline MnO_2 Electrodes. *Electrochim. Acta* **2009,** *54* (8), 2271-2275.
107. Guillemet, P.; Brousse, T.; Crosnier, O.; Dandeville, Y.; Athouel, L.; Scudeller, Y., Modeling Pseudo Capacitance of Manganese Dioxide. *Electrochim. Acta* **2012,** *67* (0), 41-49.
108. Toupin, M.; Brousse, T.; Bélanger, D., Influence of Microstucture on the Charge Storage Properties of Chemically Synthesized Manganese Dioxide. *Chem. Mater.* **2002,** *14* (9), 3946-3952.
109. Hu, C.-C.; Tsou, T.-W., Ideal Capacitive Behavior of Hydrous Manganese Oxide Prepared by Anodic Deposition. *Electrochem. Commun.* **2002,** *4* (2), 105-109.
110. Zolfaghari, A.; Naderi, H. R.; Mortaheb, H. R., Carbon Black/Manganese Dioxide Composites Synthesized by Sonochemistry Method for Electrochemical Supercapacitors. *J. Electroanal. Chem.* **2013,** *697* (0), 60-67.
111. Xu, C.; Wei, C.; Li, B.; Kang, F.; Guan, Z., Charge Storage Mechanism of Manganese Dioxide for Capacitor Application: Effect of the Mild Electrolytes Containing Alkaline and Alkaline-Earth Metal Cations. *J. Power Sources* **2011,** *196* (18), 7854-7859.
112. Podvorica, F. I.; Kanoufi, F.; Pinson, J.; Combellas, C., Spontaneous Grafting of Diazoates on Metals. *Electrochim. Acta* **2009,** *54* (8), 2164-2170.
113. Simons, B. M.; Lehr, J.; Garrett, D. J.; Downard, A. J., Formation of Thick Aminophenyl Films from Aminobenzenediazonium Ion in the Absence of a Reduction Source. *Langmuir* **2014,** *30* (17), 4989-4996.
114. Brooksby, P. A.; Downard, A. J., Electrochemical and Atomic Force Microscopy Study of Carbon Surface Modification Via Diazonium Reduction in Aqueous and Acetonitrile Solutions. *Langmuir* **2004,** *20* (12), 5038-5045.
115. Toupin, M.; Bélanger, D., Thermal Stability Study of Aryl Modified Carbon Black by in Situ Generated Diazonium Salt. *J. Phys. Chem. C* **2007,** *111* (14), 5394-5401.
116. Lyskawa, J.; Grondein, A.; Bélanger, D., Chemical Modifications of Carbon Powders with Aminophenyl and Cyanophenyl Groups and a Study of Their Reactivity. *Carbon* **2010,** *48* (4), 1271-1278.
117. Ni, W.; Wang, D.; Huang, Z.; Zhao, J.; Cui, G., Fabrication of Nanocomposite Electrode with Mno_2 Nanoparticles Distributed in Polyaniline for Electrochemical Capacitors. *Mater. Chem. Phys.* **2010,** *124* (2–3), 1151-1154.
118. Brymora, K.; Fouineau, J.; Eddarir, A.; Chau, F.; Yaacoub, N.; Grenèche, J.-M.; Pinson, J.; Ammar, S.; Calvayrac, F., Grafting of Diazonium Salts on Oxides Surface: Formation of Aryl-O Bonds on Iron Oxide Nanoparticles. *J. Nanopart. Res.* **2015,** *17* (11), 1-9.
119. Nesbitt, H. W.; Banerjee, D., Interpretation of XPS Mn(2p) Spectra of Mn Oxyhydroxides and Constraints on the Mechanism of MnO_2 Precipitation. *Am. Mineral.* **1998,** *83* (3-4), 305-315.
120. Gupta, R. P.; Sen, S. K., Calculation of Multiplet Structure of Core P-Vacancy Levels. *Phys. Rev. B* **1974,** *10* (1), 71-77.
121. Gupta, R. P.; Sen, S. K., Calculation of Multiplet Structure of Core P -Vacancy Levels. Ii. *Phys. Rev. B* **1975,** *12* (1), 15-19.
122. Toupin, M.; Belanger, D., Spontaneous Functionalization of Carbon Black by Reaction with 4-Nitrophenyldiazonium Cations. *Langmuir* **2008,** *24* (5), 1910-1917.

123. Miller, D. J.; Biesinger, M. C.; McIntyre, N. S., Interactions of CO_2 and CO at Fractional Atmosphere Pressures with Iron and Iron Oxide Surfaces: One Possible Mechanism for Surface Contamination? *Surf. Interface Anal.* **2002,** *33* (4), 299-305.
124. Roodenko, K.; Gensch, M.; Rappich, J.; Hinrichs, K.; Esser, N.; Hunger, R., Time-Resolved Synchrotron XPS Monitoring of Irradiation-Induced Nitrobenzene Reduction for Chemical Lithography. *J. Phys. Chem. B* **2007,** *111* (26), 7541-7549.
125. Biniak, S.; Szymański, G.; Siedlewski, J.; Świątkowski, A., The Characterization of Activated Carbons with Oxygen and Nitrogen Surface Groups. *Carbon* **1997,** *35* (12), 1799-1810.
126. Pantea, D.; Darmstadt, H.; Kaliaguine, S.; Roy, C., Heat-Treatment of Carbon Blacks Obtained by Pyrolysis of Used Tires. Effect on the Surface Chemistry, Porosity and Electrical Conductivity. *J. Anal. Appl. Pyrolysis* **2003,** *67* (1), 55-76.
127. Richard, W.; Evrard, D.; Gros, P., New Insight into 4-Nitrobenzene Diazonium Reduction Process: Evidence for a Grafting Step Distinct from NO_2 Electrochemical Reactivity. *J. Electroanal. Chem.* **2012,** *685* (0), 109-115.
128. Combellas, C.; Delamar, M.; Kanoufi, F.; Pinson, J.; Podvorica, F. I., Spontaneous Grafting of Iron Surfaces by Reduction of Aryldiazonium Salts in Acidic or Neutral Aqueous Solution. Application to the Protection of Iron against Corrosion. *Chem. Mater.* **2005,** *17* (15), 3968-3975.
129. Lee, L. Modification of Glassy Carbon Electrodes with Diazonium Cation Terminated Films: “Sticky Surfaces”. Masters Thesis, University of Canterbury, Christchurch, New Zealand, 2011.
130. Fic, K.; Lota, G.; Meller, M.; Frackowiak, E., Novel Insight into Neutral Medium as Electrolyte for High-Voltage Supercapacitors. *Energy Environ. Sci.* **2012,** *5* (2), 5842-5850.
131. Grondein, A.; Bélanger, D., Chemical Modification of Carbon Powders with Aminophenyl and Aryl-Aliphatic Amine Groups by Reduction of in Situ Generated Diazonium Cations: Applicability of the Grafted Powder Towards CO_2 Capture. *Fuel* **2011,** *90* (8), 2684-2693.

5 Electrochemical Investigations of Electrodeposited MnO_2 Films Modified with Aryldiazonium Ions

5.1 Introduction

As described previously in Chapter 4, one of the primary applications of MnO_2 is as an electrochemical energy storage material due to its pseudocapacitance properties.[1] As the goal of surface modification of MnO_2 is to enhance the performance and stability of the electrode, the effect of modification on the electrochemical behaviour of MnO_2 must be determined. Although the successful modification of MnO_2 nanoparticles by aryldiazonium ions was demonstrated previously in Chapter 4, the effect of modification on the electrochemical properties of MnO_2 could not be determined due to the difficulty of preparing reproducible nanoparticle electrodes. To overcome this, the effect of modification on MnO_2 was investigated using electrochemically-deposited MnO_2 films on GC electrodes. As no further preparation steps were required before the use of the surfaces as electrodes, this enables direct comparison of the electrochemical performance of the same MnO_2 layers before and after modification with aryldiazonium ions.

In this chapter, the preparation and characterisation of electrochemically-deposited MnO_2 on GC disc electrodes, and subsequent modification in aqueous solutions with aryldiazonium ions is described. The effect of pH and modifier on capacitance and stability of the electrode surface is examined by CV experiments. Electrochemical impedance spectroscopy (EIS) was used to study the effect of modification on the frequency response of MnO_2 electrodes. The origin of these effects is investigated by the development of equivalent circuit models for the modified electrodes.

5.2 Experimental Methods

5.2.1 Electrodeposition

Electrodeposited MnO_2 films were prepared on carbon substrates potentiostatically or galvanostatically according to the overall process described in Equation 4.3:

$$Mn^{2+} + 2H_2O \rightarrow MnO_2 + 4H^+ + 2e^- \qquad \text{Equation 5.1}$$

5.2.1.1 Potentiostatic deposition

Potentiostatic electrodeposition was carried out based on conditions developed by Cross et al.[2] at 1.1 V for 12 s in 0.1 M $MnSO_4$/0.1 M H_2SO_4 solution onto polished GC electrodes (plates and discs) in

a three electrode cell setup (SCE reference electrode, Pt mesh counter electrode). The solution was sparged with $O_{2(g)}$ before deposition and maintained under $O_{2(g)}$ atmosphere during the deposition reaction. After deposition, the electrodes were rinsed with ultrapure water and dried under N_2 gas. The mass of the MnO_2 deposit was estimated by integrating the *i* vs. *t* curve to determine the charge passed, assuming all charge transfer results in MnO_2 deposition.[2] The transferred charge was then converted into the mass of MnO_2 (m_{MnO2}) by Equation 5.2 where *q* is the charge transferred in Coulombs, M_{MnO2} is the molar mass of MnO_2 (86.94 g mol^{-1}) and *F* is the Faraday constant.

$$m_{MnO2} = q \times \frac{M_{MnO2}}{2F}$$ Equation 5.2

5.2.1.2 Galvanostatic Deposition

The cell setup and electrolyte for galvanostatic electrodeposition of MnO_2 films were the same as for potentiostatic deposition but the deposition procedure was carried out galvanostatically at 0.2 mA with the deposition time adjusted to replicate the charge density from the potentiostatic experiments (33.9 mC cm^{-2}). The mass of MnO_2 deposited was determined as above using the value of charge transferred.

5.2.2 SEM

SEM of electrodeposited films was conducted on samples electrodeposited onto the top face of GC plate substrates with the conducting path to the SEM stage through the thickness of the sample.

5.2.3 Electrochemical Analysis

For electrochemical analysis, the electrodeposited MnO_2 films were used still attached to the GC electrodes used in the deposition process as the working electrode. General electrochemical experiments were conducted using the standard methods and equipment described in Chapter 2, however, extended stability studies were conducted using a Princeton Applied Research Model 362 Scanning Potentiostat connected to an ADInstruments Powerlab 4SP analogue-to-digital converter controlled by eDAQ EChem version 2.1.5 software.

EIS experiments were conducted using the same cell setup and instrumentation as for general CV experiments. EIS measurements were carried out potentiostatically at 0.4 V in 0.5 M Na_2SO_4 with a 10 mV amplitude and 100 kHz - 0.1 Hz frequency range. Analysis of EIS data was conducted in

Autolab NOVA versions 1.9-1.11. Equivalent circuits were fitted to the experimental data with the built-in Fit and Simulation tool.

5.2.4 Profilometry

Profilometry experiments were conducted by scratching away areas of the MnO_2 film with a scalpel and line profiling across the scratched areas at multiple points with a Dektak 150 Surface Profilometer. The resulting line profiles were then analysed using Gwyddion image analysis software to determine the step height from the MnO_2 film to the substrate.

5.2.5 XRD

Samples for powder XRD were prepared by potentiostatically depositing MnO_2 onto a Pt sheet working electrode (geometric area = 2.5 cm^2). The electrode was rinsed in ultrapure water and dried with N_2 gas before the deposited material was removed with a scalpel blade to give a dry powder.

5.2.6 Modification of MnO_2 Films by Aryldiazonium Ions

MnO_2-coated carbon substrates were modified by immersion in 50 mM aryldiazonium salt solutions in 0.1 M buffer (pH 8 and pH 10) for a range of reaction times (15 min, 30 min and 1 hour) with stirring. The modified MnO_2 surfaces were rinsed with ultrapure water and acetone before use in further experiments.

5.3 Results & Discussion

5.3.1 Potentiostatic Electrodeposition

MnO_2 films were initially prepared on GC electrodes by potentiostatic electrodeposition from 0.1 M $MnSO_4$/0.1M H_2SO_4 solutions for 12 s at 1.1 V. This process was monitored by chronoamperometry and a typical deposition curve is shown in Figure 5.1. The sharp rise in the current followed by a steady decline arises due to the Mn^{2+} ions at the surface of the electrode being rapidly consumed before being replenished by diffusion processes.[3] A short deposition time was chosen in order to minimise the thickness of the deposited film and thus maximise the surface area to volume ratio of the MnO_2 layer to better detect changes after modification with aryldiazonium ions. It was found that sparging the deposition solution with $O_{2(g)}$ and maintaining an $O_{2(g)}$ atmosphere above the solution during deposition improved the uniformity of the MnO_2 films. The mass of MnO_2 deposited was estimated by integrating the *i* vs. *t* curve and potentiostatic deposition was found to give deposits with an average mass of 1.3 ± 0.2 µg (n = 20) on a 3 mm diameter GC disk electrode. As this method assumes all the charge transferred during the deposition process is

associated with the deposition reaction itself, it most likely overestimates the mass of the MnO_2 deposit as side reactions (such as oxidation of the GC electrode) may occur during deposition.

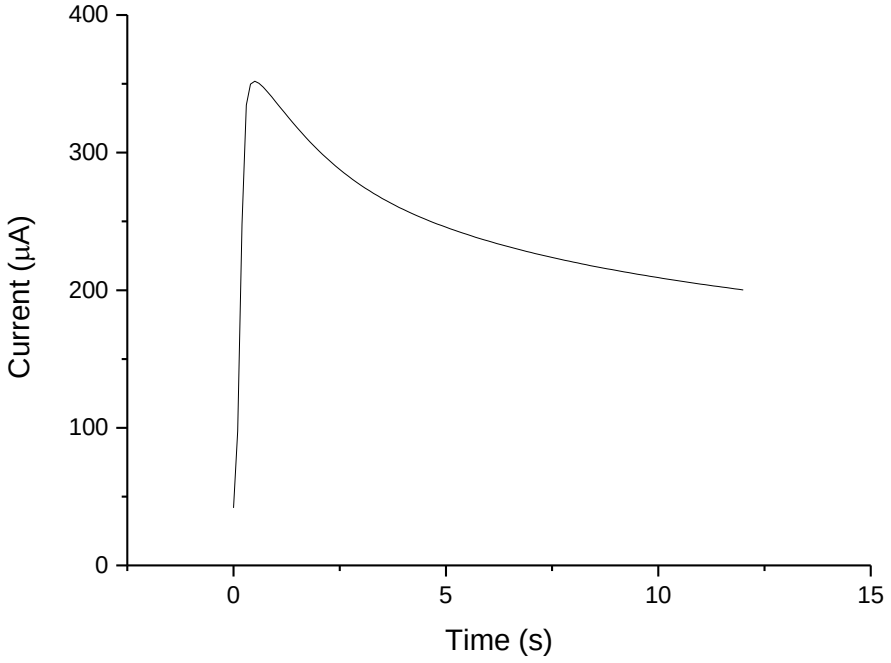

Figure 5.1: Chronoamperometric curve of MnO_2 electrodeposition on a GC disc electrode in 0.1 M $MnSO_4/H_2SO_4$ at 1.1 V.

5.3.1.1 Characterisation

The morphology and film thickness were examined by SEM imaging and profilometry respectively. SEM imaging of MnO_2 films deposited on GC plates (Figure 5.2A) shows that these surfaces have a porous structure comprised of randomly-oriented interconnected ~20 nm thick flakes. This type of structure has been observed previously for electrodeposited MnO_2.[4, 5] Coverage of the deposited area was uniform with only ~50 nm pinholes visible, apart from at the extreme edges where deposition most likely occurs by leakage under the edge of the o-ring and thus under constrained diffusion. The thickness of the MnO_2 layer was measured by scratching away areas of the film with a scalpel and line profiling across the scratch with a profilometer (an example profile is shown in Figure 5.2B). The average film thickness for potentiostatically deposited MnO_2 was 47 ± 8 nm (n = 7) indicating that the deposition process gives thin films with variability in thickness comparable to the variation in the charge transferred during the deposition process (± 17% c.f. ± 15% respectively). The crystal structure of potentiostatically electrodeposited MnO_2 was investigated by XRD using a powder sample collected from a Pt electrode after deposition. As can be seen from Figure 5.2C, the

XRD pattern for this material is very noisy and has few visible peaks, indicating that the material is primarily amorphous.

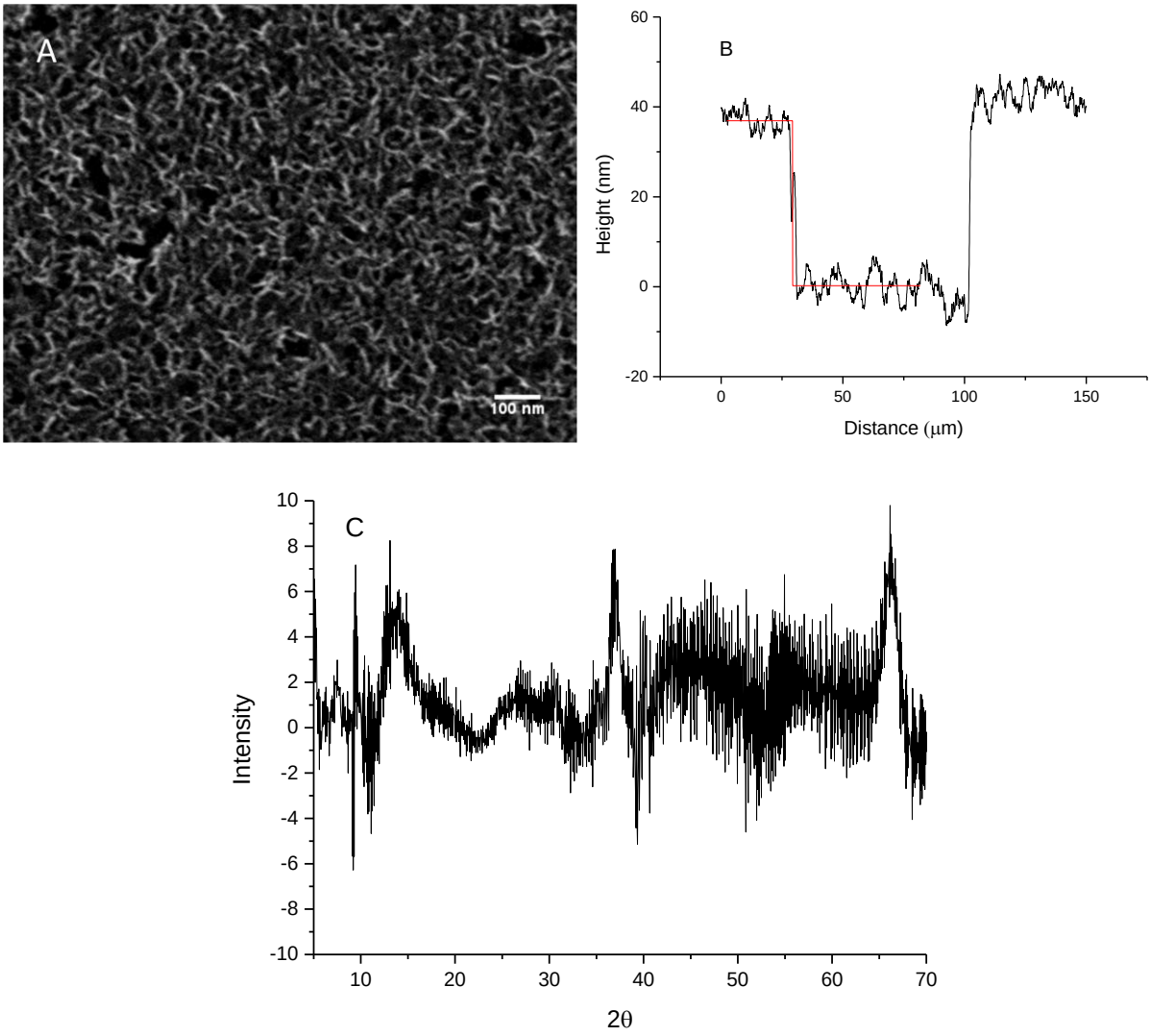

Figure 5.2: A. SEM image of potentiostatically deposited MnO_2 on GC. B. Example line profile across potentiostatically deposited MnO_2 with fitted step height measurement (red line). C. XRD pattern of potentiostatically electrodeposited MnO_2

The electrochemical behaviour of the electrodeposited MnO_2 surfaces on GC was investigated by CV in 0.5 M Na_2SO_4 at various scan rates (Figure 5.3) between 0 and 0.8 V (a commonly-used potential window for MnO_2 electrodes).[2, 6] At 5 mV s^{-1} (Figure 5.3a), the voltammogram deviates significantly from the symmetric quasi-rectangular response that is expected for a pseudocapacitor. The electrochemical response is dominated by an oxidation process starting at ~0.7 V that is stable over 5 scans with no apparent corresponding reduction process involving similar charge transfer. This

peak has previously been assigned to water oxidation and oxygen evolution.[7] There is also the start of a small reduction peak at ~0.15 V that may be due to the onset of Mn^{2+} formation, however, as this peak is stable over a number of scans, any dissolved Mn^{2+} may be re-deposited on cycling.[8] At 50 mV s^{-1}, the oxidation and reduction processes at the potential limits are more symmetrical and the CV curve has a more rectangular shape. When the scan rate is increased to 500 mV s^{-1}, the CV is almost perfectly rectangular, indicative of an ideal capacitor. The increasingly-ideal response at higher scan rates is most likely due to double-layer capacitance becoming dominant over pseudocapacitance mechanisms. At high scan rates, pseudocapacitance mechanisms are limited by counter-ion diffusion whereas double-layer charge storage has no such limitation. Compared to the nanoparticle electrodes prepared in Chapter 4, the electrodeposited MnO_2 electrode behaviour is more typical of an ideal capacitor, with a more level baseline and highly rectangular responses at high scan rates. These differences in response most likely arise from the shorter conduction pathways in the electrodeposited MnO_2 layer due to it being thin and highly porous lowering electrical resistance and favouring cation diffusion.

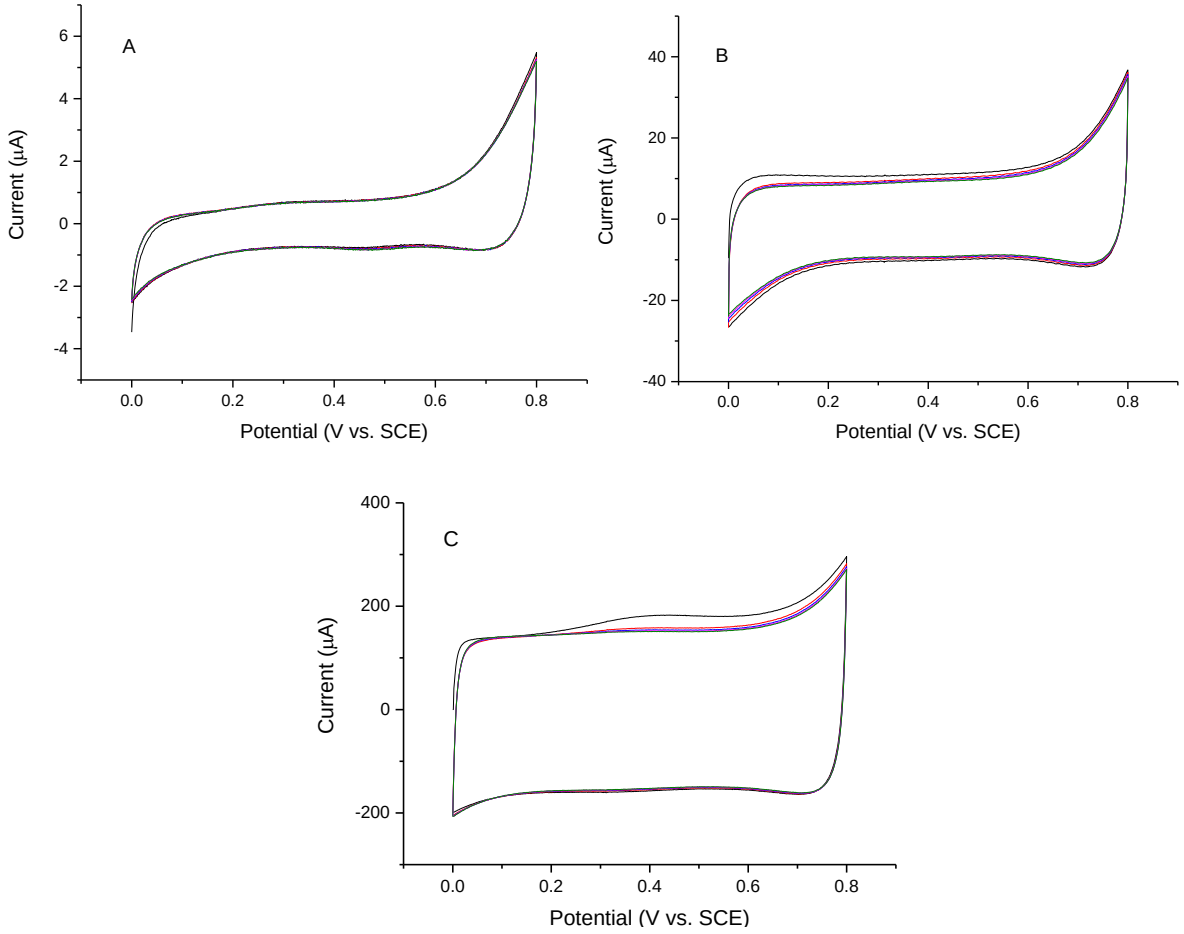

Figure 5.3: CV curves (scans 1-5) of potentiostatically deposited (1.1 V, 12 s) MnO_2 on GC in 0.5 M Na_2SO_4 at various scan rates. A. 5 mV s^{-1}, B. 50 mV s^{-1} and C. 500 mV s^{-1}.

The capacitance of the electrodeposited MnO_2 film was calculated by the method outlined in Chapter 4 at each scan rate. Specific capacitance values were found to be 200 ± 20 F g^{-1}, 170 ± 10 F g^{-1} and 237 ± 7 F g^{-1} at 5, 50 and 500 mV s^{-1} respectively (n = 12). These capacitance values are comparable to literature reports for other electrodeposited MnO_2 systems which range from 130-230 F g^{-1} depending on preparation conditions and scan rate.[4, 9, 10] There have also been reports of anomalously high specific capacitance values (>2000 F g^{-1} compared to the theoretical maximum capacitance of 1386 F g^{-1})[2] for thin electrodeposited MnO_2 films, however, this behaviour was not observed in this work. The lower capacitance at low scan rates is anomalous compared to what is understood about the charge storage mechanism in MnO_2 and literature observations on similar systems.[11, 12] As described previously, the pseudocapacitance processes in MnO_2 are limited at high rate due to their reliance on diffusion of counter-ions and thus capacitance should decrease at high scan rates. Additionally, the capacitance arising from double-layer mechanisms is typically lower than the pseudocapacitance.[13] At this time the reason for this scan rate response is unknown, however, some possibilities can be ruled out. Firstly, the oxidation peak at > 0.6 V vs. SCE is largest at 5 mV s^{-1} and almost completely absent at 500 mV s^{-1} suggesting this process may be responsible for loss of capacitance at low scan rates, for example through decomposition of the electrode. However, the measured capacitance did not vary between experiments when the order of CV scan rates was changed. This suggests a degradation process cannot be involved as the capacitance of the electrode recovers between experiments and thus a transient process is required to explain the observed behaviour. As explained earlier, the peak at high potentials is most likely the onset of $O_{2(g)}$ evolution and it is possible that the formation of gas bubbles could block areas of the electrode and thus lower its electroactive area. If these bubbles were regenerated on continued cycling at low scan rate but lost in between experiments and unable to form at high scan rates, it would explain the transient nature of the capacitance loss. Although no bubbles were observed in the solution during cycling, the nanometre-scale pores on the surface could be blocked by bubbles too small to see.

5.3.1.2 Modification of Electrodeposited MnO_2 films with Aryldiazonium Ions

In initial experiments, electrodeposited MnO_2 films were modified by immersion in stirred 50 mM NBD solution in pH 10 buffer for 1 h. After modification, the surface was rinsed in acetone and ultrapure water. The MnO_2 electrode was then cycled in 1:9 ethanol:water mixture to determine if NP-groups were present (Figure 5.4A). On the first reduction scan, there is a peak at -0.89 V that was previously observed to correspond to NP-reduction on modified MnO_2 nanoparticles (Chapter 4). The NP-reduction peak was integrated to estimate the coverage of NP-groups at the surface, giving an average value of 3.8 ± 0.8 × 10^{-9} mol cm^{-2} (n = 4), based on the geometric area of the electrode.

This is larger than the typical monolayer concentration of ~2 × 10^{-10} mol cm^{-2}, which may suggest the presence of a multilayer.[14] However, the geometric area is much lower than the actual surface area as seen in SEM imaging of the surface (Figure 5.2) and thus using the geometric area will overestimate the true coverage. To compare the effect of grafting with non-specific adsorption, freshly prepared MnO_2 electrodes were soaked in 4-nitroaniline in pH 10 buffer solution for one hour. The NP-reduction responses for these electrodes were investigated (Figure 5.4B) and the average surface coverage was calculated to be 1.9 ± 0.8 × 10^{-9} mol cm^{-2} (n = 4). Compared to the modified sample, the average surface coverage for the adsorption sample is significantly lower, indicating modification with NBD improves the retention of NP groups at the surface. However, it is assumed there is also a high proportion of material trapped within the layer for NBD-modified surfaces due to the inability to sonicate these surfaces without damaging them, making the surface coverage difficult to estimate.

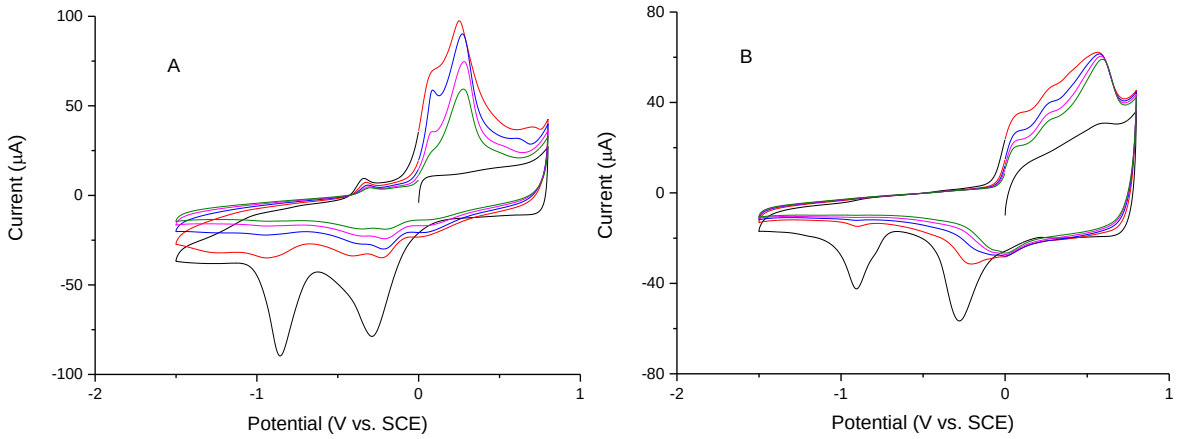

Figure 5.4: CV curves (scans 1-5) for potentiostatically deposited MnO_2 at 50 mV s^{-1} in 1:9 ethanol:water 0.1 M KCl for: A. 1 h pH 10 NP-modifed MnO_2 and B. 1 h pH 10 4-nitroaniline treated MnO_2.

The effect of modification with NP-groups on the electrochemical behaviour of electrodeposited MnO_2 was investigated at various scan rates and contrasted with blank MnO_2 surfaces treated in pH 10 buffer in the absence of aryldiazonium salt. Each surface was examined by CV at 5, 50 and 500 mV s^{-1} before and after treatment or modification (Figure 5.5). At all scan rates, treatment with pH 10 buffer causes only minor changes in the CV curves compared to the as-prepared material, confirming that the MnO_2 surfaces are stable in the modification buffer (Figure 5.5A, C and E). In contrast, NP-modification results in significant changes in the CV response of the modified surfaces. At 5 and 50 mV s^{-1}, the CV curves for the surface before and after modification are shaped identically but the area within the CV curve (scan area) increases, suggesting that the capacitance of the

electrode increases after modification (Figure 5.5B and D). However at 500 mV s^{-1}, the CV response after NP-modification deviates from ideal capacitive behaviour as there is significant curvature at the edges of the scan window (Figure 5.5F). The deviation from ideality at high scan rates indicates that the modification of the electrode is impeding the ability of the electrode to rapidly respond to changes in potential, possible due to the aryl layer impeding diffusion into the electrode by blocking access to pores.

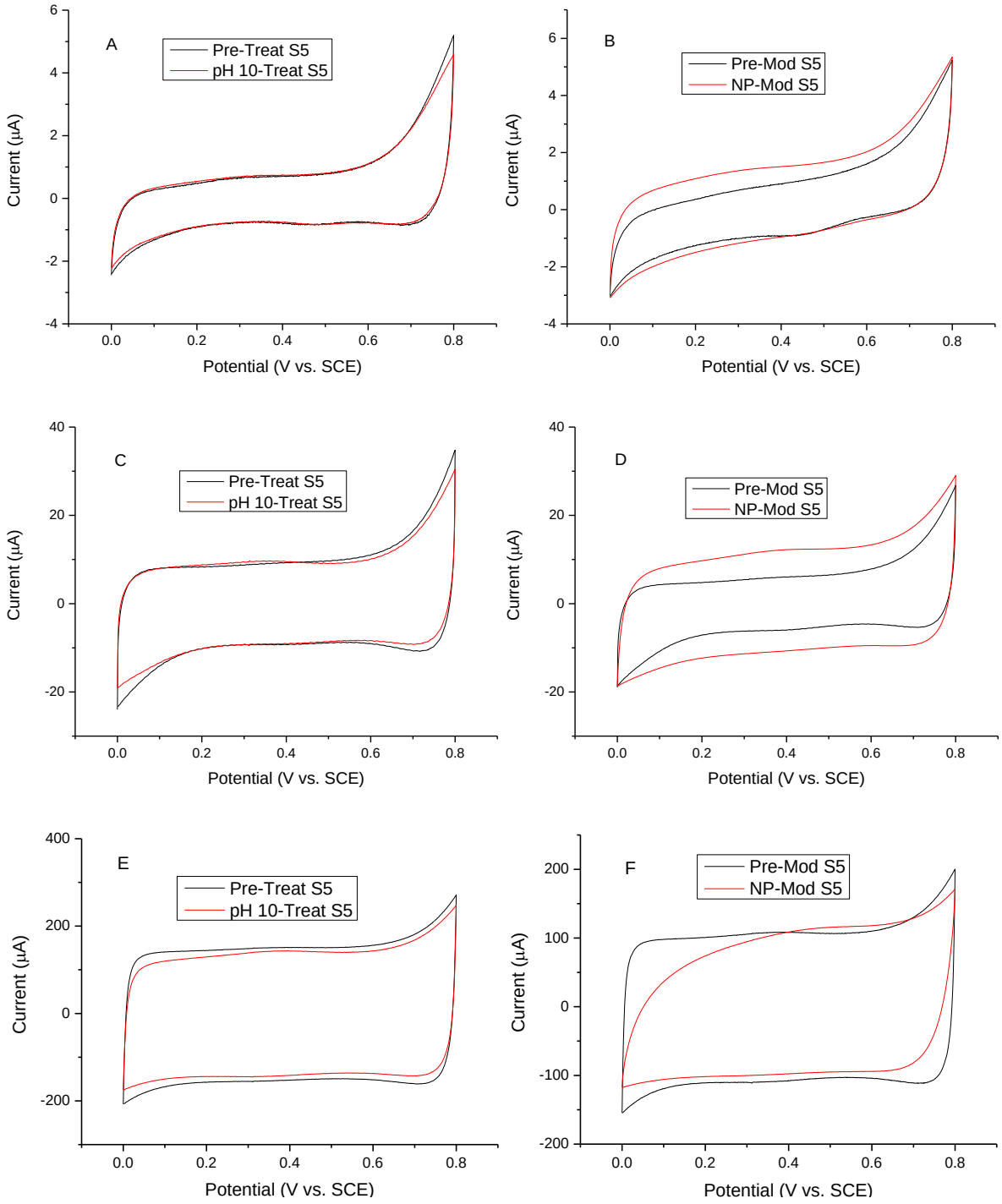

Figure 5.5: CV curves (5th scan, S5) of potentiostatically deposited MnO_2 films in 0.5 M Na_2SO_4 before (black) and after (red): 1 h pH 10 buffer treatment (A, C and E) and 1 h NP-modification (B, D and F). Scans were carried out at 5 mV s^{-1} (A and B), 50 mV s^{-1} (C and D) and 500 mV s^{-1} (E and F).

The effect of modification on capacitance was determined by integrating the 5th scan CV curves at each scan rate before and after treatment (Table 5.1). In agreement with the CV curves shown in Figure 5.5, treatment with pH 10 buffer results in only minor changes in capacitance at high scan

rates. Modification with NP-groups in pH 10 buffer results in an increase in capacitance at lower scan rates, however, the change at 5 mV s^{-1} may not be significant. As observed in the CV data (Figure 5.5D), the capacitance increase is associated with an overall increase in the charge storage across the entire scan window rather than the introduction of discrete redox processes (e.g. through reactions of the NP groups). At 500 mV s^{-1}, the capacitance decreased significantly after modification, which aligns with the observed loss of rate capability in the CV data (Figure 5.5F). Additionally, modification with NP groups resulted in an increase in the variability of the capacitance data. This variability likely arises due to the presence of competing effects arising from modification (i.e. restriction of diffusion due to film growth competes against the process that increases capacitance) and the relative influence of these effects varies between samples due to variations in the morphology of the grafted film.

Table 5.1: Capacitance data calculated from CV scans (scan 5) at various scan rates between 0 and 0.8 V in 0.5 M Na_2SO_4 on potentiostatically deposited MnO_2 before (C_{Bare}) and after (C_{Treat}) treatment in pH 10 buffer or NP-modification for 1 h.

Sample	Scan Rate (mV s^{-1})	C_{Bare} (F g^{-1})	C_{Treat} (F g^{-1})	C_{Treat}/C_{Bare}
pH 10 treat[a]	5	159 ± 9	170 ±20	1.03 ± 0.05
	50	180 ± 10	170 ±10	0.93 ± 0.03
	500	237.8 ± 0.9	221 ±3	0.93 ± 0.01
NP-Mod[b]	5	200 ± 20	240 ±40	1.2 ± 0.2
	50	160 ± 10	220 ±20	1.3 ± 0.2
	500	228 ± 8	190 ±20	0.8 ± 0.1

[a] n = 4, [b] n = 8

The cause of the observed increase in capacitance was not readily apparent and thus the effect of modification conditions and modifier was investigated. For these experiments, MnO_2 films were prepared by galvanostatic electrodeposition (Figure 5.6A) as this method more reliably produced stable films. The parameters (deposition current and time) were selected to give the same total charge transfer as the potentiostatic method (33.9 mC cm^{-2}). Galvanostatically prepared MnO_2 had identical CV response to the poteniostatic films (Figure 5.6B) and gave comparable film thickness values measured by profilometry (45 ± 3 nm and 47 ± 8 nm for galvanostatic and potentiostatic deposition respectively).

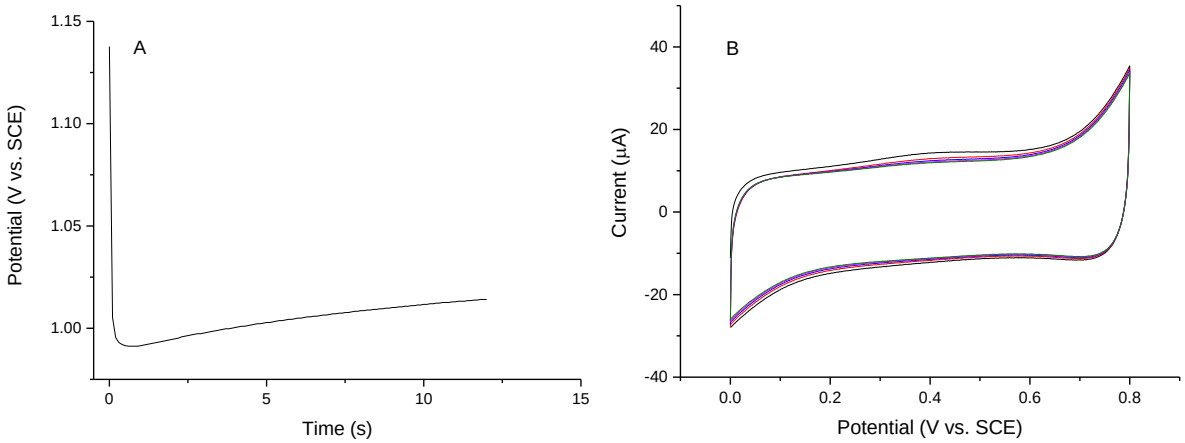

Figure 5.6: A. Galvanostatic MnO_2 electrodeposition curve on GC in 0.1 M $MnSO_4/H_2SO_4$ at 0.2 mA. B. CV curves (scans 1-5) of galvanostatically deposited MnO_2 on GC in 0.5 M Na_2SO_4 at 50 mV s^{-1}.

The effect of modification time on the electrochemical behaviour of galvanostatically deposited MnO_2 films was investigated by modifying surfaces in NBD pH 10 buffer solution for 15 min and 1 h. CV curves of the MnO_2 surfaces before and after modification are shown in Figure 5.7. Both modification times resulted in an increase in scan area after modification and minimal apparent change in the ability of the electrode to cycle at 50 mV s^{-1}. This indicates that the capacitance enhancement effect relies on a process that occurs rapidly in these reaction conditions. At 500 mV s^{-1}, modification results in a decrease in scan area and switching ability regardless of reaction time, however, this is particularly magnified for the 1 h modification reaction. Becoming more pronounced at longer reaction times (where aryl film thickness would be expected to be highest) confirms that the decline in performance at high scan rates is most likely due to the aryl film impeding diffusion to areas of the surface.

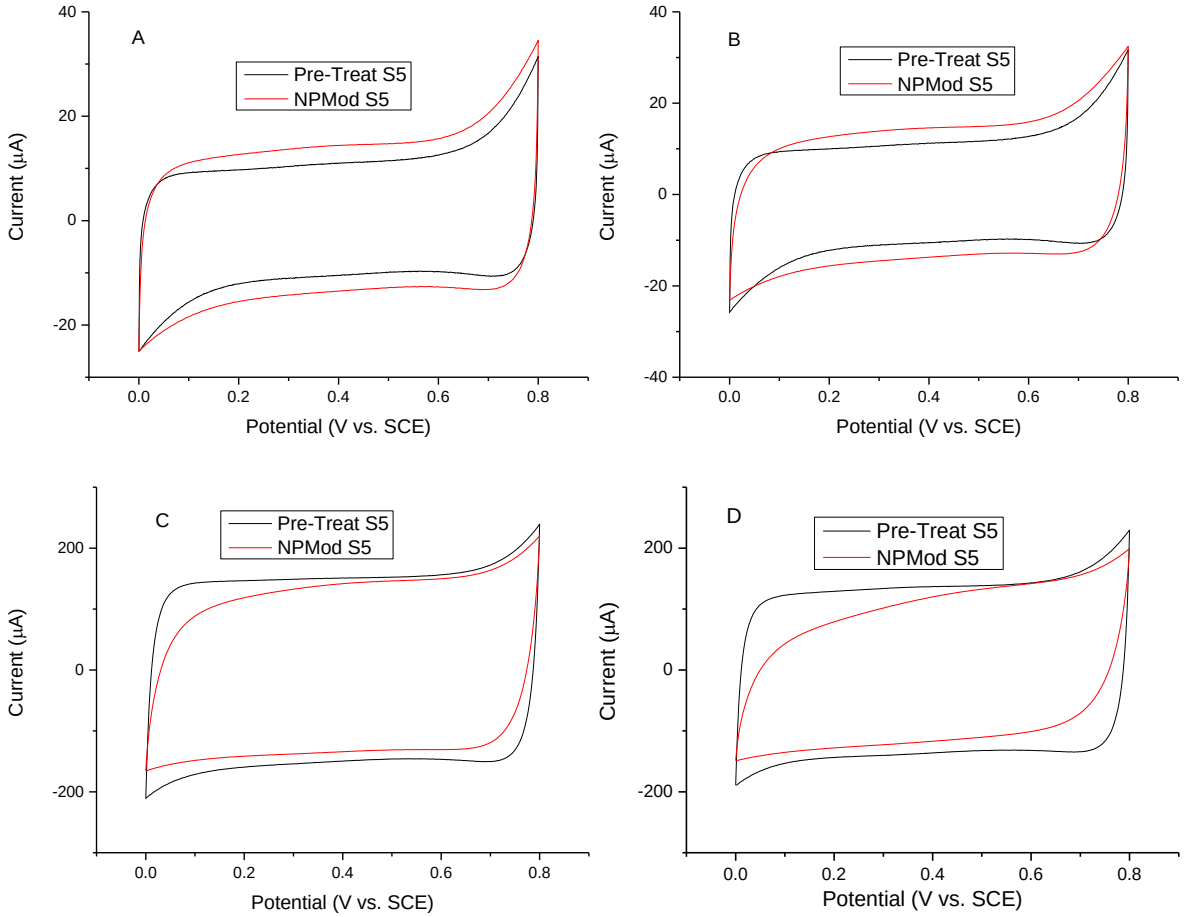

Figure 5.7: CV curves (5th scan, S5) of galvanostatically deposited MnO_2 films in 0.5 M Na_2SO_4 before (black) and after (red) NP modification in pH 10 buffer for 15 min (A and C) and 1 h (B and D). Scans were carried out at 50 mV s^{-1} (A and B) and 500 mV s^{-1} (C and D).

The average capacitance of MnO_2 films before and after modification with NP-groups for 15 min and 1 h at 50 and 500 mV s^{-1} are shown in Table 5.2. At 50 mV s^{-1}, the average capacitance increased with increasing reaction time, however, the significance of this is unclear due to the high variability in these measurements. At high scan rates, the capacitance decreased significantly after modification for both 15 min and 1 h, with 1 h modification resulting in significantly lower capacitance than 15 min modification. Thus the CV scans obtained at 500 mV s^{-1} reveal that increasing reaction time negatively impacts the response rate of the capacitor. This variation in capacitance retention after modification between reaction times at 500 mV s^{-1} suggests the films grafted at 1 h reaction time restrict diffusion more than those grafted at 15 min and thus are thicker. However, the increase in capacitance at 50 mV s^{-1} after modification does not appear to differ significantly between reaction times despite this apparent change in film thickness. Thus, it can be assumed that the mechanism for capacitance enhancement does not arise completely from reactions within the film itself as these would be expected to scale with film thickness. This indicates that the interaction between the layer

and the surface may be the source of this enhancement as this will vary only based on the coverage at each time scale rather than film thickness. This is supported by the AFM studies on NP-films grafted to SU-8 surfaces in pH 10 buffer solution described in Chapter 3 where film coverage did not vary between 15 min and 1 h reaction times.

Table 5.2: Capacitance data from CV scans between 0 and 0.8 V (scan 5, S5) at 50 mV s^{-1} or 500 mV s^{-1} in 0.5 M Na_2SO_4 on galvanostatically deposited MnO_2 before (C_{Bare}) and after (C_{Mod}) modification with NP-groups for 15 min or 1h in pH 10 buffer.

Reaction Time	Scan Rate (mV s^{-1})	C_{Bare} (F g^{-1})	C_{Treat} (F g^{-1})	C_{Treat}/C_{Bare}
15 min[a]	50	223 ± 6	260 ± 10	1.16 ± 0.08
	500	260 ± 10	200 ± 30	0.76 ± 0.08
1 h[a]	50	180 ± 40	240 ± 20	1.4 ± 0.2
	500	190 ± 60	90 ± 40	0.44 ± 0.09

[a]n = 3

As observed in Chapter 3, the pH of the grafting reaction can have a significant effect on the morphology of the grafted aryl layer. The effect of pH on the modification of galvanostatically deposited MnO_2 was investigated by grafting NP-groups in pH 7 buffer for 15 min and 1 h. CV curves of these surfaces are shown in Figure 5.8 along with surfaces treated in pH 7 buffer in the absence of aryldiazonium salt. As found for modification at pH 10 (Figure 5.7 A and B), the response after modification in pH 7 solution for both 15 min and 1 h modification gives an increase in capacitance and no change in the capacitor switching behaviour (Figure 5.8 A and B). In the absence of aryldiazonium salt, treatment with pH 7 buffer has a minor effect on the CV response at 15 min (Figure 5.8C) whereas 1 h treatment time (Figure 5.8D) causes significant changes in the response. After 1 h treatment, the voltammogram has a large degree of curvature at the switching potential, indicating deviation from ideal capacitance switching behaviour. There is also an increase in the scan area between 0.2 to 0.7 V indicating that additional charge storage is occurring within this region. This behaviour is not observed in the presence of the modifier or with treatment at pH 10. This change in the CV curve could arise from either the lower pH affecting the material (e.g. etching to increase the surface area) or the components in the pH 7 buffer (e.g. phosphates) interacting with the surface, however, the exact mechanism is currently unknown. The absence of this effect on surfaces prepared in the presence of aryldiazonium ions may be due to the growing film protecting the surface from corrosion or from unfavourable interactions of buffer components with the surface. It was noted in Chapter 4 that the grafted film could inhibit dissolution of MnO_2 nanorods in acidic

conditions and it is possible that grafting NP groups is providing similar protection in pH 7 buffer. Alternatively, components from the pH 7 buffer solution may be binding to the surface and inhibiting the capacitance processes. The binding of phosphates to MnO_2 has been reported as a method to purify water.[15-17] However, the stability of phosphates on the surface under the cycling conditions used in this work is unknown.

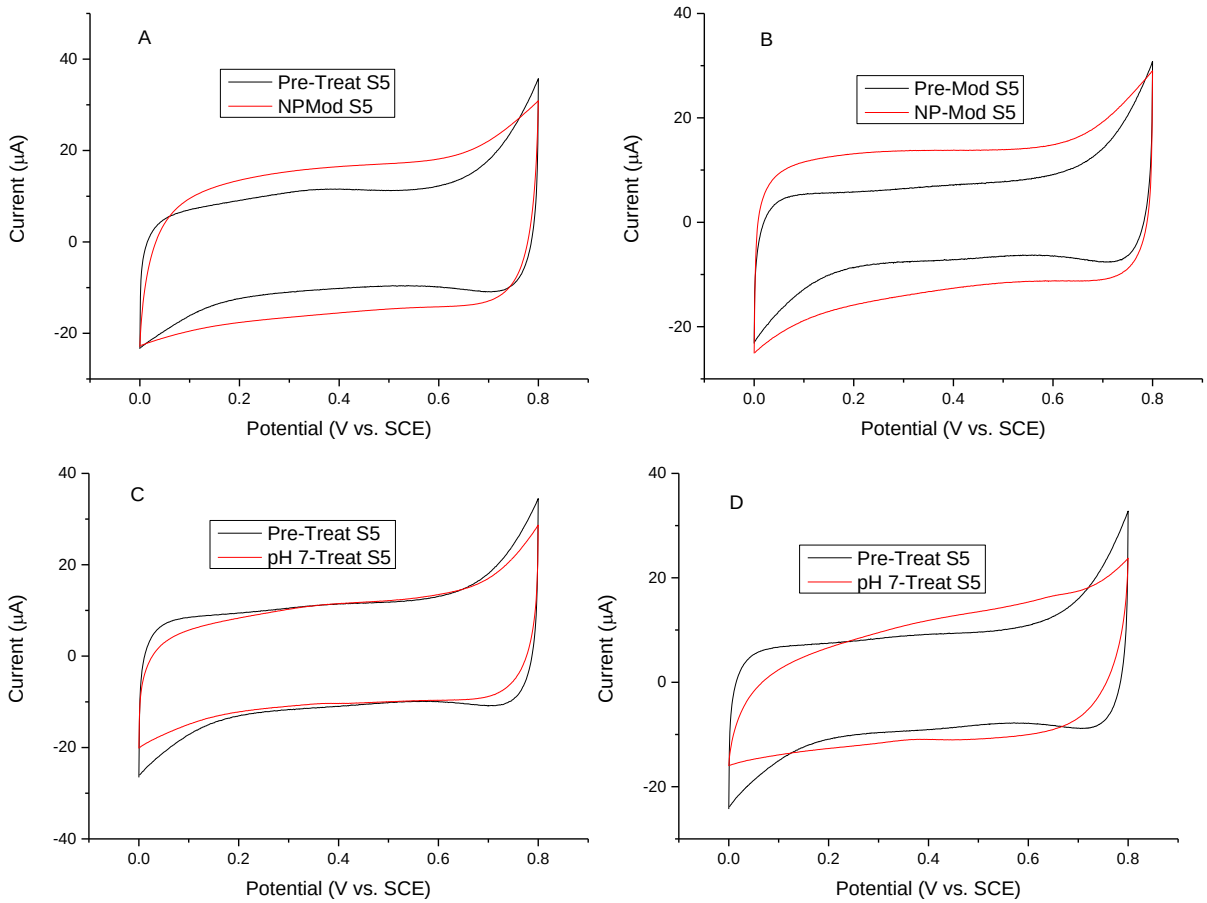

Figure 5.8: CV curves (5th scan, S5) of galvanostatically deposited MnO_2 films in 0.5 M Na_2SO_4 at 50 mV s^{-1} before (black) and after (red): NP modification for 15 min (A) and 1 h (B) in pH 7 buffer and pH 7 buffer treatment in the absence of modifier for 15 min (C) and 1 h (D).

The capacitance data determined by integration of the CV curves before and after NP modification at pH 7 is shown in Table 5.3. Modification resulted in a significant increase in capacitance whereas treatment in buffer without aryldiazonium salt resulted in only a minor decrease. As with modification at pH 10, the average capacitance after 1 h modification at pH 7 is greater than after 15 min modification but not significantly so. However, the fact that this behaviour was observed at both pH values may indicate that it is significant, despite the variability in the data. Comparison between modification in pH 7 and pH 10 shows that the effect on the capacitance of the system is identical after modification at both pH values. The amount of NP-film on the surface after modification in pH

7 solution was estimated by reduction of NP-groups as described above. For a 1 h reaction, the coverage (based on geometric electrode area) was calculated to be 6.0 ± 1 × 10^{-9} mol cm^{-2} (n = 3). This value is higher than the coverage after modification at pH 10 (3.8 ± 0.8 × 10^{-9} mol cm^{-2}) suggesting more complete coverage or thicker multilayer formation. These results align with the relatively higher film thicknesses of NP films grafted to SU-8 surfaces at pH 7 compared to at pH 10 described in Chapter 3.

Despite the clear differences in the CV curves of the MnO_2 sample before and after treatment in pH 7 buffer without aryldiazonium salt (Figure 5.8D), the capacitance of the surface (measured between 0 and 0.8 V) does not significantly change after treatment. This suggests that the changes in the CV curve shape may be due to inhibition of the pseudocapacitance reactions, causing them to be shifted to a higher potential, rather than the introduction of new processes or damage to the surface which would be expected to more drastically change the overall capacitance after treatment.

Table 5.3: Capacitance data from CV scans between 0 V and 0.8 V (scan 5, S5) at 50 mV s^{-1} in 0.5 M Na_2SO_4 on galvanostatically deposited MnO_2 before (C_{Bare}) and after (C_{Treat}) NP-modification, MP-modification or base treatment at pH 7 or pH 10 for 15 min or 1h. pH 10 NP-modified data is replicated from Table 5.2 for convenience.

Modifier	Conditions		C_{Bare} (F g^{-1})	C_{Treat} (F g^{-1})	C_{Treat}/C_{Bare}
NP-mod	pH 10	15 min[a]	223 ± 6	260 ± 10	1.2 ± 0.1
		1 h[a]	180 ± 40	240 ± 20	1.4 ± 0.2
	pH7	15 min[a]	218 ± 4	260 ± 30	1.2 ± 0.1
		1 h[a]	166 ± 8	240 ± 10	1.5 ± 0.2
MP-mod	pH 10	15 min[a]	212 ± 3	262 ± 3	1.23 ± 0.03
		1 h[a]	180 ± 20	260 ± 10	1.5 ± 0.1
	pH7	15 min[a]	209 ± 7	200 ± 14	0.95 ± 0.04
		1 h[a]	190 ± 20	208 ± 6	1.1 ± 0.1
Blank	pH 10	15 min[a]	210 ± 10	210 ± 20	1.01 ± 0.01
		1 h[a]	210 ± 40	200 ± 40	0.95 ± 0.02
	pH7	15 min[a]	222 ± 6	200 ± 3	0.90 ± 0.01
		1 h[a]	190 ± 10	194 ± 4	1.00 ± 0.04

[a] n = 3

In addition to controlling the structure of the aryl layer through manipulation of the grafting conditions, the chemical nature of the film may also be used to tune the properties of the modified

substrate. This possibility was investigated by modifying electrodeposited MnO_2 films with MP groups at pH 7 and pH 10 for 15 min and 1 h. Methoxy groups were chosen as the aryl substituent as they have opposite electronic character to nitro substituents (electron donating vs. electron withdrawing respectively). CV curves obtained at 50 mV s^{-1} scan rate for MnO_2 films modified under various conditions with MP-groups are shown in Figure 5.9. At pH 10 (Figure 5.9 A and B), the area of the CV curve increases after modification with MP groups for both reaction times. Capacitance values determined from the CV curves (Table 5.3) reveal that the average capacitance after 1 h modification is significantly higher than at 15 min. This difference in reaction time dependence to that observed for NP-modification may be due to the different growth rates for the two modifiers. As observed in Chapter 3, MP films were found to grow more slowly than NP films and would be expected to require a longer modification time to attain similar coverage (and thus similar capacitance increase). This may be the main factor accounting for the difference in MP- and NP-modification, rather than the influence of the electronic properties of the aryl substituent. This lack of aryl-substituent dependence may arise due to the multilayer nature of the film causing the electronic effect of the substituent to be dominated by the effect of the network of aryl rings within the multilayer.

At pH 7 however, the CV response after treatment in MBD solution (Figure 5.9 C and D) appears identical to the behaviour observed for the pH 7 blank sample (Figure 5.8 C and D), suggesting that grafting of MP-groups may be minimal at pH 7. Capacitance values for these surfaces (Table 5.3) are also identical to the pH 7 blank material. In experiments described in Chapter 3, it was observed that the grafting of MP-groups to SU-8 was much slower in pH 7 solution than pH 10. This may explain the observed differences between NP-modification and MP-modification at pH 7 as if the film is providing a protective effect in the former case, the slower film growth for MP-groups will result in behaviour more like the pH 7 blank MnO_2 towards the modification solution.

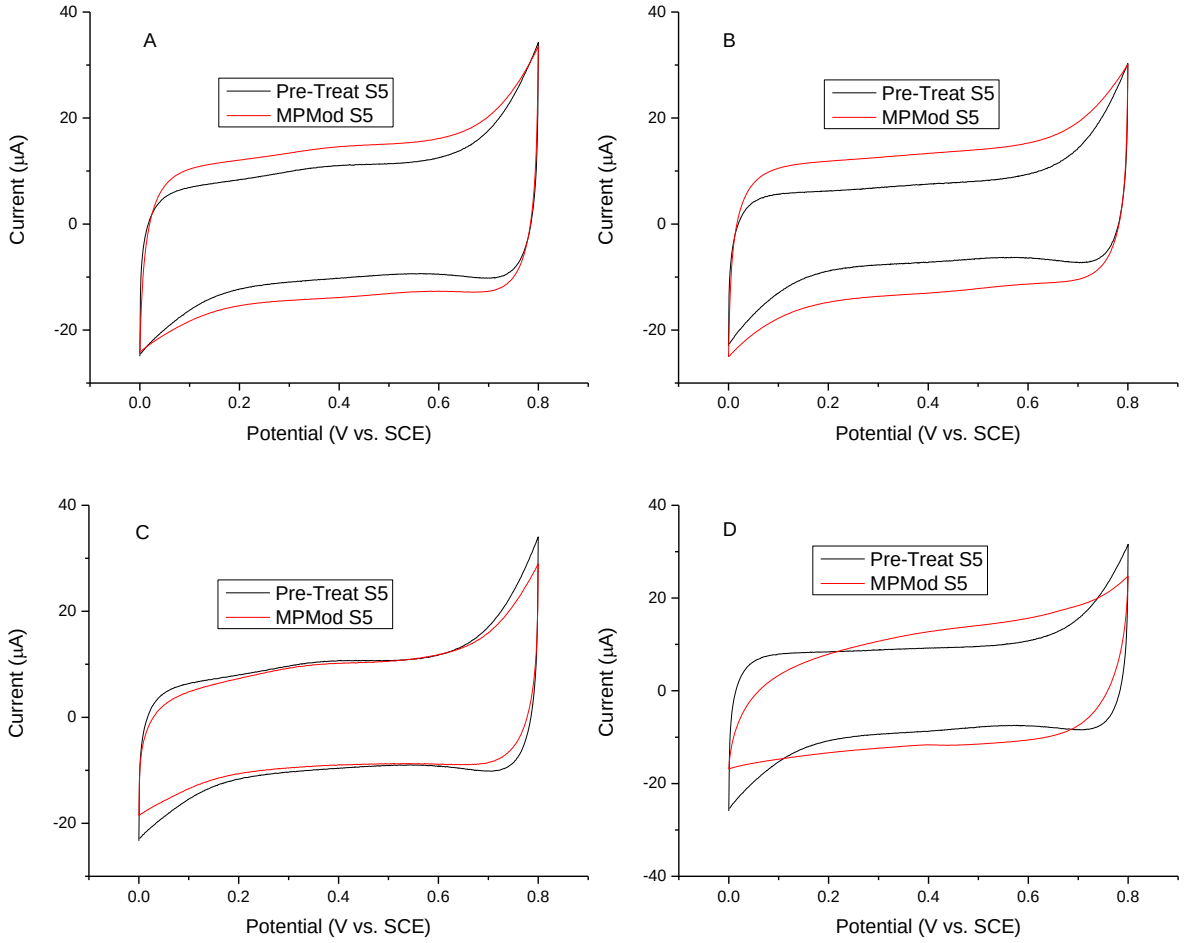

Figure 5.9: CV curves (5th scan, S5) at 50 mV s^{-1} scan rate of galvanostatically deposited MnO_2 films in 0.5 M Na_2SO_4 before (black) and after (red) MP modification for 15 min (A and C) and 1 h (B and D) in pH 10 (A and B) and pH 7 (C and D) buffers.

The effect of modification on the stability of MnO_2 films galvanostatically electrodeposited onto GC plates was investigated by cycling the electrode between 0 and 0.8 V for 10000 cycles. Figure 5.10 (A and B) shows example CV data from cycling experiments with as-prepared and NP-modified MnO_2 respectively. Both surfaces behave identically throughout the cycling experiment: initially the curve area drops between scans 1 and 50 before stabilising around scan 2000. By scan 5000, the CV response is more similar to bare GC electrode than MnO_2 and only minor further changes are observed at scan 10000. The effect of cycling on the capacitance of as prepared and modified MnO_2 was quantified by integrating the CV curve every 25 scans (Figure 5.10C). The capacitance trends are similar under all the conditions studied (as-prepared, pH 10 NP- and MP- modification, and pH 7 NP-modification) where the capacitance gradually declines throughout the experiment. There is a slight step observed in some of the data at ~2500 scans which signifies the onset of the changes in CV response observed in Figure 5.10 A and B between 2-5000 scans. The most likely cause of the decline

in capacitance is gradual decomposition of the MnO_2 film – either by mechanical breakdown or dissolution. The step observed in the capacitance curve may correspond to the film structure breaking down to the point where the film becomes unstable, hastening the film degradation. It is expected that the capacitance will eventually stabilise to the value of the bare GC electrode after all of the MnO_2 is lost on sufficient cycling. From these results it is apparent that modification has no effect on the cycling stability of these electrodes. It is possible that the failure mode in this electrode architecture is lifting of the film off the GC substrate, in which case the modification of the outer surface will provide little protection. However, surface modification may improve the stability of 3-dimensional array electrode architectures where the integrity of the MnO_2 material itself is more important than the adhesion to a substrate.

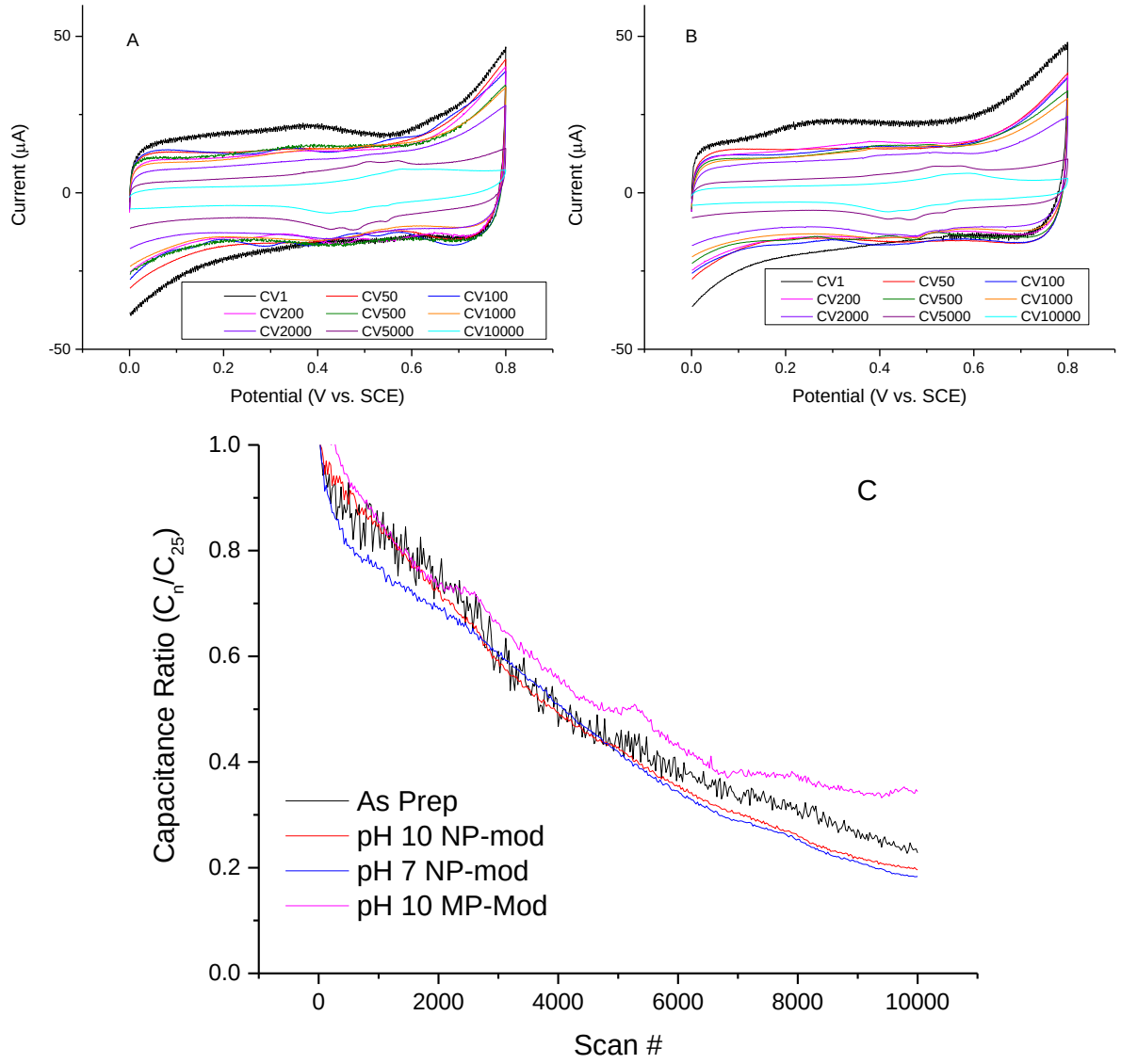

Figure 5.10: CV stability studies of galvanostatically deposited MnO_2 on GC plates in 0.5 M Na_2SO_4 at 50 mV s^{-1}: CV curves of as-prepared (A) and NP-modified (B) MnO_2. C: Plot of capacitance (measured

every 25 scans) normalised to the 25th scan vs. scan rate for as-prepared and pH 10 NP, pH 7 NP and pH 10 MP modified MnO_2.

5.3.2 Electrochemical Impedance Spectroscopy

EIS has been used previously with metal oxide pseudocapacitors to determine the effect of material composition and morphology on capacitor characteristics.[9, 18-21] For the modified electrodes in this work, it was expected that EIS analysis might provide information about the effect of modification on the cycling response of the MnO_2, changes to the electrode structure or introduction of new redox processes after modification. EIS data was collected at 0.4 V in 0.5 M Na_2SO_4 for as-prepared MnO_2 and, modified (NP and MP) and blank MnO_2 surfaces treated at pH 7 and pH 10.

Complex plane impedance (Z) plots (Nyquist) for as-prepared MnO_2 and pH 10 blank and modified surfaces are shown in Figure 5.11A. The Nyquist plot for as-prepared MnO_2 shows a small arc at high frequency and a steep portion at low frequencies. The high frequency impedance arc is associated with the double-layer processes as these are more rapid than the Faradaic charge storage processes.[21] The near-vertical increase in imaginary impedance at low frequency is typical of capacitor characteristics, however, the slight curvature and deviation from a 90° slope angle in this region indicates that the capacitor response in non-ideal. This deviation from ideality is thought to arise due to the diffusional aspects of the charge storage mechanism in metal oxide pseudocapacitors.[9, 23] The pH 10 blank sample has an identical response to the as prepared sample which supports the observation from the CV data that the pH 10 buffer has no effect on the MnO_2 surface. Modification with NP and MP groups causes significant changes in the impedance behaviour. For both modifiers, the arc at high frequency is extended along the real axis (Z'), indicating an increase in the resistance of the double layer process. NP-modification results in the largest broadening of the high frequency arc and also introduces a second arc at lower frequencies as can be seen in the inset of Figure 5.11A. This suggests that NP modification introduces an additional time constant into the system. There is no clear evidence of this new feature in the Nyquist plot for the MP-modified sample. However, as the high frequency arc is smaller than after NP modification, the new feature may also be proportionately smaller (and thus hard to identify) if these processes are related.

The lower limit of the high frequency region can be determined from the knee frequency in the admittance (Y = 1/Z) plot (Figure 5.11B). The knee frequency denotes the highest frequency at which purely capacitive behaviour is dominant and thus gives some indication of the electrochemical response rate of the MnO_2.[23, 24] For as-prepared and pH 10 blank MnO_2, the knee frequency was

found to be 1.5 kHz whereas NP- and MP-modified samples have knee frequencies at 470 and 700 Hz respectively. The drop in knee frequency after modification corresponds to a decline in the rate capability of the MnO_2 electrode.

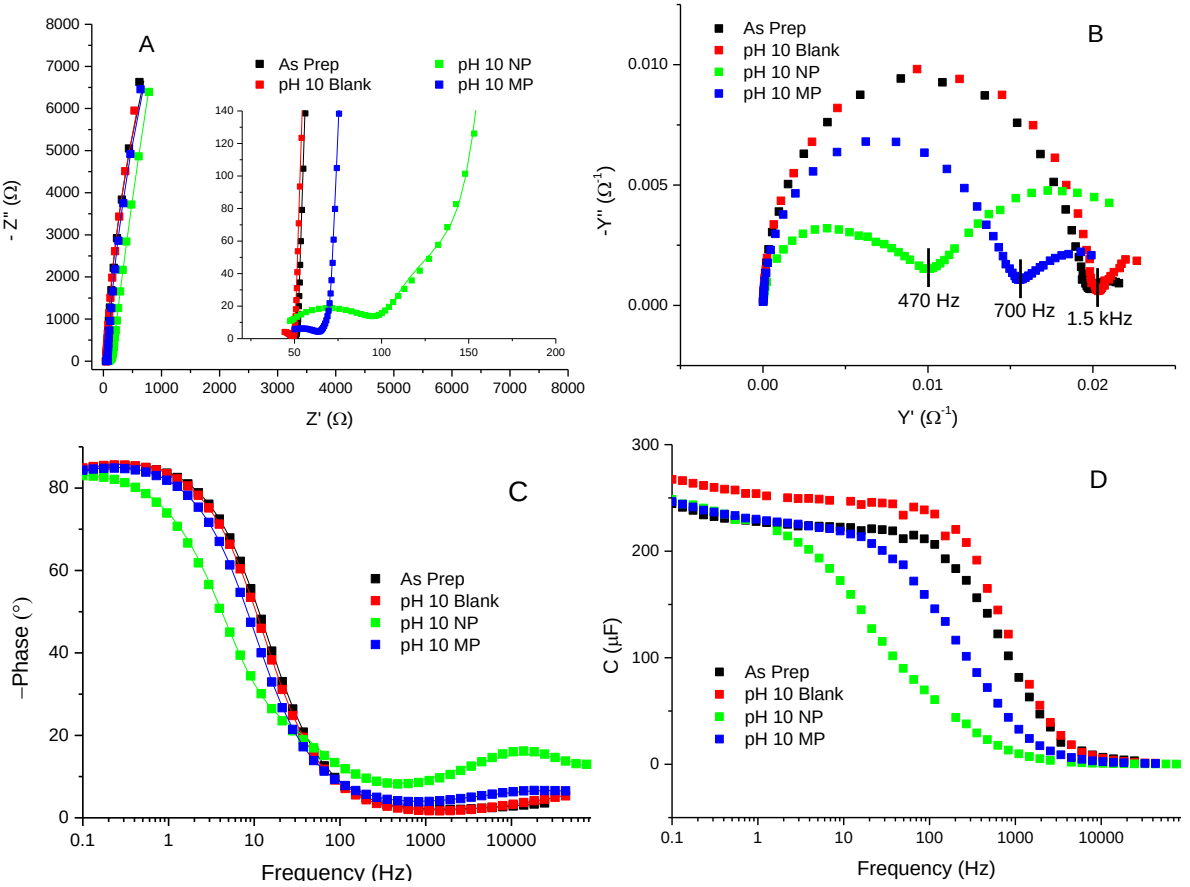

Figure 5.11: EIS data at 0.4 V in 0.5 M Na_2SO_4 for galvanostatically deposited MnO_2 on GC: as prepared and blank, NP and MP-modified for 1 h in pH 10 buffer. A. Complex plane impedance plots, inset is a magnification of the high frequency region. B. Complex plane admittance plots. C. Phase frequency-dependency plots. D. Capacitance frequency-dependency plots. Plotted points represent measured data, solid lines represent data fitted from the equivalent circuit model described below.

Further information about the frequency dependence of the MnO_2 electrode can be obtained from the phase vs. frequency and capacitance vs. frequency Bode plots (Figure 5.11 C and D). In the high frequency region of the Bode plots for as-prepared, pH 10 blank and MP-modified samples, the phase angle and capacitance are near 0, indicating purely resistor-like behaviour at these frequencies.[25] Modification with NP groups results in a peak at ~10 kHz. A peak at this frequency has previously been assigned to the introduction of a diffusive resistance in reduced graphene oxide supercapacitors.[26] This peak appears to be present in the MP-modified sample but at a lower intensity than for the NP-modified sample. The frequency where the phase angle (ϕ) is -45°

corresponds to the frequency where ideal capacitive behaviour occurs (the capacitor response frequency).[23] For as-prepared and pH 10 blank MnO_2, the capacitor response frequency is 16 Hz, giving a response time for the electrode of 6 ms. After modification, the response frequencies are reduced to 5 Hz and 10 Hz for NP- and MP-modified samples respectively. This results in response times of 200 ms (NP-mod) and 100 ms (MP-mod), providing more evidence of the modification process negatively affecting the rate capability of the MnO_2 electrode. This is also apparent from the capacitance-frequency plots where the onset of capacitive behaviour is shifted to lower frequencies for the modified samples. At low frequencies, the capacitance of the electrode becomes much less frequency dependent, however, a slight increase is still observed at the lowest frequencies for all samples. The capacitance increase at low frequency arises from the diffusion-dependent pseudocapacitance mechanism where electrolyte access to the surface, and thus capacitance, increases as the cycle rate decreases. Additionally, at the lowest frequencies, the differences between the capacitance of the modified and blank samples is negligible, indicating that the modification process only negatively affects the rate capability of the electrode rather than its total capacitance.

Impedance data for pH 7 blank and modified samples are shown in Figure 5.12 along with the data for as-prepared MnO_2 reproduced from Figure 5.11. Treatment with pH 7 buffer in the absence of aryldiazonium salt causes the high frequency impedance arc to extend to higher impedance along the real axis (Figure 5.12A) and the high frequency limit is shifted down to 470 Hz (Figure 5.12B). Additionally the low frequency region for the pH 7 blank sample further deviates from 90°, indicating less ideal capacitor behaviour than the as-prepared samples. As was observed by CV (Figure 5.8D), pH 7 buffer treatment without NBD negatively affects the performance of the MnO_2 electrode and the EIS data supports this. The lowered performance of the pH 7 blank electrode is not readily apparent in the Bode phase plot (Figure 5.12C) as the ideal capacitor frequency is 15 Hz giving a similar capacitor response time to the as-prepared sample. However, the capacitance-frequency Bode plot (Figure 5.12D) shows that the onset of capacitance is delayed and very low frequencies are required to achieve peak capacitance from the electrode.

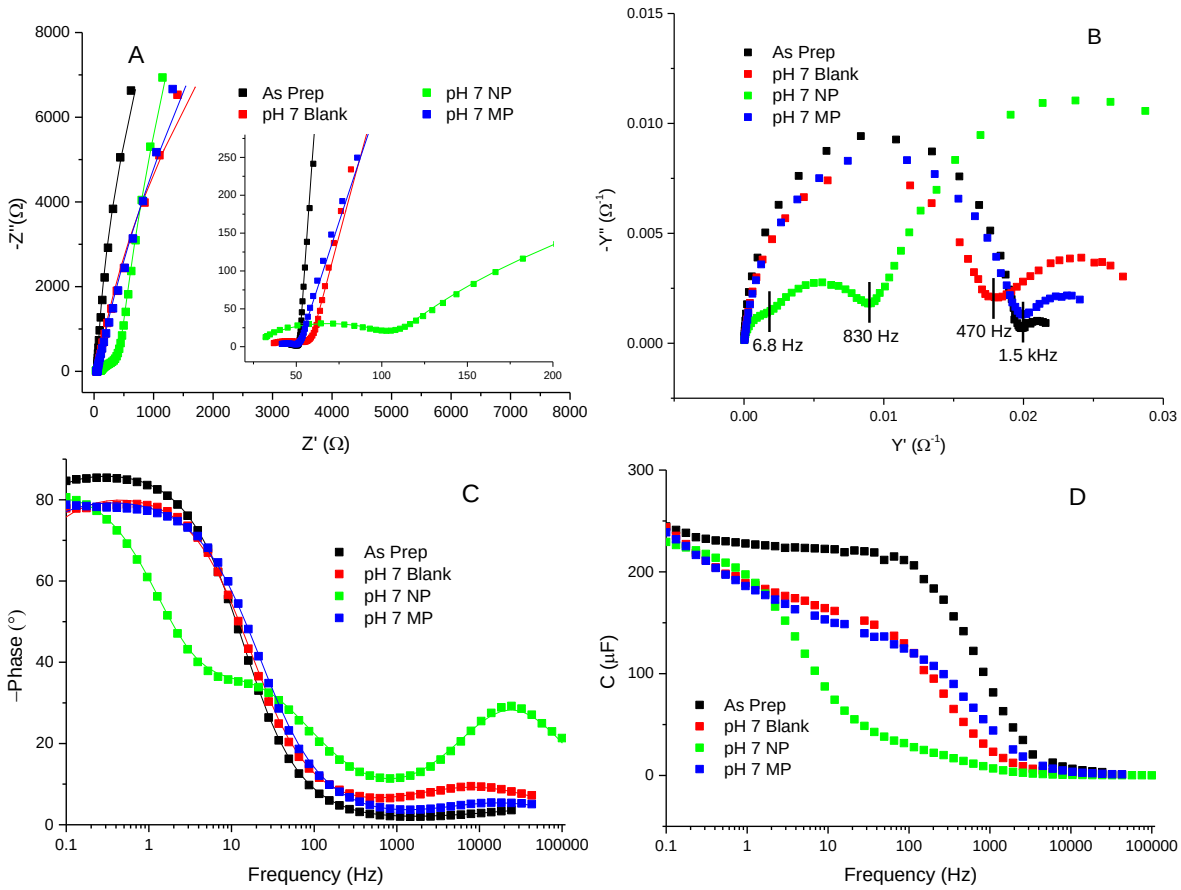

Figure 5.12: EIS data at 0.4 V in 0.5 M Na_2SO_4 for galvanostatically deposited MnO_2 on GC: as prepared (reproduced from Figure 5.11) and blank, NP and MP-modified for 1 h in pH 7 buffer. A. Complex plane impedance plots. B. Complex plane admittance plots, inset is a magnification of the high frequency region. C. Phase frequency-dependency plots. D. Capacitance frequency-dependency plots. Plotted points represent measured data, solid lines represent data fitted from the equivalent circuit model described below.

Modification in pH 7 solution produces differing impedance responses depending on whether NBD or MBD ions are grafted. Modification with MBD ions results in impedance responses that are similar to the pH 7 blank in the Nyquist impedance and Bode plots (Figure 5.12 A, C and D). However, the Nyquist admittance plot (Figure 5.12B) is most similar to the as-prepared sample with a knee frequency of 1.1 kHz. These results suggest that the presence of MBD in the grafting solution has little effect on the MnO_2 surface at pH 7 and that the behaviour after this reaction is dominated by the interactions of the buffer with the surface.

At pH 7, modification with NP-groups results in impedance behaviour more similar to the pH 10 modified samples than to the MP-modified sample at pH 7. The high frequency impedance arc (Figure 5.12A) is extended to higher impedance values than for the MP-modified sample and there is

a clear second arc before the near-vertical portion of the curve. The near-vertical portion of the curve is closer to 90° than the MP-modified or blank samples and thus indicates a more ideal capacitor response after NP-modification. The admittance Nyquist plot (Figure 5.12B) shows that the frequency response is negatively impacted by NP-modification as the knee frequency is shifted to 830 Hz. This is supported by the capacitor response frequency from the Bode phase plot (Figure 5.12C) shifting to 2.5 Hz. There is also an additional knee point in the admittance plot at 6.8 Hz suggesting that the modification process introduces an additional frequency regime into the electrochemical response of the material. This is apparent in the Bode phase plot for the pH 7 NP-modified sample where two plateaus in phase angle are apparent at low frequency (~40 Hz and ~0.2 Hz) in addition to the phase shift peak at high frequency that was also observed for the pH 10 NP-modified sample. Similarly, there are three distinct slopes in the capacitance-frequency Bode plot (Figure 5.12D) indicating that modification with NP groups in pH 7 solution significantly changes the frequency dependence of the charge storage processes in the electrode. These features may also be present in the pH 10 NP-modified sample but are too small to resolve. As these changes in frequency dependence occur within two different frequency ranges, it suggests that there are two time constants involved in the process restricting the capacitance at higher frequencies. A possible explanation for this is that the formation of an aryl multilayer produces a hierarchically porous structure. Gaps in the film may allow some access to the MnO_2 surface at intermediate frequencies while cations may be able to penetrate through the film itself at slow enough cycle rates.

In the CV studies of modified MnO_2 surfaces described earlier, modification at pH 10 with NP and MP groups and at pH 7 with NP groups resulted in increased capacitance of the MnO_2 film at 50 mV s^{-1}, however, there appears to be no corresponding change in the EIS data at low frequencies. As the capacitance-frequency plots are not normalised to the initial capacitance before treatment, capacitance changes are difficult to identify. As this effect was only observed at some scan rates, the lack of a direct comparison between AC frequency and CV scan rate further complicates this identification. From the increased effect on frequency response in the EIS data, it also appears that the NP film is thicker than the MP film whereas the capacitance data was similar for both modifiers at pH 10. This is in contrast to the film thickness measurements on modified SU-8 surfaces described in Chapter 3 where the MP-modified surface at pH 10 was thicker than NP films grafted at both pH 7 and pH 10. This variation between modifiers suggests that the diffusion restriction may include contributions from film morphology beyond just thickness (e.g. porosity). Alternatively, the substituent-dependence of the grafting reaction at MnO_2 may be different than to that at SU-8 which could result in thicker NP films than MP films at MnO_2.

To gain further insight into the effect of modification on MnO_2 electrodes, the EIS data was fitted with an equivalent circuit model. Literature models fitted to pseudocapacitor electrodes are generally based on the Randles circuit (Figure 5.13A) which models the solution resistance between the electrodes in the cell (R_S), capacitance due to the electrochemical double layer (C_{dl}), charge transfer resistance due to the Faradaic pseudocapacitance reaction (R_{CT}) and a Warburg element (W) to account for the diffusion of counter-ions within the electrode. In prior studies, the standard Randles circuit has been modified to suit metal oxide pseudocapacitors through the addition of a capacitor element to account for the low frequency capacitance (C_P) arising from the pseudocapacitance reaction (Figure 5.13B).[27]

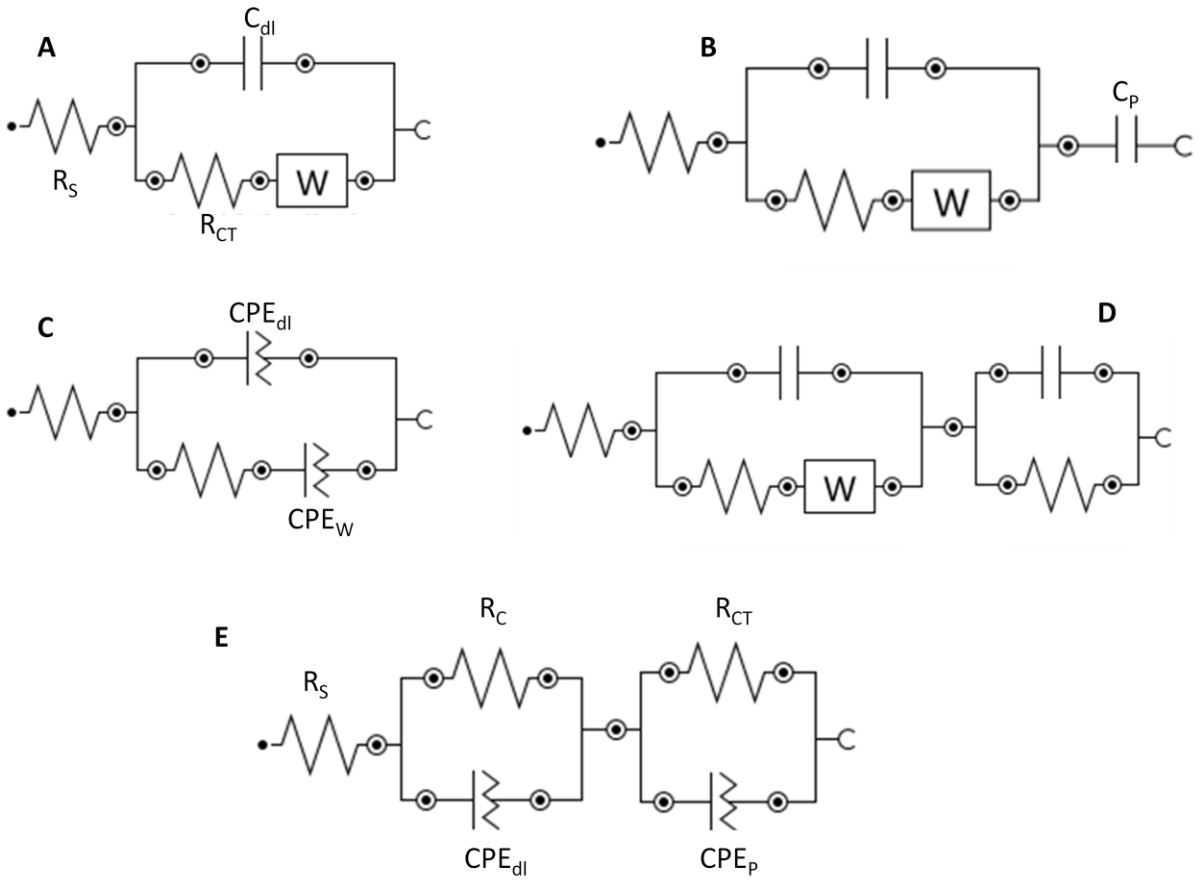

Figure 5.13: Equivalent circuit models for fitting EIS data for pseudocapacitor electrodes: A. Randles circuit, B. equivalent circuit describing MnO_2-graphene composite electrodes from reference [27], C. equivalent circuit describing electrodeposited MnO_2 thin films from reference [19], D. equivalent circuit describing RuO_2 thin films from reference [21], E. Equivalent circuit for unmodified MnO_2 films used in this work.

For real systems, capacitor elements are usually replaced with constant-phase elements (CPE) to account for heterogeneous electrode behaviour due to roughness or porosity (Figure 5.13C).[19] The expression for a CPE is shown in Equation 5.3 where Q_0 and n are fitting parameters, j is the complex number and ω is the angular frequency. Q_0 is an admittance parameter that effectively represents the capacitance of the CPE, whereas n ($0 \leq n \leq 1$) represents the deviation from an ideal capacitor for which $n = 1$. The CPE also equates to a Warburg element for the case of semi-infinite planar diffusion when $n = 0.5$.[28]

$$Z_{CPE} = \frac{1}{Q_0(j\omega)^n} \qquad \text{Equation 5.3}$$

Initially, the fit of various literature models (Figure 5.13 B-D) was tested against the experimental data for as-prepared MnO_2 as this represents the simplest system studied in this work.[9, 18-21, 27] However, none of these literature models provided satisfactory fit for the experimental data because the fitting procedure failed to converge or gave an unacceptable goodness-of-fit χ^2 statistic (values > 0.1). This required development of a new model to account for the EIS data.

The simple model used in this work for the MnO_2 electrode in the absence of an aryl layer (Figure 5.13E) consists of a solution resistance (R_s) in series with two parallel R-CPE components. The first R-CPE component consists of the contact resistance (R_C) within the MnO_2 material and between the MnO_2 and the GC electrode and a CPE (CPE_{dl}) representing the double-layer capacitance at a heterogeneous electrode. The second R-CPE component represents the pseudocapacitance charge storage mechanism by the resistance of the Faradaic process (R_{CT}) and the diffusion processes within the electrode at low frequencies (CPE_P). CPEs were used rather than pure capacitors or Warburg elements in this model due to the roughness and porosity of the surface. The equivalent circuit parameters and fitting statistic (χ^2) for fitting the as-prepared MnO_2 data are shown in Table 5.4. The low χ^2 value and sensible fitting parameters suggest that this model is a good fit for the experimental data. It is apparent from the values for n for CPE_{dl} (0.98) and CPE_P (0.42) that these elements are close to an ideal capacitor and Warburg element respectively. This aligns with the expected behaviour of the system where the surface double-layer should be ideally polarisable (high n) but the pseudocapacitance reaction will be diffusion-controlled ($n \approx 0.5$).

Table 5.4: Equivalent circuit modelling parameters for EIS data fitted by the circuit shown in Figure 5.13E for as-prepared MnO_2, pH 10 solution-treated blank, and MnO_2 samples treated in pH 7 buffer solution in the presence (pH 7 MP) and absence (pH 7 blank) of MBD.

Sample	R_s (Ω)	CPE_{dl} ($\mu\Omega^{-1}$)	n_{dl}	R_c (kΩ)	CPE_P ($\mu\Omega^{-1}$)	n_p	R_{ct} (Ω)	χ^2
As Prep MnO2	33	235	0.98	97	144	0.42	20	0.001
pH 10 Blank	12	263	0.98	98.5	15.4	0.47	39	0.0006
pH 7 Blank	32	218	0.93	53.1	64.3	0.61	27	0.01
pH 7 MP	37	218	0.91	88.6	37.8	0.66	14	0.01

The fit of the model to the pH 10 blank is also very good (low χ^2) and the majority of the parameters are similar to the as-prepared MnO_2 sample (Table 5.4), providing further evidence for the model's suitability to this system. However, there is a factor of 10 decrease in the value of CPE_P for the pH 10 blank and as-prepared sample while the value of *n* is approximately similar. This may arise from the charge balancing cations in as-prepared MnO_2 being protons from the acidic deposition conditions, whereas in the pH 10 buffer solution they have been exchanged with Na^+ ions (as found by XPS as described in Chapter 4). The differing diffusion characteristics of protons and Na^+ ions could thus influence the impedance response of the mass-transport dependent components in the system. The variation in the solution resistance is due to differences in the positioning of electrodes between experiments. In comparison, the model is a relatively poor fit for the pH 7 blank data. Despite the differences observed in the experimental data for the pH 7 and pH 10 blanks, the fitting process gave similar parameters for both apart from the values of n_P. The difference in this parameter suggests different diffusive behaviour for the two samples. Application of this model to modified surfaces resulted in convergence for only the pH 7 MP-modified sample which gives similar parameters to the pH 7 blank sample with a similarly poor fitting statistic. This supports the hypothesis that minimal modification with MP groups occurs at the MnO_2 electrode under these conditions.

The fit of the model to the other modified samples was not satisfactory as it failed to account for the additional impedance arc present in these samples. This indicates that the changes observed in the EIS data do not arise simply due to changes in the diffusion behaviour as this would manifest as variation in the diffusive element CPE_P. Instead, the presence of an aryl layer on these samples seems to add an additional time constant to the electrochemical response of the system. A third parallel CPE-R (CPE_{Aryl} and R_{Aryl}) circuit was added in series between the solution resistance and the double-layer to account for diffusion through the aryl film to the MnO_2 electrode surface. This

arrangement of elements is commonly used to model the solid electrolyte interface that passivates Li-ion battery electrodes.[29-31] This is a porous interface that provides resistance to diffusion of cations into the electrode structure which is analogous to the expected role of the aryl layer at a modified MnO_2 electrode. The final proposed equivalent circuit model for the modified MnO_2 samples, along with the physical processes represented by the components, is shown in Figure 5.14.

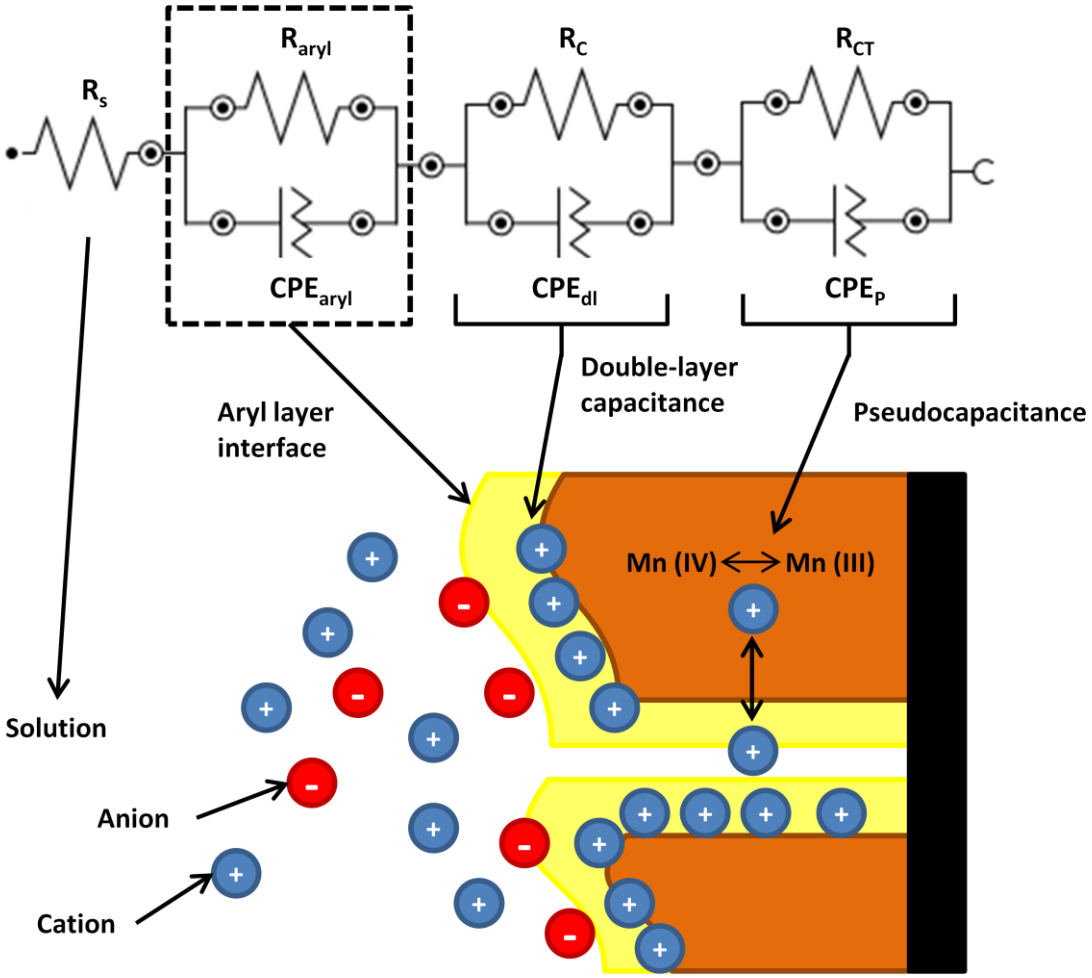

Figure 5.14: Proposed equivalent circuit model for modified MnO_2 electrodes with a schematic diagram of the corresponding physical processes involved during charge storage. In the absence of an aryl layer, the circuit elements in the dashed square were excluded.

The fitting parameters for the pH 10 MP and NP modified samples and the pH 7 NP modified sample using the extended equivalent circuit are shown in Table 5.5. In all cases, the equivalent circuit model fits the data well (low χ^2) however there is some variation between duplicate samples modified under the same conditions and compared to the blank samples. The nature of this variation was investigated by adjusting the fitting procedure for the equivalent circuit. One possibility that was examined was that all the variation in the EIS response observed after modification is due to the

aryl film, and the intrinsic double-layer and pseudocapacitance behaviour of the MnO_2 surface is preserved during modification. This hypothesis was tested by fixing these parameters to be identical to the values for unmodified surfaces (either as-prepared or the appropriate blank). Using this approach, the model was unable to fit the experimental data for the modified surfaces, indicating that modification with the aryl layer influences the behaviour of the double-layer and/or pseudocapacitance mechanisms.

Table 5.5: Equivalent circuit modelling parameters for EIS data fitted by the extended circuit shown in Figure 5.14 for MnO_2 samples modified in pH 10 solution with NP and MP groups and samples modified in pH 7 solution with NP groups. S1 and S2 refer to duplicate samples prepared under identical conditions.

Sample	R_s (Ω)	CPE_{aryl} ($\mu\Omega^{-1}$)	n_{aryl}	R_{aryl} (Ω)	CPE_{dl} ($\mu\Omega^{-1}$)	n_{dl}	R_C (kΩ)	CPE_P ($\mu\Omega^{-1}$)	n_p	R_{ct} (Ω)	χ^2
pH 10 NP S1	37	395	0.77	57.9	246	0.95	175	16.0	0.64	63.4	0.009
pH 10 NP S2	36	96.1	1.00	14.3	159	0.88	40	15.3	0.62	68.7	0.007
pH 10 MP S1	40	548	1	2.9	241	0.98	111	85.3	0.52	28	0.0007
pH 10 MP S2	32	3.90	1.00	1.80	255	0.97	112	119	0.45	25	0.002
pH 7 NP S 1	25	151	0.75	331	225	0.96	148	2.24	0.78	81.7	0.008
pH 7 NP S2	25	147	0.75	579	176	0.87	119	2.50	0.76	87.80	0.008

Of the six samples studied, the double-layer parameters (CPE_{dl}, n_{dl} and Rc) were similar to the blank and as-prepared samples for four of them, suggesting the aryl layer has limited influence on the double-layer processes. The other two samples (pH 10 NP S2 and pH 7 NP S2) have lower double-layer capacitance and less ideal capacitor response (lower CPE_{dl} and n_{dl}) than the corresponding blanks. The double-layer parameters are related to the structure of the MnO_2 electrode and these changes may arise due to variability in the MnO_2 deposition process. Alternatively variation in film growth and coverage under similar conditions may lead to occlusion of the surface to varying extents and thus lowering of the double-layer capacitance. As the double-layer capacitance of the MnO_2 surfaces is largely unaffected by modification, this indicates that the capacitance increases observed in the CV data at 50 mV s^{-1} after modification are not due to etching of the surface increasing the surface area (and thus capacitance due to surface area-dependent mechanisms) as this would significantly affect the double-layer capacitance of the MnO_2 surface.

The mass-transport limited pseudocapacitance elements of the circuit (CPE_P, n_P and R_{CT}) also vary after modification and between modifiers. This suggests that the aryl layer has a large influence on the pseudocapacitance storage mechanism. This is not an unexpected result as the influence of the aryl layer is modelled as a partial impediment to diffusion through to the electrode surface and thus would influence the mass transport-controlled pseudocapacitance mechanism. This means that these elements overlap in frequency-dependence, making the deconvolution of the effect of modification on the pseudocapacitance mechanism difficult without independent experimental measurement of some of the parameters to fix them in the modelling procedure. However, it is apparent that the parameters associated with the aryl layer itself are highly variable even between duplicate samples. This may arise from the disordered nature of the multilayer aryl film on the surface.

5.4 Conclusions

The effect of modification by aryldiazonium grafting on the electrochemical behaviour of MnO_2 was investigated by CV and EIS on MnO_2 films prepared by electrodeposition. Modification of MnO_2 electrodes prepared on GC allowed for direct comparison of the properties of the MnO_2 film before and after modification.

To summarise the results of CV experiments on NP- and MP-modified MnO_2 surfaces, modification caused differing effects on the electrochemical behaviour depending on the modification conditions used. In pH 10 solution, modification with NP and MP groups was found to enhance the capacitance of the electrode at low scan rates but lowers it at high scan rates. Both the enhancement of capacitance at low scan rates and decrease at high scan rates were amplified at longer grafting times. In pH 7 solution, the performance of the electrode was degraded by treatment in the absence of aryldiazonium salt. This behaviour is also observed in the presence of MBD, suggesting limited grafting of MP-groups as was expected based on the findings described in Chapter 3. Modification with NBD at pH 7 resulted in similar behaviour to modification at pH 10 which indicates that successful grafting limits the damaging effects of the pH 7 buffer solution.

The frequency response of electrodeposited MnO_2 surfaces after modification and buffer treatment at pH 10 and pH 7 was investigated by EIS. The rate characteristics of the modified surfaces were significantly worse after modification and new features at medium to low frequencies were apparent in the EIS response of modified surfaces. The origin of these features was investigated by equivalent circuit modelling and it was determined that they did not arise solely due to changes in the existing double-layer and pseudocapacitance processes in the MnO_2 material. It is proposed that

the aryl film acts as a porous layer that impedes diffusion to the surface analogous to a solid electrolyte interface in Li-ion batteries. The equivalent circuit model incorporating these elements fits the experimental data well but due to convolution with the mass transport processes involved in the pseudocapacitance mechanism, the effect of modification on the model parameters cannot be accurately determined. However, it is apparent from these results that a multilayer film negatively impacts the rate capability of modified MnO_2 electrodes beyond any enhancement effects apparent at lower scan rates. Thus controlling the thickness of the grafted layer to a monolayer appears necessary to produce modified electrodes with desirable rate characteristics.

Although it cannot be definitively determined from these results, some conclusions can be drawn about the origin of the capacitance enhancement observed at 50 mV s^{-1} scan rate after modification. One possible mechanism by which the capacitance of the MnO_2 surface could be enhanced is by etching of the surface to increase surface area and thus charge storage. However, none of the expected changes in the double-layer parameters in the EIS data that would occur if the surface area of the electrode had increased were observed. The increase of capacitance could also arise from the aryl layer introducing new redox processes and thus enhancing the pseudocapacitance of the electrode. This explanation seems unlikely as there was no sign of new redox peaks in the CV curves of the surfaces after modification and the increase in charge storage was uniform throughout the potential window. Furthermore, the changes in the EIS data observed for the modified samples are due to the aryl layer impeding diffusion and there was no sign of new electrochemical processes at low frequencies where the capacitance enhancement was observed by CV. This suggests that the increase in charge storage observed after modification arises due to an enhancement of the MnO_2 charge storage process. It has been proposed that the charge storage mechanism in MnO_2 occurs due to charge-switching states in the MnO_2 band gap induced by cations incorporated into the MnO_2 structure.[32] It is possible that modification of the MnO_2 surface with aryl layers introduces surface states into the band gap that act as additional charge-switching states and enhance the charge storage of the electrode. The introduction of gap states after surface modification has been demonstrated previously with aryldiazonium-modified carbon nanotubes,[33] and ZnO and TiO_2 surfaces modified with self-assembled monolayers.[34, 35]

The effect of modification on the stability of MnO_2 films was investigated by monitoring the capacitance of the film over repeat cycling up to 10000 scans, however, no change in stability was observed in the modified surface. The lack of change after modification may be due to the failure mode in this electrode architecture being due to the attachment between the MnO_2 and the GC electrode failing which would not be affected by modifying the outer surface of the MnO_2. It is

possible that stability enhancements may be observed in 3-dimensional electrodes where all of the MnO_2 surfaces are involved in electrode breakdown.

5.5 References

1. Zhang, K.; Han, X.; Hu, Z.; Zhang, X.; Tao, Z.; Chen, J., Nanostructured Mn-Based Oxides for Electrochemical Energy Storage and Conversion. *Chem. Soc. Rev.* **2015,** *44* (3), 699-728.
2. Cross, A.; Morel, A.; Cormie, A.; Hollenkamp, T.; Donne, S., Enhanced Manganese Dioxide Supercapacitor Electrodes Produced by Electrodeposition. *J. Power Sources* **2011,** *196* (18), 7847-7853.
3. Cross, A. D.; Olcomendy, I.; Drozd, M.; Hollenkamp, A. F.; Donne, S. W., Electrochemical Quartz Crystal Microbalance and Rotating Ring Disk Electrode Analysis of Manganese Dioxide Electrodeposition for Thin Film Electrochemical Capacitors. *J. Electrochem. Soc.* **2013,** *160* (2), A368-A375.
4. Ali, G. A. M.; Yusoff, M. M.; Ng, Y. H.; Lim, H. N.; Chong, K. F., Potentiostatic and Galvanostatic Electrodeposition of Manganese Oxide for Supercapacitor Application: A Comparison Study. *Curr. Appl. Phys.* **2015,** *15* (10), 1143-1147.
5. Wei, W.; Cui, X.; Mao, X.; Chen, W.; Ivey, D. G., Morphology Evolution in Anodically Electrodeposited Manganese Oxide Nanostructures for Electrochemical Supercapacitor Applications—Effect of Supersaturation Ratio. *Electrochim. Acta* **2011,** *56* (3), 1619-1628.
6. Cao, J.; Li, X.; Wang, Y.; Walsh, F. C.; Ouyang, J.-H.; Jia, D.; Zhou, Y., Materials and Fabrication of Electrode Scaffolds for Deposition of MnO_2 and Their True Performance in Supercapacitors. *J. Power Sources* **2015,** *293*, 657-674.
7. Ataherian, F.; Wu, N.-L., Long-Term Charge/Discharge Cycling Stability of MnO_2 Aqueous Supercapacitor under Positive Polarization. *J. Electrochem. Soc.* **2011,** *158* (4), A422-A427.
8. Brousse, T.; Toupin, M.; Bélanger, D., A Hybrid Activated Carbon-Manganese Dioxide Capacitor Using a Mild Aqueous Electrolyte. *J. Electrochem. Soc.* **2004,** *151* (4), A614-A622.
9. Wei, W.; Cui, X.; Chen, W.; Ivey, D. G., Improved Electrochemical Impedance Response Induced by Morphological and Structural Evolution in Nanocrystalline MnO_2 Electrodes. *Electrochim. Acta* **2009,** *54* (8), 2271-2275.
10. Babakhani, B.; Ivey, D. G., Effect of Electrodeposition Conditions on the Electrochemical Capacitive Behavior of Synthesized Manganese Oxide Electrodes. *J. Power Sources* **2011,** *196* (24), 10762-10774.
11. Guillemet, P.; Brousse, T.; Crosnier, O.; Dandeville, Y.; Athouel, L.; Scudeller, Y., Modeling Pseudo Capacitance of Manganese Dioxide. *Electrochim. Acta* **2012,** *67* (0), 41-49.
12. Zhao, H.; Han, G.; Chang, Y.; Li, M.; Li, Y., The Capacitive Properties of Amorphous Manganese Dioxide Electrodeposited on Different Thermally-Treated Carbon Papers. *Electrochim. Acta* **2013,** *91* (0), 50-57.
13. Dupont, M. F.; Donne, S. W., Separating the Faradaic and Non-Faradaic Contributions to the Total Capacitance for Different Manganese Dioxide Phases. *J. Electrochem. Soc.* **2015,** *162* (5), A5096-A5105.
14. Brooksby, P. A.; Downard, A. J., Electrochemical and Atomic Force Microscopy Study of Carbon Surface Modification Via Diazonium Reduction in Aqueous and Acetonitrile Solutions. *Langmuir* **2004,** *20* (12), 5038-5045.
15. Mustafa, S.; Zaman, M. I.; Khan, S., Ph Effect on Phosphate Sorption by Crystalline MnO_2. *J. Colloid Interface Sci.* **2006,** *301* (2), 370-375.
16. Yao, W.; Millero, F. J., Adsorption of Phosphate on Manganese Dioxide in Seawater. *Environ. Sci. Technol.* **1996,** *30* (2), 536-541.
17. Pan, B.; Han, F.; Nie, G.; Wu, B.; He, K.; Lu, L., New Strategy to Enhance Phosphate Removal from Water by Hydrous Manganese Oxide. *Environ. Sci. Technol.* **2014,** *48* (9), 5101-5107.

18. Kiani, M. A.; Khani, H.; Mohammadi, N., Mno_2/Ordered Mesoporous Carbon Nanocomposite for Electrochemical Supercapacitor. *J. Solid State Electrochem.* **2014,** *18* (4), 1117-1125.
19. Dupont, M. F.; Hollenkamp, A. F.; Donne, S. W., Large Amplitude Electrochemical Impedance Spectroscopy for Characterizing the Performance of Electrochemical Capacitors. *J. Electrochem. Soc.* **2014,** *161* (4), A648-A656.
20. Zhang, J.; Zhao, X. S., A Comparative Study of Electrocapacitive Properties of Manganese Dioxide Clusters Dispersed on Different Carbons. *Carbon* **2013,** *52*, 1-9.
21. Dubal, D. P.; Gund, G. S.; Holze, R.; Jadhav, H. S.; Lokhande, C. D.; Park, C.-J., Solution-Based Binder-Free Synthetic Approach of RuO_2 Thin Films for All Solid State Supercapacitors. *Electrochim. Acta* **2013,** *103*, 103-109.
22. Hu, C.-C.; Wang , C.-C., Nanostructures and Capacitive Characteristics of Hydrous Manganese Oxide Prepared by Electrochemical Deposition. *J. Electrochem. Soc.* **2003,** *150* (8), A1079-A1084.
23. Sugimoto, W.; Iwata, H.; Yokoshima, K.; Murakami, Y.; Takasu, Y., Proton and Electron Conductivity in Hydrous Ruthenium Oxides Evaluated by Electrochemical Impedance Spectroscopy: The Origin of Large Capacitance. *J. Phys. Chem. B* **2005,** *109* (15), 7330-7338.
24. Hughes, M.; Shaffer, M. S. P.; Renouf, A. C.; Singh, C.; Chen, G. Z.; Fray, D. J.; Windle, A. H., Electrochemical Capacitance of Nanocomposite Films Formed by Coating Aligned Arrays of Carbon Nanotubes with Polypyrrole. *Adv. Mater.* **2002,** *14* (5), 382-385.
25. Zhang, G.-Q.; Zhao, Y.-Q.; Tao, F.; Li, H.-L., Electrochemical Characteristics and Impedance Spectroscopy Studies of Nano-Cobalt Silicate Hydroxide for Supercapacitor. *J. Power Sources* **2006,** *161* (1), 723-729.
26. Sankar, K. V.; Kalai Selvan, R., Improved Electrochemical Performances of Reduced Graphene Oxide Based Supercapacitor Using Redox Additive Electrolyte. *Carbon* **2015,** *90*, 260-273.
27. Liu, Y.; Yan, D.; Li, Y.; Wu, Z.; Zhuo, R.; Li, S.; Feng, J.; Wang, J.; Yan, P.; Geng, Z., Manganese Dioxide Nanosheet Arrays Grown on Graphene Oxide as an Advanced Electrode Material for Supercapacitors. *Electrochim. Acta* **2014,** *117*, 528-533.
28. Bard, A. J.; Faulkner, L. R.; Leddy, J.; Zoski, C. G., *Electrochemical Methods: Fundamentals and Applications*. Wiley New York: 1980; Vol. 2.
29. Mahmoud, A.; Chamas, M.; Lippens, P.-E., Electrochemical Impedance Study of the Solid Electrolyte Interphase in $MnSn_2$ Based Anode for Li-Ion Batteries. *Electrochim. Acta* **2015,** *184*, 387-391.
30. Guo, J.; Sun, A.; Chen, X.; Wang, C.; Manivannan, A., Cyclability Study of Silicon–Carbon Composite Anodes for Lithium-Ion Batteries Using Electrochemical Impedance Spectroscopy. *Electrochim. Acta* **2011,** *56* (11), 3981-3987.
31. Piao, T.; Park, S. M.; Doh, C. H.; Moon, S. I., Intercalation of Lithium Ions into Graphite Electrodes Studied by AC Impedance Measurements. *J. Electrochem. Soc.* **1999,** *146* (8), 2794-2798.
32. Young, M. J.; Holder, A. M.; George, S. M.; Musgrave, C. B., Charge Storage in Cation Incorporated A-MnO_2. *Chem. Mater.* **2015,** *27* (4), 1172-1180.
33. Bouilly, D.; Janssen, J. L.; Cabana, J.; Côté, M.; Martel, R., Graft-Induced Midgap States in Functionalized Carbon Nanotubes. *ACS Nano* **2015,** *9* (3), 2626-2634.
34. Cowan, S. R.; Schulz, P.; Giordano, A. J.; Garcia, A.; MacLeod, B. A.; Marder, S. R.; Kahn, A.; Ginley, D. S.; Ratcliff, E. L.; Olson, D. C., Chemically Controlled Reversible and Irreversible Extraction Barriers Via Stable Interface Modification of Zinc Oxide Electron Collection Layer in Polycarbazole-Based Organic Solar Cells. *Adv. Funct. Mater.* **2014,** *24* (29), 4671-4680.
35. Li, S.-C.; Wang, J.-g.; Jacobson, P.; Gong, X. Q.; Selloni, A.; Diebold, U., Correlation between Bonding Geometry and Band Gap States at Organic−Inorganic Interfaces: Catechol on Rutile TiO_2(110). *J. Am. Chem. Soc.* **2009,** *131* (3), 980-984.

6 Modification of ZnO Surfaces with Aryldiazonium Ions

6.1 Introduction

ZnO is a transparent semiconductor with a wide direct band gap in the UV region (3.37 eV) with a high free exciton binding energy (60 meV).[1] These properties, along with its abundance compared to commonly-used materials like ITO,[2] make it an attractive material for use in a range of electronic, optoelectronic, electrochemical and electromechanical applications.[3]

6.1.1 Structure

ZnO typically adopts the wurtzite crystal structure (Figure 6.1) composed of alternating planes of tetrahedrally coordinated O^{2-} and Zn^{2+} ions stacked along the c-axis. By varying the growth conditions, rocksalt and zincblende structures can also be obtained.[4] As all three structures lack inversion symmetry, ZnO forms polar crystals where one face terminates in Zn ions (Zn-polar, 0001) and the other terminates in O ions (O-polar, $000\bar{1}$).[5] The bonding character in ZnO is intermediate between ionic and covalent,[4] resulting in these polar surfaces being charged (positively charged Zn-polar and negatively charged O-polar). The mechanism that stabilises these charged surfaces is disputed but is thought to be a combination of structural reconstructions and termination by atmospheric adatoms.[6-8] ZnO also exhibits non-polar faces such as the m-plane ($10\bar{1}0$ surface (Figure 6.1) which are composed of Zn-O dimers, giving mixed Zn and O termination.

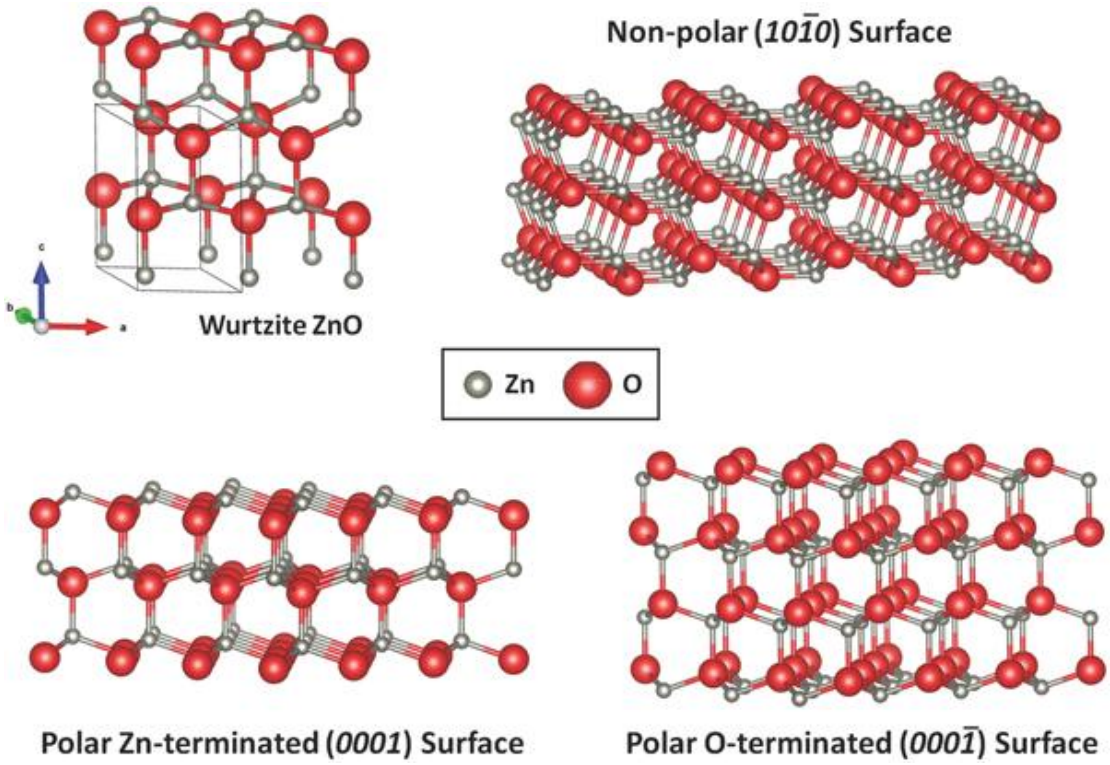

Figure 6.1: Crystal structure of wurtzite ZnO. Reproduced from reference 9.

6.1.2 Synthesis

6.1.2.1 Bulk Crystals

ZnO is particularly attractive for applications as a semiconductor because, unlike a number of other materials, it is possible to prepare large single crystals.[1] Bulk ZnO can be grown using hydrothermal, melt, vapour-phase and solution growth techniques.[10] As the bulk single-crystal ZnO material used in this work was grown hydrothermally, this growth method will be discussed in greater detail.

Hydrothermal growth takes place at elevated temperature and pressure (300-400 °C and ~100 MPa) in a Pt-lined autoclave using ZnO dissolved in a KOH/LiOH solution.[1, 10] The growth reaction proceeds according to Equation 6.1 (Zn-polar surface) and Equation 6.2 (O-polar surface) where supersaturation of ZnO_2^{2-} causes nucleation of ZnO at the surface of a seed crystal.[11]

$$Zn^{2+}(surface) + ZnO_2^{2-} \rightarrow 2ZnO\ (crystal) \qquad \text{Equation 6.1}$$

$$O^{2-}(surface) + ZnO_2^{2-} + 2H_2O \rightarrow 4OH^- + ZnO\ (crystal) \qquad \text{Equation 6.2}$$

This approach has been used to give large crystals of high quality at lower processing temperatures than other methods. However, crystal growth is relatively slow and the mineralising KOH and LiOH

result in Li^+ and K^+ contamination of the resulting crystal. Contamination by group 1 elements has been found to introduce donor and acceptor states into ZnO, making it difficult to control the electronic behaviour of the crystal.[12]

6.1.2.2 Thin Films

ZnO thin films can be prepared by a range of processes including magnetron sputtering, pulsed laser deposition, chemical vapour deposition, molecular beam epitaxy (MBE),[1, 5, 13] atomic layer deposition,[14] electrodeposition[15] and sol-gel.[16] These methods produce films with a range of morphologies and degrees of crystallinity from amorphous to single crystals.[1] The substrate for film growth is critical to producing films with few defects, requiring a substrate material with a near lattice-match to reduce strain and dislocations.[5] One of the applications of large single-crystal ZnO is as substrates for homoepitaxial growth of ZnO thin films.[1] Buffer layers of other materials or even ZnO itself have been used to pre-coat substrates such as sapphire to reduce the influence of lattice mismatch.[17] In this work, ZnO thin films prepared by magnetron sputtering and MBE were studied and these methods will be described briefly.

Magnetron sputtering has been used extensively as a growth technique for ZnO films due to its low cost, simplicity and low deposition temperature. ZnO films are deposited onto the substrate by ablation of a zinc target by an argon/oxygen plasma prepared by radio-frequency power.[13] As the impact of the sputtered particles on the target is essentially uncontrolled, uniform film growth is difficult to achieve and the resulting material is typically polycrystalline with a high defect density.[1]

Molecular beam epitaxy uses solid sources in effusion cells that are heated under high vacuum such that a beam of gaseous materials sublimes towards the substrate. The atoms condense on the substrate and the film will grow epitaxially from the surface. The composition of the film is varied by using additional effusion sources or other sources such as plasma. Film growth can be monitored throughout the process by reflection high-energy electron diffraction.[18] In the case of ZnO, growth typically occurs using a Zn effusion cell and an oxygen plasma source.[19] MBE growth of ZnO with high crystal quality on materials such as sapphire has been reported extensively.[20]

6.1.2.3 Nanostructures

ZnO nanostructures, especially one-dimensional structures such as nanorods and nanowires, have been extensively researched for a number of applications including solar cells, nanogenerators, biosensors, LEDs and transistors.[3, 4, 21-23] ZnO nanostructures have been grown by vapour deposition methods,[22, 23] wet chemical synthesis[3] and electrodeposition.[21]

Vapour deposition methods such as chemical vapour deposition and physical vapour deposition utilise a vapour phase of either ZnO itself (physical vapour deposition) or a reactive precursor (chemical vapour deposition) which reacts with a substrate to nucleate growth. Catalytic particles are frequently employed to improve the crystallinity and dimensions of the nanostructures, however, they can also contaminate the ZnO material and influence its properties.[24]

Wet chemical synthesis methods employed for ZnO nanostructures include solvothermal, sol-gel and controlled precipitation.[3, 23, 25] The solvothermal method is identical in principle to the hydrothermal method used for bulk crystal growth discussed above, however, the time and temperature is such that nanoscale ZnO is produced.[25]

Electrodeposition of ZnO nanostructures occurs by reaction of Zn^{2+} with OH^- (Equation 6.3) formed by electroreduction of O_2 (Equation 6.4) or NO_3^{2-} (Equation 6.5).[26, 27] The composition of the resulting nanomaterials can be varied by changing the Zn^{2+} precursor and the electrolyte. Growth can occur with or without a seed layer to aid nucleation of the ZnO nanostructures where the seed layer improves adhesion and control over the ZnO at the cost of additional processing steps.[3, 21]

$$Zn^{2+} + 2OH^- \rightarrow ZnO + H_2O \qquad \text{Equation 6.3}$$

$$O_2 + 2H_2O^+ + 4e^- \rightarrow 4OH^- \qquad \text{Equation 6.4}$$

$$NO_3^- + H_2O + 2e^- \rightarrow NO_2^- + 2OH^- \qquad \text{Equation 6.5}$$

6.1.3 Electronic Properties

Despite the favourable electronic and optoelectronic properties of ZnO such as its transparency, wide direct band gap and high exciton binding energy, exploiting these properties has been hindered by the poor control over its conductivity and surface behaviour.[1]

Regardless of preparation method, ZnO is natively n-doped and difficult to prepare as p-type. The mechanisms of this native n-type behaviour are still disputed, however, interstitial and substitutional hydrogen impurities along with native defects are the likely causes.[28, 29] These defects responsible for the intrinsic n-type nature of ZnO also complicate the preparation of p-type ZnO as they act as compensating sites for the acceptor impurities introduced during p-type doping.[30] Recent attempts to overcome this include co-doping or using large group 5 dopants such as Sb.[30-32]

Another unusual property of ZnO is its tendency to form an electron accumulation layer at the material surface.[1] This metallic behaviour at the surface of ZnO arises due to downward band

bending in the near-surface region caused by donor-like surface states.[33] These states are caused by hydrogen or hydroxyl termination of the surface on exposure to moisture and have varying stability based on the structure of the ZnO surface.[7, 34] The adsorption of acceptor molecules such as oxygen can also change the surface conductivity by inducing upward band bending.[35] This sensitivity to environmental conditions has been exploited to prepare gas sensors based on ZnO, however, it complicates the preparation of stable junctions for electronic devices.[36-39]

6.1.4 Applications

Aside from its industrial applications in rubber, textiles, pharmaceuticals and cosmetics,[25] ZnO has attracted significant research interest for applications in electronic, optoelectronic, electromechanical and electrochemical devices – some of which will be detailed briefly below.

ZnO is an ideal material for transparent electronics due to its high optical transparency, high electron mobility, availability and favourable processing parameters.[40] ZnO thin films[41] and nanowires[42] have both been used to prepare transparent transistor devices.

In addition to its electronic transport properties, ZnO is also an attractive material for optoelectronics. The wide direct band gap and high exciton binding energy of ZnO make it a promising material for short-wavelength lasing and luminescence applications.[21] ZnO has been used in light emitting diodes (LEDs) based on heterojunctions with p-type materials such as GaN[43] or as a light extraction layer incorporated into other LED structures.[44] Homojunction LEDs using ZnO have also been reported,[45] despite the difficulties in preparing p-type ZnO.[40] The high exciton binding energy is particularly important for lasing applications where stable excitons are necessary.[3] Room temperature lasing in ZnO has been studied extensively[46] with more recent developments relying on nanostructured materials.[47] As the band gap of ZnO is in the UV region, it has also been applied as a material in UV photodetectors.[40, 48]The high optical transparency and carrier mobility of ZnO is also desirable in photovoltaic applications.[49] ZnO materials have been explored for a number of solar cell configurations including perovskite,[50, 51] semiconductor-sensitised,[52] dye-sensitised [53] and polymer devices.[54, 55]

The high electromechanical coupling constants of ZnO make it an exciting material for piezoelectric devices. These properties have been exploited to make memory devices,[56] logic elements,[57] surface acoustic wave devices,[58] nanogenerators[59] and self-powered devices.[60] Piezotronic effects have also been used in sensor devices for temperature,[61] humidity,[62] gases[63] and biomolecules.[64, 65]

In addition to sensors based on piezoelectric effects, sensors exploiting the surface reactivity of ZnO have also been fabricated.[40] ZnO gas sensors rely on measuring these conductivity changes when target gas molecules adsorb to the surface, resulting in a change in resistivity compared to a bare or oxygen-coated surface.[37-39] In addition to its favourable electronic properties ZnO is biocompatible, enabling its use in biosensors.[66] Biosensors based on enzymes immobilised on ZnO transistors have been used in the detection of biomolecules including glucose,[67] cholesterol[68] and uric acid.[69]

ZnO has also been explored as a photocatalyst for degrading organic contaminants[70] and hydrogen production via water splitting.[71] ZnO is cheaper and more environmentally friendly than the more commonly-used TiO_2. However, the wide band gap of ZnO means that it only absorbs in the UV region which only accounts for 4-5% of the solar spectrum.[72] Methods to improve this include tailoring the structure of ZnO,[73] the incorporation of defects[72] and the use of sensitisers such as graphene.[74]

6.1.5 Surface Modification

Surface modification of ZnO has been extensively studied as a method to control its electronic properties and attach new functionalities. ZnO modification has been previously reported using thiol, phosphonate and carboxylate SAMs,[75-80] silanes,[81] catechols[82] and alkenes.[83] Most surface modifiers attach through condensation-type reactions with surface hydroxyls and the ease and strength of modification depends on the ZnO crystal structure.[80-84]

A major application of ZnO surface modification is tuning electronic behaviour such as work function and band bending due to the electronic coupling between the modifier and the surface.[76, 79-83, 85] The nature of the modifier has been found to influence the work function based on the dipole moment or para-substituent Hammett parameter for aryl modifiers where more electron-withdrawing groups increased the work function and vice versa.[76, 80, 86] By changing the charge density at the surface of the material, the amount of band bending is also affected by surface modification.[82] Another objective of surface modification is to stabilise the ZnO surface to environmental variation and corrosion. As noted earlier, the ZnO surface is very sensitive to environmental factors such as humidity and gas adsorption. While this property can be exploited to produce sensor devices, for other applications, it results in erratic performance when ambient conditions change.[75, 85] Surface modification has also been used to immobilise interesting functionalities to ZnO surfaces by molecular tethering approaches. Functionalities that have been molecularly tethered to ZnO surfaces include biosensor recognition elements,[87] electroactive and photoactive molecules[88] and quantum dots.[89]

6.1.5.1 Modification with Thiols

While they are extensively studied for the modification of metal surfaces,[90] thiols are one of the least studied modifiers for metal oxide modification, having been used to modify oxidised Cu surfaces, cuprate superconductors, and ZnO.[75, 78, 91, 92] The small number of examples is likely due to the instability of thiol modifiers, especially to oxidation.[93] Despite this general instability, thiol layers have been found produce stable uniform layers on the m-plane face of ZnO.[78] However, this does not extend to O-polar surfaces,[75] indicating that the structure of the substrate has a significant effect on thiol binding. The lack of reports of thiol modification of oxides also extends to the binding modes and mechanisms which are poorly understood.[94] Cowan et al. modified ZnO surfaces with benzylphosphonic acids and alkanethiol layers and found that the modified surfaces were less sensitive to aging in air and light soaking than bare ZnO.[85] Surface modification was also found to improve the resistance of ZnO to etching by NH_4Cl with the density of the attached modifier layer corresponding to the reduction in etch rate.[75]

6.1.5.2 Modification with Carboxylates

Carboxylates are widely studied due to the ready availability of their derivatives enabling a range of surface chemistries after modification. Carboxylates have been used to modify oxides such as TiO_2, Al_2O_3, ZnO, Fe_2O_3 and WO_3.[95-97] Carboxylates can attach via several different modes (Figure 6.2) involving covalent or non-covalent interactions depending on the molecule, conditions and the substrate.

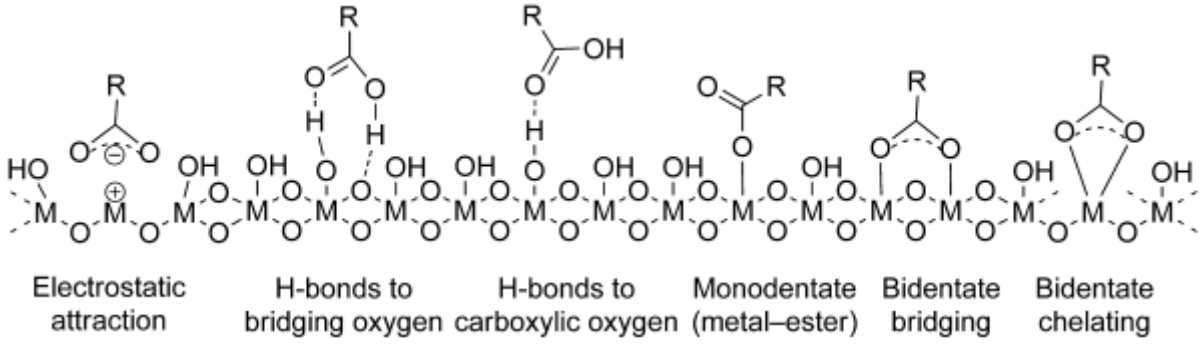

Figure 6.2: Binding modes of carboxylates ($R\text{-}COO^-$) to metal oxide (M-O) surfaces. Adapted from reference 94.

This can lead to widely varying stabilities between different systems.[94] The stability of carboxylates on surfaces is typically weak and they are vulnerable to hydrolysis,[98] however, multi-dentate modifiers can be used to improve stability. For example: on m-plane single crystal ZnO surfaces,

octadecanoic acid was unable to form stable monolayers[78] whereas citric acid formed a multidentate complex to ZnO nanoparticles that was stable for 6 days at 80 °C in acetonitrile.[95]

6.1.5.3 Modification with Phosphonates

Phosphonates are attractive for surface modification due to their ease of preparation and storage and stability to hydrolysis.[94] The assembly of phosphonates on the oxide surface depends on the reaction conditions and substrate.[99] The attachment mechanism varies based on the Lewis acidity of the oxide surface but generally proceeds via heterocondensation reactions to give P-O-metal bonding (Scheme 6.1). Additionally, a thermal annealing step is sometimes necessary to induce the heterocondensation reaction leading to covalent attachment to the surface.[100, 101]

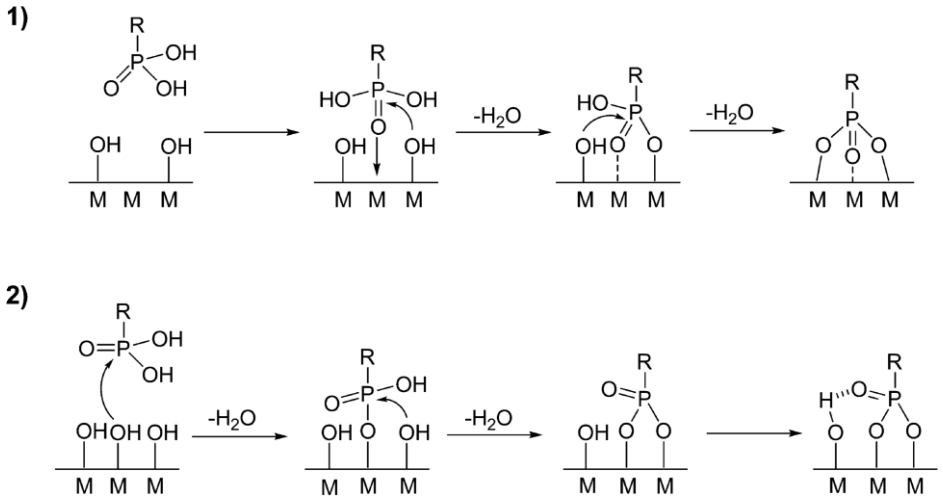

Scheme 6.1: Attachment of phosphonates to: 1) Lewis acidic metal oxides, 2) poorly Lewis acidic metal oxides. Adapted from reference 101.

Phosphonates can bind in either mono-, bi- or tri-dentate modes either covalently or through electrostatic and hydrogen bonding interactions (Figure 6.3). The presence of these bonding modes can be determined by FT-IR based on the relative intensity of P-O, P=O and P-OH vibrations.[84]

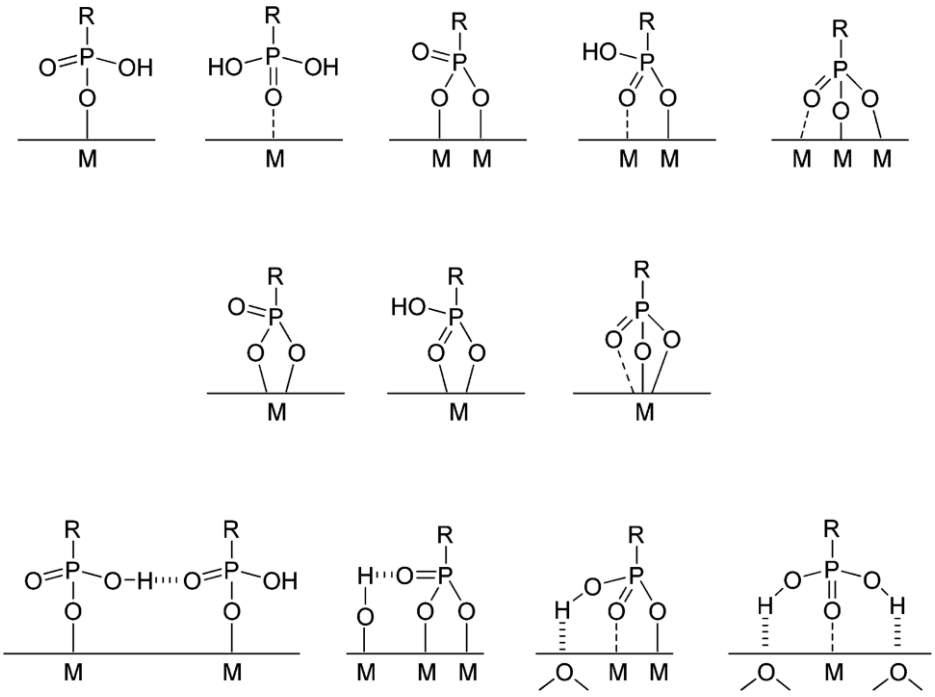

Figure 6.3: Binding modes of phosphonates to metal oxide surfaces. Adapted from reference 101.

Phosphonates have been used to modify a wide variety of metal oxides including ZnO, TiO_2, ZrO_2, SnO_2, and ITO.[75, 101, 102] Timpel et al. attached fluorinated aryl and alkyl phosphonates to Zn-polar ZnO single crystal surfaces and characterised the morphology of the layer and its effect on the work function of the surface.[79] The stacking interactions between adjacent aryl molecules were found to improve packing density compared to the alkyl layer. The change in work function due to binding was higher for the alkyl phosphonate, possibly due to its higher dipole moment than the aryl layer.

6.1.5.4 Modification with Silanes

Silanes have been widely studied for the modification of silica-based materials and have since been extended to metal oxides including ZnO, TiO_2, Al_2O_3, and Fe_3O_4.[103-105] Silane monolayer formation occurs by a three-step mechanism (Scheme 6.2). Initially, the silane molecules hydrolyse at the surface to create hydroxysilanes which then self assemble by hydrogen bonding interactions with the substrate and attractive forces between the chains. Attachment to the surface occurs via a condensation reaction with surface OH groups. Additionally, silanisation reactions have the possibility of forming disordered multilayers at the surface due to condensation reactions occurring between adjacent molecules rather than the substrate.[94] The stability of silane monolayers on metal oxides is generally poor. In a comparative study by Sakeye and Smått, the attachment of silanes to metal oxide surfaces was much weaker than silica and the layers hydrolysed more rapidly at both pH

2 and pH 10.[102] Silanisation has been used to increase the hydrophobicity and tune the work function of ZnO nanowires. Single nanowire field-effect transistor devices prepared from silyl-modified nanowires had improved I-V characteristics over as-prepared and hydroxylated nanowires.[81]

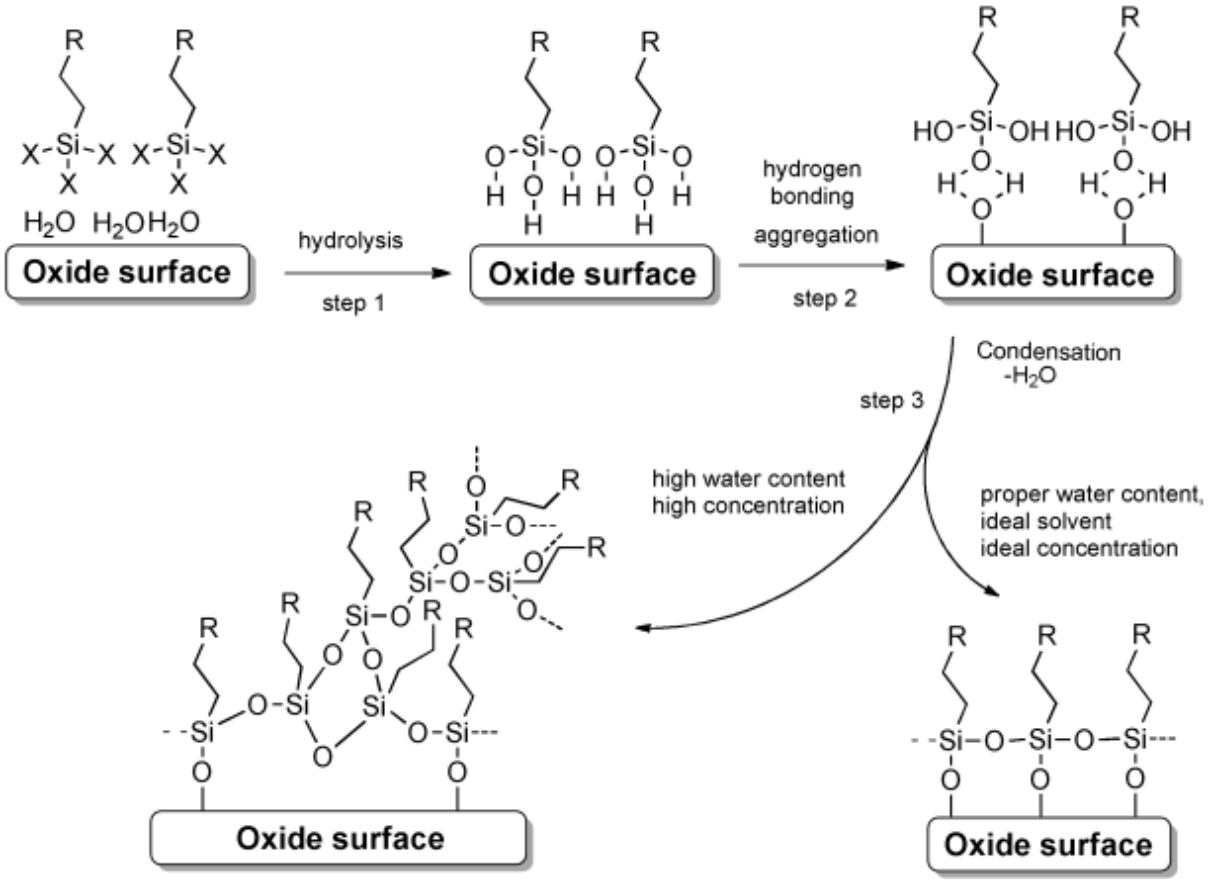

Scheme 6.2: Formation of monolayers by alkyl silanes on metal oxide surfaces. Adapted from reference 94.

6.1.5.5 Other Modification Methods:

In addition to alkyl and aryl self-assembled monolayers, ZnO surfaces have been modified with catechols and alkenes.[77, 82, 83] Arnaud et al. modified m-plane single crystal ZnO surfaces with nitrocatechol in order to shift the surface band positions. The shift in band energies at the surface was associated with the proposed formation of Zn-O bonding between the nitrocatechol and the surface as determined by DFT calculations. Alkene-derived layers were attached to ZnO by photochemical grafting as a platform for attaching sensing elements and tune the electronic properties of ZnO interfaces. The linkage between the ZnO surface and alkyl layer was not directly identified, however, the loss of C=C and O-H functionalities was observed by FT-IR.

Prior to the commencement of this work, there were no reports of aryldiazonium modification at metal oxide surfaces. Recently, electrochemical modification of ZnO in non-aqueous conditions with aryldiazonium salts has been reported by Wang et al. and this will be discussed below in context with this thesis work.[106]

This chapter describes the development of conditions to modify MBE-grown ZnO surfaces with aryldiazonium ions by non-electrochemical and electrochemical methods. These methods were then extended to bulk single crystal ZnO surfaces to investigate the effect of modification on the properties of different crystal faces.

6.2 Materials and Methods

6.2.1 ZnO Substrates

6.2.1.1 MBE-Grown ZnO

ZnO samples grown by MBE were prepared by Adam Hyndman from the Department of Physics and Astronomy, University of Canterbury. These samples were ~450 nm ZnO films deposited on Al_2O_3 substrates. Before use, the ZnO samples were cleaned ultrasonically in HPLC grade acetone, methanol and IPA and then dried in N_2 gas.

6.2.1.2 Single Crystal ZnO

Single crystal ZnO samples used in this work were cut from 0.5 mm thick hydrothermally grown m-plane and c-axis double-sided polished single crystal wafers obtained from Tokyo Denpa Co. Ltd (Japan).[107] Before use, the ZnO samples were cleaned ultrasonically in HPLC grade acetone, methanol and IPA and then dried in N_2 gas.

6.2.2 FT-IR Measurements

IR Spectra for ZnO samples were collected by gently pressing the ZnO surface onto a diamond ATR prism. Mid-IR spectra were recorded using 1024 scans at 4 cm^{-1} resolution from 600 to 4000 cm^{-1}.

6.2.3 XPS Measurements

6.2.3.1 Monochromatic XPS

Monochromatic XPS data was collected according to the parameters described in Chapter 2. Samples were mounted onto a sample bar by pressing them into conductive silver paste which was used to contact to the top surface of the sample. Peak positions were referenced to aromatic C at 284.8 eV.

6.2.3.2 Synchrotron XPS

Synchrotron XPS data was collected by Assoc. Prof. Martin Allen, Alexandra McNeill and Rodrigo Gazoni on the soft X-ray beamline at the Australian Synchrotron, Melbourne. Samples were electrically grounded to the spectrometer by a Ta foil sample holder and platinum paste to prevent charging. Photoemission spectra were collected using a Specs Phoibos 150 hemispherical electron energy analyser with the detector axis normal to the sample surface. To maximise surface sensitivity, the incident x-ray photon energy (hv) was varied for each scan: O 1s and C 1s core level spectra were collected at hv = 680 eV, P 2p core level spectra were collected at hv = 280 eV and valence band spectra were collected at hv = 150 eV. Survey spectra were collected at hv = 1486.6 eV to allow comparison with data from monochromatic X-ray sources. The binding energy scale of each scan was calibrated using the Au 4f core level doublet of a sputter-cleaned Au reference foil.

6.2.4 Electrochemical Measurements

Electrochemical measurement of ZnO surfaces was conducted in 0.1 M pH 8 phosphate buffer using a top-loading cell setup. The ZnO working electrode architecture used in electrochemical experiments is shown in Figure 6.4. These electrodes were prepared by affixing a strip of Cu foil to the top face of the ZnO sample with polyimide tape, more polyimide tape was then used to mask the Cu foil from both sides. This resulted in the Cu foil and ZnO sample sandwiched together between two pieces of polyimide tape such that half of the top ZnO surface was exposed to act as a working electrode (area = ~0.18 cm^2) and the end of the Cu strip was exposed to allow electrical contact with the potentiostat leads. The contact between the ZnO surface and Cu strip was maintained by a Teflon clamp (Figure 6.4B). For MBE samples, only the top face is conducting whereas single crystal samples can conduct through to the bottom face. Single crystal samples are referred to in this chapter by the top face contacting the Cu foil e.g. O-polar even though both faces are exposed to solution.

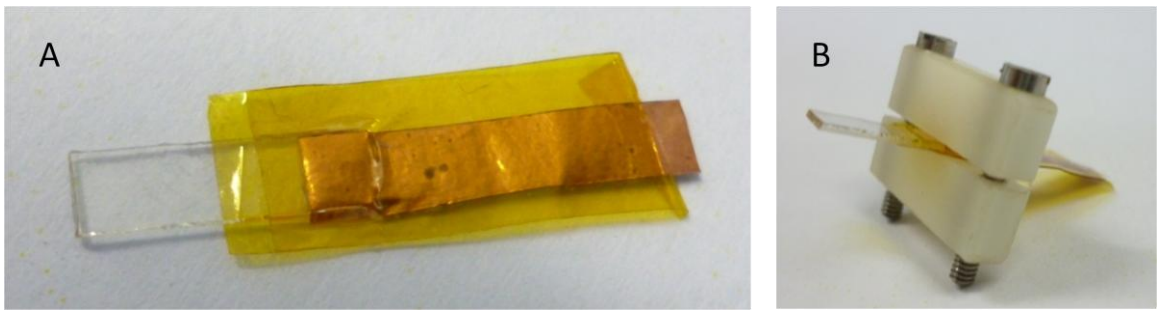

Figure 6.4: Photographs of ZnO working electrode showing polyimide tape sealing and Cu foil top-contact (A), and (B) Teflon clamp compressing Cu contact.

6.2.5 Modification with Aryldiazonium Ions

6.2.5.1 Non-electrochemical Modification

Unless stated otherwise, ZnO samples were modified with aryl layers by immersion for 1 h in 5 mL of 0.1-1 M pH 8 phosphate buffer solution containing 50 mM aryldiazonium BF_4^- salt on an orbital shaker. Samples were cleaned after modification by rinsing in ultrapure water then sonicated in HPLC grade acetone, methanol and IPA.

6.2.5.2 Electrochemical Modification

Aryldiazonium ions were electrochemically grafted to ZnO electrodes prepared by the method described above. Electrochemical grafting was carried out by cycling between 0.2 and -1.5 V for 20 scans at 50 mV s^{-1} scan rate in degassed 0.1 M pH 8 phosphate buffer solution with 5 mM aryldiazonium BF_4^- salt. After rinsing in ultrapure water, the electrodes were disassembled and the modified ZnO surface was ultrasonically cleaned in HPLC grade acetone methanol and IPA.

6.3 Results and Discussion

6.3.1 Modification of MBE-grown ZnO using Aryldiazonium Ions

Preliminary experiments were conducted on ZnO samples grown by MBE on sapphire substrates. The properties of MBE-grown ZnO can be controlled by adjustment of the growth conditions, however, MBE-grown ZnO tends to be O-terminated regardless of the crystal orientation of the surface.

6.3.1.1 Initial MBE-grown ZnO Characterisation

As the growth system for the MBE samples used in this work was still being developed while this work was ongoing, the crystal quality of the surfaces used was variable. As shown by the AFM images in Figure 6.5, early surfaces (Figure 6.5A) had a very rough and granular morphology (RMS roughness ≈ 6 nm) whereas later samples (Figure 6.5B) had smoother surfaces (RMS roughness ≈ 2 nm) with visible triangle terrace rearrangements typical of crystalline ZnO surfaces.[8]

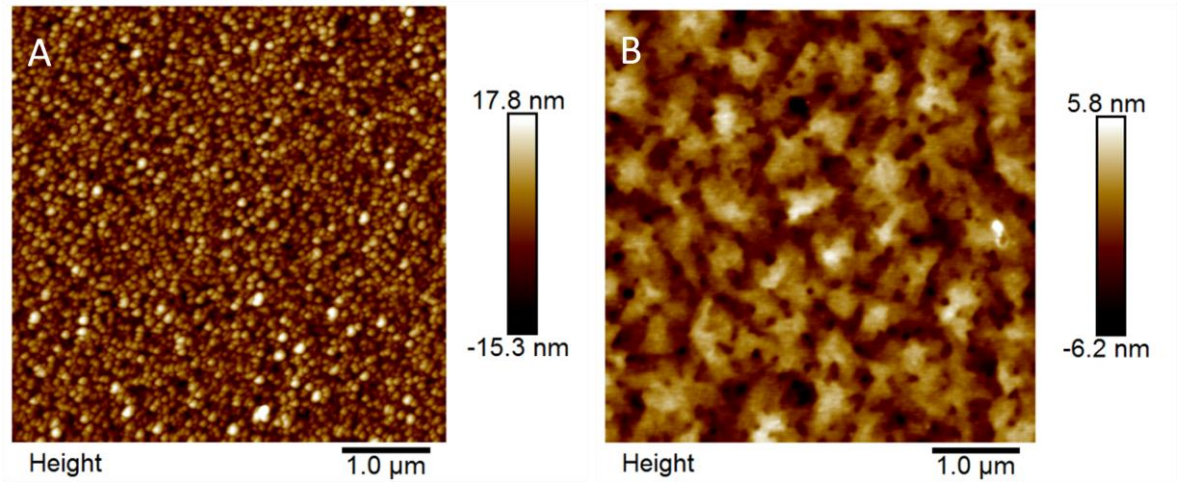

Figure 6.5: Representative AFM height images of MBE-grown ZnO surfaces: A. Early sample showing high roughness and granularity, B. later sample showing smoother and more crystalline surface.

The FT-IR spectrum of bare MBE-grown ZnO (Figure 6.6A) shows a steeply curved baseline that was observed for all samples. This baseline complicates the baseline fitting procedure on the steep areas of the curve and at the inflection points. The baseline-corrected spectrum of bare MBE ZnO is shown in Figure 6.6B where a number of ill-defined features are visible between 1800 cm^{-1} and 1000 cm^{-1} with sharper peaks below 1000 cm^{-1}. Overlaid on the MBE-grown ZnO spectrum shown in Figure 6.6B is the FT-IR spectrum for the Al_2O_3 substrate where it is apparent that the majority of the features visible in the ZnO spectrum are present in the spectrum for the support. There are small differences visible between 1800-1500 cm^{-1}, however, these are likely artifacts from the baseline fitting as this range is near the inflection point in the raw data. This suggests that most of the observed features in the ZnO spectrum are from the underlying Al_2O_3 support due to the evanescent wave at the ATR prism penetrating through the ~450 nm ZnO film. These features have been assigned to OH species and adsorbed water on Al_2O_3 and ZnO surfaces.[108, 109]

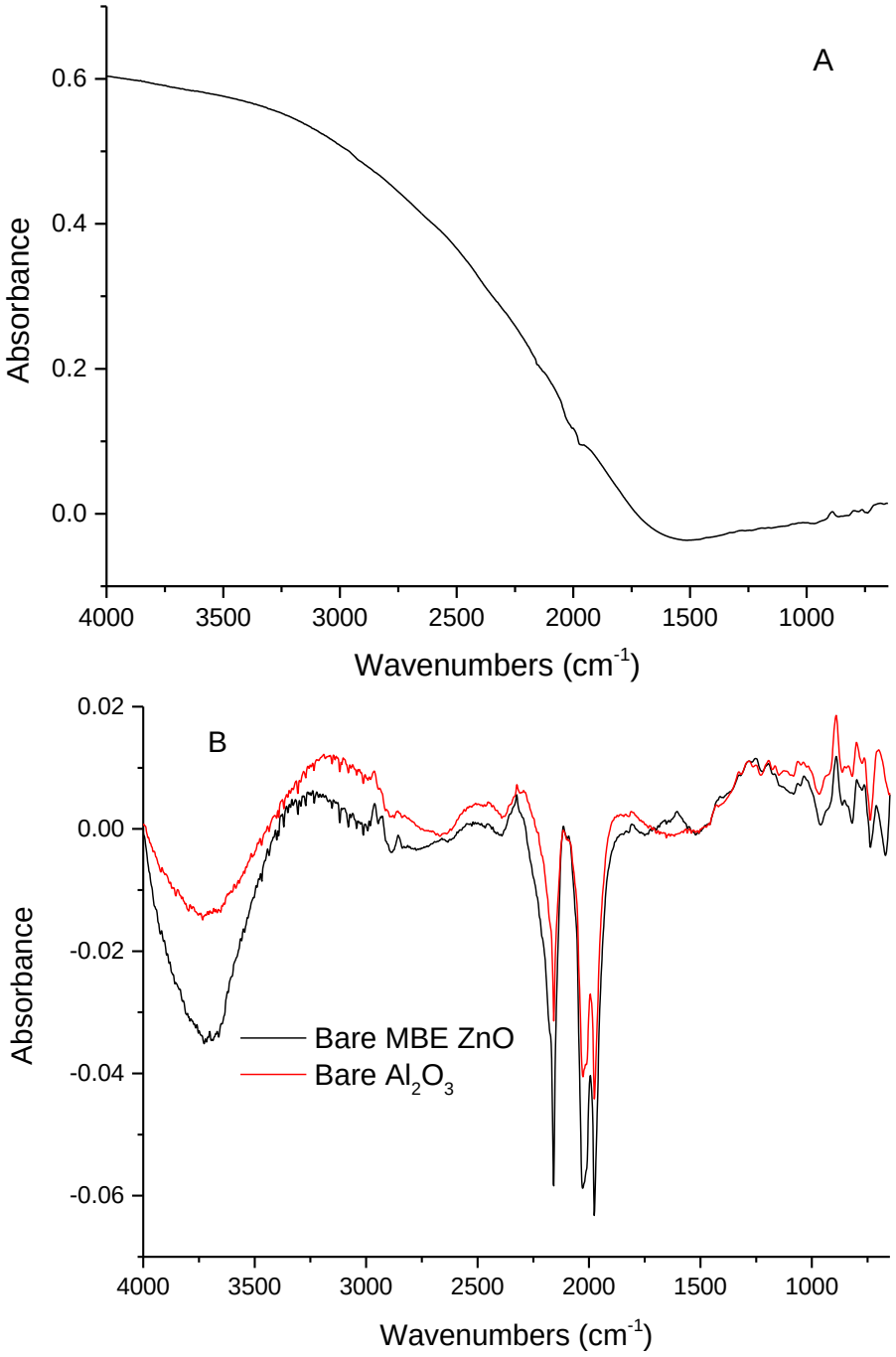

Figure 6.6: FT-IR spectra of: A. MBE-grown ZnO as-collected, B. the front ZnO face and back Al_2O_3 face of and MBE-grown ZnO sample after baseline correction.

6.3.1.2 Non-Electrochemical Modification with Aryldiazonium Ions

As ZnO is amphoteric, it has a limited pH stability window in aqueous solution which limits the available modification conditions. Additionally, as a semi-conducting oxide, it is assumed that ZnO cannot reduce the aryldiazonium ion spontaneously, requiring other conditions to generate reactive species to graft to the surface. However, the surface electron accumulation layers observed at single

crystal ZnO surfaces may be able to act as a reduction source.[1] The instability of ZnO at acidic pH was observed when grafting was attempted using H_3PO_2 as a reducing agent; the ZnO film was stripped from the Al_2O_3 substrate in the acidic conditions.

As was shown in Chapter 3, neutral or high pH solutions can be used to modify planar non-conducting substrates. This approach was extended to the modification of ZnO as it is stable above pH 7.[110] Initially, pH 10 was used as this is within the centre of the stability window for ZnO and thus small changes in the stability of the surface (such as from high energy morphologies on rough substrates) should not cause the surface to dissolve at this pH.[111] ZnO samples were immersed in 0.1 M pH 10 HCO_3^-/CO_3^{2-} buffer with 50 mM NBD and 4-carboxybenzenediazonium (CBD) for 1 h. These surfaces were characterised by AFM before (Figure 6.7A) and after modification (Figure 6.7 B and C). It is apparent from these images that reaction in 0.1 M pH 10 buffer causes damage to the ZnO sample with both modifiers. After reaction with NBD (Figure 6.7B), significant pitting was present on the sample and the roughness of the surface increased to ~12 nm. It is possible that the scattered nature of this pitting is due to it being initiated at defects on the ZnO surface. After treatment in CBD solution, the ZnO surface appears to be stripped back to the Al_2O_3 substrate as seen by the smooth underlying surface (Figure 6.7C) and the low RMS roughness (~0.8 nm). The effect of buffer on the surface was investigated by treating a sample for 1 h in 0.1 M pH 10 buffer solution. As seen in Figure 6.7D, treatment in buffer in the absence of aryldiazonium ion resulted in no changes in the morphology of the surface and thus the damage to the ZnO surfaces observed in their presence must arise from reaction with the aryldiazonium ions. Measurement of the pH of NBD solution after the 1 h reaction showed that the pH of the solution had decreased from pH 10 to pH 4-5 indicating that the observed corrosion is due to this pH decrease. The origin of this pH change is unknown, however, the larger amount of corrosion present in the CBD-modified sample may be due to interactions between the surface and the carboxylate group that have been observed when forming carboxylate monolayers.[78] Although the grafting reaction was conducted in buffer solution, the buffer concentration was only twice that of the aryldiazonium ion solution and thus it may not have sufficient buffering capacity to counteract this pH change.

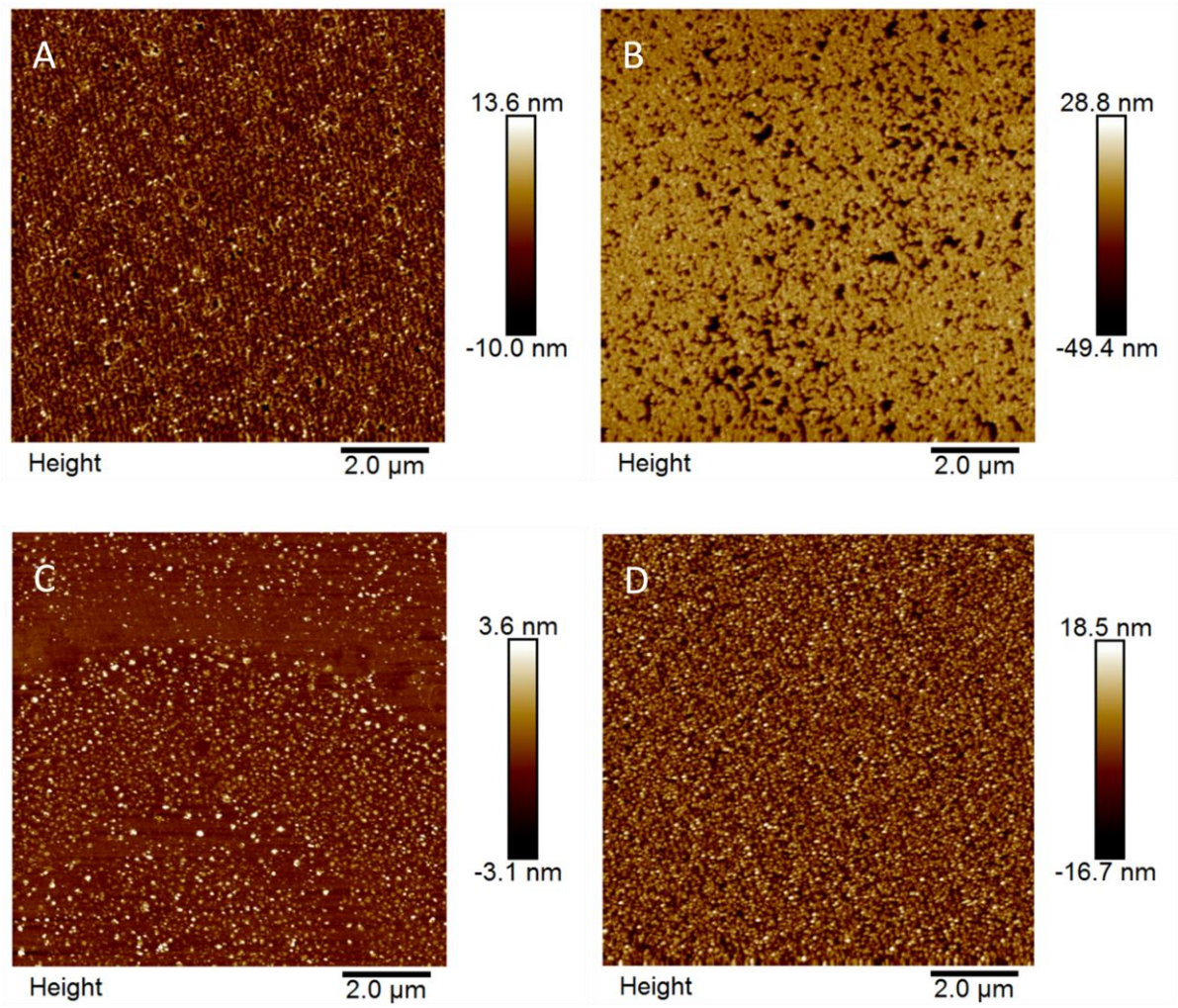

Figure 6.7: AFM height images of MBE-grown ZnO: A. Bare sample, B. ZnO sample after 1 h reaction with 50 mM NBD in 0.1 M pH 10 buffer, C. ZnO sample after 1 h reaction with 50 mM CBD in 0.1 M pH 10 buffer and D. ZnO sample after 1 h treatment in 0.1 M pH 10 buffer.

To prevent this corrosion from occurring, grafting reactions were conducted with the concentration of the buffer solution increased to 1 M. ZnO surfaces were imaged after reaction with NBD (Figure 6.8A) and CBD (Figure 6.8B) in 1 M pH 10 buffer and it is apparent that the increase in buffer concentration prevents corrosion of the surface. However, there are no clear signs of the aryl layer on either surface, possibly due to the high roughness of the ZnO samples.

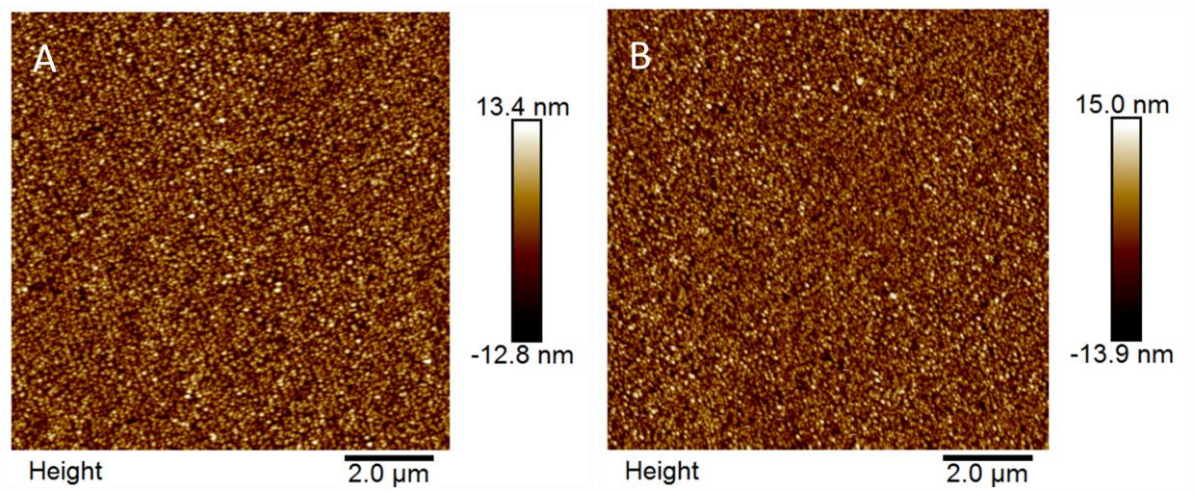

Figure 6.8: AFM height images of MBE ZnO: A. ZnO sample after 1 h modification with 50 mM NBD in 1 M pH 10 buffer and B. ZnO sample after 1 h modification with 50 mM CBD in 1 M pH 10 buffer.

The presence of chemical functionalities on the surface after grafting was investigated by FT-IR. A selected region from the spectra for samples modified for 1 h in 1M pH 10 buffer with NP and carboxyphenyl (CP) groups along with a blank sample prepared under the same conditions in the absence of aryldiazonium ion collected with an air background are shown in Figure 6.9A. It is apparent from these spectra that the modified samples have additional features associated with the attachment of the aryl modifier, however, these features are low intensity and difficult to resolve from the ZnO background. In contrast, the pH 10 buffer-treated blank sample appears identical to the as-prepared ZnO sample spectrum shown in Figure 6.6B.

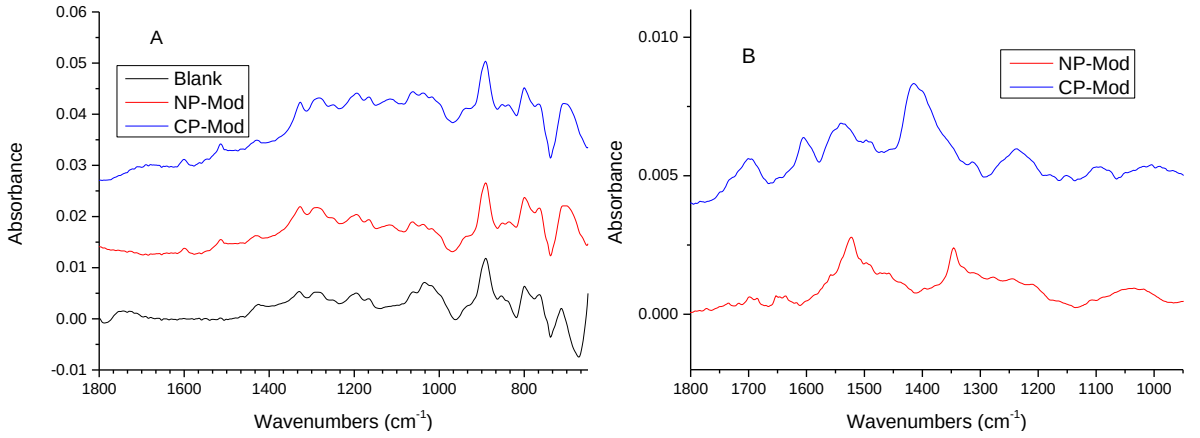

Figure 6.9: FT-IR spectra of MBE-grown ZnO: A. 1 h 1 M pH 10 buffer-treated blank, NP-modified and CP-modified samples collected with an air background. B. 1 h 1 M pH 10 NP-modified and CP-modified samples collected using a 1 h 1 M pH 10 buffer-treated blank sample as the background.

Figure 6.9B shows spectra for the same modified samples collected using the pH 10 buffer blank sample as a background to remove the features associated with the underlying ZnO sample. Peak assignments for these spectra are shown in Table 6.1. After the ZnO/Al_2O_3 features are removed, the only clear features present in the spectrum for the NP-modified sample are the N=O asymmetric and symmetric peaks (1524 cm^{-1} and 1344 cm^{-1} respectively) from the nitro group. For the CP-modified sample, features associated with the carboxy group and the aryl ring were observed. The peaks at 1697 cm^{-1}, 1416 cm^{-1} and 1235 cm^{-1} correspond to the C=O stretching, C-OH bend and O-C stretch vibrations respectively. The peak assigned to the C-OH bend is unusually intense, however, this is most likely an artifact from the background subtraction due to a mismatch in the baselines of the CP-modified and pH 10 blank samples. There are also two C=C stretching peaks (1607 cm^{-1} and 1542 cm^{-1}) present due to the para-substituted aryl ring.

Table 6.1: Table of FT-IR peak assignments for samples modified for 1h in 1 M pH 10 buffer solution with CP and NP groups.

NP-Mod		CP-Mod	
Peak Position	Peak Assignment	Peak Position	Peak Assignment
1524 cm^{-1}	N=O asymmetric stretch	1697 cm^{-1}	C=O stretch
1344 cm^{-1}	N=O symmetric stretch	1607 cm^{-1}	C=C stretch
		1542 cm^{-1}	C=C stretch
		1416 cm^{-1}	C-OH bend
		1235 cm^{-1}	O-C stretch

In summary, these results show that spontaneous modification of MBE-grown ZnO with aryldiazonium ions can be achieved in aqueous solution at high pH. However, the reaction of aryldiazonium ions leads to corrosion of the ZnO surface at low buffer concentrations through acidification of the reaction solution by an unknown mechanism. At high buffer concentrations, the corrosion of the surface is prevented and successful modification with NP and CP groups has been determined from FT-IR spectra. The relatively low intensity of the IR response for these samples suggests that the amount of film grafted to the surface is small. This is supported by the AFM images which show no changes in morphology resulting from an aryl layer after modification.

6.3.1.3 Electrochemical Modification of MBE-grown ZnO with Aryldiazonium ions

One approach to improve surface coverage of aryldiazonium ions is to use electrochemical grafting. As the surface itself acts as the working electrode to reduce the aryldiazonium ions to aryl radicals, this localises the production of radicals to the surface and limits side reactions in solution. As ZnO surfaces are natively n-type, they are conducting at negative potentials and thus have the capability to reduce aryldiazonium ions.

6.3.1.3.1 Electrode Preparation and Testing

ZnO electrodes were prepared by contacting Cu foil to the ZnO surface and using polyimide tape to mask the Cu from the solution and define the area of the ZnO working electrode (~0.18 cm^2). The electrochemical response of MBE-grown ZnO electrodes was tested in a 3-electrode cell in pH 8 phosphate buffer solution: this medium was selected to prevent damage to the ZnO surface by acidic solutions or Cl^-. The ZnO samples were used without additional doping or UV light exposure to influence their conductivity. When cycling in 0.1 M pH 8 buffer solution between 0.8 V and -1.5 V (Figure 6.10), no current flow is observed above ~-0.2 V and below this value the electrode response is capacitive until the onset of a reduction process at -1.2 V (most likely due to solvent decomposition).[112] In 1 mM solution of the redox probe $K_3[Fe(CN)_6]$ in pH 8 buffer, reduction of the redox probe is evident beginning at -0.2 V, however, a complete reduction peak for this process is not observed within the scan window (Figure 6.10). On the return scan to positive potentials, no corresponding oxidation peak is observed and with repeated cycling, the size of the reduction peak decreases. These results are consistent with local depletion of the Fe^{3+} form of the redox probe at the electrode surface and the lack of p-type conductivity in the ZnO electrode prevents oxidation of the Fe^{2+} form to regenerate the Fe^{3+} at the surface. The clear change in CV response in the presence of a redox probe indicates that the MBE-grown ZnO is able to act as an electrode for reduction reactions.

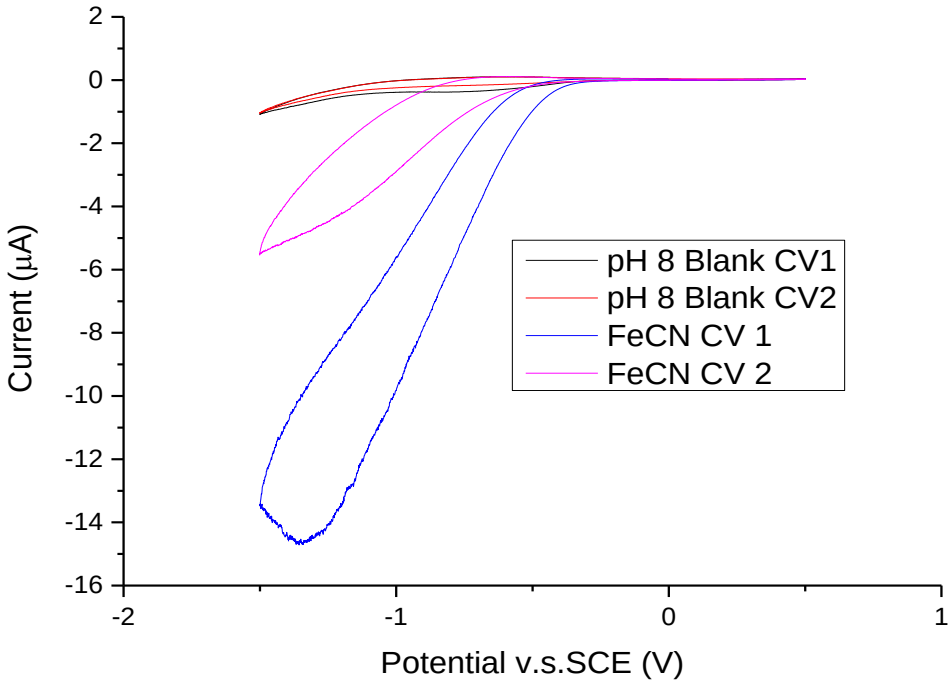

Figure 6.10: CV curves (scans 1 and 2) of MBE-grown ZnO surfaces collected in 0.1 M pH 8 buffer with (FeCN) and without (pH 8 blank) 1 mM $K_3[Fe(CN)_6]$ at 100 mV s^{-1} scan rate.

6.3.1.3.2 Electrochemical Modification of MBE-grown ZnO

Electrografting of aryldiazonium ions to MBE-grown ZnO surfaces was investigated by CV in 5 mM solutions of nitro-, methoxy- and iodobenzenediazonium salt (IBD) in 0.1 M pH 8 phosphate buffer (Figure 6.11). These modifiers were chosen to provide a range of electronic properties in the aryl layer. In the presence of each modifier, the CV response involves a reduction process at low potentials that decreases in peak current with decreasing scan rate. The onset potential of this process varies depending on the modifier: -0.2 V, -0. 4 V and -0.3 V for NBD, MBD and IBD respectively. As with the pH 8 buffer blank and redox probe experiments described above, there is no current flow above ~-0.2 V, confirming that all electrochemical processes observed are occurring at the surface of the ZnO rather than at the Cu foil connector. There appear to be broad reduction peaks centred at ~-0.55 V on the first scans for MBD and IBD grafting whereas there is no defined peak for the NBD grafting process. None of the modifiers form complete blocking films on the surface even after 20 scans. However, the decline in peak current of the reduction process on continued cycling may indicate partial blocking of the electrode surface. Alternatively, the loss in peak current over time may be due to the depletion of the aryldiazonium ion at the surface, either through grafting to the electrode or reaction in solution.

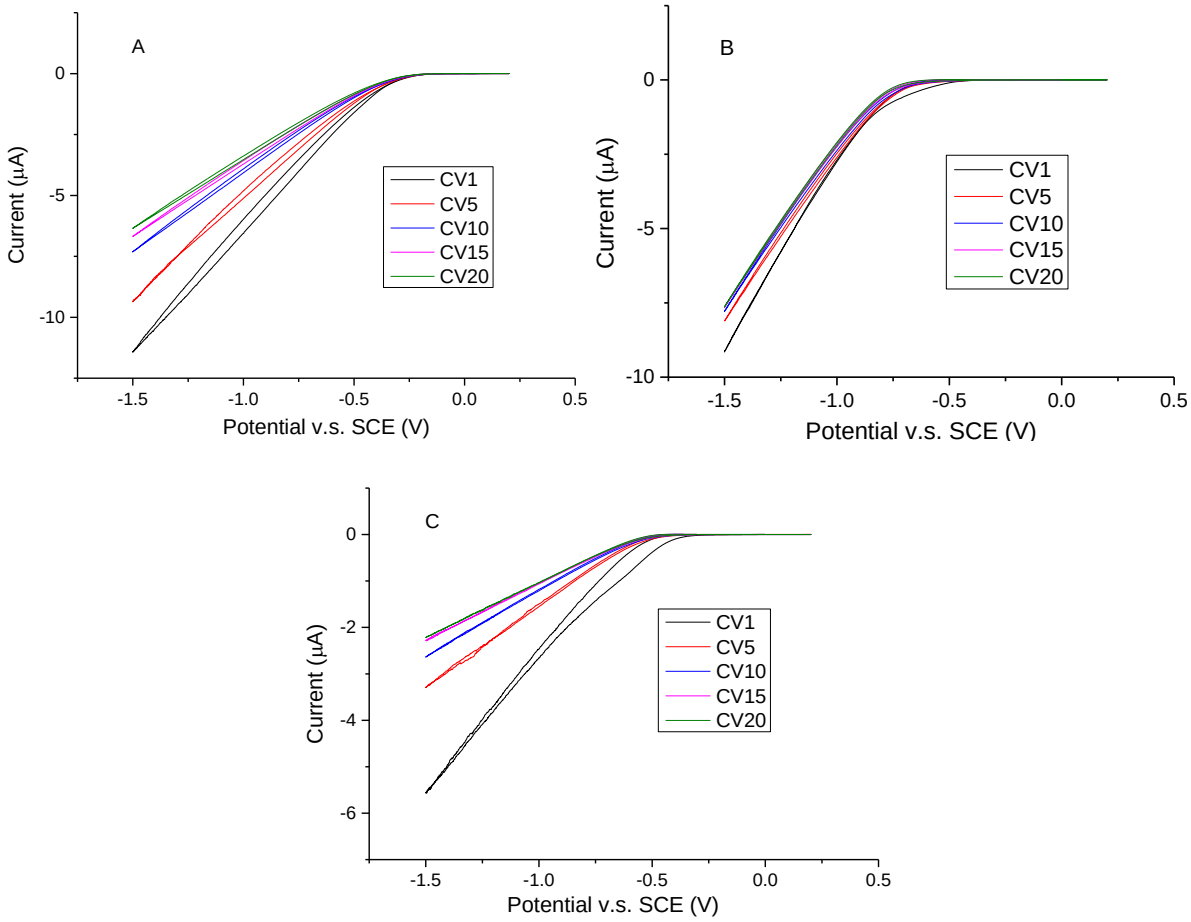

Figure 6.11: CV curves (scans 1, 5, 10, 15 and 20) of MBE-grown ZnO surfaces collected in 0.1 M pH 8 buffer at 50 mV s^{-1} scan rate with 5 mM NBD (A), MBD (B) and IBD (C).

For comparison, the first scan for each modifier and buffer solution in the absence of modifier is shown in Figure 6.12. It is apparent from the increased reduction current in the presence of aryldiazonium salt that the reduction processes observed during the grafting scans is due to the modifiers rather than the buffer solution. Compared to reduction of aryldiazonium salts in acidic solution, the onset of the reduction processes observed here is at significantly more negative potential (e.g. 0.25 V vs. SCE for NBD in acidic solution at GC).[113] However, this decrease in reduction potential has been observed previously for the grafting of diazoates and diazohydroxides which are the most likely species present in solution at pH > 7.[114]

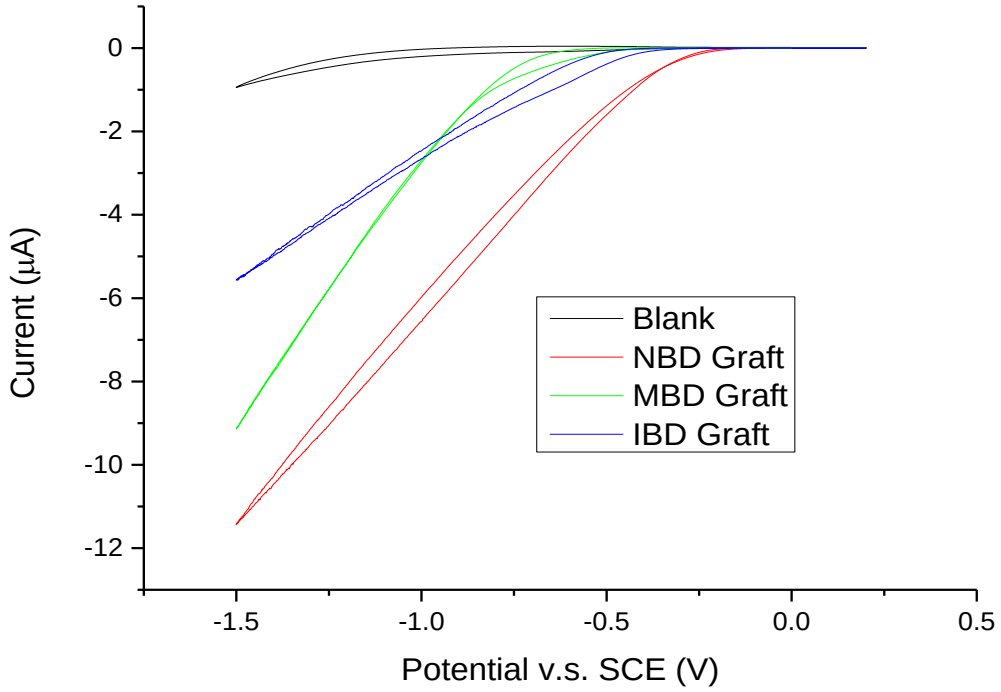

Figure 6.12: CV curves (scan 1) of MBE-grown ZnO surfaces collected in 0.1 M pH 8 buffer at 50 mV s^{-1} scan rate in the absence (Blank) and presence of 5 mM aryldiazonium ion (NBD, MBD and IBD).

6.3.1.3.3 Characterisation of Surface Morphology

The effect of modification and electrochemical cycling on the MBE-grown ZnO surfaces was investigated by AFM (Figure 6.13). After disassembly and cleaning of the ZnO surface, the areas of the surfaces that were masked by polyimide tape during the grafting experiment were imaged to provide an image of the untreated ZnO as the morphology varies significantly between samples (Figure 6.13 A, C and E). From these images it is apparent that the masking process leaves the surfaces unchanged compared to bare MBE-grown ZnO surfaces (Figure 6.5) and that there are minimal tape residues left after cleaning the surface. Comparing these masked regions with the modified regions of the surface (Figure 6.13 B, D and F) it can be seen that the modification process results in significant changes in the appearance of the surface. The unmodified regions of the NP-modified sample have a 'pebbled' morphology with ~500 nm features (Figure 6.13A) whereas the modified regions appear to be covered by a much finer structure with ~100 nm pinholes (Figure 6.13B). The unmodified areas of the MP-modfied surface are more granular in appearance (Figure 6.13C) which becomes covered with small globules after modification (Figure 6.13D). The micron-scale pitting visible on the modified surface is most likely due to damage by bubbles formed during ultrasonic cleaning as they are significantly larger than the pits observed on the spontaneously

modified samples due to etching of the surface (Figure 6.7). The IP-modified surface sample has a pebbled texture in the unmodified regions (Figure 6.13E) which is covered by scattered material after modification that is most likely polymeric aryl species (Figure 6.13F). These images show that for all modifiers, electrochemical modification deposits material on the surface that is stable to sonication. Additionally it appears that the electrochemical grafting process does not damage the ZnO surface as only the MP-modified sample showed pitting and it most likely resulted from the cleaning process rather than modification.

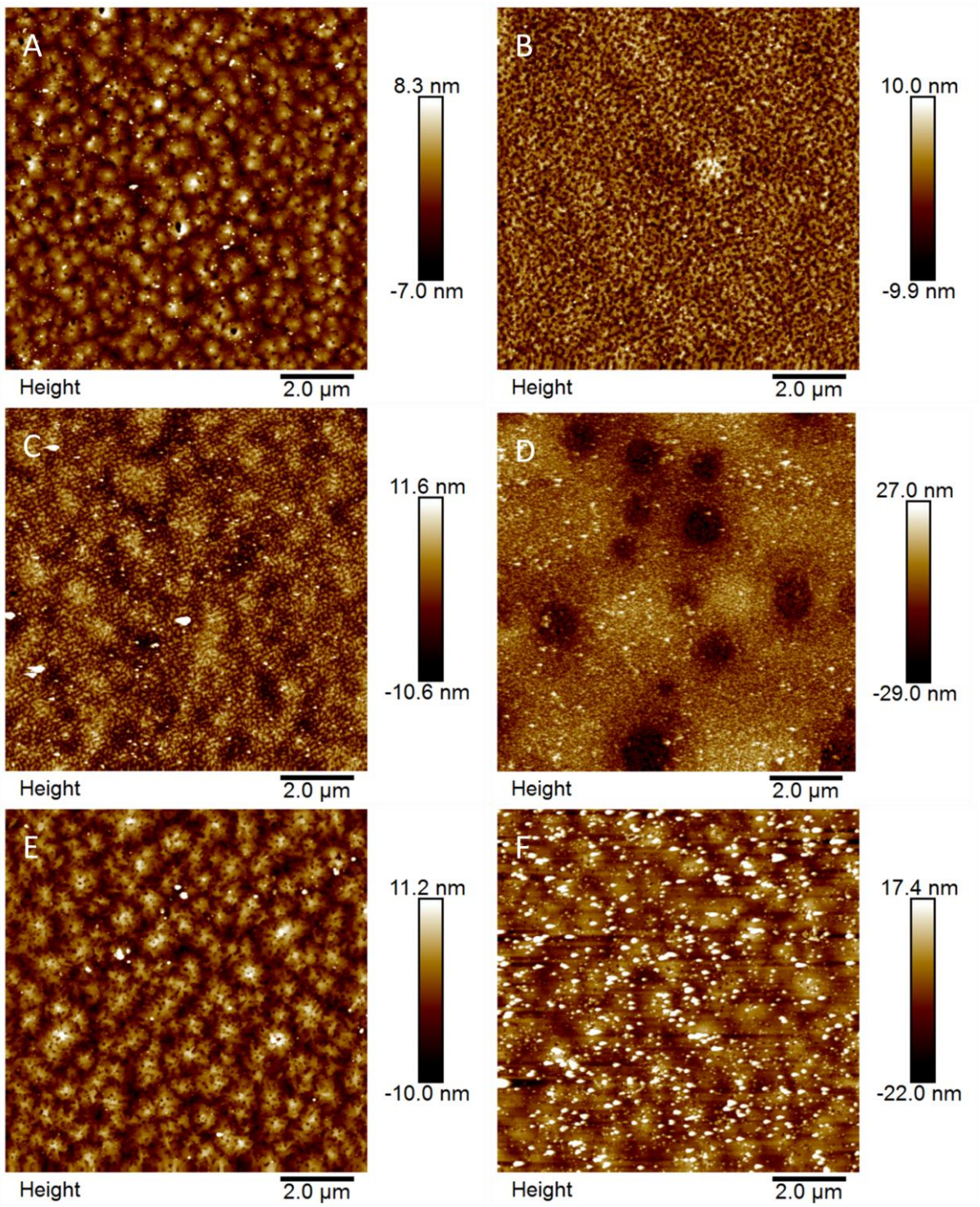

Figure 6.13: AFM height images of masked (A, C and E) and solution-exposed (B, D and F) regions of MBE-grown ZnO electrodes after electrochemical modification with NBD (A and B), MBD (C and D) and IBD (E and F).

6.3.1.3.4 FT-IR Spectroscopy of Modified MBE-Grown ZnO

The successful attachment of aryl layers to the electrochemically modified surfaces was investigated by FT-IR. The FT-IR spectra for the modified and masked regions of an MBE-grown ZnO sample modified with NBD is shown in Figure 6.14 (peak assignments are presented in Table 6.2) along with a spontaneously modified sample for comparison. The spectrum of the modified region for the electrografted NP-modified sample has peaks at 1597, 1525 and 1348 cm^{-1} associated with the C=C stretch, N=O asymmetric stretch and N=O symmetric stretch of the NP groups. In contrast, the spectrum for the masked region of this sample show only peaks associated with ZnO/Al_2O_3 (Figure 6.6) which suggests that the grafting reaction was successfully contained to the solution-exposed areas of the electrode.

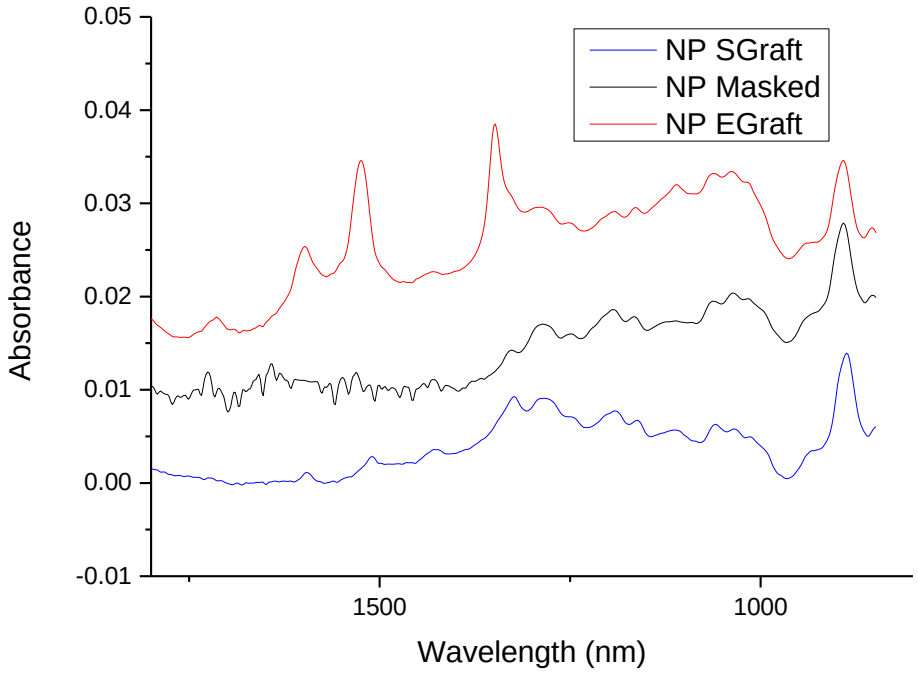

Figure 6.14: FT-IR spectra of NP-modified MBE-grown ZnO surfaces: spontaneously modified (NP SGraft), and masked (NP Masked) and modified (NP EGraft) regions of an electrografted sample.

In comparison with the spontaneously grafted sample, the intensity of the peaks associated with the aryl layer on the electrografted sample are more intense, suggesting increased coverage is achieved by electrochemical modification even though the NBD concentration is significantly lower (5 mM vs. 50 mM). This result is not unexpected as the utilisation of aryldiazonium ions is more efficient in the electrografting process due to the aryl radicals being produced near the surface rather than in solution and thus the proportion that successfully graft to the surface is increased.[115]

Table 6.2: Table of FT-IR peak assignments for samples modified by electrochemical cycling in pH 8 buffer with NBD (NP-Mod), MBD (MP-Mod) and IBD (IP-Mod).

NP-Mod		MP-Mod		IP-Mod	
Peak Position	Assignment	Peak Position	Assignment	Peak Position	Assignment
1597 cm^{-1}	C=C Stretch	1608 cm^{-1}	C=C Stretch	1483 cm^{-1}	C=C Stretch
1525 cm^{-1}	N=O Asym.	1511 cm^{-1}	C=C Stretch	1006 cm^{-1}	C-I Stretch
1348 cm^{-1}	N=O Sym.	1250 cm^{-1}	C-O Stretch		

Analysis of the FT-IR spectra of MP-modified (Figure 6.15A) and IP-modified (Figure 6.15B) samples prepared by electrografting show significant differences between the modified and masked regions. Peak assignments for the modified regions of each sample are presented in Table 6.2. As with the NP-modified sample, the IR response is the same as bare ZnO/Al_2O_3 for both samples. MP-modification results in the introduction of peaks at 1608 cm^{-1} and 1511 cm^{-1} assigned to aryl ring modes and a peak assigned to C-O stretching in the methoxy group at 1250 cm^{-1}. Modification with IP-groups introduces peaks due to C=C stretching from the aryl ring (1483 cm^{-1}) and C-I stretching in the iodo group (1006 cm^{-1}). These results indicate that the electrochemical modification successfully attaches aryl groups to the surface with a range of aryl substituents and that these groups are stable to ultrasonic cleaning.

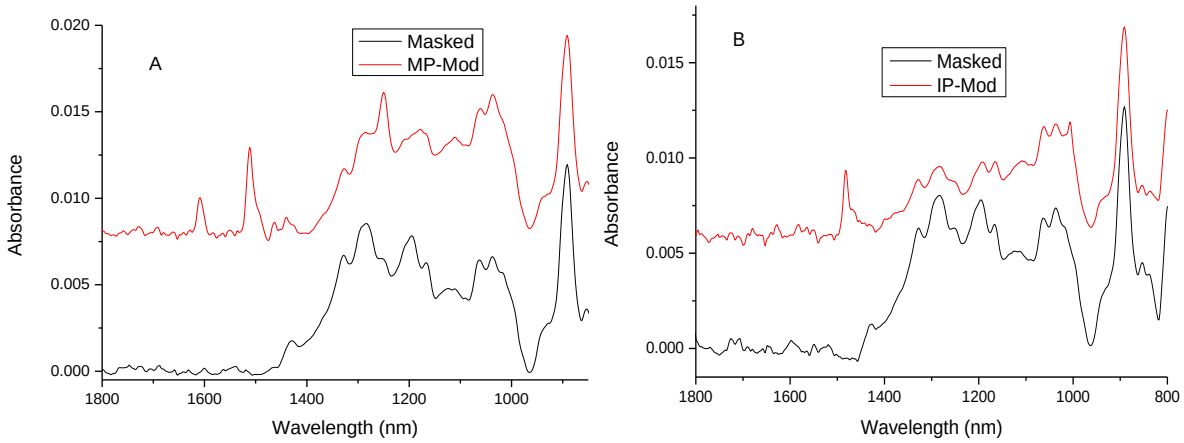

Figure 6.15: FT-IR spectra of masked and modified regions of MP-modified (A) and IP-modified (B) MBE-grown ZnO surfaces.

6.3.1.3.5 XPS Analysis of Modified MBE-Grown ZnO

To further investigate the effect of electrochemical modification on ZnO surfaces, XPS analysis was conducted on MBE-grown samples cycled in 0.1 M pH 8 buffer in the presence (NP-mod) and absence (Blank) of 1 mM NBD.

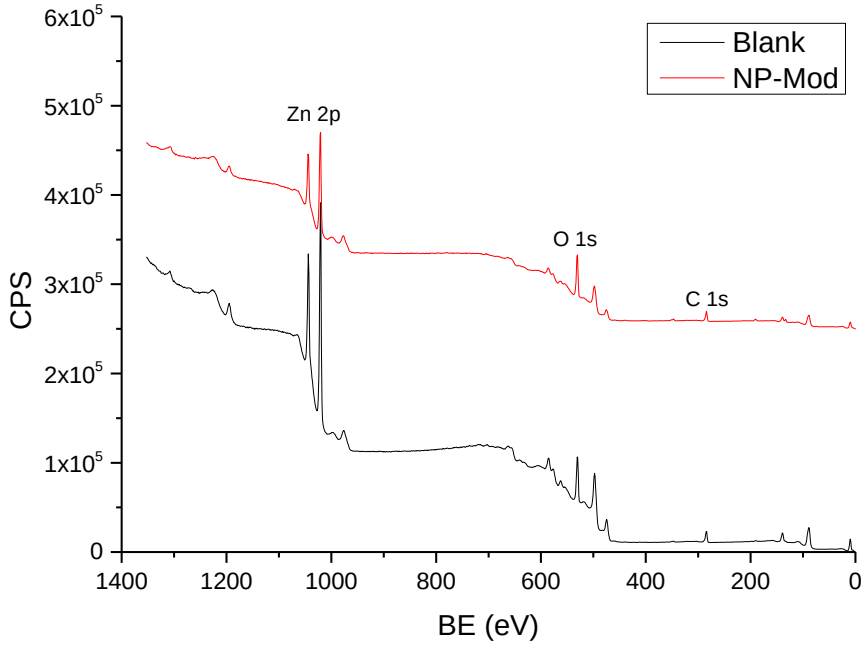

Figure 6.16: Survey XPS spectra of MBE-grown ZnO electrochemically cycled in 0.1 M pH 8 buffer in the presence (NP-Mod) and absence (Blank) of NBD.

Survey XPS spectra of the NP-modified and blank samples are shown in Figure 6.16 and the atomic concentration values calculated from these spectra are shown in Table 6.3. Values from the blank sample show the expected 1:1 Zn:O ratio for ZnO and signals due to adventitious C. Additionally there is a significant P signal present in this sample, most likely arising from buffer components adsorbed to the surface. Modification with NP groups results in an increase in O, C and P content and introduction of N. Increases in C, N and O indicate that the NP groups are present on the surface after modification, however, the increased P content suggests that further phosphate adsorption is occurring at the surface during modification compared to the blank sample. This may also account for the increase in O content being much larger than would be expected from just the introduction of NP groups. As described in section 6.1.5.3, the absorption of phosphonates on ZnO surfaces has been researched extensively and it is assumed that the adsorption of phosphates to ZnO occurs by similar mechanisms, however, the enhancement of this adsorption during the modification process is unexpected.

Table 6.3: Atomic concentrations and ratios for MBE-grown ZnO electrochemically cycled in 0.1 M pH 8 buffer in the presence (NP-Mod) and absence (Blank) of NBD.

Sample	Zn (At %)[a]	O (At %)[a]	C (At %)[a]	P (At %)[a]	N (At %)[a]	C/Zn[a]	O/Zn[a]	P/Zn[b]
pH 8 Blank	31.9	36.5	30.1	1.5	< 0.1	0.94	1.14	0.046
pH 8 NP-Mod	14.1	45.5	34.3	5.1	1.1	2.43	3.23	0.36

[a]Determined from survey spectra, [b]Determined from Zn 3s spectra.

These changes in surface chemistry were further analysed using the high resolution O 1s, C 1s, N 1s and Zn 3s core-level spectra for the modified and blank sample (Figure 6.17). The O 1s spectra (Figure 6.17A) for both the blank and NP-modified samples show a main peak at ~530 eV and a shoulder at 531.5 eV. In untreated ZnO, the main peak is assigned to bulk O species whereas the shoulder is attributed to surface hydroxyls.[116] In the NP-modified sample, the intensity of the higher energy peak is proportionately higher than the bulk O peak compared to the blank sample. This is consistent with the modification process influencing the surface chemistry of the ZnO. Work by Chen et al. on ZnO surfaces surfaces modified with phosphonate and thiolate monolayers showed that the intensity of the surface O peak increased upon the attachment of phosphonates but decreased after thiolate modification due to replacement of surface O species with thiol groups.[78] From prior studies on modification of metal oxide surfaces with aryldiazonium ions in this thesis work (Chapter 4) and literature, it is expected that the aryl layer would bind to the surface O species and cause a shift in the binding energy of the surface O peak.[117] There is no clear evidence of this shift occurring in the modified sample and it is unlikely that electrochemical modification with aryl layers would result in increased surface O content as the aryl radical does not introduce O species to the surface. The most likely origin of these surface O species is adsorbed phosphates from the modification buffer as indicated by the increased P content in the modified sample. Phosphate O species have been observed at similar energy on carbon surfaces, further supporting this assignment.[118]

Comparing the C 1s core level spectra for the modified and blank samples (Figure 6.17B), it is apparent that the modification process does not change the features in the C 1s spectrum significantly. Both spectra have a large peak assigned to C-C bonding that is set at 284.8 eV due to the charge correction process and smaller peaks at 286.5 eV and 289 eV that are assigned to C-O and C=O respectively.[119] Their presence in both modified and unmodified samples suggests these peaks are most likely primarily due to adventitious contamination. However, there is an increase in the proportion of C-C bonding in the modified sample that may be due to the aryl layer. Although an increase in the C/Zn ratio was observed in the survey spectra after modification (Table 6.3), the magnitude of this C/Zn ratio increase (from 0.94 to 2.43) does not correspond to the increase in C-C

bonding (from 86% to 93%) observed in the C 1s spectra. This discrepancy is most likely due to the layer of NP groups and adsorbed phosphates at the surface reducing the proportion of bulk ZnO and thus Zn atoms sampled, resulting in the C/Zn ratio being artificially high.

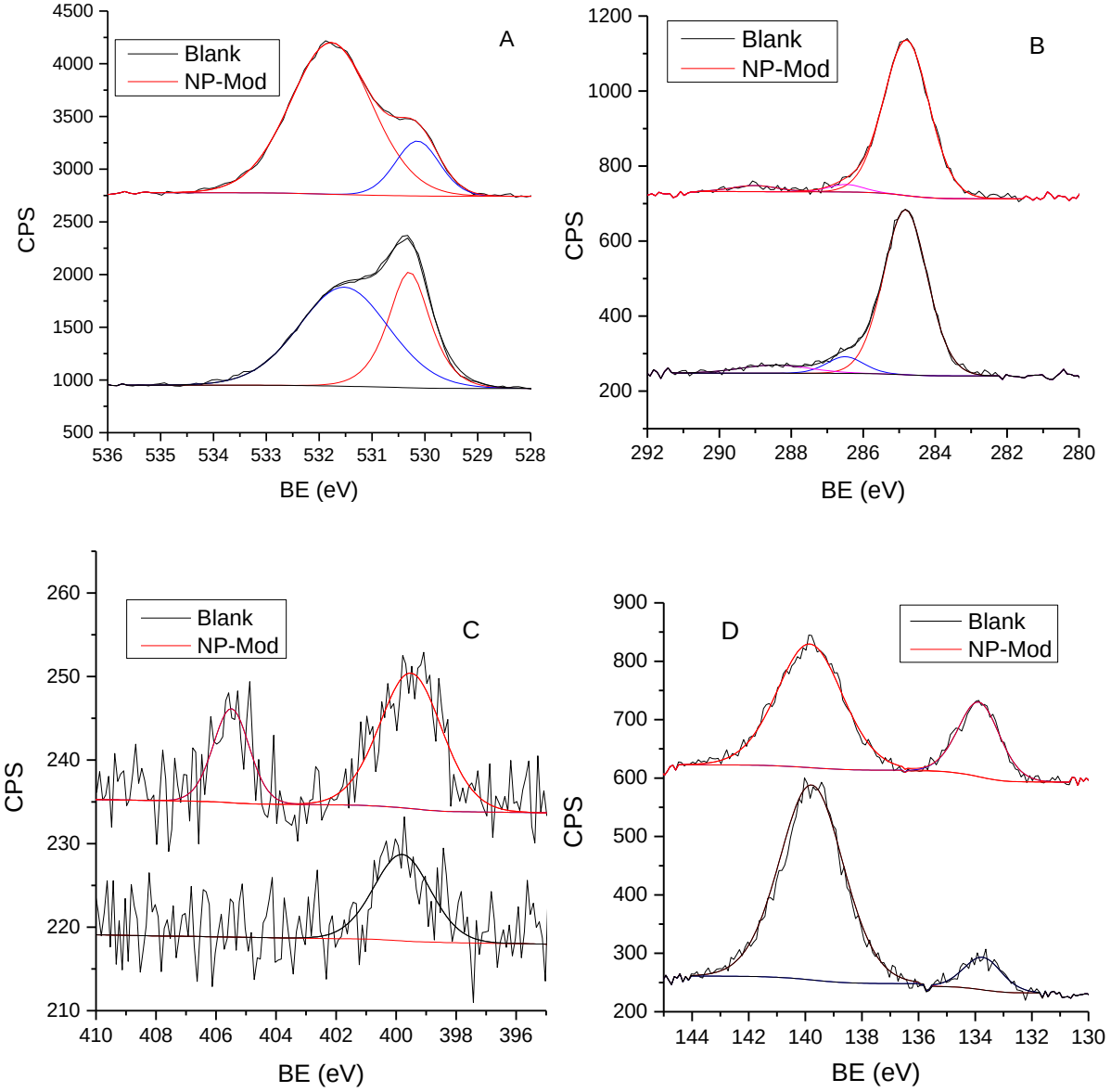

Figure 6.17: XPS spectra of the O 1s (A), C 1s (B), N 1s (C) and Zn 3s (D) regions for MBE-grown ZnO electrochemically cycled in 0.1 M pH 8 buffer in the presence (NP-Mod) and absence (Blank) of NBD.

The N 1s spectrum for the blank sample (Figure 6.17C) shows a single peak at 400 eV that is assigned to amine species in the adventitious C contamination. A peak at this energy is also present in the NP-modified sample in addition to a peak at 406 eV. The peak at 406 eV is assigned to NO_2 groups, providing further evidence of the presence of the NP film on the surface.[120] The peak at 400 eV likely contains contributions from the adventitious amine contaminants observed in the blank sample but

may also include contributions from azo linkages or reduced NP groups in the aryl layer. The convolution of these different N species along with the possibility of azo linkages occurring within the film makes it impossible to confirm the presence of azo linkages between the film and the ZnO surface.

The Zn 2p and P 2p regions are adjacent (Figure 6.17D) and thus can be used to determine the P/Zn ratio more accurately than from survey spectra. P/Zn ratios for blank and NP-modified samples calculated from core level spectra are presented in Table 6.3. Compared to the blank sample, there is an 8-fold increase in P/Zn ratio in the NP-modified sample. As both samples are subjected to identical buffer and potential cycling conditions, this increase in P content must arise from an interaction with the aryldiazonium salt or the aryl layer on the surface. The nature of this interaction is unknown.

A recent publication by Wang et al. describes the electrochemical grafting of aryldiazonium salts in non-aqueous conditions to Al-doped polycrystalline ZnO surfaces as a platform to covalently link DNA for a hybridisation biosensor.[106] Under these conditions, a well-defined irreversible reduction peak was observed that decreased on continued cycling due to blocking of the surface as is typical for electrografting aryldiazonium salts. Successful modification was confirmed by CV, XPS and water contact angle measurements. The differences in grafting CV response compared to this thesis work may arise due to the sputtered ZnO substrates used by Wang et al. being more conducting and defect-rich, and thus more reactive to aryldiazonium ion grafting. Additionally, the lack of interference by phosphate ions adsorbing to the surface during the grafting reaction may also contribute to the observed differences in CV response.

6.3.2 Modification of Single Crystal ZnO Surfaces

To examine the effect of the ZnO surface chemistry on the formation of aryl layers, polar (O-polar, Zn-polar) and non-polar (m-plane) bulk single crystal ZnO samples were modified electrochemically. The crystal structure of each face is shown in Figure 6.1. Although these surfaces are crystallographically controlled, as explained in section 6.1.3, the surface chemistry of these materials is dependent on the environment due to adsorption of hydroxyl groups and water molecules from the atmosphere. The strength of the attachment of the adsorbed species varies based on the crystal face and it is expected that this will influence the attachment of aryl layers to the surface.[7, 34] After modification, these samples were characterised by synchrotron XPS, AFM and FT-IR.

6.3.2.1 Electrochemical Modification of Single Crystal ZnO Surfaces

Single-crystal O-polar, Zn-polar and m-plane ZnO electrodes were prepared by the same method as MBE-grown ZnO and electrochemically modified in 5 mM NBD, MBD and IBD in pH 8 solution. Blank samples were prepared by electrochemical treatment in pH 8 solution in the absence of aryldiazonium salt. Phosphate buffer was used as the electrolyte solution because at the time, the potentially problematic involvement of phosphate had not been identified for the MBE-grown samples described above as the XPS analysis on MBE samples had not been completed.

CV curves collected during the modification and electrochemical treatment of O-polar ZnO surfaces are shown in Figure 6.18. Voltammograms of electrochemical modification in NBD and MBD solution (Figure 6.18 A and B) have a primarily linear shape with a broad feature on the first scan, similar to the curves observed during modification of MBE surfaces (Figure 6.11). The CV of modification with IBD (Figure 6.18C) is similar on the first scan above -1 V, however, a defined reduction peak is visible at -1.2 V that was not observed with the other modifiers. On subsequent scans, this feature is replaced by a peak at -1.05 V that increases with scan number up to scan 15. For all modifiers, there is no sign of blocking behaviour during the modification process, suggesting incomplete coverage. The blank sample cycled in the absence of aryldiazonium salt (Figure 6.18D) has only weak features in the voltammogram similar to the response of the MBE-grown sample (Figure 6.10) up to scan 5. The oxidation features present in scans 10-20 indicate leakage of electrolyte through to the Cu foil connector. However, comparison of the early scans of the blank and modified samples show clear differences in the shape of the voltammograms in the presence of aryldiazonium ions. The similarity of the response on O-polar ZnO surfaces to MBE-grown ZnO is not unexpected as the MBE-grown surfaces are primarily O-terminated.[20]

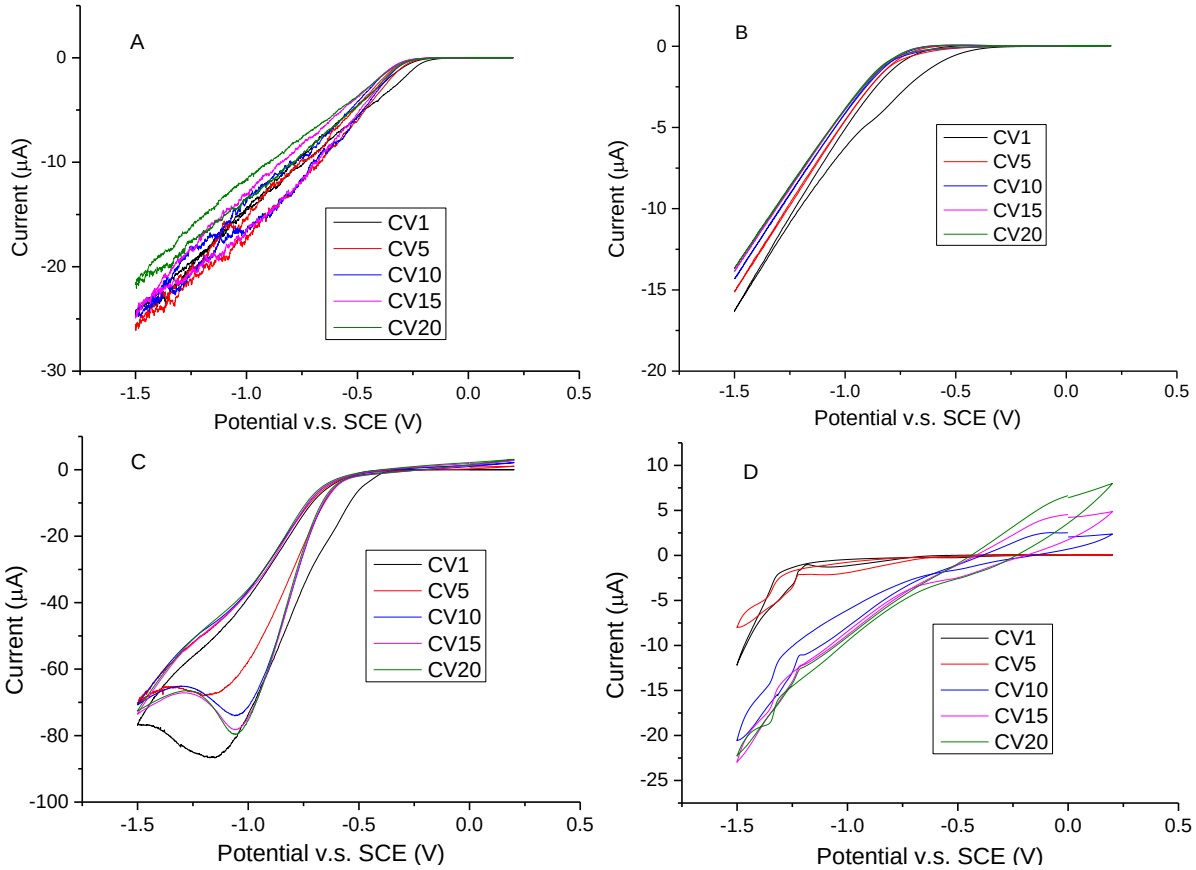

Figure 6.18: CV curves (scans 1, 5, 10, 15 and 20) of O-polar ZnO surfaces collected in 0.1 M pH 8 buffer at 50 mV s^{-1} scan rate with 5 mM NBD (A), MBD (B) and IBD (C) and in the absence of aryldiazonium salt (D).

CV curves for the modification of Zn-polar single crystal ZnO surfaces with aryldiazonium ions are shown in Figure 6.19. They are shaped similarly to the curves for O-polar surfaces, however, the curve for MBD modification of Zn-polar ZnO is more similar to the curve for IBD modification of O-polar ZnO and vice versa. This suggests that the presence of a defined reduction peak during the grafting to ZnO may be unrelated to the crystal face or aryl substituent. The blank sample again shows signs of electrolyte leakage after 15 scans as well as a reduction process present on the first cycle, possibly due to adsorbed species. However, scans 5 and 10 for the blank sample show no significant features.

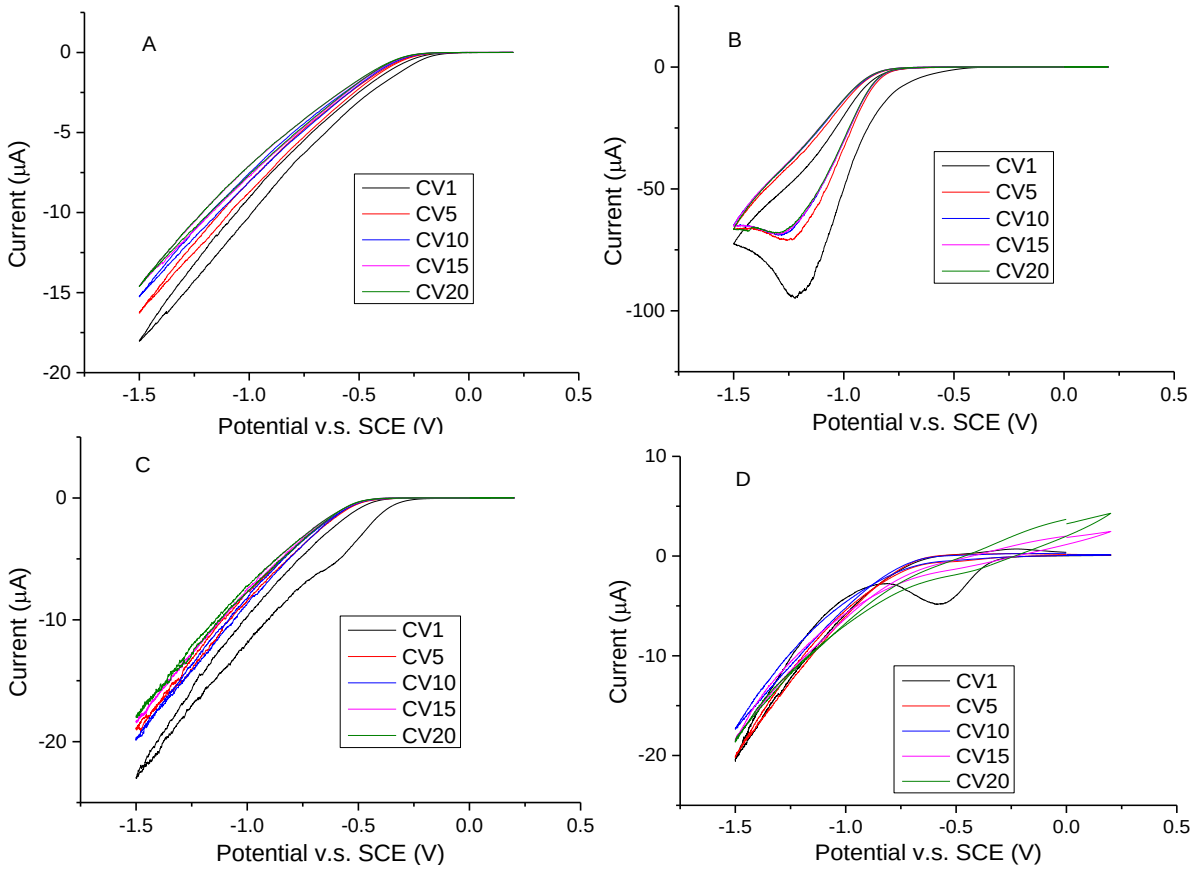

Figure 6.19: CV curves (scans 1, 5, 10, 15 and 20) of Zn-polar ZnO surfaces collected in 0.1 M pH 8 buffer at 50 mV s^{-1} scan rate with 5 mM NBD (A), MBD (B) and IBD (C) and in the absence of aryldiazonium salt (D).

For m-plane ZnO (Figure 6.20), the CV curves for all modifiers have a defined redox peak at either -1.25 V (NBD and MBD modification) or -1 V (IBD modification). Comparing IBD modification of O-polar (Figure 6.18C) and m-plane surfaces (Figure 6.20C), and MBD modification of Zn-polar (Figure 6.19B) and (Figure 6.20B), the positions of these peaks appears to be consistent across different crystal faces. In comparison with the modification of MBE-grown ZnO where no defined peaks were

observed, it is possible that the single crystal surfaces have a catalytic effect that causes the reduction peak to shift to within the scan window or there is a new process unique to these surfaces.

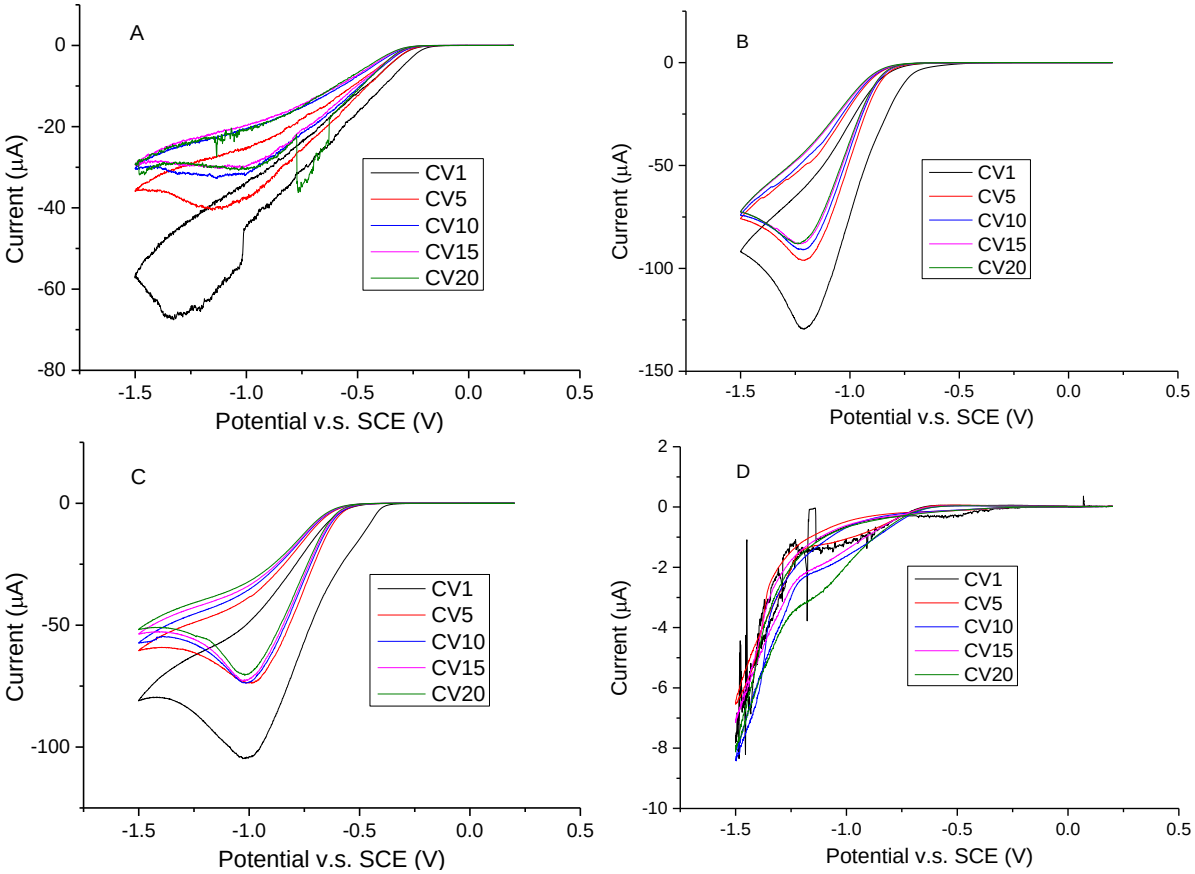

Figure 6.20: CV curves (scans 1, 5, 10, 15 and 20) of m-plane ZnO surfaces collected in 0.1 M pH 8 buffer at 50 mV s^{-1} scan rate with 5 mM NBD (A), MBD (B) and IBD (C) and in the absence of aryldiazonium salt (D).

6.3.2.2 Characterisation of Electrochemically Modified Single Crystal ZnO surfaces

From the grafting scans obtained at all crystal faces, it is apparent that electrochemical processes are occurring in the presence of aryldiazonium ions that are not occurring in the blanks. The effect of electrochemical modification on the surface chemistry of ZnO was investigated by synchrotron XPS. Using a synchrotron X-ray source allows greater surface sensitivity than a monochromatic source as the X-ray energy can be selected to minimise the penetration of the X-ray beam into the surface. Due to time constraints, only the NBD- and IBD-modified ZnO surfaces were characterised.

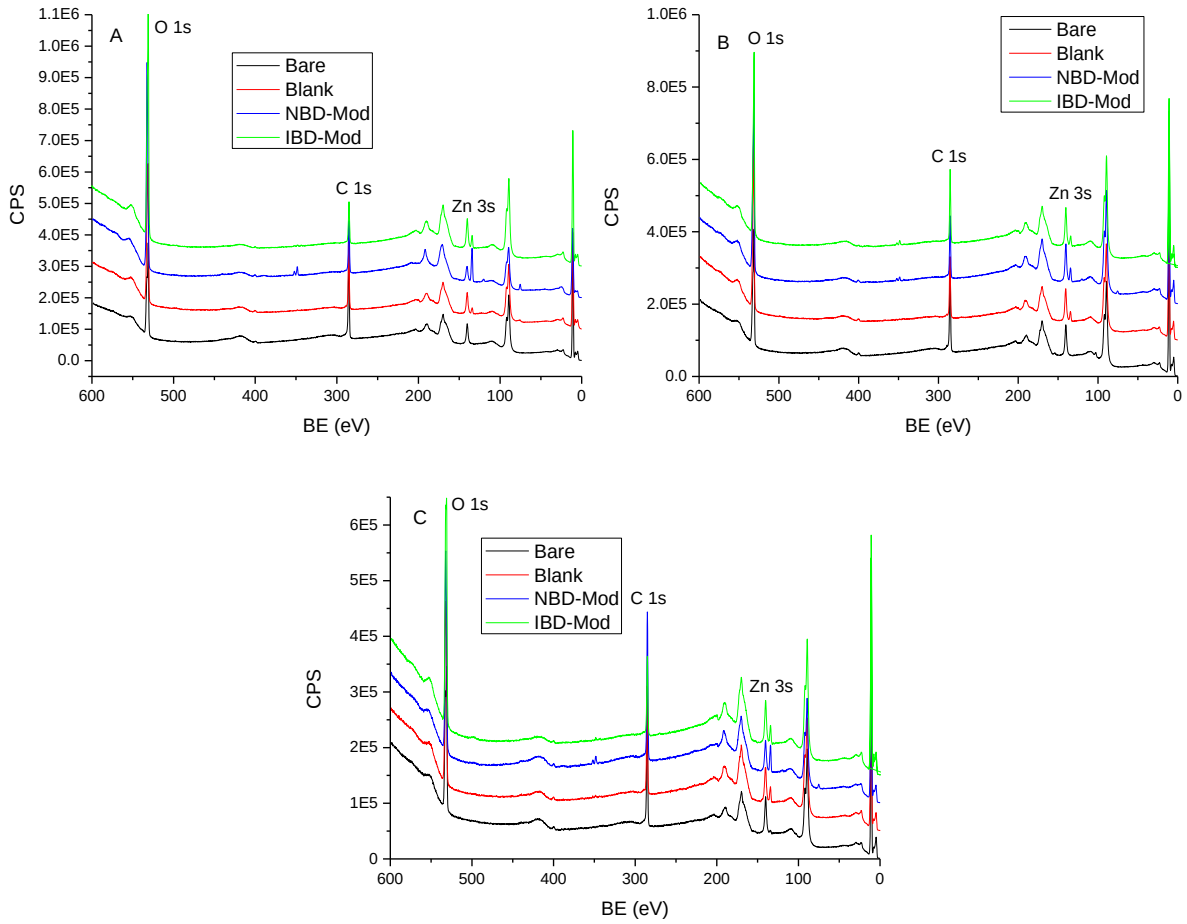

Figure 6.21: XPS survey spectra of O-polar (A), Zn-polar (B) and m-plane (C) ZnO surfaces modified in 0.1 M pH 8 buffer with 5 mM NBD (NBD-Mod) and IBD (IBD-Mod) and in the absence of aryldiazonium salt (Blank). 'Bare' spectra were obtained at as-received ZnO samples.

Survey XPS spectra for single crystal surfaces electrochemically treated in the presence and absence of aryldiazonium salts are shown in Figure 6.21. Atomic concentrations and ratios calculated from survey spectra for each sample are shown in Table 6.4. For all samples, the surfaces show significant Zn, O and C signals. The highest C content is observed in the bare samples (as-received ZnO) where it can only derive from ambient contamination. This high C content in the untreated samples is possibly due to the modified and blank surfaces undergoing additional solution processing steps. The blank and modified samples all have significant P content, as was observed for the MBE-grown ZnO samples (Table 6.3), suggesting significant adsorption of buffer components can also occur at single crystal surfaces. At each crystal face, the highest P content was observed for the NBD-modified samples and the IBD-modified samples had similar P content to the blank samples. Additionally, the P-content was found to vary between crystal faces (Zn-polar < m-plane < O-polar), suggesting the amount of adsorbed phosphates increases with the O-termination of the ZnO surface. For the modified samples, no N or I signals (N 1s at 399 eV and I 4p at 123 eV) due to the substituents on the

aryl layer were observed for the NBD- and IBD-modified samples respectively. This result, along with the low C content for the modified samples, suggests that little or no modification is occurring.

Table 6.4: Atomic concentrations and ratios, and valence band edge (ξ) for pristine O-polar, Zn-Polar and m-plane ZnO surfaces (Bare) and surfaces electrochemically cycled in 0.1 M pH 8 buffer with 5 mM NBD (NBD-Mod) and IBD (IBD-Mod) and in the absence of aryldiazonium salt (Blank).

O-Polar								
Sample	Zn (At %)[a]	O (At %)[a]	C (At %)[a]	P (At %)[a]	C/Zn[a]	O/Zn[a]	P/Zn[b]	ξ (eV)[c]
Bare	15.3	44.9	39.8	-	2.7	3.0	0	3.3
Blank	15.7	52.4	29.0	2.9	1.9	3.3	1.8	2.9
NBD-Mod	9.3	56.2	19.6	15.0	2.1	6.1	12.0	4.1
IBD-Mod	16.3	64.1	14.7	4.8	0.9	3.9	2.3	4.0
Zn-Polar								
Sample	Zn (At %)[a]	O (At %)[a]	C (At %)[a]	P (At %)[a]	C/Zn[a]	O/Zn[a]	P/Zn[b]	ξ (eV)[c]
Bare	22.1	38.6	39.26	-	1.8	1.7	0	3.7
Blank	21.3	48.9	25.73	4.1	1.2	2.3	1.8	4.1
NBD-Mod	20.8	52.0	21.64	5.5	1.0	2.5	2.4	4.3
IBD-Mod	22.2	47.3	26.21	4.2	1.2	2.1	1.4	4.0
m-Plane								
Sample	Zn (At %)[a]	O (At %)[a]	C (At %)[a]	P (At %)[a]	C/Zn[a]	O/Zn[a]	P/Zn[b]	ξ (eV)[c]
Bare	19.2	42.4	38.42	-	2.0	2.2	0	3.4
Blank	17.1	48.5	29.62	4.8	1.7	2.8	2.1	3.6
NBD-Mod	12.7	43.2	36.09	8.0	2.8	3.4	4.7	3.6
IBD-Mod	18.9	56.1	19.88	5.1	1.0	3.0	2.1	3.9

[a]Determined from survey spectra, [b]Determined from Zn 2p spectra, [c]Determined from valence band spectra.

Core level O 1s spectra for single crystal O-polar, Zn-polar and m-plane ZnO surfaces are shown in Figure 6.22. For each crystal face, the bare sample spectra have the peaks associated with bulk (531 eV) and surface (532 eV) O species typical of ZnO.[116] The O-polar blank and IBD-modified samples show similar response to the bare sample, however for the NBD-modified sample, the surface O peak is increased in intensity to the point where the bulk peak can no longer be resolved (Figure 6.22A). This increase in surface O content most likely arises due to the phosphates adsorbed at the ZnO surface during the electrochemical modification process. There is no clear evidence of O 1s peaks associated with NO_2 groups.[121] Zn-polar samples (Figure 6.22B) show much less variation with treatment conditions which aligns with the lower variation in P content observed in the survey spectra. For the m-plane samples, the surface O peak is proportionately higher than the bulk O peak after electrochemical treatment for both the blank and IBD-modified samples, despite the comparable P content to the Zn-polar and O-polar samples treated under the same conditions. This

may arise due to differences in the interactions of phosphate groups with polar and non-polar (such as m-plane) ZnO surfaces.

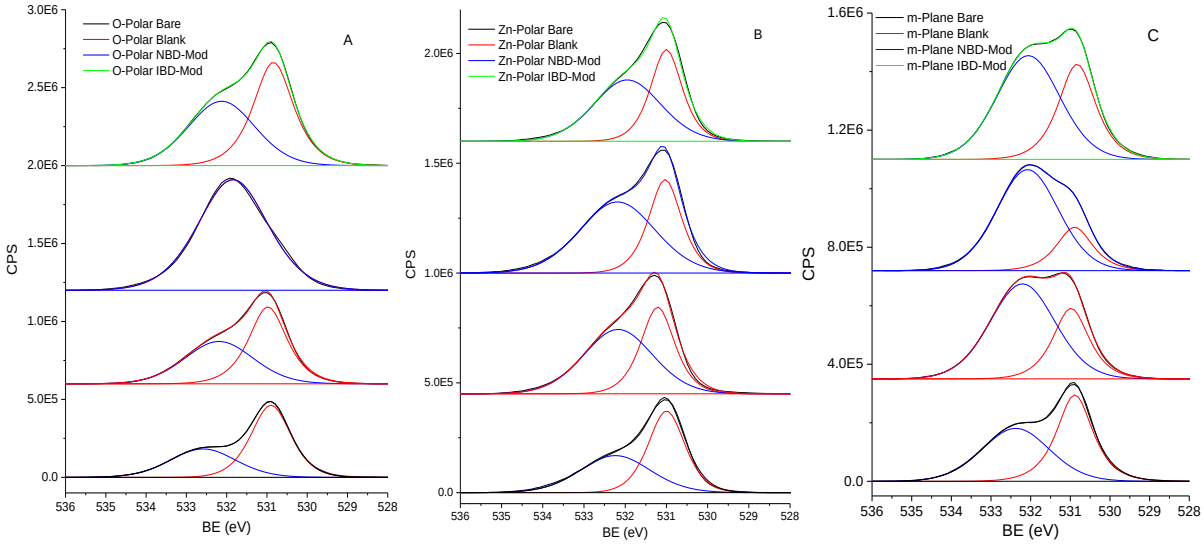

Figure 6.22: O 1s core level XPS spectra for O-polar (A), Zn-polar (B) and m-plane (C) ZnO, as received (Bare) and surfaces electrochemically cycled in 0.1 M pH 8 buffer with 5 mM NBD (NBD-Mod) and IBD (IBD-Mod) and in the absence of aryldiazonium salt (Blank).

C 1s XPS spectra for bare and electrochemically treated single crystal ZnO surfaces are shown in Figure 6.23. For each surface, the C 1s spectrum consists of the C-C peak that has been fixed to 284.8 eV during the charging correction process and additional low intensity components associated with C-O bonding, both of which most likely arise due the adventitious C contamination. There are no clear signs of pi-pi shakeup peaks or an increase in C content associated with the aryl layer.

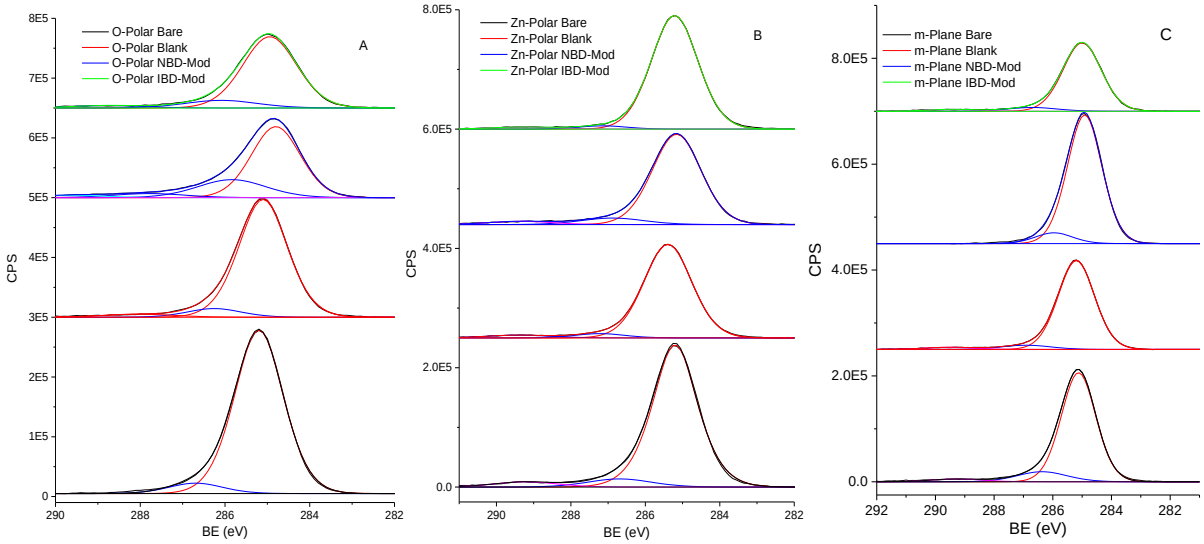

Figure 6.23: C 1s core level XPS spectra for O-polar (A), Zn-polar (B) and m-plane (C) ZnO, as received (Bare) and surfaces electrochemically cycled in 0.1 M pH 8 buffer with 5 mM NBD (NBD-Mod) and IBD (IBD-Mod) and in the absence of aryldiazonium salt (Blank).

The effect of electrochemical treatment on the electronic properties of the ZnO surface was investigated by collecting the valence band spectra (Figure 6.24). The low binding energy edge of the valence band spectrum can be used as a measure of the valence band position in the near surface region and thus the surface band bending.[122] The valence band positions (ξ) determined from the linear fit of the valence band edge for each sample are shown in Table 6.4. All samples show shifts in the valence band positions between the blank and bare samples that could be a result of the electrochemical treatment. The as-received ZnO surfaces show varying degrees of downward band bending depending on the crystal face (Zn-polar > m-plane > O-polar) and is most likely due to the polarisation of ZnO along the c-axis.[34] For the O-polar samples (Figure 6.24A), it is apparent that electrochemical treatment in the presence of aryldiazonium ions causes a significant shift in the valence band positions (from 3.3 eV to 4.1 eV and 4.0 eV for NBD- and IBD-modified samples respectively). In contrast, the valence band position of the O-polar blank sample is shifted to higher energy compared to the as-received surface (from 2.9 eV to 3.3 eV), however, there is a significant non-linear region present below the extrapolated band edge energy due to gap states.[123] This suggests the surface has a high defect density which may affect the valence band edge position. On Zn-polar (Figure 6.24B) and m-plane (Figure 6.24) surfaces, the shifts in valence band position are much smaller and only the NBD-modified Zn-polar and IBD-modified m-plane samples show shifts compared to the blank.

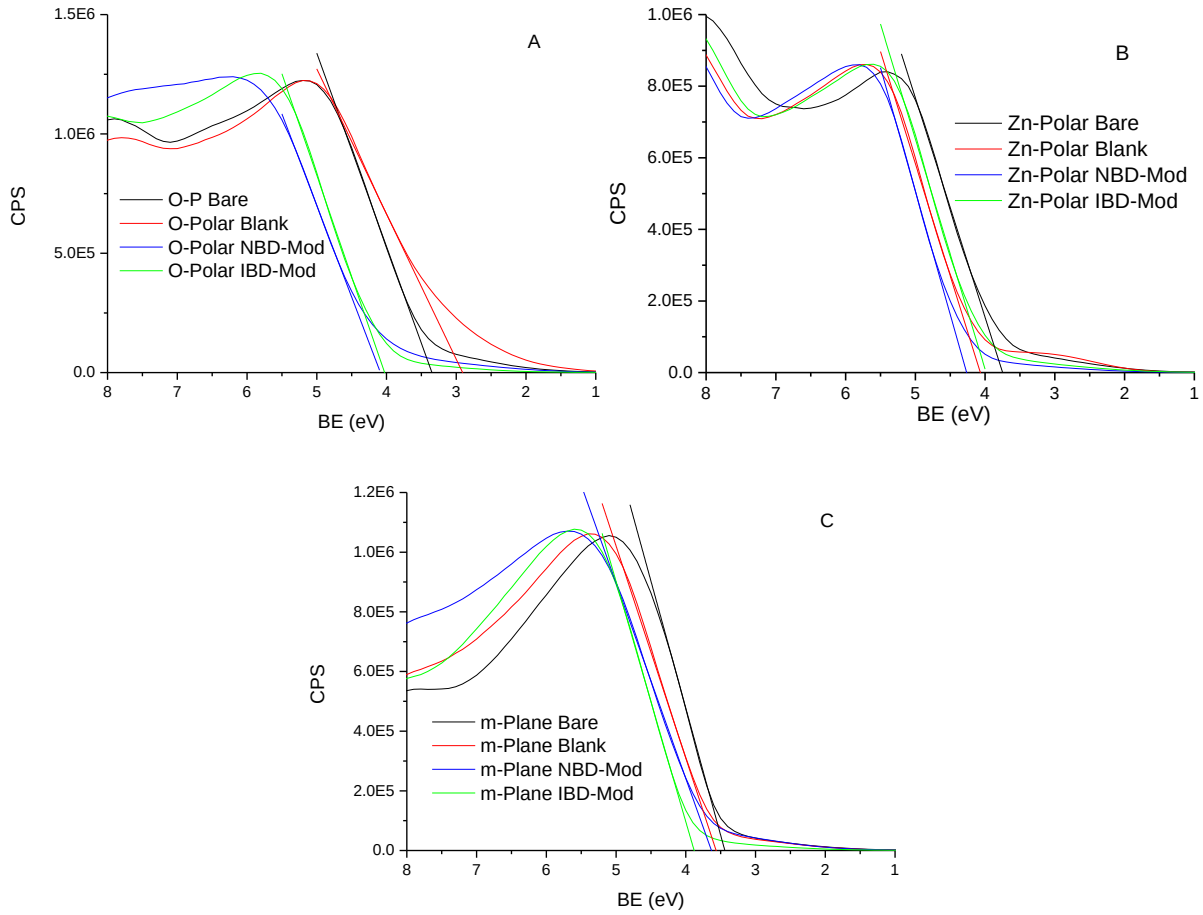

Figure 6.24: Valence band XPS spectra of pristine O-polar (A), Zn-polar (B) and m-plane (C) ZnO surfaces (Bare) and surfaces modified in 0.1 M pH 8 buffer with 5 mM NBD (NBD-Mod) and IBD (IBD-Mod) and in the absence of aryldiazonium salt (Blank).

The shift in valence band edge position to higher binding energy for the majority of samples after electrochemical treatment indicates an increase in downward band bending and thus electron accumulation at the surface. This suggests the introduction of a donor species onto the surface of the ZnO. As the most striking consequence of the electrochemical modification process is the increase in P content after modification in the presence of aryldiazonium ions, it would be expected that the valence band shifts would be related to interactions with phosphate groups adsorbed on the surface. However from the values in Table 6.4, it is apparent that there is no direct correlation between P/Zn ratio and the shift in valence band position. For example, between the m-plane blank and NBD-modified samples, there is a twofold increase in P/Zn ratio but no change in valence band position. This suggests that the interaction between the ZnO surface and adsorbed phosphate is complex and may involve multiple phosphate species, not all of which act as surface donors.

The effect of electrochemical treatment on the morphology of these single crystal ZnO samples was investigated by AFM (Figure 6.25-Figure 6.27). As the AFM studies were conducted after the synchrotron studies, there were problems with sample cleanliness due to the additional preparation and transportation steps. After ultrasonic cleaning, the O-polar blank and NBD-modified samples showed large scale debris across both the masked and exposed areas on each sample (Figure 6.25 A-D), most likely due to the deposition of conducting carbon tape residues from the sample-mounting process onto the front face of the sample. For this reason, the other single crystal surfaces were cleaned without ultrasonic treatment. For the MBD- and IBD-modified samples, there are no clear differences between the modified and unmodified regions of the surfaces and thus no changes in roughness due to film formation or etching during the electrochemical treatment. For the Zn-polar surfaces (Figure 6.26), the debris present across the surface due to the mild cleaning process makes it difficult to see changes in the underlying substrate but there appear to be no significant differences between the masked and electrochemically treated regions. However, for the m-plane samples (Figure 6.27) there is clear evidence of pitting in the electrochemically treated regions of the sample. This may explain the increased proportion of surface O species observed by XPS in Figure 6.22C due to the increase in surface area resulting from the etching process. It is possible that the reduction peak observed between -1 to -1.25 V for the m-plane samples in Figure 6.20 is associated with this etching process. However, this peak is also observed for IBD-modified O-polar and MBD-modified Zn-polar surfaces (Figure 6.18C and Figure 6.19B respectively) but the AFM images for these samples do not show significant etching (Figure 6.25H and Figure 6.26F). The mechanism behind this preferential etching process at m-plane surfaces is currently unknown.

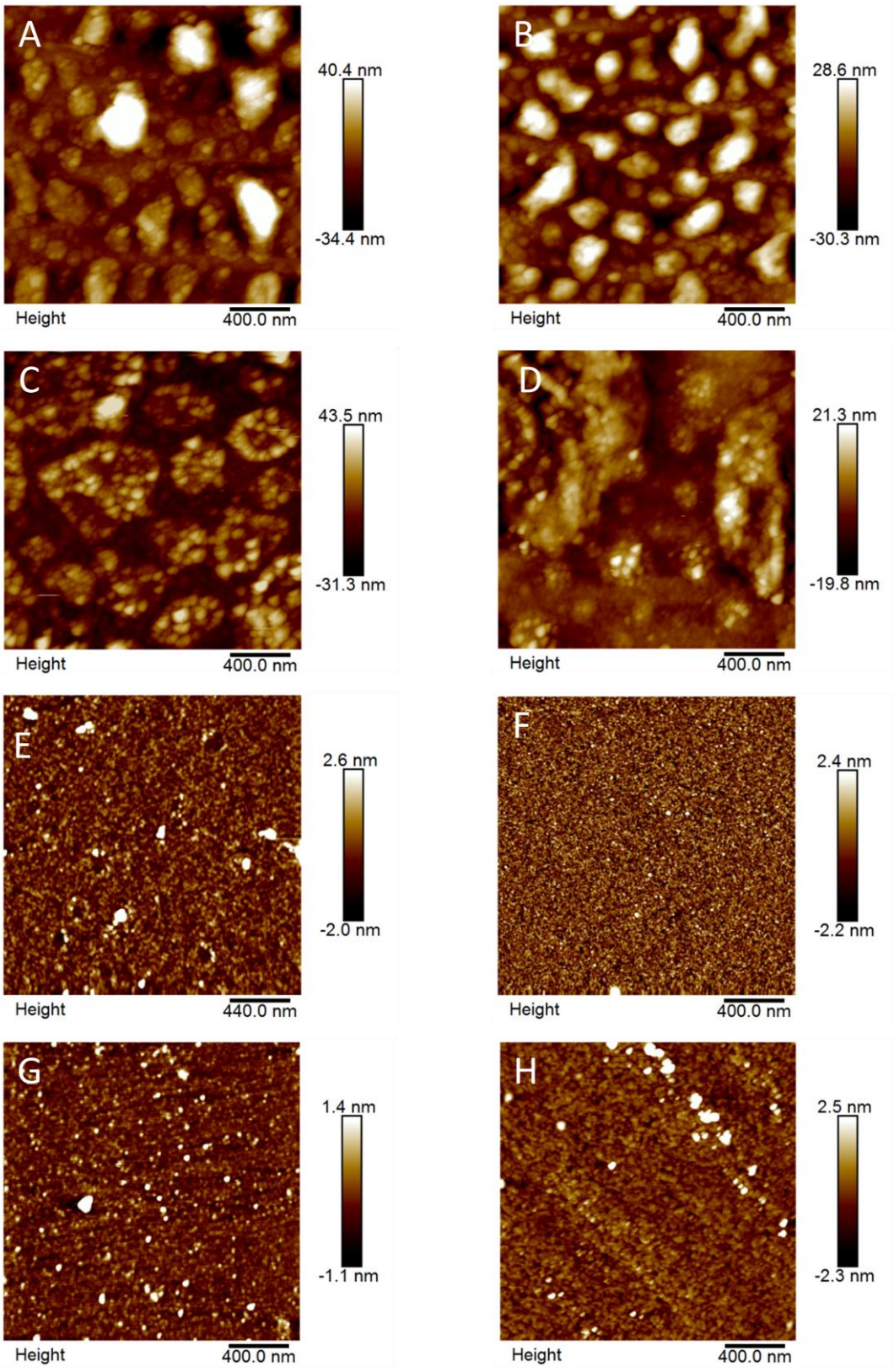

Figure 6.25: AFM height images of masked (A, C, E and G) and solution-exposed (B, D, F and H) regions of O-polar ZnO electrodes after electrochemical modification without aryldiazonium salts (A and B) with NBD (C and D), MBD (E and F) and IBD (G and H).

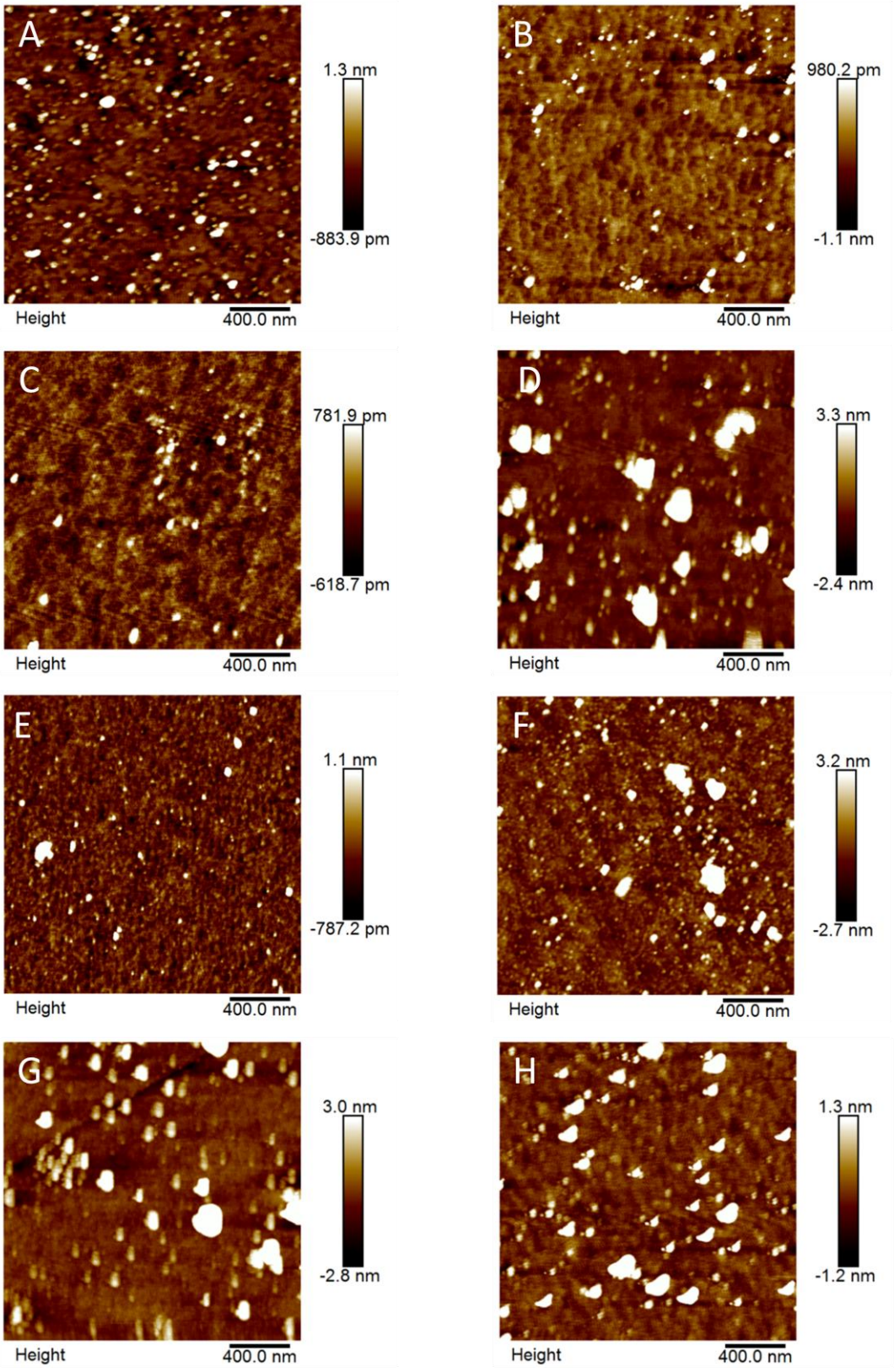

Figure 6.26: AFM height images of masked (A, C, E and G) and solution-exposed (B, D, F and H) regions of Zn-polar ZnO electrodes after electrochemical modification without aryldiazonium salts (A and B) with NBD (C and D), MBD (E and F) and IBD (G and H).

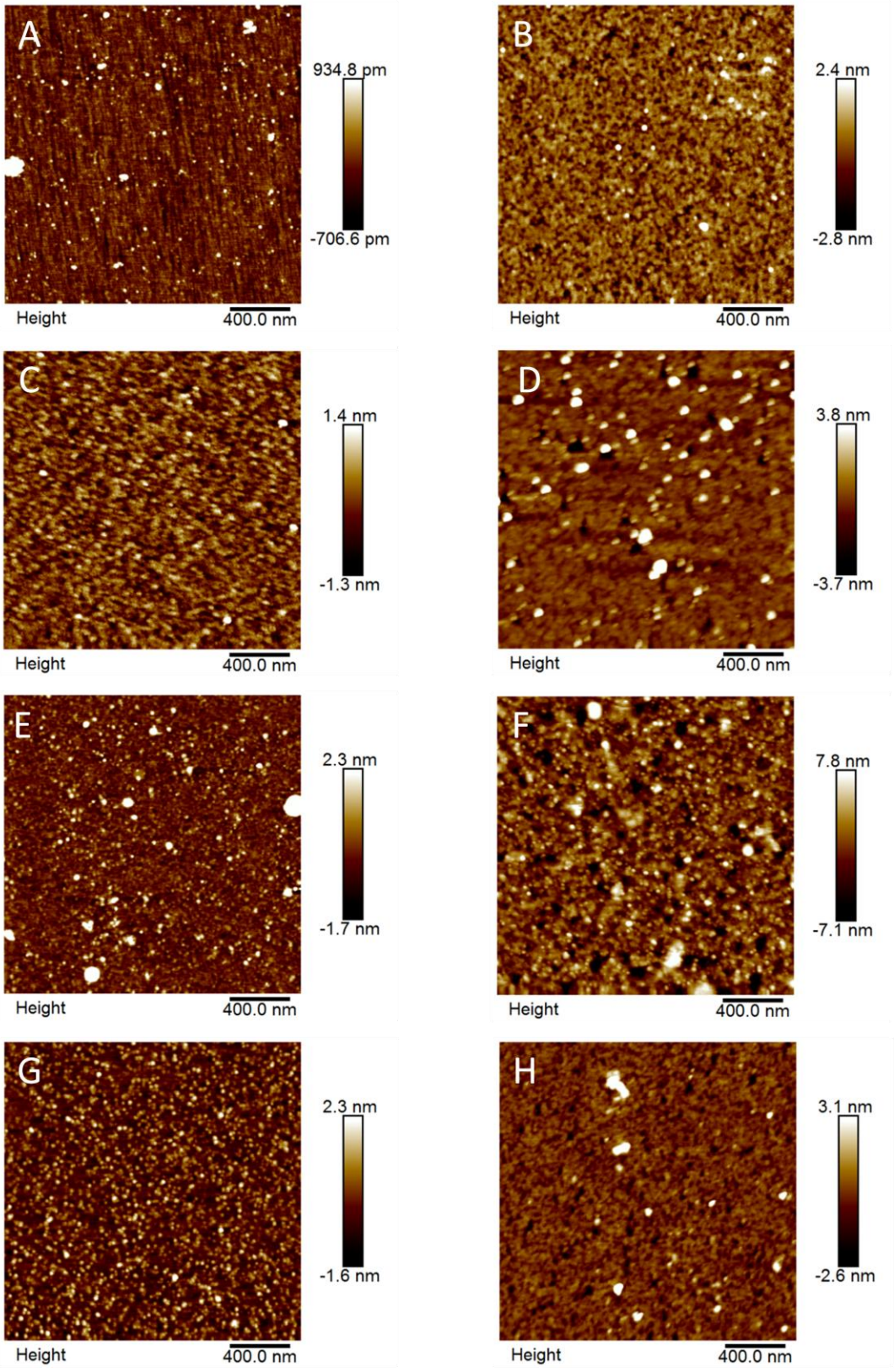

Figure 6.27: AFM height images of masked (A, C, E and G) and solution-exposed (B, D, F and H) regions of m-plane ZnO electrodes after electrochemical modification without aryldiazonium salts (A and B) with NBD (C and D), MBD (E and F) and IBD (G and H).

FT-IR spectra for the electrochemically-treated regions of single crystal ZnO surfaces are shown in Figure 6.28. For all modifiers on each crystal face, only low intensity peaks that are also present in the blank sample. The lack of peaks characteristic of the aryl modifiers provides further evidence that the changes in valence band position are not due to attachment of an aryl layer at the ZnO surface.

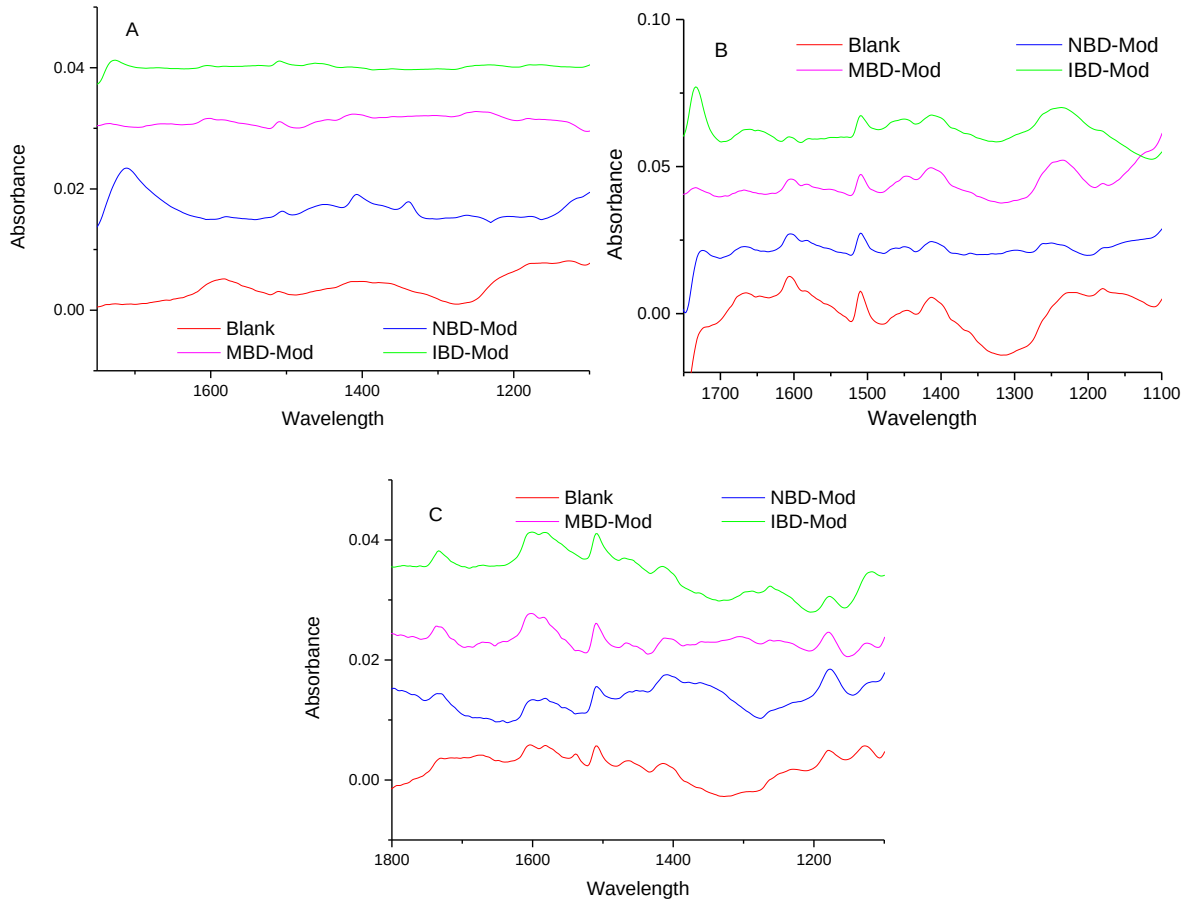

Figure 6.28: FT-IR spectra of O-polar (A), Zn-polar (B) and m-plane (C) ZnO surfaces modified in 0.1 M pH 8 buffer with 5 mM NBD (NBD-Mod), MBD (MBD-Mod) and IBD (IBD-Mod) and in the absence of aryldiazonium salt (Blank). Spectra are normalised to the peak at ~1500 cm^{-1} for the blank sample.

From the results above, it is apparent that there is no significant attachment of an aryl layer to the surface during the electrochemical modification process regardless of crystal face. However, the CV curves of the electrochemical modification step show clear differences between when the surfaces are cycled in the presence and absence of aryldiazonium salt (Figure 6.18-Figure 6.20). It is possible that reduction of the aryldiazonium ion is occurring at the ZnO surfaces but that the subsequent attachment step of the aryl radical to the surface is not occurring. Additionally, the higher P/Zn ratio

for samples modified in the presence of NBD compared to blank and IBD treated samples suggests an interaction between the aryldiazonium ion and phosphate ions.

6.4 Conclusions

The modification of MBE-grown ZnO surfaces with aryldiazonium ions spontaneously and electrochemically in aqueous solution was investigated. The electrochemical modification approach developed was then extended to modify O-polar, Zn-polar and m-plane single crystal surfaces to investigate the effect of crystal face on the modification process.

Modification of MBE-grown ZnO surfaces was successful via both spontaneous grafting and electrografting in pH 8 aqueous solution. It was found that spontaneous modification at low buffer concentrations resulted in corrosion of the surface due to a decrease in pH by an unknown mechanism. Modification at increased buffer concentration was used to attach NP and CP groups to ZnO, as confirmed by FT-IR spectroscopy. Electrochemical modification of the MBE-grown ZnO surfaces was attempted under the same conditions due to the ability of natively n-type ZnO to perform reduction reactions. Electrochemical cycling in the presence of aryldiazonium ions at pH 8 resulted in larger reduction currents than in the absence of aryldiazonium ions, suggesting successful formation of aryl radicals. Successful electrochemical grafting of NP, MP and IP groups was confirmed by FT-IR and AFM. Electrochemical modification gave increased coverage compared to spontaneous modification based on a comparison of FT-IR peak areas for NP-modified surfaces. XPS analysis of a NP-modified surface showed signals due to NO_2 groups and reduced N, either from azo groups or reduction of the NP groups during grafting. Additionally, an increase in surface O and significant incorporation of P was observed for the NP-modified surface, most likely due to the adsorption of phosphates from the buffer solution.

Due to the increased surface coverage, electrochemical grafting was selected as the method to modify single crystal ZnO surfaces. A range of crystal faces (O-polar, Zn-polar and m-plane) were used to determine the effect of their differing surface chemistries on the grafting process. Electrochemical modification in the presence of NBD, MBD and IBD again gave a very different CV response to the blank sample prepared in the absence of aryldiazonium ion. However, characterisation of these modified surfaces by XPS and FT-IR showed no clear evidence of attachment of an aryl layer. As was observed for the MBE-grown samples, electrochemical cycling resulted in introduction significant P content to the sample surface. This was especially enhanced for the NBD-modified samples and appeared to depend on the degree of O termination of the surface (O-polar > m-plane > Zn-polar). Additionally, shifts were observed in the band edge positions after

electrochemical treatment as determined by valence band XPS spectra. Most significantly, large shifts were observed for the NBD- and IBD-modified O-polar samples. This change in valence band position did not strongly correlate with the variation in P/Zn ratio and thus the adsorption of phosphate at the ZnO surface must not be the sole process occurring during electrochemical modification.

Considering grafting of aryldiazonium salts to both types of ZnO surface studied, it is clear that the grafting reaction proceeds readily at the MBE surfaces but not at single crystal ZnO. However at both types of surface, there are clearly features in the modification CV curves that are only observed in the presence of aryldiazonium ion. Thus it appears that all surfaces studied are able to reduce aryldiazonium ions to aryl radicals but subsequent attachment of the radical to the surface is only observed for MBE-grown ZnO. The MBE-grown surfaces are much more disordered and have higher defect density than the bulk single crystal materials which may make them more reactive to aryldiazonium ion attachment. From the XPS results it is clear that significant adsorption of phosphates from the buffer solution is occurring at the surface. That this adsorption is stable to ultrasonic cleaning is unexpected. Phosphate adsorption does not appear to rely on an electrochemical process as only very weak CV response is observed for the blank samples but appreciable P content was measured for these surfaces by XPS. Coverage of phosphates on the surface appears to vary based on the proportion of O termination at the surface as determined from the crystal structure dependence. Additionally, there appears to be an interaction between the aryldiazonium ion/aryl radical and phosphate ions in the buffer – especially with NBD. This may introduce a competing mechanism that consumes aryl radicals or otherwise impedes their attachment. It is possible that the aryl radicals produced at the ZnO surface abstract chemisorbed H or OH from surface O or Zn atoms to produce benzene or phenol derivatives in solution rather than attaching to the electrode surface. The loss of these terminal groups may promote attachment of phosphate ions in their place. Although no attachment of the aryl groups was observed on the single-crystal ZnO surfaces, the electrochemical modification process increased the downward band bending of the ZnO surfaces. However, these changes in band bending did not directly correlate to the P-content of the ZnO samples. This indicates some of the adsorbed phosphates are acting as surface donors but also that there other phosphate species present that are not contributing charge to the surface.

The interaction of aryl radicals with single-crystal ZnO surfaces could be more readily determined by conducting the electrografting reaction in either a different buffer system or in non-aqueous conditions to remove the effects of phosphate adsorption. Additionally, spectroelectrochemical

studies on the electrochemical grafting process to determine the products of the reduction of aryldiazonium salts at ZnO surfaces may provide further insight into this process.

6.5 References

1. Janotti, A.; Van de Walle, C. G., Fundamentals of Zinc Oxide as a Semiconductor. *Rep. Prog. Phys.* **2009,** *72* (12), 126501.
2. Kim, H.; Gilmore, C. M.; Horwitz, J. S.; Piqué, A.; Murata, H.; Kushto, G. P.; Schlaf, R.; Kafafi, Z. H.; Chrisey, D. B., Transparent Conducting Aluminum-Doped Zinc Oxide Thin Films for Organic Light-Emitting Devices. *Appl. Phys. Lett.* **2000,** *76* (3), 259-261.
3. Xu, S.; Wang, Z. L., One-Dimensional ZnO Nanostructures: Solution Growth and Functional Properties. *Nano Research* **2011,** *4* (11), 1013-1098.
4. Wang, Z. L., Zinc Oxide Nanostructures: Growth, Properties and Applications. *J. Phys.: Condens. Matter* **2004,** *16* (25), R829.
5. Özgür, Ü.; Alivov, Y. I.; Liu, C.; Teke, A.; Reshchikov, M. A.; Doğan, S.; Avrutin, V.; Cho, S.-J.; Morkoç, H., A Comprehensive Review of ZnO Materials and Devices. *J. Appl. Phys.* **2005,** *98* (4), 041301.
6. Li, Y.; Huang, B.; Zhang, R.-Q.; Lin, Z.; Van Hove, M. A., Stabilizing Reconstruction Induced by O Protrusions of the ZnO (0001) Polar Surface. *RSC Advances* **2014,** *4* (97), 54249-54255.
7. Heinhold, R.; Williams, G. T.; Cooil, S. P.; Evans, D. A.; Allen, M. W., Influence of Polarity and Hydroxyl Termination on the Band Bending at ZnO Surfaces. *Phys. Rev. B* **2013,** *88* (23), 235315.
8. Önsten, A.; Stoltz, D.; Palmgren, P.; Yu, S.; Göthelid, M.; Karlsson, U. O., Water Adsorption on ZnO(0001): Transition from Triangular Surface Structures to a Disordered Hydroxyl Terminated Phase. *J. Phys. Chem. C* **2010,** *114* (25), 11157-11161.
9. Hewlett, R. M.; McLachlan, M. A., Surface Structure Modification of ZnO and the Impact on Electronic Properties. *Adv. Mater.* **2016**, n/a-n/a.
10. Triboulet, R., Growth of ZnO Bulk Crystals: A Review. *Prog. Cryst. Growth Charact. Mater.* **2014,** *60* (1), 1-14.
11. Ehrentraut, D.; Sato, H.; Kagamitani, Y.; Sato, H.; Yoshikawa, A.; Fukuda, T., Solvothermal Growth of ZnO. *Prog. Cryst. Growth Charact. Mater.* **2006,** *52* (4), 280-335.
12. Neuvonen, P. T.; Vines, L.; Kuznetsov, A. Y.; Svensson, B. G.; Du, X.; Tuomisto, F.; Hallén, A., Interaction between Na and Li in ZnO. *Appl. Phys. Lett.* **2009,** *95* (24), 242111.
13. Kumar, R.; Kumar, G.; Al-Dossary, O.; Umar, A., ZnO Nanostructured Thin Films: Depositions, Properties and Applications: A Review. *Materials Express* **2015,** *5* (1), 3-23.
14. Banerjee, P.; Lee, W.-J.; Bae, K.-R.; Lee, S. B.; Rubloff, G. W., Structural, Electrical, and Optical Properties of Atomic Layer Deposition Al-Doped ZnO Films. *J. Appl. Phys.* **2010,** *108* (4), 043504.
15. Lupan, O.; Pauporté, T.; Chow, L.; Viana, B.; Pellé, F.; Ono, L. K.; Roldan Cuenya, B.; Heinrich, H., Effects of Annealing on Properties of ZnO Thin Films Prepared by Electrochemical Deposition in Chloride Medium. *Appl. Surf. Sci.* **2010,** *256* (6), 1895-1907.
16. Znaidi, L., Sol–Gel-Deposited ZnO Thin Films: A Review. *Mater. Sci. Eng., B* **2010,** *174* (1–3), 18-30.
17. Kang, H. S.; Pang, S. S.; Kim, J. W.; Kim, G. H.; Kim, J. H.; Lee, S. Y.; Li, Y.; Wang, H.; Jia, Q. X., The Role of a ZnO Buffer Layer in the Growth of ZnO Thin Film on Al_2O_3 Substrate. *Superlattices Microstruct.* **2006,** *40* (4–6), 501-506.
18. Arthur, J. R., Molecular Beam Epitaxy. *Surf. Sci.* **2002,** *500* (1–3), 189-217.
19. Triboulet, R.; Perrière, J., Epitaxial Growth of ZnO Films. *Prog. Cryst. Growth Charact. Mater.* **2003,** *47* (2–3), 65-138.
20. Özgür, Ü.; Avrutin, V.; Morkoç, H., Chapter 16 - Zinc Oxide Materials and Devices Grown by MBE. In *Molecular Beam Epitaxy*, Henini, M., Ed. Elsevier: Oxford, 2013; pp 369-416.

21. Skompska, M.; Zarębska, K., Electrodeposition of ZnO Nanorod Arrays on Transparent Conducting Substrates–a Review. *Electrochim. Acta* **2014,** *127*, 467-488.
22. Panda, D.; Tseng, T.-Y., One-Dimensional ZnO Nanostructures: Fabrication, Optoelectronic Properties, and Device Applications. *J. Mater. Sci.* **2013,** *48* (20), 6849-6877.
23. Gomez, J.; Tigli, O., Zinc Oxide Nanostructures: From Growth to Application. *J. Mater. Sci.* **2013,** *48* (2), 612-624.
24. Xu, L.; Li, X.; Zhan, Z.; Wang, L.; Feng, S.; Chai, X.; Lu, W.; Shen, J.; Weng, Z.; Sun, J., Catalyst-Free, Selective Growth of ZnO Nanowires on SiO_2 by Chemical Vapor Deposition for Transfer-Free Fabrication of UV Photodetectors. *ACS Appl. Mater. Interfaces* **2015,** *7* (36), 20264-20271.
25. Kołodziejczak-Radzimska, A.; Jesionowski, T., Zinc Oxide—from Synthesis to Application: A Review. *Materials* **2014,** *7* (4), 2833.
26. Peulon, S.; Lincot, D., Mechanistic Study of Cathodic Electrodeposition of Zinc Oxide and Zinc Hydroxychloride Films from Oxygenated Aqueous Zinc Chloride Solutions. *J. Electrochem. Soc.* **1998,** *145* (3), 864-874.
27. Yoshida, T.; Tochimoto, M.; Schlettwein, D.; Wöhrle, D.; Sugiura, T.; Minoura, H., Self-Assembly of Zinc Oxide Thin Films Modified with Tetrasulfonated Metallophthalocyanines by One-Step Electrodeposition. *Chem. Mater.* **1999,** *11* (10), 2657-2667.
28. Feng, W.-W.; Cho, S.; Wang, M.-S.; Dung, D. D., Co-Contribution of Hydrogen Impurities and Native Defects Might Be the Answer for the N-Type Conductivity in ZnO. *Phys. Lett. A* **2016,** *380* (3), 480-484.
29. King, P. D. C.; Veal, T. D., Conductivity in Transparent Oxide Semiconductors. *J. Phys.: Condens. Matter* **2011,** *23* (33), 334214.
30. Avrutin, V.; Silversmith, D. J.; Morkoc, H., Doping Asymmetry Problem in ZnO: Current Status and Outlook. *Proc. IEEE* **2010,** *98* (7), 1269-1280.
31. Mannam, R.; Eswaran, S. K.; DasGupta, N.; Rao, M. S. R., Zn-Vacancy Induced Violet Emission in P-Type Phosphorus and Nitrogen Codoped ZnO Thin Films Grown by Pulsed Laser Deposition. *Appl. Surf. Sci.* **2015,** *347*, 96-100.
32. Kao, T.-H.; Chen, J.-Y.; Chiu, C.-H.; Huang, C.-W.; Wu, W.-W., Opto-Electrical Properties of Sb-Doped P-Type ZnO Nanowires. *Appl. Phys. Lett.* **2014,** *104* (11), 111909.
33. Piper, L. F. J.; Preston, A. R. H.; Fedorov, A.; Cho, S. W.; DeMasi, A.; Smith, K. E., Direct Evidence of Metallicity at ZnO(0001)-(1×1) Surfaces from Angle-Resolved Photoemission Spectroscopy. *Phys. Rev. B* **2010,** *81* (23), 233305.
34. Heinhold, R.; Cooil, S. P.; Evans, D. A.; Allen, M. W., Stability of the Surface Electron Accumulation Layers on the Nonpolar (10$\bar{1}$0) and (11$\bar{2}$0) Faces of ZnO. *J. Phys. Chem. C* **2014,** *118* (42), 24575-24582.
35. Heiland, G.; Kunstmann, P., Polar Surfaces of Zinc Oxide Crystals. *Surf. Sci.* **1969,** *13* (1), 72-84.
36. Brillson, L. J.; Lu, Y., ZnO Schottky Barriers and Ohmic Contacts. *J. Appl. Phys.* **2011,** *109* (12), 121301.
37. Alenezi, M. R.; Henley, S. J.; Emerson, N. G.; Silva, S. R. P., From 1D and 2D ZnO Nanostructures to 3D Hierarchical Structures with Enhanced Gas Sensing Properties. *Nanoscale* **2014,** *6* (1), 235-247.
38. Hassan, J. J.; Mahdi, M. A.; Chin, C. W.; Abu-Hassan, H.; Hassan, Z., A High-Sensitivity Room-Temperature Hydrogen Gas Sensor Based on Oblique and Vertical ZnO Nanorod Arrays. *Sens. Actuators, B* **2013,** *176*, 360-367.
39. Katoch, A.; Sun, G.-J.; Choi, S.-W.; Byun, J.-H.; Kim, S. S., Competitive Influence of Grain Size and Crystallinity on Gas Sensing Performances of ZnO Nanofibers. *Sens. Actuators, B* **2013,** *185*, 411-416.
40. Ozgur, U.; Hofstetter, D.; Morkoc, H., Zno Devices and Applications: A Review of Current Status and Future Prospects. *Proc. IEEE* **2010,** *98* (7), 1255-1268.

41. Lin, Y.-H.; Faber, H.; Zhao, K.; Wang, Q.; Amassian, A.; McLachlan, M.; Anthopoulos, T. D., High-Performance Zno Transistors Processed Via an Aqueous Carbon-Free Metal Oxide Precursor Route at Temperatures between 80–180 °C. *Adv. Mater.* **2013,** *25* (31), 4340-4346.
42. Opoku, C.; Dahiya, A. S.; Cayrel, F.; Poulin-Vittrant, G.; Alquier, D.; Camara, N., Fabrication of Field-Effect Transistors and Functional Nanogenerators Using Hydrothermally Grown ZnO Nanowires. *RSC Adv.* **2015,** *5* (86), 69925-69931.
43. Fu, Q.-M.; Cao, W.; Li, G.-W.; Lin, Z.-D.; Chen, Z.; Xu, C.-B.; Tu, Y.-F.; Ma, Z.-B., Blue/Green Electroluminescence from a ZnO Nanorods/P-GaN Heterojunction Light Emitting Diode under Different Reverse Bias. *Appl. Surf. Sci.* **2014,** *293*, 225-228.
44. Jeong, H.; Park, D. J.; Lee, H. S.; Ko, Y. H.; Yu, J. S.; Choi, S.-B.; Lee, D.-S.; Suh, E.-K.; Jeong, M. S., Light-Extraction Enhancement of a GaN-Based LED Covered with ZnO Nanorod Arrays. *Nanoscale* **2014,** *6* (8), 4371-4378.
45. Shen, H.; Shan, C.-X.; Qiao, Q.; Liu, J.-S.; Li, B.-H.; Shen, D.-Z., Stable Surface Plasmon Enhanced ZnO Homojunction Light-Emitting Devices. *J. Mater. Chem. C* **2013,** *1* (2), 234-237.
46. Bagnall, D. M.; Chen, Y. F.; Zhu, Z.; Yao, T.; Koyama, S.; Shen, M. Y.; Goto, T., Optically Pumped Lasing of ZnO at Room Temperature. *Appl. Phys. Lett.* **1997,** *70* (17), 2230-2232.
47. Zhang, N.; Yu, K.; Li, Q.; Song, C.; Zhu, L.; Zhu, Z., Room-Temperature Blue–Violet Laser Emission from Individual Ultra-Long ZnO Microbelts. *Mater. Lett.* **2014,** *121*, 231-233.
48. Tian, C.; Jiang, D.; Li, B.; Lin, J.; Zhao, Y.; Yuan, W.; Zhao, J.; Liang, Q.; Gao, S.; Hou, J.; Qin, J., Performance Enhancement of ZnO UV Photodetectors by Surface Plasmons. *ACS Appl. Mater. Interfaces* **2014,** *6* (3), 2162-2166.
49. Xu, J.; Chen, Z.; Zapien, J. A.; Lee, C.-S.; Zhang, W., Surface Engineering of ZnO Nanostructures for Semiconductor-Sensitized Solar Cells. *Adv. Mater.* **2014,** *26* (31), 5337-5367.
50. Kumar, M. H.; Yantara, N.; Dharani, S.; Graetzel, M.; Mhaisalkar, S.; Boix, P. P.; Mathews, N., Flexible, Low-Temperature, Solution Processed ZnO-Based Perovskite Solid State Solar Cells. *Chem. Commun.* **2013,** *49* (94), 11089-11091.
51. Son, D.-Y.; Im, J.-H.; Kim, H.-S.; Park, N.-G., 11% Efficient Perovskite Solar Cell Based on ZnO Nanorods: An Effective Charge Collection System. *J. Phys. Chem. C* **2014,** *118* (30), 16567-16573.
52. Yan, K.; Zhang, L.; Qiu, J.; Qiu, Y.; Zhu, Z.; Wang, J.; Yang, S., A Quasi-Quantum Well Sensitized Solar Cell with Accelerated Charge Separation and Collection. *J. Am. Chem. Soc.* **2013,** *135* (25), 9531-9539.
53. Magne, C.; Moehl, T.; Urien, M.; Gratzel, M.; Pauporte, T., Effects of ZnO Film Growth Route and Nanostructure on Electron Transport and Recombination in Dye-Sensitized Solar Cells. *J. Mater. Chem. A* **2013,** *1* (6), 2079-2088.
54. Shao, S.; Zheng, K.; Pullerits, T.; Zhang, F., Enhanced Performance of Inverted Polymer Solar Cells by Using Poly(Ethylene Oxide)-Modified ZnO as an Electron Transport Layer. *ACS Appl. Mater. Interfaces* **2013,** *5* (2), 380-385.
55. Liao, S.-H.; Jhuo, H.-J.; Cheng, Y.-S.; Chen, S.-A., Fullerene Derivative-Doped Zinc Oxide Nanofilm as the Cathode of Inverted Polymer Solar Cells with Low-Bandgap Polymer (Ptb7-Th) for High Performance. *Adv. Mater.* **2013,** *25* (34), 4766-4771.
56. Wu, W.; Wang, Z. L., Piezotronic Nanowire-Based Resistive Switches as Programmable Electromechanical Memories. *Nano Lett.* **2011,** *11* (7), 2779-2785.
57. Wu, W.; Wei, Y.; Wang, Z. L., Strain-Gated Piezotronic Logic Nanodevices. *Adv. Mater.* **2010,** *22* (42), 4711-4715.
58. Magnusson, E. B.; Williams, B. H.; Manenti, R.; Nam, M.-S.; Nersisyan, A.; Peterer, M. J.; Ardavan, A.; Leek, P. J., Surface Acoustic Wave Devices on Bulk ZnO Crystals at Low Temperature. *Appl. Phys. Lett.* **2015,** *106* (6), 063509.
59. Liao, Q.; Zhang, Z.; Zhang, X.; Mohr, M.; Zhang, Y.; Fecht, H.-j., Flexible Piezoelectric Nanogenerators Based on a Fiber/ZnO Nanowires/Paper Hybrid Structure for Energy Harvesting. *Nano Research* **2014,** *7* (6), 917-928.

60. Xinyu, X.; Yuxin, N.; Bin, H.; Lili, X.; Yan, Z.; Zhong Lin, W., Surface Free-Carrier Screening Effect on the Output of a ZnO Nanowire Nanogenerator and Its Potential as a Self-Powered Active Gas Sensor. *Nanotechnology* **2013,** *24* (22), 225501.
61. Xue, F.; Zhang, L.; Tang, W.; Zhang, C.; Du, W.; Wang, Z. L., Piezotronic Effect on ZnO Nanowire Film Based Temperature Sensor. *ACS Appl. Mater. Interfaces* **2014,** *6* (8), 5955-5961.
62. He, X. L.; Li, D. J.; Zhou, J.; Wang, W. B.; Xuan, W. P.; Dong, S. R.; Jin, H.; Luo, J. K., High Sensitivity Humidity Sensors Using Flexible Surface Acoustic Wave Devices Made on Nanocrystalline ZnO/Polyimide Substrates. *J. Mater. Chem. C* **2013,** *1* (39), 6210-6215.
63. Sundara Venkatesh, P.; Dharmaraj, P.; Purushothaman, V.; Ramakrishnan, V.; Jeganathan, K., Point Defects Assisted NH_3 Gas Sensing Properties in ZnO Nanostructures. *Sens. Actuators, B* **2015,** *212*, 10-17.
64. Zhao, Y.; Deng, P.; Nie, Y.; Wang, P.; Zhang, Y.; Xing, L.; Xue, X., Biomolecule-Adsorption-Dependent Piezoelectric Output of ZnO Nanowire Nanogenerator and Its Application as Self-Powered Active Biosensor. *Biosens. Bioelectron.* **2014,** *57*, 269-275.
65. Yu, R.; Pan, C.; Chen, J.; Zhu, G.; Wang, Z. L., Enhanced Performance of a ZnO Nanowire-Based Self-Powered Glucose Sensor by Piezotronic Effect. *Adv. Funct. Mater.* **2013,** *23* (47), 5868-5874.
66. Zhou, J.; Xu, N. S.; Wang, Z. L., Dissolving Behavior and Stability of ZnO Wires in Biofluids: A Study on Biodegradability and Biocompatibility of ZnO Nanostructures. *Adv. Mater.* **2006,** *18* (18), 2432-2435.
67. Hwa, K.-Y.; Subramani, B., Synthesis of Zinc Oxide Nanoparticles on Graphene–Carbon Nanotube Hybrid for Glucose Biosensor Applications. *Biosens. Bioelectron.* **2014,** *62*, 127-133.
68. Ahmad, R.; Tripathy, N.; Hahn, Y.-B., High-Performance Cholesterol Sensor Based on the Solution-Gated Field Effect Transistor Fabricated with ZnO Nanorods. *Biosens. Bioelectron.* **2013,** *45*, 281-286.
69. Liu, X.; Lin, P.; Yan, X.; Kang, Z.; Zhao, Y.; Lei, Y.; Li, C.; Du, H.; Zhang, Y., Enzyme-Coated Single ZnO Nanowire FET Biosensor for Detection of Uric Acid. *Sens. Actuators, B* **2013,** *176*, 22-27.
70. Ahmad, M.; Ahmed, E.; Hong, Z. L.; Xu, J. F.; Khalid, N. R.; Elhissi, A.; Ahmed, W., A Facile One-Step Approach to Synthesizing ZnO/Graphene Composites for Enhanced Degradation of Methylene Blue under Visible Light. *Appl. Surf. Sci.* **2013,** *274*, 273-281.
71. Kargar, A.; Sun, K.; Jing, Y.; Choi, C.; Jeong, H.; Zhou, Y.; Madsen, K.; Naughton, P.; Jin, S.; Jung, G. Y.; Wang, D., Tailoring n-ZnO/p-Si Branched Nanowire Heterostructures for Selective Photoelectrochemical Water Oxidation or Reduction. *Nano Lett.* **2013,** *13* (7), 3017-3022.
72. Zhang, X.; Qin, J.; Xue, Y.; Yu, P.; Zhang, B.; Wang, L.; Liu, R., Effect of Aspect Ratio and Surface Defects on the Photocatalytic Activity of ZnO Nanorods. *Sci. Rep.* **2014,** *4*, 4596.
73. Hong, Y.; Tian, C.; Jiang, B.; Wu, A.; Zhang, Q.; Tian, G.; Fu, H., Facile Synthesis of Sheet-Like ZnO Assembly Composed of Small ZnO Particles for Highly Efficient Photocatalysis. *J. Mater. Chem. A* **2013,** *1* (18), 5700-5708.
74. Bai, X.; Wang, L.; Zong, R.; Lv, Y.; Sun, Y.; Zhu, Y., Performance Enhancement of ZnO Photocatalyst Via Synergic Effect of Surface Oxygen Defect and Graphene Hybridization. *Langmuir* **2013,** *29* (9), 3097-3105.
75. Perkins, C. L., Molecular Anchors for Self-Assembled Monolayers on ZnO: A Direct Comparison of the Thiol and Phosphonic Acid Moieties. *J. Phys. Chem. C* **2009,** *113* (42), 18276-18286.
76. Ha, Y. E.; Jo, M. Y.; Park, J.; Kang, Y.-C.; Yoo, S. I.; Kim, J. H., Inverted Type Polymer Solar Cells with Self-Assembled Monolayer Treated ZnO. *J. of Phys. Chem. C* **2013,** *117* (6), 2646-2652.
77. Nicholas, N. J.; Franks, G. V.; Ducker, W. A., Selective Adsorption to Particular Crystal Faces of ZnO. *Langmuir* **2012,** *28* (18), 7189-7196.
78. Chen, J.; Ruther, R. E.; Tan, Y.; Bishop, L. M.; Hamers, R. J., Molecular Adsorption on ZnO(10$\bar{1}$0) Single-Crystal Surfaces: Morphology and Charge Transfer. *Langmuir* **2012,** *28* (28), 10437-10445.

79. Timpel, M.; Nardi, M. V.; Krause, S.; Ligorio, G.; Christodoulou, C.; Pasquali, L.; Giglia, A.; Frisch, J.; Wegner, B.; Moras, P.; Koch, N., Surface Modification of ZnO(0001)–Zn with Phosphonate-Based Self-Assembled Monolayers: Binding Modes, Orientation, and Work Function. *Chem. Mater.* **2014,** *26* (17), 5042-5050.
80. Lange, I.; Reiter, S.; Pätzel, M.; Zykov, A.; Nefedov, A.; Hildebrandt, J.; Hecht, S.; Kowarik, S.; Wöll, C.; Heimel, G.; Neher, D., Tuning the Work Function of Polar Zinc Oxide Surfaces Using Modified Phosphonic Acid Self-Assembled Monolayers. *Adv. Funct. Mater.* **2014,** *24* (44), 7014-7024.
81. García Núñez, C.; Sachsenhauser, M.; Blashcke, B.; García Marín, A.; Garrido, J. A.; Pau, J. L., Effects of Hydroxylation and Silanization on the Surface Properties of ZnO Nanowires. *ACS Appl. Mater. Interfaces* **2015,** *7* (9), 5331-5337.
82. Arnaud, G. F.; De Renzi, V.; del Pennino, U.; Biagi, R.; Corradini, V.; Calzolari, A.; Ruini, A.; Catellani, A., Nitrocatechol/ZnO Interface: The Role of Dipole in a Dye/Metal-Oxide Model System. *J. Phys. Chem. C* **2014,** *118* (8), 3910-3917.
83. Ruther, R. E.; Franking, R.; Huhn, A. M.; Gomez-Zayas, J.; Hamers, R. J., Formation of Smooth, Conformal Molecular Layers on ZnO Surfaces Via Photochemical Grafting. *Langmuir* **2011,** *27* (17), 10604-10614.
84. Smecca, E.; Motta, A.; Fragalà, M. E.; Aleeva, Y.; Condorelli, G. G., Spectroscopic and Theoretical Study of the Grafting Modes of Phosphonic Acids on ZnO Nanorods. *J. Phys. Chem. C* **2013,** *117* (10), 5364-5372.
85. Cowan, S. R.; Schulz, P.; Giordano, A. J.; Garcia, A.; MacLeod, B. A.; Marder, S. R.; Kahn, A.; Ginley, D. S.; Ratcliff, E. L.; Olson, D. C., Chemically Controlled Reversible and Irreversible Extraction Barriers Via Stable Interface Modification of Zinc Oxide Electron Collection Layer in Polycarbazole-Based Organic Solar Cells. *Adv. Funct. Mater.* **2014,** *24* (29), 4671-4680.
86. Kedem, N.; Blumstengel, S.; Henneberger, F.; Cohen, H.; Hodes, G.; Cahen, D., Morphology-, Synthesis- and Doping-Independent Tuning of ZnO Work Function Using Phenylphosphonates. *PCCP* **2014,** *16* (18), 8310-8319.
87. Zhang, B.; Kong, T.; Xu, W.; Su, R.; Gao, Y.; Cheng, G., Surface Functionalization of Zinc Oxide by Carboxyalkylphosphonic Acid Self-Assembled Monolayers. *Langmuir* **2010,** *26* (6), 4514-4522.
88. Liu, D.; Wu, W.; Qiu, Y.; Yang, S.; Xiao, S.; Wang, Q.-Q.; Ding, L.; Wang, J., Surface Functionalization of ZnO Nanotetrapods with Photoactive and Electroactive Organic Monolayers. *Langmuir* **2008,** *24* (9), 5052-5059.
89. Chizhov, A. S.; Rumyantseva, M. N.; Vasiliev, R. B.; Filatova, D. G.; Drozdov, K. A.; Krylov, I. V.; Abakumov, A. M.; Gaskov, A. M., Visible Light Activated Room Temperature Gas Sensors Based on Nanocrystalline ZnO Sensitized with Cdse Quantum Dots. *Sens. Actuators, B* **2014,** *205*, 305-312.
90. Love, J. C.; Estroff, L. A.; Kriebel, J. K.; Nuzzo, R. G.; Whitesides, G. M., Self-Assembled Monolayers of Thiolates on Metals as a Form of Nanotechnology. *Chem. Rev.* **2005,** *105* (4), 1103-1170.
91. Zhang, Y.; Zhou, J.; Zhang, X.; Hu, J.; Gao, H., Solvent Polarity Effect on Quality of N-Octadecanethiol Self-Assembled Monolayers on Copper and Oxidized Copper. *Appl. Surf. Sci.* **2014,** *320*, 200-206.
92. Carmeli, I.; Lewin, A.; Flekser, E.; Diamant, I.; Zhang, Q.; Shen, J.; Gozin, M.; Richter, S.; Dagan, Y., Tuning the Critical Temperature of Cuprate Superconductor Films with Self-Assembled Organic Layers. *Angew. Chem. Int. Ed.* **2012,** *51* (29), 7162-7165.
93. Gooding, J. J.; Ciampi, S., The Molecular Level Modification of Surfaces: From Self-Assembled Monolayers to Complex Molecular Assemblies. *Chem. Soc. Rev.* **2011,** *40* (5), 2704-2718.
94. Pujari, S. P.; Scheres, L.; Marcelis, A. T. M.; Zuilhof, H., Covalent Surface Modification of Oxide Surfaces. *Angew. Chem. Int. Ed.* **2014,** *53* (25), 6322-6356.
95. Bishop, L. M.; Yeager, J. C.; Chen, X.; Wheeler, J. N.; Torelli, M. D.; Benson, M. C.; Burke, S. D.; Pedersen, J. A.; Hamers, R. J., A Citric Acid-Derived Ligand for Modular Functionalization of Metal Oxide Surfaces Via “Click” Chemistry. *Langmuir* **2012,** *28* (2), 1322-1329.

96. Lim, M. S.; Feng, K.; Chen, X.; Wu, N.; Raman, A.; Nightingale, J.; Gawalt, E. S.; Korakakis, D.; Hornak, L. A.; Timperman, A. T., Adsorption and Desorption of Stearic Acid Self-Assembled Monolayers on Aluminum Oxide. *Langmuir* **2007,** *23* (5), 2444-2452.
97. Weisz, A. D.; Regazzoni, A. E.; Blesa, M. A., Atr–Ftir Study of the Stability Trends of Carboxylate Complexes Formed on the Surface of Titanium Dioxide Particles Immersed in Water. *Solid State Ionics* **2001,** *143* (1), 125-130.
98. Martini, L. A.; Moore, G. F.; Milot, R. L.; Cai, L. Z.; Sheehan, S. W.; Schmuttenmaer, C. A.; Brudvig, G. W.; Crabtree, R. H., Modular Assembly of High-Potential Zinc Porphyrin Photosensitizers Attached to TiO_2 with a Series of Anchoring Groups. *J. Phys. Chem. C* **2013,** *117* (28), 14526-14533.
99. Forget, A.; Limoges, B.; Balland, V., Efficient Chemisorption of Organophosphorous Redox Probes on Indium Tin Oxide Surfaces under Mild Conditions. *Langmuir* **2015,** *31* (6), 1931-1940.
100. Hanson, E. L.; Guo, J.; Koch, N.; Schwartz, J.; Bernasek, S. L., Advanced Surface Modification of Indium Tin Oxide for Improved Charge Injection in Organic Devices. *J. Am. Chem. Soc.* **2005,** *127* (28), 10058-10062.
101. Hotchkiss, P. J.; Jones, S. C.; Paniagua, S. A.; Sharma, A.; Kippelen, B.; Armstrong, N. R.; Marder, S. R., The Modification of Indium Tin Oxide with Phosphonic Acids: Mechanism of Binding, Tuning of Surface Properties, and Potential for Use in Organic Electronic Applications. *Acc. Chem. Res.* **2012,** *45* (3), 337-346.
102. Sakeye, M.; Smått, J.-H., Comparison of Different Amino-Functionalization Procedures on a Selection of Metal Oxide Microparticles: Degree of Modification and Hydrolytic Stability. *Langmuir* **2012,** *28* (49), 16941-16950.
103. Zhao, J.; Milanova, M.; Warmoeskerken, M. M. C. G.; Dutschk, V., Surface Modification of TiO_2 Nanoparticles with Silane Coupling Agents. *Colloids Surf., A* **2012,** *413*, 273-279.
104. Mallakpour, S.; Dinari, M., Investigating the Nanostructure and Thermal Properties of Chiral Poly(Amide-Imide)/Al_2O_3 Compatibilized with 3-Aminopropyltriethoxysilane. *Mater. Res. Bull.* **2013,** *48* (10), 3865-3872.
105. Mahdavian, A. R.; Mirrahimi, M. A.-S., Efficient Separation of Heavy Metal Cations by Anchoring Polyacrylic Acid on Superparamagnetic Magnetite Nanoparticles through Surface Modification. *Chem. Eng. J.* **2010,** *159* (1–3), 264-271.
106. Wang, C.; Huang, N.; Zhuang, H.; Jiang, X., Enhanced Performance of Nanocrystalline ZnO DNA Biosensor Via Introducing Electrochemical Covalent Biolinkers. *ACS Appl. Mater. Interfaces* **2015,** *7* (14), 7605-7612.
107. Katsumi, M.; Mitsuru, S.; Ikuo, N.; Tsuguo, F., Growth of 2 Inch ZnO Bulk Single Crystal by the Hydrothermal Method. *Semicond. Sci. Technol.* **2005,** *20* (4), S49.
108. Vlaev, L.; Damyanov, D.; Mohamed, M. M., Infrared Spectroscopy Study of the Nature and Reactivity of a Hydrate Coverage on the Surface of γ-Al_2O_3. *Colloids Surf.* **1989,** *36* (3), 427-437.
109. Sowri Babu, K.; Ramachandra Reddy, A.; Sujatha, C.; Venugopal Reddy, K.; Mallika, A. N., Synthesis and Optical Characterization of Porous ZnO. *J. Adv. Ceram.* **2013,** *2* (3), 260-265.
110. Wippermann, K.; Schultze, J. W.; Kessel, R.; Penninger, J., The Inhibition of Zinc Corrosion by Bisaminotriazole and Other Triazole Derivatives. *Corros. Sci.* **1991,** *32* (2), 205-230.
111. Bian, S.-W.; Mudunkotuwa, I. A.; Rupasinghe, T.; Grassian, V. H., Aggregation and Dissolution of 4 nm ZnO Nanoparticles in Aqueous Environments: Influence of Ph, Ionic Strength, Size, and Adsorption of Humic Acid. *Langmuir* **2011,** *27* (10), 6059-6068.
112. Becker, J. P.; Pust, S. E.; Hüpkes, J., Effects of the Electrolyte Species on the Electrochemical Dissolution of Polycrystalline ZnO:Al Thin Films. *Electrochim. Acta* **2013,** *112*, 976-982.
113. Mesnage, A.; Lefèvre, X.; Jégou, P.; Deniau, G.; Palacin, S., Spontaneous Grafting of Diazonium Salts: Chemical Mechanism on Metallic Surfaces. *Langmuir* **2012,** *28* (32), 11767-11778.
114. Sienkiewicz, A.; Szymula, M.; Narkiewicz-Michalek, J.; Bravo-Díaz, C., Formation of Diazohydroxides ArN_2OH in Aqueous Acid Solution: Polarographic Determination of the Equilibrium Constant Kr for the Reaction of 4-Substituted Arenediazonium Ions with H_2O. *J. Phys. Org. Chem.* **2014,** *27* (4), 284-289.

115. Belanger, D.; Pinson, J., Electrografting: A Powerful Method for Surface Modification. *Chem. Soc. Rev.* **2011,** *40* (7).
116. Hotchkiss, P. J.; Malicki, M.; Giordano, A. J.; Armstrong, N. R.; Marder, S. R., Characterization of Phosphonic Acid Binding to Zinc Oxide. *J. Mater. Chem.* **2011,** *21* (9), 3107-3112.
117. Hurley, B. L.; McCreery, R. L., Covalent Bonding of Organic Molecules to Cu and Al Alloy 2024 T3 Surfaces Via Diazonium Ion Reduction. *J. Electrochem. Soc.* **2004,** *151* (5), B252-B259.
118. Puziy, A. M.; Poddubnaya, O. I.; Socha, R. P.; Gurgul, J.; Wisniewski, M., XPS and NMR Studies of Phosphoric Acid Activated Carbons. *Carbon* **2008,** *46* (15), 2113-2123.
119. Pantea, D.; Darmstadt, H.; Kaliaguine, S.; Roy, C., Heat-Treatment of Carbon Blacks Obtained by Pyrolysis of Used Tires. Effect on the Surface Chemistry, Porosity and Electrical Conductivity. *J. Anal. Appl. Pyrolysis* **2003,** *67* (1), 55-76.
120. Richard, W.; Evrard, D.; Gros, P., New Insight into 4-Nitrobenzene Diazonium Reduction Process: Evidence for a Grafting Step Distinct from NO_2 Electrochemical Reactivity. *J. Electroanal. Chem.* **2012,** *685* (0), 109-115.
121. Toupin, M.; Belanger, D., Spontaneous Functionalization of Carbon Black by Reaction with 4-Nitrophenyldiazonium Cations. *Langmuir* **2008,** *24* (5), 1910-1917.
122. Chambers, S. A.; Droubay, T.; Kaspar, T. C.; Gutowski, M., Experimental Determination of Valence Band Maxima for $SrTiO_3$,TiO_2, and SrO and the Associated Valence Band Offsets with Si(001). *J. Vac. Sci. Technol., B* **2004,** *22* (4), 2205-2215.
123. Heinhold, R.; Allen, M. W., Polarity-Dependent Photoemission of in Situ Cleaved Zinc Oxide Single Crystals. *J. Mater. Res.* **2012,** *27* (17), 2214-2219.

7 Conclusion

Metal oxides are used in a range of applications including energy storage and conversion, catalysis and electronics. For all of these applications, control of the properties of the metal oxide surface is essential to the performance and stability of these materials. The aim of this thesis work was to develop conditions to modify metal oxide materials with aryldiazonium ions, with particular focus on MnO_2 as an energy storage material and ZnO as a transparent electronics material.

Non-electrochemical methods to modify poorly conducting metal oxides with aryldiazonium ions in aqueous and non-aqueous conditions were investigated using SU-8 as a model non-conducting surface. Grafting of aryldiazonium ions to a non-conducting substrate has been achieved in aqueous conditions, at pH 7 and pH 10 using aryldiazonium ions with both electron-donating (MP) and electron-withdrawing (NP) aryl substituents. This provides a range of conditions that can be used to modify materials with different pH stability windows. At both pH values, it is expected that the mechanism proceeds by formation of aryl radicals. In pH 10 solution, grafting occurred rapidly regardless of substituent whereas in pH 7 solution, MP films formed more slowly than NP films. It is proposed that this difference in behaviour can be attributed to the diazohydroxide intermediate forming more easily for NBD than MBD. Thus grafting at pH 10 is recommended for attaching a larger range of functionalities with a shorter reaction time than in pH 7 solution. However, it should be noted that for reactive aryldiazonium ions like NBD, grafting at pH 7 resulted in thicker films – possibly due to the increased stability of the aryldiazonium ion at lower pH. In non-aqueous conditions, spontaneous grafting does not occur or is very slow. In the presence of a reducing agent, grafting was found to occur to produce dispersed polymeric species. This is likely a result of the rapid reaction with the reducing agent resulting in uncontrolled grafting, primarily between radicals in solution. Coverage of the surface may be improved by optimising the reaction conditions, such as by controlling the addition of reducing agent.

Modification of MnO_2 nanoparticles and electrodeposited films with aryldiazonium ions in aqueous and non-aqueous conditions was investigated as a method to improve performance and stability and as a platform to prepare novel electrode architectures for MnO_2 pseudocapacitors.

MnO_2 nanoparticles were successfully modified without an external reduction source with NP groups in basic aqueous solutions and AP groups in acetonitrile. In aqueous conditions, modification with NP groups is expected to occur by spontaneous formation of aryl radicals as proposed at SU-8 surfaces above. Modification with AP groups in acetonitrile without a reducing agent appears to be

unique to this modifier. Spontaneous reduction of the aryldiazonium ion by the MnO_2 material does not appear to have occurred as the average oxidation state of the MnO_2 decreased, rather than increasing as would be expected if it was acting as a reducing agent. The binding of NP and AP groups to MnO_2 surfaces was found to occur through Mn-O-C linkages as determined by XPS. Attachment by azo linkages may also occur, however, these are convoluted in the N 1s spectra by reduced NO_2 species and AP groups in NP- and AP-modified samples respectively. Characterisation of the effect of modification on the electrochemical behaviour of MnO_2 was complicated by variability in the modified nanoparticle electrodes. This difficulty was addressed in subsequent work using electrodeposited MnO_2 films discussed below. Modification of MnO_2 with aryldiazonium ions was also investigated as a method to prepare tethered assemblies with carbon particles to improve the conductivity and stability of MnO_2 electrodes. However, these materials contained a significant proportion of non-specifically adsorbed MnO_2 and unreacted particle aggregates. Further investigation of tethered assemblies requires development of optimised separation conditions to remove the unreacted material.

The effect of modification on the electrochemical behaviour of MnO_2 was investigated using CV and EIS on electrodeposited MnO_2 films. Surfaces prepared by electrodepositing MnO_2 films on GC electrodes allow direct comparison of the electrochemical response of the MnO_2 before and after modification. Electrodeposited MnO_2 films were modified non-electrochemically at pH 7 and pH 10 with NP and MP groups.

In pH 10 solution, measurement of the capacitance of the MnO_2 surfaces by CV before and after modification showed that the capacitance of the electrode after modification was enhanced at low scan rates but lowered at high scan rates. Both of these effects were larger at longer grafting times. In pH 7 solution, modification with NBD also resulted in enhanced capacitance at low scan rates whereas modification in MBD solution and treatment in the absence of aryldiazonium ion caused the capacitance to decrease significantly. The similar response for treatment at pH 7 in the presence and absence of MBD suggests that minimal modification with MP groups is occurring at pH 7, as was observed on SU-8 surfaces. As electrode performance was enhanced after modification with NP groups at pH 7 rather than degraded, this suggests that the modification process stabilises the surface.

The effect of modification on the frequency response of the MnO_2 was investigated by EIS. For all modified surfaces, the rate characteristics of the material were decreased significantly, supporting the decrease in capacitance at high scan rates observed by CV. Additionally, new features were

observed at medium to low frequencies associated with the aryl layer. It was determined by equivalent circuit modelling that these processes do not solely arise due to changes in the double-layer and pseudocapacitance processes of the MnO_2. It was proposed that these features arise due to the aryl film acting as a porous layer that impedes diffusion and thus negatively affecting the rate capability of the electrode. Convolution of this diffusion resistance with the pseudocapacitance process makes it difficult to accurately determine the effect of modification on the pseudocapacitance behaviour of the MnO_2 and thus the nature of the capacitance enhancement observed by CV. However, as no changes were observed in the parameters for the double-layer charge storage process, it can be inferred that the increase in capacitance after modification does not arise from etching of the MnO_2 increasing the active surface area and thus the double-layer capacitance. As no new redox peaks were observed in the CV curves, it is unlikely the enhanced capacitance is due to the introduction of new pseudocapacitance processes associated with the aryl layer. It was therefore proposed that the enhanced capacitance arises due to the modification of the MnO_2 surface with aryl layers introducing surface states into the MnO_2 band gap that act as additional sites for charge storage. Modification with monolayer films may enable this capacitance enhancement to be retained while decreasing the diffusive resistance introduced by the aryl layer.

The effect of modification on the stability of MnO_2 surfaces was investigated using CV by repeated cycling up to 10000 scans. The degradation of the surface was monitored by calculating the capacitance of the surface at each scan number. However, modification with aryl layers resulted in no change in the stability of the electrode compared to bare MnO_2 surfaces. The absence of an effect of modification on the stability of the surface may be due to the electrode architecture used in this work failing by loss of adhesion of the MnO_2 from the GC surface rather than breakdown of the outer MnO_2 surface. Thus it is possible that stability enhancements may be observed after modification for 3-dimensional MnO_2 electrode architectures where the dominant decomposition mechanism is by decomposition of the MnO_2 surface.

Conditions were developed to modify ZnO surfaces with aryldiazonium ions to improve their environmental stability and tune their electronic properties. Modification of polycrystalline MBE-grown surfaces was investigated using spontaneous and electrochemical grafting in aqueous solution. Electrochemical grafting was then applied to bulk single crystal ZnO surfaces to examine the effect of crystal structure on the modification process.

Modification of MBE-grown surfaces by non-electrochemical methods in pH 8 buffer solution was found to damage the surface at low buffer concentration. Increasing the buffer concentration

enabled attachment of NP and CP groups as determined by FT-IR spectroscopy. Electrochemical modification in pH 8 buffer was used to attach NP, MP and IP groups to the surface. Although enhanced reduction currents compared to the blank samples were observed when cycling in the presence of aryldiazonium ions, there were no clear reduction peaks or blocking behaviour observed, as would be expected from an electrochemical grafting reaction. Analysis of the modified surfaces by FT-IR showed successful grafting for all aryldiazonium salts, indicating modifiers with a range of electronic characters can be attached to ZnO by this method. Comparison of the FT-IR peak areas showed that electrochemical modification resulted in increased coverage of the surface compared to spontaneous modification. XPS analysis of an electrochemically-prepared NP-modified surface provided further evidence of successful modification as signals associated with NO_2 groups were observed in the N 1s spectrum. A second peak related to either reduced NO_2 groups or azo-linkages within the film or to the surface was present, however, this could not be definitively assigned. No additional peaks associated with covalent bonding as for the MnO_2 materials were observed in the O 1s spectrum of the NP-modified ZnO surface, however, there was a significant increase in the peak associated with surface O content for the modified sample. As this was accompanied by an increase in P content in the modified sample, it is most likely caused by adsorption of phosphates from the buffer solution at the surface.

O-polar, Zn-polar and m-plane single crystal ZnO surfaces were modified to investigate the interaction between their differing surface chemistries and the grafting process. Electrochemical modification was used due to the higher grafting density observed using this method on MBE-grown surfaces. As with modification of MBE-grown ZnO surfaces, the CV response for modification of single crystal ZnO in the presence of aryldiazonium ions had higher maximum currents than in the blank samples. However, no signs of modification with an aryl layer were observed by XPS or FT-IR. This suggests that reduction of aryldiazonium ions is occurring at the single crystal ZnO surfaces, but the subsequent grafting of the aryl radical does not occur at the surface. Significant P content was observed for all samples after electrochemical cycling, but was highest for samples treated with aryldiazonium ions. Additionally, the P-content of the modified samples was found to vary between crystal phases based on the extent of O-termination of the surface (O-polar > m-plane > Zn-polar). Shifts in valence band edge position corresponding to an increase in downward band bending were observed by XPS for NBD- and IBD-modified O-polar samples, suggesting introduction of a surface donor species. As these changes did not directly correlate to P-content, multiple phosphate species may be involved and only some of them contribute to the electron accumulation at the ZnO surface. For ZnO surfaces, where modification by self-assembled monolayers is well-established, modification

using aryldiazonium ions has the advantage of producing stable covalently attached layers without additional processing steps such as annealing or lengthy reaction times. However, further experiments in either a different buffer system or in non-aqueous conditions to remove the interference of phosphate adsorption are needed to improve aryldiazonium ion grafting to ZnO and properly investigate the effect of modification on these surfaces.

In summary, this thesis work illustrates that aryldiazonium ion modification can be used to modify materials with varying conductivity and solution stability with a range of chemical functionalities. However, the reaction conditions need to be carefully optimised to achieve controllable modification and avoid side reactions such as those observed at ZnO surfaces. Changes in chemical, physical and electronic properties after modification were observed for the metal oxide materials in this study but fine tuning through selection of aryl substituents was not achieved. This most likely arose due to the films grafted in this work being multilayers and thus the effect of the aryl substituent is diminished by the aryl groups grafted at adjacent positions.

Future work on modifying metal oxide materials with aryldiazonium ions could improve control over the modified surfaces by using techniques to limit grafting to a monolayer. In addition to producing more well-defined surfaces, this may also allow improved tuning of the properties of the modified surface through the aryl substituent as it will have a more significant influence with a monolayer film. This is particularly relevant for the MnO_2 materials studied in this thesis work as monolayer modification may enable capacitance to be increased without negatively impacting the rate capability of the electrode by lowering the diffusion resistance associated with the aryl layer. As modification of MnO_2 materials has been conclusively demonstrated, the use of aryl layers as a platform to attach new functionalities or prepare new electrode architectures can be fully explored. The use of aryl tether layers to prepare MnO_2 electrodes with array-type architectures has the possibility to improve conductivity and stability in pseudocapacitors, electrocatalytic devices and sensors based on MnO_2. In addition to these performance improvements, aryl tether layers could be used to prepare tandem sensing platforms by introducing functionalities that operate via a different mechanism to the electrocatalytic processes used in MnO_2-based sensors and thus detect multiple analytes on the same sensor. Although the method used in this work to prepare tethered assemblies requires further improvement to isolate the assemblies, these preliminary results and work by other researchers suggests this concept has merit. To further the development of modification conditions for poorly conducting surfaces, refinement of the grafting procedure in non-aqueous solutions is needed to produce uniform aryl layers on materials requiring processing in dry conditions. These non-aqueous modification conditions, in addition to alternative aqueous buffer conditions, could be

adapted to the modification of ZnO surfaces to avoid interference from the phosphate buffer system used in this thesis work. This would then enable characterisation of the effect of aryl modification on the electronic properties and stability of ZnO and whether these properties can be tuned by selection of appropriate aryl substituents.